الادارة الكلفوية الكفؤة في مشاريع الاسكان

د. د.صفاء الدين حسين
استاذ مساعد
قسم العمارة / الجامعة التكنولوجية

د. ساجدة كاظم الكندي
مدرس
كلية الهندسة/ جامعة بغداد

د.كريم حسن علوان
استاذ
المعهد التكنولوجي/ بغداد

الخلاصة

تعد الادارة الكلفوية لمؤشرات الكلفة في المشاريع الاسكانية على مستوى التخطيط والتصميم من اهم مؤشرات جودة المشاريع الاسكانية لاعتمادها الستراتيجيات التخطيطية والتصميمية الكفؤة في ادارة تلك المؤشرات لذا يجد البحث الحالي ضرورة تسليط الضوء على اهم المؤشرات الكلفوية الفاعلة والمؤثرة في كلفة المشاريع الاسكانية ليتم تحديد كفاءة الستراتيجيات التخطيطية والتصميمية المنتخبة في ادارة تلك المؤشرات لرفع كفاءة جودة المشاريع االسكانية بما يلائم مستوى دخل الفئة المستهدفة مع مراعاة جودة المعايير الاسكانية اللائقة لتوفير اهم احتياجات الساكن الاساسية لذا يسلط البحث الضوء على اهمية الادارة الكلفوية وانواع الكلف الاسكانية واساليب السيطرة على الكلف وابرز الستراتيجيات التخطيطة والتصميمية الواجب اعتمادها لتحقيق ادارة كلفوية كفؤة في المشاريع الاسكانية معتمدة احدى المشاريع المحلية المحالة للتنفيذ لقياس مؤشراتها الكلفوية واختبار مدى كفاءة الادارة الكلفوية المعتمدة على مستوى التخطيط والتصميم للمشروع الاسكاني .

الكلمات الرئيسية: الادارة الكلفوية. المؤشرات الكلفوية.ستراتيجيات الادارة الكلفوية

Efficient Cost Management in the Housing Projects

Safaa AL-Deen Husain
Assistant professo
Safaa Alsamaraee.@yahoo.com

sajeda kadum alkindi
instructor
Sajeda.kathum@yahoo.com

Kreem Hassn Alwan
professor

ABSTRACT

The cost management of cost indicators in housing projects, on the level of planning and design, is the most important quality indicators, for adoption of strategies of planning and design efficient in managing these indicators. So this research points out the need to highlight the most effective and influential cost indicators in housing projects, and to determine strategies in the management of these indicators in order to raise the efficiency of housing projects quality, to seemly the income level target group, taking into consideration the quality of housing standards, to achieve the basic requirements of housing. This paper highlights the importance of the cost management, the types of housing cost, the method of control and the most important planning and design strategies to be adopted in order to achieve efficient cost management in housing projects. One local project under construction was selected as case study, to evaluate the application of the indicators the efficiency of the cost management on planning and design levels.

1- المقدمة: تعد الادارة الكلفوية في المشاريع عموما والاسكانية خصوصا مؤشرا حقيقيا على نجاح المشاريع في تلبية حاجة الفئة المستهدفة منها بانتخابهاالستراتيجيات التخطيطية الكفؤة في ادارة كلفة المشاريع ،جاعلة من امكانية الفئة المستهدفة وتلبية متطلباتها الاساسية هدفا استراتيجيا في تحديد الانشطة الادارية والتخطيطية في ادارة المؤشرات التخطيطة والتصميمية للمشاريع الاسكانية لذا **يحدد البحث الحالي مشكلته البحثية** في تحديد ابرزالمؤشرات الكلفوية ذات التاثير المباشر وغير المباشر على الكلفة التخطيطية والتصميمية للمشاريع الاسكانية للسيطرة اوللتحكم بها، بانتخاب الستراتيجيات الادارية الكفؤة على مستوى الادارة التخطيطية والتصميمية لهذه المشاريع لتحقيق الاهداف الاستراتيجية المحددة لها لتحقيق جودة الاداء، والالتزام بالبرنامج الزمني المحدد والادارة الكلفوية الكفؤة لتحقق مشاريع

اسكانية تلائم المدخولات المتنوعة للفئات المستهدفة من تلك المشاريع وبهذايكون البحث الاطار العام لمشكلته البحثية، لذا تطلب الامر تسليط الضوء على اهم تلك المؤشرات الكلفوية المؤثرة في الادارة الكلفوية لمشاريع الاسكان وتحديد اهم الاستراتيجات التخطيطية والتصميمية التى يمكن اعتمادها لادارة تلك المؤشرات ، و**لتحقيق الاهداف** في ايجاد مشاريع اسكانية ملائمة لامكانيات ومتطلبات الفئة المستهدفة من تلك المشاريع تم تسليط الضوء على اهم الستراتيجيات التخطيطية والتصميمية الفاعلة في خفض كلف المشاريع الاسكانية مع الحفاظ على المعايير اللائقة للسكن،وليحدد البحث بذلك **فرضيته:**ان الادارة الكفؤة للمؤشرات الكلفوية دور في رفع كفاءة الادارة التخطيطية والتصميمية لمشاريع الاسكان.ليحدد البحث ابرز الستراتيجيات التخطيطية–التصميمية الواجب اعتمادها في ادارة المؤشرات الكلفوية الفاعلة والمؤثرة في كلفة الوحدة السكنية لتلائم مستوى مدخولات الفئة المستهدفة من تلك المشاريع الاسكانية معتمدة مشروع ضفاف كربلاء السكني مستوى مدينة متكاملة الخدمات(احد مشاريع الهيئة الوطنية للاستثمار) حالة تطبيقية للاهم الستراتيجيات الادارية الفاعلة على مستوى الادارة التخطيطية –التصميمية في تلك المشاريع.

2- الادارة الكلفوية: تعرف الادارة الكلفوية في المشاريع ،بانها مجموعة العمليات المتضمنة عملية تخطيط الكلفة ،عملية تخطيط الميزانية وعملية مراقبة الكلف والتحكم بها. يطلق على هذه العمليات بالأدارة الكلفوية للمشاريع والتي تعني بإدارة تكاليف المشروع وكلفة الموارد اللازمة لأنهاء أنشطة المشروع والجدولة الخاصة به أخذة بنظر الأعتبار كلفة الصيانة ودعم منتج المشروع أو خدمته أو نتائجه خلال دورة حياه المشروع (المرجع الاساس لادارة المشاريع ،2011، ص- 76). تظهر الحاجة الى دراسة الأدارة الكلفوية لمشاريع الأسكان أهمية قصوى لمعرفة أدارة الكلف الأجمالية لمشاريع الأسكان في مرحلة التصميم وقبل التنفيذ، لتقليص الفجوة الحاصلة بين عملية التصميم والتنفيذ لتحقيق ادارة كلفوية كفؤة لمشاريع الاسكان وتمكين الفئة المستهدفة من تلك المشاريع. ولمعرفة أدارة الكلف التخطيطية والتصميمية لمشاريع الأسكان لابد لنا من معرفة عمليات ادارة الكلف وادارة عناصرها لتحديد أهم المؤشرات الكلفوية و الستراتيجيات الادارية الكفؤة لتحقيق ادارة كلفوية كفؤة في المشاريع الاسكانية ،تمكن الفئة المستهدفة من كلفة الوحدة السكنية في تلك المشاريع .ومن هنا تظهر اهمية الادارة الكلفوية في المشاريع (المصدر السابق،،ص-77).

3- أهمية الأدارة الكلفوية : لقد شكلت مجموعة المسببات المتراكمة من تغييرات في الكلف وأنظمة التمويل عبر الوقت سبباً رئيساً في توجيه جميع المهتمين بقضايا الأسكان من معماريين و مخططين ومطورين وممولين وصانعي القرارالى الأهتمام بتوفير الأسكان الأقل كلفة والملائم للأحتياجات الأجتماعية والمتطلبات الوظيفية والبيئية للأسر ولمختلف المدخولات ، ما أسفر عن ظهور الحاجة الى سكن يلائم الظروف الأقتصادية(T.Achoff,2004,p.9)، ليصبح التوجه في مجال الأسكان يصبو نحو تحقيق الأقتصاد في كلف المشاريع معتمدا الأدارة الكلفوية الكفؤة للمشاريع الأسكانية،ساعياً لتوفير سكن ملائم ضمن الإماكانيات المادية لشريحة كبيرة من المجتمع وخاصة بعد الأرتفاع الكبير في الكلف التي يشهدها العالم عموماً والعراق على وجه الخصوص . فضلاً عن سياسات التمويل التي كانت سببا في العجز السكني والنقص الواضح في معدلات التشييد الأسكاني، ما أدى الى تفاقم المشكلة وتحويلها الى أزمة سكنية خانقة . أن تحقيق أدارة كلفوية كفوءة في مشاريع الأسكان يعد من أولويات وقتنا الحالي الذي يعاني من تقلبات أقتصادية ومحدودية دخل شريحة كبيرة من المجتمع .

4- ادارة العمليات الكلفوية في مشاريع الاسكان: تتضمن الأدارة الكلفوية في المشاريع الهندسية مجموعة عمليات اللازمة لتقدير الكلف ووضع الميزانيات والتحكم بها ليتم أنجاز المشاريع ضمن الميزانية المحددة مسبقاً ، تتألف عمليات أدارة الكلفة من :

- عملية تخمين الكلفة(Estimate Cost) : حيث يتم تقدير الكلفة اللازمة(بعد تحديد انواعها وتصنيفها الى مباشرة وغير مباشرة) لأنجاز أنشطة المشروع.

- عملية تحديد الميزانية(Determine budget): وهي عملية تحديد الكلف المقدرة للأنشطة الفردية أو لمجموعات الأعمال لتأسيس خطة كلف مرجعية (أسترشادية) معتمدة .
- عملية السيطرة (التحكم) بالكلف (Control Cost): هي عملية مراقبة المشروع لتحديث الميزانية وأدارة التغيرات الحاصلة في خطة الكلف المرجعية (الأسترشادية) المعتمدة .

يطلق على مجموع هذه العمليات بالأدارة الكلفوية للمشروع والتي تعني بإدارة تكاليف المشروع وكلفة الموارد اللازمة لأنهاء أنشطة المشروع والجدولة الخاصة به أخذة بنظر الأعتبار كلفة الصيانة ودعم منتج المشروع أو خدمته أو نتائجه خلال دورة حياه المشروع (Thomton,2008,p.29).

5- انواع الكلف في مشاريع الأسكان: تعتمد الادارة الكلفوية على نمط الكلف بالدرجة الاولى ،وبمان تصنيفات كلف المشاريع الهندسية المتعددة تنطبق على المشاريع الأسكانية ، لذا سيتم اعتماد اكثرها شيوعا لاغراض البحث ،و يجد البحث ضرورة عرض التصنيفات المتعددة لكلف المشاريع الاسكانية كما يلي :-

اولا: يصنف بوني (Bonnie) كلف المشاريع الأسكانية الى :

- كلف مباشرة : وهي الكلف القابلة للتحميل على الأنشطة المحددة للمشروع وتشمل (كلف الأرض الحضرية – كلف أنشاء الطرق – عناصر التنظيم الفضائي – كلف الخدمات الفنية – كلف الخدمات الأجتماعية – كلف بناء الوحدات السكنية)
- كلف غير مباشرة : والتي لايمكن تحميلها على الأنشطة المحددة للمشروع وتشمل الكلف المستقبلية مثل (الصيانة – التشغيل – جمع النفايات – كلف الأستبدال – الكلف المهنية (الأجور الأستشارية) تصميم تخطيط الكلف والتأمين وتعديلات التصاميم وكلف الادارة الهندسية.(Bonnie j.B,1998,P.15).

ثانيا: ويصنفها باري (Barry) الى :

- الكلف المتعلقة بالأرض : طبوغرافية الأرض وأنحدار التربة وأنواعها وتحملها .
- الكلف المالية والقانونية للمشروع : كلف أستعمالات الأرض الحضرية والضرائب والرسوم وغيرها .
- الكلف للخدمات العامة : وتتعلق بتوفير أبنية الخدمات العامة (التعليمية – الصحية – الدينية .. الخ) .
- كلف الخدمات الفنية : وهي كلف الطرق وتجهيز البنى التحتية (الكهرباء – ماء – نقل العام وأضاءة الشوارع وتجميع النفايات) . (Barry,1983,p.3-7)

ثالثا: ويصنفها (Oktay) كلف مشاريع الأسكان الى :

- كلف الأرض (كلف الموقع – الخدمات) .
- الخدمات الفنية وتشمل البنى الفنية والخدمات العامة .
- مواد البناء (عناصر الأنتاج ، الطابوق ، البلوك ، السمنت) .
- الموارد البشرية (الأيدي العامة) . (Oktay,1980,p.7)

6- تصنيف الكلف في المشاريع الاسكانية : يصنف البحث الكلف في المشاريع الاسكانية في ضوء التصنيفات السابقة كما يلي :-

6-1- الكلف التخطيطية للمشاريع الأسكانية : وهي تشمل مرحلة التقويم الأقتصادي للمشروع وتحديد رؤية الممول للمشروع الأسكاني (تحديد رأس مال المشروع (الكلف) – تحديد عوائد المشروع (الأرباح) والتي تقع ضمن ثلاثة مرحل تخطيطية هي كما يلي :

- تخمين كلف المشروع Estimate Cost ⇐ لتحديد كلف انشطة المشروع الاسكاني .

- تحديد الميزانية Determine budget ⇐ لتحديد الكلفة المرجعية (الأسترشادية) لكل نشاط في المشروع الاسكاني .
- السيطرة اوالتحكم بالكلف Control Cost ⇐ أدارة التغيرات المتوقعة اوالمحتملة لكلف المشروع الاسكان .(المرجع الاساس لادارة المشاريع,p.77,2008). يتم خلال مرحلة تخطيط كلف المشاريع الاسكان تحويل الرؤية الى أهداف ، بتحديد نسب أستعمالات الأرض وتحديد نمط السكني للمشروع وتحديد الكثافة الأسكانية للمشروع والافراز السكني للوحدات السكنية.. وتشمل مجموعة من الكلف على المستوى التخطيطي للمشاريع الاسكانية مايلي :

6-1-1- تخطيط كلف الموقع للمشروع الأسكاني :وتشمل الكلف التالية:

اولا- تخطيط كلف أنشاء الوحدات السكنية: والتي ترتكز على المعايير التخطيطية والتصميمية الأسكانية والتي بمجملها تتحكم بكلفة المسكن ومدى ملائمتها للمدخولات المتنوعة للأسر وتشمل :- **القرارات التصميمية - المساحة البنائية - التقنية التنفيذية - تمويل المشروع**

ثانيا - الكلف التشغيلية : وهي كلف مهمة لها دور كبير في كلف المشاريع الأسكانية والتي تشمل :- كلف الأستهلاك - كلف الأدامة .

ثالثا- الكلف المهنية : وهي كلف الدراسات الأولية والتصاميم والتعديلات والتأمينات والضمانات فضلاً عن الكلف التسويقية والدعائية للمشروع السكني . أي أن الكلف التخطيطية تتضمن الكلف المباشرة وغير المباشرة للمشروع الأسكاني خلال دورة حياة المشروع ككل.

6-2- الكلف التصميمية للمشروع الأسكاني: وتشمل كلف تصاميم ارض الموقع السكني وكلف تصاميم الوحدات السكنية ،وكلفة البنى التحتية (الفنية والاجتماعية). وعليه يمكن تصنيف الكلف التصميمية لمشاريع الاسكان الى الانواع التالية:-

اولا:كلفة الأرض للموقع السكني : تبلغ كلفة الأرض للموقع السكني حاليا ثلاث - اربع اضعاف كلفة المشروع السكني والتي تنعكس على ارتفاع كلفة أنشاء الوحدات السكنية. تحتل كلفة الأرض أهمية كبيرة في أرتفاع أسعار المساكن في المشاريع الأسكانية المختلفة . ترتبط كلفة ارض الموقع السكني بمجموعة عوامل تؤثر على معدل كلفة الأرض وهي كما يلي :

- موقع الأرض للمشروع السكني وبعدها عن المراكز الحضرية.
- مساحة الأرض للمشروع والظروف الطبيعية المحيطة .
- قلة الأراضي السكنية المتوفرة نتيجة المضاربات .
- قلة الأراضي القابلة للتطوير والأستثمار السكني وهي من أكبر تحديات العمل في القطاعات الأسكانية والعقارية ،مما يولد فجوة بين كلفة الأرض ومستوى دخل الأسرة في أمتلاك الأرض السكنية وأقتصرها على ذوي الدخل العالي .
- الكثافات المنخفضة التي تسبب بأرتفاع كلف الأرض وخدمات البنى التحتية . **فضلا عن عوامل اخرى مؤثرة كتوفر المياه ،العوامل المناخية ،التلوث في الموقع ، طرق النقل والمواصلات ،مقومات الموقع السكني ،التنظيم الفضائي،الأفراز السكني والكثافات الأسكانية**

ثانيا:كلف الوحدة السكنية: ترتبط الأدارة الكلفوية للوحدة السكنية بعناصر تشيد الوحدة السكنية وهي الأعتبارات التخطيطية والتصميمية والمساحة المبنية ومراحل التشيد البنائية (المواد الأنشائية ، الأيدي العاملة ، التقنية البنائية) وتمويل الوحدة السكنية الذي يتلائم مع الدخل السنوي للمستفيدين(والتي سيتم تفصيلها في الفقرات اللاحقة) .

ثالثا:كلف خدمات البنى التحتية:وتشمل كلف البنى التحتية الاجتماعية (الابنية التعليمية والثقافية والتجارية المتنوعة والصحية) وكلف البنى التحتية الفنية (الماء الكهرباء الصرف الصحي ومياه الامطار والطرق والمواصلات ...الخ)،والتي سيتم تفصيلها في الفقرات اللاحقة.

6-3- الكلف التنفيذية والتقنية البنائية – كلف الانشاء: وتشمل كلف الانظمة و الاساليب والتقنيات البنائية المستخدمة في تنفيذ المشاريع الاسكانية واثر الانظمة القنيات البنائية المستخدمة في خفض الكلف المشاريع الاسكانية من خلال ترشيد المواد الانشائية المستخدمة استخدام والتقيس والتنسيق النمطي فضلا عن ادارة العوامل المؤثرة بكلفة المشاريع الاسكانية (الكلف المباشرة- وغير المباشرة)و ادارة العوامل التنفيذية المؤثرة في كلفة المشاريع و ادارة المؤشرات التنفيذيةالمؤثرة في الكلفة وتشمل كلف التقنية البنائية المنتخبة لانشاء الموقع السكني والوحدات السكنية وخدمات البنى التحتية (الاجتماعية- الفنية) ،لتحديد كلفة المتر المربع للانشاء وكلف المواد والايدي العاملة ..الخ،حيث سيتم شرحها لاحقا بالتفصيل وهي ليست محور البحث.

7- أدارة اساليب تقدير الكلفة في المشاريع الاسكانية : يعد تقدير كلفة المشاريع الاسكانية ذي تاثير كبير في المراحل الاولى من المشروع السكني حيث يقوم فريق ادارة المشروع بجهد تخطيطي يسبق العمل اللازم لانجاز عمليات ادارة كلفة المشروع الاسكاني الثلاثة ،هذا الجهد التخطيطي المسبق هو جزء من عملية تطوير خطة ادارة المشروع الاسكاني والذي ينتج عنه ادارة كلفوية كفؤة للمشروع(المرجع الاساس لادارة المشاريع،2011،ص.77). وهومساويا في أهميته الجدوى الاقتصادية والجدولة لمراحل التنفيذ في أثناء التأخير الناتج من المناقصات المرتفعة التكاليف وقلة مصادر التمويل أو قلة عوائد المشاريع خاصة السكنية منها ،حيث أن مسائل التضخم المالي ومشاكل العمالة وشح الموارد اللازمة وقلة الوقت وبعض المشاكل التي تؤثر بشكل مباشر في التحكم أو السيطرة على بعض الكلف ولاسيما في العراق.ان أدارة تقدير الكلفة التي تتم عادة كجزء من مرحلة التصميم ويتم مراجعتها تباعاً الى المراحل النهائية للمشروع ، بأعتماد ثلاثة أساليب لأحتساب الكلفة ترتبط أرتباطا وثيق بمراحل العملية التخطيطية والتصميمية لأعداد تقديرات الكلفة كما يلي .(اليوسفي ،2008،ص.95):

اولا:أسلوب التقديرات الأجمالية : حيث يتم أعتماد التقديرات الأجمالية لأنشطة المشروع وهي الأكثر شيوعاً في المراحل المبكرة في أعمال التصميم ، معتمدة عملية تحديد ميزانية المشروع السكني (مرحلة الدراسات الأولية) وقبل الشروع في أعمال التصميم أو في مرحلة التصميم الأولية (Concept) حيث يتم أعتماد وحدة العمل (الفقرة) قياساً لتقدير الكلفة الأجمالية (المتر المربع للمباني كوحدة قياس – أو متر طول لأعمال الحفريات أو الطن لأعمال التبريد وهكذا) حيث تكون الكلفة الأجمالية للفقرة عبارة عن (حاصل ضرب عدد الوحدات في سعر وحدة العمل) ليكون المجموع النهائي ناتجاً للفقرة من مجموع أسعار الفقرات كافة . ((عدد الوحدات × سعر الوحدة = سعر الفقرة الواحدة)).(المصدر السابق،ص.97)

ثانيا: أسلوب تقدير الكلفة بالنسق أو النظام الموحد: يتم تقسيم أعمال المشروع ومكوناته وتصنيفها الى أنظمة ثانوية أعتماداً على.المجال الوظيفي ،أوالأدائي وكل مكون يتفرع الى فقرات أصغر تسمى مستويات (مثل أعمال الأنشائية – المدنية – الميكانيكية – الكهربائية – الصحية وهكذا) حيث يتم تقسيمها كل من هذه الأنشقاق الى فقرات فرعية وعناصر أكثر تفصيلاً ، يمتاز هذا الأسلوب قابليته على مواطن التكلفة العالية بوضوح وهي أسلوب مراجعة واضحة لأعمال التصميم حيث قد يكون سعرا المتر المربع من أعمال التغليف بالمرمر معقول لكن كمية التغليف مبالغ فيها . يعتمد هذا الأسلوب نسق موحد يطلق عليه نسق أو نموذج الكلفة حيث يقسم أنشطة المشروع الى أثنى عشر تبدأ بناء على المجال الوظيفي وكل بند من تلك البنود يتفرع الى مستويات أصغر حتى يصل الى المستوى الرابع لأغراض تخص حسابات الكلفة ويعتمد الكثير من مخمني الكلفة أن هذا الأسلوب ملائماً حينما يكون التصميم في حدود 50% فما دون وهو يستخدم في الدراسات القيمة لتقدير الكلف. (المصدر السابق،ص.98)

ثالثا: أسلوب تقدير الكلفة التفصيلية :يتم أحتساب الكلف على واقع وثائق التصميم (مخططات – جداول الكميات – مواصفات) وتكون هذه التنقديرات نهائية ، حيث المخططات مكتملة والكميات محدودة والعناصر معرفة . وهذا مايطلق عليه جداول الكميات وهي مرحلة متقدمة لايتم تغير المخططات التصميمية فيها إلا في حالات نادرة كأن يكون المشروع مصمم منذ فترة طويلة مما يعني أجراء الدراسة واعادة التصميم بناء على نتائجها. أن تقدير الكلفله تأثير كبير في العمل الأستشاري لمشاريع الأسكان من خلال جدوى أختيار الأفكار

المعمارية والمقترحات التصميمية القابلة للتطبيق ، وهي أداة مهمة لأتخاذ القرار وترجيح بديل على آخر يحقق كلاهما نفس الوظيفة الأساسية (المصدر السابق،ص.99). **ومما سبق يجد البحث ان ما يخص أساليب تقدير الكلف فأن التقديرات الأجمالية هي أقل دقة من غيرها لأن المعيار المعمول به واسع في حين أسلوب النظام الموحد يعطي فرصة مراجعة الكميات نفسها بناء على الوظيفة المطلوبة ، لأيجاد مقياس تقييم الكمية والفاعلية معاً أما أسلوب التقديرات التفصيلية للمشروع فهي تعطي جدولاً مفصلاً للكميات والمواصفات أذ تنتهي التقديرات التفصيلية للمشروع بأنتهاء المخططات التفصيلية للأعمال كافة مما يساعد على أحتساب الكلف التخمينية التنفيذية للمشروع وهي مرحلة متأخرة في مفاضلة الخيارات التصميمية. ولإمكانية التحكم والسيطرة على حساب الكلفة في مرحلة التصميم يفضل اللجوء الى تقدير تكاليف الأنظمة خلال مرحلة التصاميم بغرض أختيار الأفكار والمقترحات التي تحقق نفس الوظيفة والأداء بكلفة أقل كمدخل لأدارة الكلفة التفصيلية عند الأنتهاء من الأعمال التصميمة لغرض الوصول الى الكلف الحقيقية التنفيذية الخاصة بالمشروع الأسكاني . أن مهمة الجهة الأستشارية لاتتوقف عند الأنتهاء من تقدير الكلف وأعتمادها بل تتعداها الى السيطرة عليه اوالتحكم بها ومراقبتها أثناء التنفيذ والبحث عن المسببات الأيجابية والسلبية الحاصلة في مسار تخمين الكلف.وتعد المعلومات الميدانية قاعدة بيانات مهمة للسيطرة على التغيرات الحاصلة في التعديلات في أعمال التصميم ونتيجة حجم هذه التباين لتقييم تقدم المشروع الاسكاني.**

8- أدارة اساليب السيطرة(التحكم)على الكلف في المشاريع:أنماط أدارة التحكم في أدارة الكلفة متعددة تتشابه في النتائج وتختلف بالمنهج والأسلوب ولكي نصل الى شيء من التفصيل سنقوم بتقديم أيجاز عن الأساليب التي تتقارب في منهجيتها في أدارة الكلفة وهي كما يلي: 1- أسلوب تخفيض الكلفة 2- تحليل SWOT 3- قانون باريتو 4-أسلوب تريز5- أسلوب المراجعة الفنية 6- الأدارة القيمية . (ميريديث،1999،ص.138):

9- ستراتيجيات أدارة الكلف الأجمالية للموقع السكني: بعد تعريف أنواع الكلف الأجمالية وأساليب المتبعة في أدارة تقديرالكلف والسيطرة عليها ، يتم أستعراض ستراتيجيات أدارة الكلف الأجمالية للموقع وفق منج الأدارة القيمية وهو منهج مبدع يهدف الى التوفيق بين الكلفة والأداء لنظام ما ، كما أنه يأخذ القرار التصميمي الذي يهدف الى حذف الكلفة غير الضرورية دون المساس بالقيم الجمالية أو النوعية ويمكن أعتباره ستراتيجية لكفاءة الأداء ا بأستخدام المنهج المنظم للتوازن بين أعلى كفاءة وظيفية واقل الكلفة للمشروع الاسكاني (http://investpromo.gov-2013):.تشمل ستراتيجيات ادارة الكلف الاجمالية للموقع السكني مايلي

9-1- أدارة كلفة الأرض الحضرية : تعد الأرض المكون الأساس في الأسكان وتعد كلفتها العالية مقارن بالكلف الأجمالية للوحدة السكنية وتعد أحد العوامل التي تجعل الأسكان غير متاح، ويعود سبب الأرتفاع الى (قلة الأراضي السكنية المتاحة نتيجة المضاربة باسعارها وكذلك نقص في الأراضي القابلة للتطوير بعد قرار الحكومة المتضمن تعليق توزيع أراضي الدولة لغايات التطوير الحضري مالم يتم تحديث المخططات الرئيسية للمناطق الحضرية والتي تقرر بموجبها المناطق المناسبة للغايات الأسكانية(هالة صكبان،مؤتمر الاسكان الثاني،2012،ص.240) . أن الحد من أرتفاع أسعار الأراضي تقع على عاتق الدولة من خلال أتخاذ التدابير اللازمة من عمليات تطوير الأراضي ، تعديل معايير التخصيص وحجم القطع ووضع التعليمات والتشريعات التي تكفل الحد من المضاربة في أسعار الأراضي وغيرها للحد من أرتفاع كلفة الأرض الحضرية وهو ماحدث فعلاً في سياسة الأسكان الوطنية للعراق (2010) من خلال أتخاذ سياسات من شأنها الحد من المضاربة العقارية وتزيد من العرض السكني . يجدر الأشارة الى أن المشاريع المنفذة من قبل القطاع العام تنخفض فيها قيمة الأرض الحضرية لتكون شبه مجانية مما يشجع القطاع الخاص والمستثمرين نحو الأستثمار السكني من خلال تمليك الأرض للمستثمر مجاناً على أن لاتحتسب كلفةالأرض ضمن قيمة الوحدة السكنية(قانون الاستثمارالعراقي،2006،المادة 5-اولا) .مما يخفض كلف الوحدات

السكنية الى النصف . وهذا لايعطي المخطط أو المصمم حق عدم مراعاة الجوانب الكلفوية في أستثمار الأرض الحضرية للمشروع السكني لوضع تخطيط ستراتيجي لأدارة كلفة الأرض الحضرية للموقع السكني لابد من توضيح العوامل المؤثرة في كلفتها وهي كما يلي : ((موقع المشروع السكني عدد الطوابق في المشروع – توفر الخدمات الاجتماعية البنى التحتية والفنية و للمشروع – التنظيم الفضائي المعتمد في تخطيط الموقع السكني و الأفراز السكني والكثافات الأسكانية في المشروع)) .

اولا:ادارة موقع المشروع السكني :وحسب الأدارة القيمة لابد من جمع المعلومات عن الأرض الحضرية المراد أستثمارها سكنياً ودراسة العوامل المؤثرة على الموقع السكني والتي تم تثبيتها في بداية الفصل ،أن مجموعة العوامل المؤثرة في أنتخاب الموقع المناسب يمكن المخطط تمكن المخطط الحضري بعد مقارنتها للمواقع المختلفة وأختيار البديل الأنسب لأنشاء مشاريع أسكان مستدام وأقتصادي ويحقق وفرة في كلف الموقع الأجمالية للموقع السكني . يعد أعتماد الآليات والعوامل المؤثرة في أنتخاب الموقع السكني من خلال مقارنة العوامل المؤثرة في كلفة الموقع مع عدة مواقع لأنتخاب الموقع الأقل كلفة لأرض المشروع يمكن تحديد أهم الأستراتيجيات التخطيطية في أدارة الكلف للموقع السكني.

ثانيا:أدارة كلف الموقع على مستوى عدد الطوابق في المشروع السكني : تقل كلفة المتر المربع للأرض بالنسبة للوحدة السكنية من خلال زيادة عدد الطوابق للأبنية السكنية متعددة الطوابق وهو ماتشير اليه العديد من الدراسات في مجال الأسكان للدول النامية(Dakhil–1978–p33) .**وهنا نجد أهم مؤشر لأدارة كلفة الأرض الحضرية والمتمثلة بمؤشر كلفة الأرض الحضرية : مؤشر كلفة** الأرض 1/ عدد الطوابق.

ثالثا:أدارة الخدمات للبنى التحتية : تشكل كلف خدمات البنى التحتية (ماء – مجاري – كهرباء – مياه أمطار – أنارة شوارع) مانسبته (35 – 25%) من أجمالي كلفة المشروع في معظم مشاريع وزارة الأسكان والتعمير وهي نسبة كبيرة(القريشي–2006–217–p) لذا لابد من توفير الدولة لمثل هذه الخدمات للأراضي الحضرية المخصصة للأستثمار السكني ، وهنا تجدر الأشارة الى السياسة رقم (2–1–2) للأسكان العراقي حيث نصت هذه السياسة على (بيع الأراضي بالجملة لحشد رؤوس الأموال والخيرات من أجل تطوير الأرض (21) كأحد المشاريع التجريبية الريادية في العراق (اميرة جليل –2004–38–p)، حيث يتم تحديد قطعة أرض من قبل الحكومة الأقليمية أو المحلية قطعة أرض (100 – 50) هيكتار ويتم توفير البنى التحتية المطلوبة لهذه الأرض خارج الموقع لتقوم فيما بتقسيم القطعة الى عدد من القطع الأصغر مساحة (25 – 20) هيكتار والتي تباع بنفس السوق الى مطوري الأرض من القطاع .ليعملوا على تطويرها من خلال تقسيم الأرض وتوفير خدمات البنى التحتية الأساسية في الموقع يتم تسويق القطع في سوق السكن للمواطن لشرائها وتطويرها لبناء وحداتها السكنية (سياسة الاسكان الوطنية –2010– ص–11).

رابعا:أدارة الكلفة الأرض مستوى التنظيم الفضائي : أن أرتفاع نسبة الفضاءات المفتوحة ضمن النظام الفضائي يؤدي الى أنخفاض نسبة المساحات المخصصة للسكن مما يقلل عدد الوحدات السكنية الأجمالية في الموقع المؤلفة من – فضاءات مفتوحة – وحدات سكنية – خدمات عامة . أن **زيادة نسبة المساحة المخصصة للوحدات السكنية ينتج من أستثمار الأرض الحضرية وتقليل نسبة المساحة المخصصة للفضاءات المفتوحة . أي أن مؤشر أستثمار الأرض الحضرية = المساحة المخصصة للسكن / مساحة الفضاء المفتوح وهي متغيرة بتغيير التنظيم الفضائي للموقع السكني.** يعد قيمة المؤشر على قيم موازنة أستعمالات الأرض الحضرية والتي تساوي (المساحة السكنية الصافية / المساحة السكنية الاجمالية) (كراس معايير الأسكان لعام 2010) حيث تتراوح قيمة المسكن المنفرد الاسرة المنفصل وشبه المنفصل بين (0.63 – 0.8) بينما تتراوح قيمته بين (0.55 – 0.7) في المساكن المتصلة وذات الفناء ، أي أن الحد الأعلى والأدنى تعتمد على التنظيم الفضائي المعتمد في التصميم والتخطيط الحضري للموقع أو الحي السكن . **أي أن قيمة يؤشر أستثمار الأرض الحضرية عندما يساوي واحد أو يزيد من خلال أعتماد التنظيم الفضائي المعتمد لتحقيق الكفاءة في أدارة كلفة**

الأرض الحضرية لتحقيق الجدوى الأقتصادية ومن خلال تحليل الجدول أعلاه نجد أن أفضل الأنماط الفضائية هي النمط العضوي العشوائي والنظام الشبكي المتعامد المحرف كما يفضل البديل الثاني على الأول لصعوبة تنظيم حركة المركبات فيه مع مراعاة العوامل البيئة الأجتماعية فضلاً عن الأقتصادية .

خامسا:أدارة كلف الأرض على مستوى الأفراز السكني و الكثافة الأسكانية : توجه السياسات الأسكانية في العراق (سيأتي ذكرها في الفصل القادم) نحو الأسكان العمودي في محاولة للحصول على أفضل أستغلال للأرض ولتحقيق أعلى كثافة أسكانية ممكنة ومن ثم تقليص كلف الخدمات الفنية للمشروع ، لابد أن لايغفل أن أدارة تخطيط الكلف في أطار الكثافات الأسكانية العالية على مستوى السكن الأفقي أيضاً قد تحقق نفس الهدف من خلال العلاقة التي تم ذكرها سابقاً بين الأفراز السكني والكثافة الأسكانية ، مع العلم أنه لاتوجد مقارنة بين السكن الأفقي والسكن العمودي من حيث رغبة المستفيدين ، وتفضيل الأول لما يحقق من قيم أجتماعية وأقتصادية للمستفيد إلا أن ندرة الأرض تتطلب أدارة تخطيطية تعطي رفع مستوى الرصيد السكني لسد العجز الحاصل . علماً أن الكثافة الأسكانية كما ذكرنا بالتنظيم الفضائي المنتخب وكثافة الأستعمال للأرض والأفراز السكني لتحديد المسافات المنخفضة للسكن من خلال تحديد نسبة المساحة المثبتة الى المساحة الكلية ومن ثم تحديد كلفة تلك القطع ، والمضاعفة الكثافات الأسكانية لابد من مراعاة بعض الخطوات كنمط الأسكان المفضل ،مساحة الأرض المفرزة ،مرونة الخدمات الفنية والأجتماعية ويمكن حساب الكثافة الأسكانية عند الأفراز السكني أو بأعتماد مبدأ (المسكن لكل طابق) في المسكن الأفقي المتصل وبمساحة (200^{m2}) ومقارنتها مع الكثافات الناتجة من بناء الأبنية السكنية العمودية المنخفضة وعالية الأرتفاع في الجدول (1)، نجد أن الكثافة الأسكانية للسكن الأفقي تتخذ ثلاثة سيناريوهات مختلفة تقترب في بعضها من الكثافات الأسكانية العمودية العمودية وكالآتي :

جدول (1) يقارن الكثافة الأسكانية المتنامية للسكن الأفقي والعمودي(المصدر –الباحث بالاعتماد على كراس معايير الاسكان الحضري –2010)

ت	نمط السكن	عدد الطوابق	الكثافة الأسكانية	الكثافة السكانية	الكثافة البنائية
1-	مسكن أفقي متصل	(1) طابق	(12 – 23)	72 – 192	0.6
2-	مسكن أفقي متصل	(2) طابق	24 – 64	144 – 384	1.2
3-	عمارات سكنية	(3-4) طابق	20 – 60	100 – 250	(يعتمد حسب النمط السكني المنتخب)
4-	مسكن أفقي متصل	(3) طابق	36 – 96	216 – 576	1.8
5-	عمارات سكنية	(5-8) طابق	35 – 70	210 – 420	(يعتمد حسب النمط السكني المنتخب)

*** تم أيجاد الكثافات الأسكانية في هذا الحقل بأعتماد الكثافة الأسكانية بواقع (ستة أشخاص للمسكن)**

1- السيناريو الأول : مسكن واحد لقطعة الأرض المفرزة بواقع كثلفة إسكانية أجمالية تتراوح (32 –12) وحدة سكنية/هكتار – كثافة بنائية مقدارها (0.6) .

2- السيناريو الثاني: مسكنين بطابقين لقطعة الأرض الواحدة من خلال أعادة أفراز القطعة أو أعتماد (المسكن لكل طابق) للمقارنة الى الكثافة الأسكانية في المسكن الأفقي بواقع (46 – 24) وحدة سكنية للهكتار – بكثافة بنائية مقدارها (1.2) ، وهو مقارب الى الكثافة الأسكانية للعمارات السكنية منخفضة الأرتفاع (طابق 4 – 3) حيث تتحقق كثافة إسكانية تتراوح (60 – 20) وحدة سكنية للهكتار .

3- السيناريو الثالث : ثلاثة مساكن بثلاث طوابق بأعتماد مبدأ (السكن لكل طابق) لقطعة الأرض الواحدة لنحصل على كثافة أسكانية تتراوح بين (96 – 36) وحدة/ للهكتار وبكثافة بنائية (1.8) وهو مقارب للكثافة الأسكانية في العمارات عالية الأرتفاع (8 – 5) طوابق التي تحقق كثافة إسكانية تتراوح بين (70 – 35) وحدة/للهكتار .

نستنتج من هذه السيناريوهات أن الزيادة المتنامية والمستمرة للكثافات (الأسكانية – السكانية – البنائية) لها تأثير كبير في زيادة الأنتاج السكني والرصيد السكني من خلال زيادة عدد الوحدات السكنية قدر الإمكان حيث يؤثر بهذه الزيادة مؤشر الكثافة الأسكانية

= عدد السكان / مساحة الموقع الأجمالية) ولأن هذا المؤشر متغير في المساكن الأفقية بسبب الزيادة السكانية لذا فالكثافات الأسكانية غير ثابتة بل متنامية وبالأمكان قياس هذا التنامي من خلال مؤشر الكثافة المتنامية : = (الكثافة الأسكانية للسنوات المختلفة / الكثافة الأسكانية عند الأشغال)(المصدر -كراس معايير الاسكان الحضري-2010) وهو مؤشر مهم في حساب الكثافات الأسكانية غير المنتظمة والعشوائية (المناطق العشوائية) وهنا يمكن أستخدامه في حساب التنامي في الكثافات المتوقعة والمنتظمة . يزداد المؤشر الأخير مع زيادة الحاجة الفعلية للمساكن ورغبة الأسر في الأستثمار السكني وعدد الطوابق حيث يصل الى (3) صحيح عند بناء ثلاث طوابق بينما يكون في القيمة القياسية (1) صحيح عندما تكون المساكن طابق واحد (المصدر السابق). **يمكن ان نستنتج أن السكن الأفقي يوازي السكن العمودي في حل أزمة السكن والنقص في عدد الوحدات السكنية من خلال أعتماد نماذج تصميمية تتيح لهم الأستثمار الأمثل للطابق الأرضي مع تلبية الأحتياجات الأساسية بشكل كامل مع إمكانية التوسع العمودي مستقبلاً بمسكن متكامل يمكن أيجاره أو أشتغاله من الأفراد وتكوين عائلة مستقلة** . ومع صدور التعميم (2/721/4/2) في (2004-12-7) بإمكانية بناء ثلاث طوابق للمساكن يعتبر محفز تخطيطي لهذا التوجه في زيادة الكثافة الأسكانية حيث بسمح هذا التعميم بناء ثلاث طوابق على أن لايتجاوز أرتفاع المبنى عن مستوى الرصيف الى أسفل مرد الماء عند (9^m) . أن زيادة الكثافات الأسكانية المتنامية لها أيجابيات وسلبيات التي شخصتها(امانة بغداد-(2/721/4/2) في (2004-12-7) ولامجال لادرجها في البحث الحالي.

مما تقدم نستنتج أن قيمة مؤشر الكثافة المتنامية يجب أن لايصل الى (3) صحيح حيث أن الكثافة الأسكانية ستكون عالية جداً ومقاربة للكثافات المنخفضة في العمارات السكنية عالية الأرتفاع خاصة عندما يكون موقع الأرض للمشروع في مركز المدينة .مايدفع المصمم والمخطط الحضري اللجوء الى حلول تخطيطية تتوافق مع هذه الكثافات الأسكانية كعرض الشوارع وتوفير مواقف كافية مع أعتماد تصاميم منتخبة للخدمات الأجتماعية ذات مرونة عالية مع إمكانية التوسع المستقبلي. أن تحديد الكثافة الأسكانية للموقع السكني يؤثر على كلفة الأبنية السكنية ومن ثم كلفة الوحدة السكنية كما أن الكلفة الأنشائية تختلف أستناداً الى عاملين مؤثرين هما : الكثافة الأسكانية - أرتفاع المبنى . **نستنتج أن زيادة الكثافة الأسكانية يؤدي الى زيادة كلفة الأنشاء المخصصة للشخص الواحد من خلال زيادة كلف أضافية في الأبنية عالية الأرتفاع (المصاعد - الأسس وما شابه) و عليه لتحقيق الأهداف من أنشاء مدينة سكنية متكافلة الخدمات من الباحثة العمرانية والأقتصادية لابد من دراسة الكثافة الأسكانية لتحقيق إمكانيات تحقيق مشروع سكني يلبي الإمكانيات العمرانية والأقتصادية والأجتماعية والبيئية .**

<u>سادسا : ستراتيجيات الادارة الكلفوية للخدمات الأجتماعية :</u> تعتمد أدارة كلف الخدمات الأجتماعية في المشاريع الأسكانية على العناصر المكونة لهذه الخدمات وعددها والمساحة يعتمد عدد الخدمات الأجتماعية على الكثافة الأسكانية للمشروع من خلال أعتماد معايير مساحية لكل شخص(كراس معاييرالاسكان الحضري -2010-ص،17) . يمكن أدارة كلفة الخدمات الخدمات الأجتماعية من خلال تصنيفها في المشروع الى مستويان هما:

1- كلف البنى الأجتماعية على مستوى المحلة السكنية والتي تتضمن (400 - 600) وحدة سكنية وبواقع (6) شخص للأسرة .

2- كلفة البنى الأجتماعية على مستوى الحي السكني والتي تتضمن (1600-2400) وحدة سكنية بواقع ستة أشخاص للأسر الواحدة ويمكن أحتساب المساحات الكلية للبنى الأجتماعية في المستويين(المحلة-الحي السكني) .

<u>سابعا : ستراتيجيات أدارة كلف خدمات البنى التحتية الفنية في المشاريع الاسكانية</u>: سيتم تصنيف انواع كلف خدمات البنى التحتية الفنية ليم استعراض ابرز الستراتيجيات التخطيطية لادارة كلفويا حيث يمن تصنيفها كما يلي(المصدر السابق-ص،76): اولا:كلف شبكة المجاري (المياه الثقيلة - مياه الأمطار) ثانيا:كلف شبكة المياه الصافية ثالثا: شبكات الكهرباء رابعا:كلف أنارة طرق النقل.

ثامنا :الأدارة الكلفوية لخدمات البنى التحتية الفنية للمشاريع الاسكانية: تتمثل أدارة كلفة الخدمات البنى التحتية الفنية المطلوبة من خلال القرار التخطيطي للمصمم في أعتماد أقصر مسار لهذه الخدمات مقابل خدمة أكبر عدد من قطع الأراضي السكنية أو الأبنية السكنية وهنا يبرز أهم مؤشر في أدارة الكلفة للخدمات التحتية للمشاريع الأسكان والذي يرتبط بالكثافة الأسكانية و معدل كلفة الخدمات الفنية للسكن الواحد.ويساوي (كلفة خدمات البنى التحتية /عددالوحدات السكنية). أن الأدارة الكلفوية الكفوءة تعتمد على أقل قيمة لهذا عدد الوحدات السكنية المؤشر لأنها ستعمل كدالة لقياس نجاح المخطط والمصمم في أدارة كلف البنى التحتية للمشروع الأسكاني دون المساس بالأداء الوظيفي وكفاءة في وقت تنفيذ المشروع(محمدسعيد -2014-60-p). ويمكن أعتماد أدارة كلفوية فاعلة للخدمات الفنية حسب الفقرة المكونة لهذه الكلفة ويمكن وضع منهجية تحليلية للمعلومات الخاصة بالبنى الفنية لأعتماد البديل الأفضل كلفوياً وأدائياً حسب الأدارة القيمية وكمافي الجدول (2) :

جدول (2)الادارة الكلفوية لخدمات البنى التحتية(المصدر-الباحثة)

الفقرة	أدارة قيم مؤشرات أدارة الكلفة الخدمات البنى التحتية لكل فقرة
أنشاء الطرق والأنارة	1- تنظيم فضائي تقل فيها نسبة مساحة الطرق والرصفة والتي يمكن أدراجها حسب ملائمتها فالأقل كلفة وهي 1- النمط العضوي 2- الخطي 3- اللساني 4- الشبكي المتعامد المنحرف 2- أعتماد الحد الأدنى لعرض الطرق والأرصفة والحد الأعلى لطول البلوك السكني لتقل المقاطعات حسب مواصفات شبكة الطرق .
شبكات البنى التحتية الفنية (الماء – المجاري – مياه الأمطار – الكهرباء)	1- أعتماد تنظيم فضائي يتم فيه أعتماد أقصر المسافات للطرق لمد الشبكات والتي يمكن ادراجها حسب الأكثر ملائمة فالأقل ومالآتي (1- النمط العضوي 2- النمط الشبكي المتعامد المنحرف ، الحلقي ، الخطي). 2- الأفادة من طبوغرافية الموقع السكني في مد الشبكات المجاري لأعتمادها على الجاذبية الأرضية لتقليل أعماق الحفر لهذه الأنابيب وعدد محطات الضخ . 3- أعتماد النظام المشترك في شبكات المجاري لتقليل قيمة الكلفة الى النصف . 4- أعتماد التوزيع للمياه بالمضخات دون تخزين عند توفر المياه أو بأستخدام الخزانات الأرضية لضمان عدم أنقطاع المياه وذلك كلفة الخزانات العالية وصيانتها المستمرة . 5- توزيع الكهرباء على اعمدة الأنارة المهيئة لهذا الغرض لنخفض الكلفة للأعمدة الكهربائية والأستفادة القصوى من هذه الأعمدة لأغراض الأنارة في المشروع السكني .
لجميع عناصر شبكة الخدمات الفنية	1- أختيار الموقع السكني وطبيعة وشكله له دور كبير في تقليل الكلف الخدمات البنى التحتية الأرتكازية فضلاً عن أبعاده من حيث تأثيره على المخطط الأساسي للموقع السكني ومايرافقه من توفر خدمات الكهرباء أو الماء قريبة من الموقع أو خطوط ضغط عالي وجود طرف رئيسية مجتورة للموقع السكني المنتخب أو توفر محطات معالجة مياه الصرف الصحي أو مشاريع تدوير النفايات ومالها من تأثير على الكلف التشغيلية لاحقاً فضلاً عن الأنسيابية للموقع وأستغلالها في مد شبكات المجاري التي تعمل على الجاذبية الأرضية . 2- زيادة الكثافة الأسكانية للمشروع الأسكاني من خلال زيادة الكثافة البنائية وأستثمار الأرض الحضرية بشكل كفوء على مستوى خدمات البنى التحتية . 3- أعتماد أطول مسار لأستيعاب أكبر عدد ممكن من الوحدات السكنية مع مراعاة التقليل من التقاطعات في الطرق وخدمة الأبنية السكنية ذات الوجهتين وأعتماد المسار الأقصر لمد الخدمات التحتية .

ستراتيجيات أدارة كلف الوحدة السكنية في المشاريع الاسكانية: أن أعتماد ستراتيجيات تخطيطية وتصميمية في مرحلة التصميم ودراسة القرارات التصميمية بدقة يعمل على تحقيق سكن مستدام أولاً ومتاح وأقتصادي ثانياً وأهم تلك الأستراتيجيات الواجب أعتمادها هي :

1- **أستراتيجيات وضع محددات ومعايير لتصميم وبناء الوحدات السكنية:**وضع محددات ومعايير تكفل الوصول الى الحد الدنى في كلف الوحدة السكنية من خلال الابعاد الدنيا لمساحات الوحدة السكنية وحجمها ويقلل كلفة الوحدة السكنية ويلبي متطلبات المستفيدين .(Qeenland-2004,p-2)

2- أستراتيجية التقييس والتخطيط : يمكن أعتماد التقييس والتنميط من خلال تنميط مكونات وعناصر الوحدة السكني وأستخدام وحدات قياسية متكررة (Module) في تصميم فضاءات الوحدة السكنية من خلال أعتماد مضاعفات قياسية وبما يتوافق مع أبعاد مواد البناء ويقلل الهدر فيها مما يقلل كلف الأنشاء (الهيئة العليا لمدينة الرياض-22-p) .

3- أستراتيجية خفض كلف التشغيل : المسكن المستدام الي يساهم في تقليل كلف البناء والتشغيل من خلال تقليل الهدم والبناء وخفض الأستهلاك الطاقة بزيادة العزل الحراري والصوتي وتقليل الطاقة المستهلكة في التبريد والتدفئة وخفض نسبة الحرارة المكتسبة ولحل هذا بدوره يقلل الكلف على المستفيدين في مرحلة التشغيل(Linbury howe-2007,p2-p4) .

4- أستراتيجية المرونة : أهم عوامل نجاح تصميم الوحدات السكنية لتقليل الفضاءات فعاليات مختلفة كما تؤدي دور كبير في خفض التكاليف من خلال تصميم وحدات سكنية ذات مساحات صغيرة قادرة على تلبية المتطلبات المختلفة (Rao-2010,p-40).

5- أستراتيجية التكيفية : يمكن تحقيق وحدة سكنية أكثر قدرة على تقبل عمليات التعديل والتحوير لتتوافق مع تغير متطلبات شاغلي المبنى لتكون أكثر تكيفاًو تكون أكثر كفاءة في قدرتهاعلى الأستجابة للتغيرات بشكل أفضل (Russel,Moffat-2001,p-2). ويمكن اعتماد ستراتيجيات الادارة الكلفوية للوحدة السكنية وفق ما يلي:

ستراتيجيات الادارة الكلفوية لمفردات والخصائص التصميمية للوحدة السكنية : تؤثر مفردات وخصائص الوحدة السكنية على أدارة كلفتها من خلال مايلي : **اولا:** حجم الوحدة السكنية. **ثانيا:** شكل التنظيم الفضائي وشكل الوحدة السكنية

ثالثا: أرتفاع المبنى السكني – أرتفاع الطابق. تختلف أدارة الكلفة في السكن الأفقي عنه في العمودي على مستوى أدارة كلفة التشغيل والصيانة التي تعتبر مرتفعة في العمودي عنه في الأفقي والمتوسط والواطيء والأرتفاع لكن المعادلة تنعكس بالنسبة الى أدارة كلفة البنى التحتية حيث ترتفع في المشاريع السكنية الأفقية عن معدلها في السكن العمودي حيث تتراوح الزيادة بين (25-50%) كما ذكرنا سابقاً يعود ذلك الى توفير كلف الأراضي (نتيجة التوفير في مساحة الأرض) . تنقسم أدارة كلفة المسكن بالنسبة لعدد الطوابق الى محورين هما(الملا-2008،ص-24) :

1- أنتخاب النمط السكني الأفقي والواطيء الأرتفاع على المسكن العمودي متعدد الطوابق وهذا مايمكن أستنتاجه من الجدول أعلاه حيث تقل قيمة عامل الكلفة رغم تساوي عدد الطوابق بأختلاف النمط السكني.

2- تحديد عدد الطوابق الذي يحقق عامل كلفة مناسب للنمط السكني ومراعاة أن الأبنية عالية الأرتفاع ستزداد فيها عامل الكلفة لعدد الطوابق.

نستنتج ⇐ مؤشر الكلفة لعدد الطوابق كلما أقترب من الواحد الصحيح يعني أدارة كلفوية كفوءة وأبتعاده عن الواحد يمثل أدارة كلفوية غير كفوءة ،(والذي يعتمدعلى النمط السكني المنتخب- افقي او عمودي)

رابعا:أدارة كلفة الحركة العمودية : أصبح التوجه نحو الأسكان العمودي في سياسات الأسكان أحدى الحلول لسد الحاجة السكنية في العراق فضلاً عن شحة الأراضي في مراكز المدن وأرتفاع كلفها والحاجة الى بناء مشاريع سكنية متكاملة الخدمات ، مع العلم أن كلفة ($1m^2$) المتر المربع في الأسكان العمودي أعلى منها في الأسكان الأفقي وتزداد الكلفة بعد الطابق الاربع لدخول كلفة المصاعد والحركة العمودية وكلف صيانتها التشغيلية مستقبلاً (العيساوي -1996،ص-28). تأثر كلفة المصاعد والحركة العمودية في الأسكان العمودي على كلفة عناصر وهي كما يلي :-(1- كلفة المساحة البنائية 2- الأسس 3- الهيكل الأنشائي 4- السطح نتيجة كلف التسطيح والأيدي 5- الجدران الخارجية والشبابيك (نبيل جعفر 1996،ص-79) .

ستراتيجيات الادارةالكلفوية التنفيذية – كلفة الانشاء للوحدة السكنية:- تُعَدُّ التقنية البنائية التي تشمل (المواد البناءاوالإنشائية والأيدي العاملة والانظمة البنائيةالمعتمدة) من العوامل الاساسية في رفع كلفة الإنشاء للمشاريع الاسكانية، فالعديد من الأسرالتي تمَتلك قطعة أرض لا تستطيع بناء مساكنها بسبب االكلف المرتفعة للمواد الإنشائية، إذ تُعَدُّكلف المواد الإنشائيةالمُستخدَمة في البناء ونوعيتها من العوامل الرئيسة التي تؤثّر في كلف البناء(الربيعي،2009،ص:65).ومع دخول التقنيات الحديثة اصبحت هناك المنافسة فيما بين التقنية الحديثة والتقليدية على اساس الكلفة والجودة في الاداء وسرعة الانجاز حيث تتميز التقنية التقليدية كونها طويلة جدا قد تستغرق بين 6 أشهر إلى

عدّة سنوات،في العموم تكون الكلف أكثرممّا يتصورها المالك نتيجة للتضخم المالي والتغييرات التصميميةومدّة البناء(I.E.Majzub,1978,p-397).التي تعد من عوامل ارتفاع الكلف فضلا عن (مواد البناء والأيدي العاملة)هي عناصر الكلفة الرئيسة في عملية الإنشاء حيث محدودية استخدام الآليات والمعدات وكالآتي:-

اولا: مواد البناء . ثانياأجور الايدي العاملة : ثالثا:الانظمة البنائية والتقنية البنائية:- ولأهمية هذه التقنيات الحديثة سندرج هنا أهم التقنيات التي دخلت البلد في المدّة الأخيرة وهي كما يلي :-

1- نظام البناء المصنع بالخرسانة الخفيفة الوزن Light – weight Concrete: تُعرَّف الخرسانة الخفيفة الوزن ذات الاستعمال الواسع في العالم بأنَّها الخرسانة الحاويةعلى مجاميع خفيفة الوزن حيث تزن الخرسانة الاعتيادية المُستخدَمة في المنشآت بين (2240-2400 كغم/ م^3) (الخلف،1984،ص-197) وتتحمّل هذه الخرسانة قوّة تحمّل انضغاطية عالية ، في حين يتراوح وزن الخرسانة خفيفة الوزن بين (1440-1840كغم/ م^3) وحسب المواصفة الأمريكية (ASTMC567) لسنة 2008* . وتُنتَج الخرسانة خفيفة الوزن بوسائل وطرق ومواد ومعدات مختلفة بحسب الشركات المُنتَجة للمعدات والموادالكيمياوية المُولِّدة لها وتُسمَّى الخرسانة الخفيفة بأسماءمختلفة وذلك تبعً الطرق إنتاجها،فهي تُسمَّى الخرسانةالخلوية(cellular light weight concrete) والخرسانة الكلسية lime light weight concrete والخرسانة الرغوية (foamed light weight concrete)(الحساني،2010،ص-30)

وتمتاز الخرسانة الخفيفة المُصنَّعة محلياًبالعديد من الخواص الفيزيائية التي سنقوم بمقارنتها ببقية المواد كالطابوق وكتل البناء الخرسانية في الجدول (3) حيث تُعَدُّ هذه الخواص هي الخواص المثالية لأي وحدة بناء يمكن اعتمادها في العراق فضلاً عن الخواص الاقتصادية والفنية والتي يمكن إجمالها بالنقاط التالية(الحساني،2010، ص-35).:-

1- كفاءتها الاقتصادية العالية مقارنة بمواد البناء التقليدية كالطابوق والبلوك. \الاقتصاد بالنقل لإمكانية صبّها موقعياً فضلاً عن تقليل جهدالأيدي العاملة .2- حفظ الطاقة بسبب خصائص العزل الحراري الجيدة ومن ثَمَّ تقليل كلف التكييف .3- التقليل من التلوث الناتج من معامل الطابوق ومالها من آثار جانبية سلبية في البيئة .4- الخصائص الصوتية: تزداد في هذا النوع خاصية امتصاص الصوت وتقليل الضوضاء. 5- مقاومتها العالية للحرائق وذلك بسبب معامل عزلها الحراري العالي.

2- نظام البناء بواسطة الجدران الحاملة المعزولة (ICF) ISOLATED CONCRET FORM: يُعدُّ هذا النظام أحد الأنظمة القديمة التي تتوافق مع المعايير الدولية للعمارة الخضراء والمستدامة ، وقد بدأ التوجّه مُؤخَّراً نحو نظام الجدران الحاملة المعزولة في المباني السكنية لعدّة أسباب وهي(الحساني،2010، ص-45):-

ا- الجودة العالية ب- الكلف المُنخفِضة سرعة الانجاز.

3-نظام الخرسانة المسلحة بالألياف الزجاجية (GRC) (Glass Fiber Reinforced Concrete) : يتكون نظام (GRC) من (اسمنت بروتلاندي ورمل نقي والياف زجاجية ومضافات والماء الصالح للشرب) أي بدون استخدام الحديد مطلقا وكما في الشكل(3-5)، وأنَّ خرسانة (GRC) أشبه بالعجينة فهي تأخذ شكل القالب الذي تُصَّب فيه وهذه الخاصية تجعل المُنتَج ذا مرونة عالية في تنفيذ التصاميم المعمارية غير التقليدية وتمَّتاز هذه التقنية (ساجدة كاظم،2015،ص:4) بما يلي: ا-**المزايا البيئية** ب-**الجودة العالية** ت-**الكلف المُنخفِضة**

4-نظام الألياف البلاستيكية المسلحة Fiber Reinforced plastic (FRP) والمسمى RENCO:أُستُخدِمَتْ اللدائن المدعمة بالألياف الزجاجية في المملكة المتحدة في الحرب العالمية الثانية بِوصفِها بديلاً للخشب المتعدد الطبقات الذي كان يُستخدَم في صناعة الطائرات غير القابلة للاكتشاف بواسطة الرادار. كان أول تطبيق مدني لها في بناء القوارب حيث حصلت على الموافقة عام 1950م،

* (American concrete institute (ACI). 2008)

ولقد توسّع مجال الاستخدام إلى قطاع صناعة السيارات وصناعة المعدات الرياضية على الرغم من المنافسة الكبيرة من الألياف الكربون التي لها متانة أكبرلوحدة الوزن والحجم. تُستخدَم اللدائن المُدعَّمة أيضاً في صناعة أحواض الاستحمام وأنابيب مياه الشرب والمجاريوجدران المكاتب والأسقف المستعارة وغيرها من التطبيقات المعمارية كصناعة الألواح الجاهزة لإنشاء المساكن المتنوعة ومن مميزات هذا النظام* : **الكلف المُنخفِضة : سرعة التنفيذ: الجودة العالية:**

وعليه يمكن ان نستنتج إنَّ الإدارة الكلفوية على مستوى التقنية البنائية ستتم من خلال مؤشّر التقنية البنائية التي يمكن استخراج قيمها من المعادلة :- مؤشر التقنية البنائية =(كلفة البناء بالتقنية الحديثة / كلفة البناء بالنظام التقليدي).(باعتماد مقارنة نسبية بين كلفة كل نظام). وذلك من أجل اختيار التقنية الأكثر توفيراً للكلف المادية .وعليه سيتم تناول إدارة الكلفة على مستوى التقنية التنفيذية التي تشمل (مواد البناء وأجور العمالة وانظمة التقنية البنلئية) في محورين رئيسين وذلك بحسب المعلومات المتوفّرة حول هذه التقنيات وكما يلي : **اولا:**مقارنة البناء بالمواد التقليدية مثل (الطابوق والبلوك) مع الخرسانة خفيفة الوزن ،بعمل مقارنة اقتصادية من حيث كلفة الإنشاء للمواد البنائية التقليدية المختلفة كالطابوق والكتل الخرسانية (البلوك) وبين كلف الإنشاء للخرسانة خفيفة الوزن وللمتر المكعب الواحد وذلك لاختيارالبديل الأمثل لمشاريع السكن وكما في الجدول(3) :

جدول (3) يوضح مقارنة كلف الإنشاء بالمواد المختلفة (المصدر : الباحث بالاعتماد على المصادر المُبيّنة في الجدول)

ت	كلف الفقرات المختلفة	الخرسانة خفيفة الوزن	مادة الطابوق التقليدية	كتل البناء الخرسانية
1-	كلفة المتر المكعب من المادة البنائية [1]	74667 دينار/ م^3	119625 دينار/ م3	77000 دينار/ م^3
2-	كلفة النقل والتحميل للمواد البنائية [2]	2% من كلفة الـ (م^3)	8 % من كلفة ال(م^3)	12% من كلفة ال(م^3)
3-	كلفة العمالة = نصف كلفة المواد [3]	37330 دينار / م^3	59812 دينار / م^3	38500 دينار / م^3
4-	كلفة الإنشاءالإجمالية لكل م^3	113490 دينار / م^3	189007 دينار/ م^3	124740 دينار/ م^3
5-	الكلف الاضافية مقارنة بالخرسانة الخفيفة	0% (مصدر المقارنة)	66 %	10 %

من ملاحظة الجدول (4) يُستنتج أنَّ الكلف الموفّرة عند استخدام الخرسانة خفيفة الوزن بدلا من الطابوق التقليدي قد تصل إلى 66% من إجمالي كلفة المشروع في حين تصل إلى 10% وأكثر من ذلك عند احتساب الكلف التشغيلية اللاحقة عند استخدام الخرسانة الخفيفة بدلا من الكتل الخرسانية.

جدول(4) يوضح المميزات والخصائص الفيزيائية والبيئية والاقتصادية للمواد البنائية(المصدر : الباحث بالاعتماد على المصادر المُبيّنة في الجدول)

ت	المادة البنائية المُقترَحة	المكونات الرئيسة للمادة البنائية	معامل العزل الحراري[1]	معامل خفة الوزن[2]	الامتصاص للرطوبة[3]	مقاومة الانضغاط (نت/ ملم2)
1-	الخرسانة خفيفة الوزن	أسمنت، رمل، ماء، فوم	1	1	(6-20%)	0.5-25
2-	مادة الطابوق التقليدي	تربة زراعية، ماء، طاقة	0.14	4	(65%)	4-12.5
3-	الكتل الخرسانية(البلوك)	أسمنت، رمل،حصو، ماء	0.08	6	(75%)	3-15

* زيارة الباحثة لمقر الهيئة العامة للأسكان/شعبة الدراسات والحصول على المعلومات المتعلقة بهذا النظام من قبل المهندس(طه ياسين احمد).

(1)- انتصار قدوري جمعة،فيصل كاظم عبد الحسين"**دراسة مقارنة لاستخدام الخرسانة خفيفة الوزن بدلا من الطابوق التقليدي في بناء القواطع**"بحث منشور ،2010،ص:10

(2)- تم افتراض معاملات كلف النقل والتحميل بالاعتماد على معاملات الوزن للمواد المختلفة والتي تم توضيحها سابقا في (3) .

(3)- ان كلفة المواد =66% من كلفة الانشاء الكلية لتكون كلفة العمالة في هذه الحالة =34% وهي تساوي تقريبا نصف كلفة المواد ، كما تم افتراض ان كلفة العمل لجميع المودبنفس النسبة بالرغم من ان الوقت المستغرق في البناء بالطابوق اكثر بكثير من الوقت المستغرق في البناء لمادة الخرسانة الخفيفة بسبب ابعاد الوحدة البنائية (انتصار قدوري جمعة-2010،ص-10).

نجد من الجدول (4) إنَّ اجتماع هذه المميزات والخصائص الفيزيائية والبيئية والاقتصادية في مادة بنائية تكون بديلة عن الطابوق التقليدي أو الكتل الخرسانية سيجعل من نجاح انتشار واستعمال هذه المادةأمرَيّن مُؤكّدينِ والإقبال على الطلب عليها عالياً جداً ، وسوف تكون الوحدات السكنية التي تُبنَّى من هذه المادة عالية الجودة ، وستفوق الوحدات البنائية الموجودة في العراق جميعاً من حيث الكلف المباشرة عند الإنشاء والكلف المستقبلية عند التشغيل التي تشمل (كلف الاستهلاك وكلف الإدامة وكلف الصيانة) ، **حيث يشار هنا إلى ضرورةاستثمار هذه التقنية البنائية بطاقتها القصوى وذلك من خلال تقليص كلف الإنهاء الداخلية والخارجية في البناء التقليدي التي اتشمل (اللبخ والبياض)والتي تستنزف الكثير من الوقت والمواد والأيدي العاملة ، وذلك عن طريق صب الجدران موقعياً بصورة كاملة فضلاً عن استخدام ألواح الخرسانية الخفيفة المجوفة وذات الصب الموقعي في سقوف المساكن بدلا من استخدام الخرسانة التقليدية**

<u>ثانيا:</u> مقارنة البناء التقليدي بالأنظمة البنائية الجديدة الثلاثة التي تمَّ تنفيذها في مقر وزارة الإعمار والإسكان ضمن مشروع الإسكانالاقتصادي كما يبيّن الجدول (5) الذي يوضّح مساحة البناء ومدّة التنفيذ وكلفة المتر المربع الواحد لكل تقنية، إنَّ أفضل نسبة للكلف الموفرة يمكن تحقيقها عند البناء بتقنية الجدران الحاملة المعزولة (ICF) وتبلغ ما يقارب 24% من كلفة البناء بالنظام التقليدي، في حين تصل نسبة التوفير في نظام الخرسانة المسلحة باللألياف الزجاجية (GRC) إلى ما يقارب 17%، وأخيراً تحتل تقنية الألياف البلاستيكية المسلحة (RENCO) المرتبة الأخيرة وبنسبة توفير تصل إلى7% فقط .

جدول (5) يوضح مقارنة الكلف التنفيذية للتقنيات الحديثة بالنظام التقليدي(المصدر – الباحث بالاستعانه بالمصادر المبينة في الجدول)

ت	التقنية البنائية	المساحة المبنيّة	مدّة الإنجاز	سعر (م²) للأُنموذج[1]	سعر (م²) في المشروع[2]
-1	تقنية (ICF)	226 م^2	60 يوما	430 $/ م^2	322 $/ م^2
-2	تقنية (GRC)	275 م^2	60 يوما	475$/ م^2	342$ / م^2
-3	تقنية (RENCO)	230 م^2	30 يوما	495 $/ م^2	371$/ م^2
-4	البناء التقليدي(الطابوق) [3]	250 م^2	180 يوما	400 $ / م^2	400$ / م^2

<u>الدراسة العملية / تطبيق المؤشرات الكلفوية في مشاريع الاسكان</u> : ولتحقيق اهداف البحث سيتم تطبيق المؤشرات الكلفوية على مشروع محلي محال للتنفيذ وهو مشروع ضفاف كربلاء لاثبات فرضية البحث التي تأكد على دور المؤشرات الكلفوية في الادارة الكلفوية الكفؤة لمشاريع الاسكان

<u>اولا مشروع ضفاف كربلاء:</u> قدمت شركة Bloom التابعة الى National Halding الامارتية مقترحا لمدينة ضفاف كربلاء يمكن استخلاص الفكر الاستراتيجي للمقترح كما يلي:

= يقع المشروع على مساحة بواقع (20) كيلو متر مربع و بواقع (40)الف وحدة سكنية اي اسكان (200,000) الف نسمة معتمد حجم الاسرة (5) افراد وعلى مساحة بناء كلية بواقع (6.333.277) متر مربع ومساحة بناء تجارية اقتصادية بواقع (422.388) متر مربع وخدمات اجتماعية على مساحة بناء كلية بواقع (1.329.793) متر مربع . مدينة سكنية متطورة ضمن سياق المدينة المقدسة القديمة لجذب السياحة وهي السمة الرئيسة للمدينة بحكم الموقع الاستراتيجي الذي تتمتع به خاصة اطلالتها على بحيرة الرزازه . مدينة تمنح

(1)– الهيئة العامة للإسكان/ شعبة الدراسات – زيارة الباحث بتاريخ 10/23/ 2013 وحصوله على البيانات المتعلقة بهذه الفقره خلال المهندس(طه ياسين احمد) .

(2)– تمّت الاشارة من مقاولي التنفيذ لهذه التقنيات الى أنَّ التنفيذ بهذه المواد لمسكن واحد وفي مقر الوزارة كان يزيد من البناء الكلّيّة بمقدار 25% والناتجة عن استيراد هذه المواد من الخارج والضرائب الكمركية وكلف النقل الى موقع الوزارة فضلاً عن كلف العمالة الاجنبية وما تشمله من كلف المبيت والإقامة والطعام والتأمينات، ومن الجدير بالذكر أنَّ أسعار الإنشاء المبنيّة في هذا الجدول هي أسعار الإنشاء المقدمة في التقارير الفنية لمسابقة المسكن الاقتصادي التي أُقيمت في مقر وزارة الإعمار والإسكان . (3)– تمّ افتراض هذا الأُنموذج من الباحث لأغراض المقارنة إذْ تبلغ مدّة الإنشاء تبلغ ستة أشهر وكلفة البناء تبلغ400$ / م^2 وبحسب الجهاز المركزي للإحصاء في وزارة التخطيط – كلف الإنشاء للقطاع الخاص / بتاريخ 2012 م .

السكن فضلا عن فرص العمل مع توفر كل عوامل الترفيه التي يتطلبها المجتمع لتحقيق سكن يلبي متطلبات العيش الكريم فضلا عن تحسين مستوى الحياة لساكني المدينة.انظر الجدول (6) التفصيلي للمشروع:

جدول (6) تفصيلي لمدينة ضفاف كربلاء(المصدر الهيئة الوطنية للاستثمار – شركة بلوم)

الموقع	**تفاصيل مدينة ضفاف كربلاء 20000km2**			
عدد الابنية السكنية للقطاع الواحد	عالي الارتفاع	2656	*4 قطاعات سكنية	المجموع 40000 الف وحدة سكنية
	متوسط الارتفاع	3719		
	السكن المنفرد	3785		
الكثافة الاسكانية الصافية	عالي	11071	ومساحة بناء	1675127m2
	متوسط	16000	المساحة السكنية	2198023m2
	منخفض	12542		
نوع السكن	فيلا+منفرد	16000+12542		
	عمودي	11071		
الانماط السكنية	1 فيلا = (352m2)+ (374m2)+ ثلاث انماط افقية (5Br–3Br–4Br)			
	Town house 2 ← (176 3Br) – (176 2Br)			
	3 Simi Detached Townhouse (234+234) مترمربع		Stached+townhouse(528–374) مترمربع	
	نمط عمودي (5–3) طابق +(6–4) طوابق+ (12– 10) طابق			
التوسع	الاسكان الافقي +الفعاليات التجارية والاجتماعية والاقتصادية			
الجدول الزمني	(8) سنوات سيتم انجاز كافة الوحدات السكنية			
كلفة المتر	1000–1200 دولار امريكي			

<u>ادارة المؤشرات الكلفوية لمدينة ضفاف كربلاء السكني</u> : وتتضمن استخراج القيم الرقمية للمؤشرات التي حددت بالاطار النظريوكما يلي

<u>المرحلة الاولى:</u>المؤشر الكلفوية لمشروع مدينة ضفاف كربلاء السكني كما مايلي (مصدر المعلومات الرقمية (الهيئة الوطنية الاستثمار – شركة بلوم):

1.مؤشر استثمار الارض = $\frac{\text{المساحة المخصصة للسكن}}{\text{مساحة الفضاء المفتوح}}$ = 2934.404 (10% من المساحة الكلية).

2. مؤشر الكثافة الاسكانية = $\frac{\text{عدد الوحدات}}{\text{المساحة الكلية}}$ = 2 وحدة/مترمربع .

3. مؤشر الكثافة المتنامية = للعمودي نفسها (2 او 2000 وحدة/كم2) / مؤشر الكثافة المتنامية للسكن الافقي = – السكن الافقي (3Brpo2–3Brpo1–5Br–4Br–3Br) .

4.مؤشر تهيئة الارض الحضرية (سكن افقي 2) =$\frac{2}{2}$ = 1 .

5.مؤشر تهيئة الارض (سكن 3 طوابق) 0.66 / سكن عمودي (5) طوابق = $\frac{2}{5}$ = 0.4 / سكن عمودي (4) طوابق (0.5) / سكن عمودي (6) طوابق (0.33)/ سكن عمودي (10) طوابق(0.2)/ سكن عمودي (12) طوابق (0.166) معدل تهيئة الارض (0.3 –0.28).

6.مؤشر كلفة الخدمات الفنية (كلفة تطوير الارض الكلية المناطق غير المشيداه)-(79.2).

7.مؤشر التقنية البنائية 0.66 .

8.مؤشر التمكين = $\frac{\text{معدل دخل الفرد الشهري}}{\text{معدل كلفة المتر المربع الواحد}}$ (سعر المتر(1500) مليون ونص دينار عراقي- الحد الادنى) .

سعر المتر 1200 $

1. الدخل المحدود 500 الف = $\frac{500}{1450}$ = 0.34 .
2. الدخل المتوسط 1000مليون= $\frac{1000}{1450}$ = 0.69= 0.7 ،
3. الدخل العالي 2000 مليون= $\frac{2000}{1450}$ = 1.38 .

نستنتج ان الدخل العالي هو المستفيد الوحيد من هذا المشروع .

9-.مؤشر التمويل السكني = $\frac{\text{قيمة القسط}}{\text{كلفة الوحدة السكنية}}$ و القسط 10% من كلفة الوحدة السكنية :

مؤشر التمويل السكني (الافقي والعمودي) = 0.1

10.مؤشر كلفة انشاء الابنية = كلفة البناء لعدد الطوابق = حسب نمط الوحدة-السكنية*سعر المتر(1200) دولار امريكي.

ثانيا: المرحلة الثانية : استعراض المؤشرات المؤشرات الكلفوية(للنمط السكني العمودي والافقي) وتحديد اهم المؤشرات المؤثرة في الادارة الكلفوية الكفؤة في المشروع السكني لتحديد كفاءة الادارة الكلفوية في بداية الاشغال وفي الطاقة القصوى للاشغال بسبب تغير هذه المؤشرات بمرور الزمن، لكي يتم تحديد جودة اداء المؤشرات الكلفوية في الادارة التخطيطية والتصميمية للمشاريع المنتخبةوكما يلي:

1-مؤشرات ادارة كلفة الارض الحضرية:

مؤشر كلفة الارض للمشاريع المنتخبة=(1/ عدد الطوابق السكنية)

جدول(7) مقارنة مؤشركلفة الارض للمشاريع المنتخبة (المصدر - نتائج تطبيق المؤشرات الكلفوية على العينة المنتخبة)

سنة القياس	ضفاف كربلاء	
	عمودي	افقي
2015	0.14	0.5
2020	0.14	0.5
2025	0.14	0.33
2030	0.14	0.33
2035	0.14	0.33
2040	0.14	0.33

النتائج :يتضح من تطبيق هذا المؤشر ان (ضفاف كربلاء) حققت (0.14)في بداية الاشغال وحتى الطاقة القصوى للاشغال الا انها في السكن الافقي وفي بداية الاشغال تحقق (0.5) الا انها في الطاقة القصوى تصل الى (0.33)انظر الجدول (7).

2-مؤشر استثمار الارض الحضرية = (المساحة المخصص للسكن/ مساحة الموقع المتبقية او الفضاء المفتوح)،انظرجدول(8):

جدول (8) مقارنة مؤشراستثمار الارض الحضرية للمشاريع المنتخبة- (ا (المصدر - نتائج تطبيق المؤشرات الكلفوية على العينة المنتخبة))

المشاريع المنتخبة	مساحة السكن (متر مربع)	الموقع المتبقية(متر مربع)	المؤشر
ضفاف كربلاء	8800000	11200000	1.3

النتائج :يتضح من تطبيق المؤشر ان مشروع (ضفاف كربلاء) يحقق افضل ادارة كلفوية في استثمار الارض الحضرية حيث ان قيمة المؤشر (1.3) بسبب زيادة مساحة الارض المخصصة للسكن نسبة الى الاستعمالات الاخرى واعتمادها التضام في التخطيط العام للمشروع ، انظر الجدول (9).

1- مؤشر الكثافة الاسكانية الاجمالية = (عدد الوحدات / مساحة الموقع الاجمالية) :يتضمن المؤشر مرحلتين هما كما يلي:

جدول (9) مقارنة مؤشرالكثافة الاسكانية الاجمالية للمشاريع المنتخبة (بداية الاشغال– الطاقة القصوى للاشغال

((المصدر – نتائج تطبيق المؤشرات الكلفوية على العينة المنتخبة))

المرحلة	السنة	ضفاف كربلاء(وحدة/هكتار)
بداية الاشغال	2015	20
	2020	20
الطاقة القصوى للاشغال	2025	40
	2030	40
	2035	40
	2040	40

اولا:المرحلة الاولى:الكثافة الاسكانية الاجمالية في بداية الاشغال : تحقق (ضفاف كربلاء) قيمة مؤشر(20)وحدة بالهكتارلاعتمادها على النمط الافقي بنسبة (65%) تقريبا و(25%) تقريبا سكن عمودي وهو مؤشر قليل .

ثانيا:المرحلة الثانية الكثافة الاسكانية الاجمالية في طاقتها القصوى: تحقق (ضفاف كربلاء) اخيرة بقيمة مؤشر (40) وحدة بالهكتار لاضافة طابق سكني في السكن الافقي .

النتائج :يتضح من خلال تطبيق المؤشر على المشاريع المنتخبةان المؤشر متغييرباستمرار في بعض المشاريع لذا تم قياس المؤشر على مرحلتين انظر الجدول اعلاه.

2- مؤشر الكثافة الاسكانية الاجمالية المتنامية=(الكثافة الاسكانية الاجمالية / الكثافة عند الاشغال): يتضمن المؤشر مرحلتين هما كما يلي:

جدول (10) مقارنة مؤشر الكثافة المتنامية للمشاريع المنتخبة (بداية الاشغال–الطاقة القصوى للاشغال)– **((المصدر – نتائج تطبيق المؤشرات الكلفوية على العينة المنتخبة))**

السنة	مؤشرالكثافة الاسكانية الاجمالية المتنامية – ضفاف كربلاء
2015	1
2020	1
2025	2
2030	2
2035	2
2040	2

اولا:المرحلة الاولى في بداية الاشغال:حيث تتساوى قيمة المؤشر في بداية الاشغال للمشروع وتساوي الواحد الصحيح لتساوي قيمة البسط والمقام لهذه السنة. **ثانيا:المرحلة الثانية الطاقة القصوى للاشغال:**تحقق ضفاف كربلاء اعلى قيمة للمؤشر (2) ، بسبب التنامي المستمر والناتج من التوسع العمودي بوحدة سكنية مستقلة ،في السكن الافقي.

النتائج : يتضح من تطبيق المؤشر على المشاريع المنتخبة ان قيمة هذا المؤشر متغيرة باستمرارفي بعض المشاريع لذاسيتم قياس المؤش بمرحلتين انظر الجدولاعلاه.

3- مؤشر تهيئة الارض الحضرية: مؤشر تحمل تربة الموقع =(الكثافة الاسكانية الاجمالية النهائية/ عدد الطوابق النهائية):

جدول (11) مقارنة مؤشر تهيئة الارض الحضرية للمشاريع المنتخبة (المصدر – نتائج تطبيق المؤشرات الكلفوية على العينة المنتخبة)))

المشاريع المنتخبة	الكثافة النهائية	عدد الطوابق الاجمالي	قيمة المؤشر(بالطاقة القصوى لعدد الطوابق)
ضفاف كربلاء	40	3-10	13.3- 4

النتائج :يتضح من تطبيق ان ضفاف كربلاء تحقق قيمة مؤشر (4) سكن عمودي و(13.3) افقي ، انظر الجدول اعلاه.

6-مؤشر خدمات البنى التحتية = (الكلفة الاجمالية لخدمات المشروع/ عدد الوحدات السكنية):

جدول (12) مقارنة مؤشر البنى التحتية للمشاريع المنتخبة ((المصدر – نتائج تطبيق المؤشرات الكلفوية على العينة المنتخبة))

المشاريع المنتخبة	كلفة خدمات البنى التحتية($دولار امريكي)	عدد الوحدات	قيمة المؤشر
ضفاف كربلاء	3168000	40 (الف)	79.2

النتائج :يتضح من تطبيق المؤشرتقدم (ضفاف كربلاء) بقيمة مؤشر (79.2) ،انظر الجدول اعلاه.

7- مؤشرات البنى الاجتماعية = (المساحة البنائية / مساحة الارض المفرزة).

جدول (13) مقارنة مؤشرالبنى الاجتماعية للمشاريع المنتخبة ((المصدر – نتائج تطبيق المؤشرات الكلفوية على العينة المنتخبة))

المشاريع المنتخبة	المساحة البنائية (متر مربع)	مساحة الارض المفرزة(متر مربع)	قيمة المؤشر
ضفاف كربلاء	3345172	11200000	0.29

النتائج :يتضح من تطبيق المؤشراتفاع قيمة المؤشر ب(0.69) مما يشير الى الاستثمار الامثل للمساحة المفرزة للخدمات الاجتماعية على مستوى (القطاع – الحي – وحدة الجيرة) ،انظر الجدول (13).

8- مؤشر التقنية البنائية=(كلفة البناء بالنظام الحديث / كلفة البناء بالنظام التقليدي)(تشمل كلفة المتر المكعب كلفة المواد البنائية+ كلفة النقل والايدي العاملة)

جدول (14) مقارنة مؤشر التقنية البنائية للمشاريع المنتخبة ((المصدر – نتائج تطبيق المؤشرات الكلفوية على العينة المنتخبة))

المشاريع المنتخبة	نوع النظام البنائي	كلفة البناء(دينار/للمتر المكعب)	قيمة المؤشر
ضفاف كربلاء	**خرسانة مسبقة الصنع**	**124740**	**0.65**
	طابوق	**189007**	**1**

النتائج :يتضح من تطبيق المؤشر ان افضل ادارة كلفوية في المشاريع التي اعتمدت النظام مسبق الصنع بقيمة مؤشر (0.65)في حين بلغ قيمة المؤشر (1) الصحيح في المشاريع التي اعتمدت الطابوق كما في ضفاف كربلاء،انظر الجدول (14).

9- مؤشر التمكين=(معدل دخل الفرد الشهري / معدل كلفة المتر المربع)

جدول (15) مقارنة مؤشر التمكين للمشاريع المنتخبة ((المصدر – نتائج تطبيق المؤشرات الكلفوية على العينة المنتخبة))

المشاريع المنتخبة	كلفة المتر المربع (دولار امريكي)	معدل الدخل الشهري(دولار امريكي)	قيمة المؤشر
ضفاف كربلاء	1200	500	0.41
		1000	0.83
		2000	1.66

النتائج :يتضح من خلال تطبيق المرشر ان ضفاف كربلاء تحقق اقل مؤشر لتمكين المواطن من تملك وحدة سكنية لارتفاع كلفة الوحدة السكنية فيها

10- مؤشرالتمويل السكني = (قيمة القرض او القسط / كلفة البناء الكلية للوحدة السكنية): تم تطبيق المؤشر على اصغر وحدة سكنية لكل مشروع لتنوع المساحات لكن يبقى المؤشر نفسه لكل الانماط السكنية)

جدول (16) مقارنة مؤشر التمويل السكني لمشاريع المنتخبة ((المصدر – نتائج تطبيق المؤشرات الكلفوية على العينة المنتخبة))

المشاريع المنتخبة	قيمة القسط دولار امريكي	النسبة المئوية للقسط	كلفة الوحدة السكنية(الف دولار)	قيمة المؤشر
ضفاف كربلاء	12000	%10	1440000	0.0083

النتائج :يوضح المؤشر تمكين الفئة المستهدفة من دفع كلفة الوحدة السكنية لكل المشاريع المنتخبة (تم تطبيق المؤشر على اصغر وحدة سكنية على اعتبار ان كلفة المتر المربع هو نفسه لكل الوحدات السكنية في كل من المشاريع المنتخبة) ولاهميته تم مقارنة (كلفة المتر المربع– نسبة القسط – المبلغ الاجمالي للوحدة السكنية) واعتماد نسبة (10%) كنسبة مفضلة للفئة المستهدفة من المشروع . يتضح من خلال تطبيق المؤشر ان ضفاف كربلاء تحقق مؤشر ضعيف بقيمة مؤشر(0.0083) وذلك لارتفاع كلفة المتر المربع للوحدة السكنية خاصة لمحدودي الدخل ،انظر الجدول (16).

تحليل نتائج تطبيق المؤشرات الكلفوية على ضفاف كربلاء و بمرحلتين كما يلي:

اولا: المرحلة الاولى: المؤشرات الكلفوية في بداية الاشغال انظرالجدول (17):

جدول (17) مقارنة المؤشرات الكلفوية الكلية للمشاريع المنتخبة بدايةالاشغال (المصدر – نتائج تطبيق المؤشرات الكلفوية على العينة المنتخبة))

النسلسل	المؤشرات الكلفوية		ضفاف كربلاء	
			عمودي	افقي
1	مؤشرادارةكلفةالارض الحضرية		0.14	0.5
2	مؤشر استثمار الارض الحضرية		1.3	1.3
3	مؤشر الكثافة الاسكانية الاجمالية		20	20
4	مؤشر الكثافة المتنامية الاجمالية		0.65	1
5	مؤشر تهيئة الارض الحضرية(اقصى عدد لطوابق)		13.3	4
6	مؤشر خدمات البنى التحتية		79.2	79.2
7	مؤشر خدمات البنى الاجتماعية		0.3	0.3
8	مؤشر التقنية البنائية		0.65	1
9	مؤشر التمكين	محدود الدخل	0.41	0.41
		متوسط الدخل	0.83	0.83
		عالي الدخل	1.66	1.66
10	مؤشر التمويل السكني		0.0083	0.0083

ثانيا:المرحلة الثانية :المؤشرات الكلفوية في الطاقة القصوى للاشغال انظر الجدول (18):

جدول (18) مقارنة المؤشرات الكلفوية الكلية للمشاريع المنتخبة في الطاقة القصوى للاشغال–(المصدر الباحثة)

التسلسل	المؤشرات الكلفوية		ضفاف كربلاء	
			عمودي	افقي
1	مؤشر ادارة كلفةالارض الحضرية		0.14	0.33
2	مؤشر استثمار الارض الحضرية		1.3	1.3
3	مؤشر الكثافة الاسكانية		40	40
4	مؤشر الكثافة المتنامية		2	2
5	مؤشر تهيئة الارض الحضرية(اقصى عدد لطوابق)		13.3	4
6	مؤشر خدمات البنى التحتية		79.2	79.2
7	مؤشر خدمات البنى الاجتماعية		0.3	0.3
8	مؤشر التقنية البنائية		0.65	1
9	مؤشر التمكين	محدود الدخل	0.41	0.41
		متوسط الدخل	0.83	0.83
		عالي الدخل	1.66	1.66
10	مؤشر التمويل السكني		0.0083	0.0083

الاستنتاجات :

1- اعتماد ادارة كلفوية كفؤة لمشاريع الاسكان تحقق سكن يتلائم ومدخولات الفئة المستهدفة من المشاريع من خلال معرفة العمليات والعناصر الاساسية لادارة عمليات الكلفة في مرحلة التخطيط والتصميم للمشاريع وقبل عمليات التنفيذ للمشاريع الاسكانية.

2- تعتمد الادارة الكلفوية ثلاثةعمليات اساسية تتضمن: (ادارة تخطيط الكلفة –ادارة تقدير الكلفة(الميزانية)–ادارة التحكم بالكلفة).تحقيق مشاريع اسكانية تتناسب وحجم الموارد المالية المخصصة لها باعتماد تصنيف كلفوي للمشاريع الاسكانية وفق هيكل تنظيمي واضح وكفؤ لتحديد الاهداف والانشطة الادارية اللازمة لتحقيق المتطلبات الكلفوية الاساسية لمشاريع الاسكان.

3- تعتمد الادارة الكلفوية لمشاريع الاسكان على محورين اساسيين هما :الادارة الكلفوية التخطيطية للمشاريع الاسكانية والادارة الكلفوية التصميمية لمشاريع الاسكان والتي تعتبر القاعدة الاساسية في التحكم في خفض الكلف للادارة التنفيذية من خلال اعتماد المؤشرات والمعايير التخطيطية والتصميمية الكفؤة لادارة العوامل المؤثرة في الكلفة الاجمالية للمشاريع الاسكانية على مستوى التخطيط والتصميم.

4- ترتبط الادارة التخطيطية والتصميمية لمشاريع الاسكان على الادارة الكفؤة للمؤشرات الكلفوية المؤثرة في المشاريع الاسكانية والتي يمكن تصنيفها على المستوى التخطيطي (لوحدة الجيرة السكنية) المرتبطة بالكثافات الاسكانية والبنائية ومعايير الخدمات العامة للمشاريع الاسكانية وعلى المستوى التصميمي (للوحدة السكنية) والمتضمنة مؤشرات المساحة البنائية ومؤشرات النمط السكني (الافقي–العمودي) لتحقيق ادارةعمليات كلفوية كفؤة تضمن تحقيق مشاريع اسكانية ملائمة لجميع المدخولات تلبي المعايير البيئية والاقتصادية والاجتماعية والعمرانية .

5- تصنف الكلف في المشاريع الاسكانية الى كلف مباشرة وغير مباشرة على مستوى :(الكلف التخطيطية)المتضمنة الموقع الاسكاني للمشاريع الاسكانية –كلف انشاءالوحدات السكنية –الكلف الصيانة و التشغيلية – الكلف المهنية، وعلى مستوى (الكلف التصميمية) والمتضمنة كلف الارض للموقع الاسكاني –كلف خدمات البنى التحتية –كلف التنظيم الفضائي –كلف الافراز والكثافة الاسكانية .

6- اعتماد الاستراتيجيات الكفؤة في ادارة الكلف التخطيطية والتصميمية للمشاريع الاسكانية من خلال ادارة المؤشرات الكلفوية الاجمالية للموقع السكني على مستوى التخطيط ، واعتماد ادارة المؤشرات الكلفوية التفصيلية للمشاريع الاسكانية على مستوى التصميم وفق منهج استراتيجي في ادارة وتخطيط كلف المشاريع الاسكانية معتمدا ستراتيجيات واساليب متنوعة في خفض كلف المشاريع مثل (الادارة القيمية – خفض الكلف –SWOT.....الخ).

7- الادارة التخطيطية والتصميمية لمشاريع الاسكان تعتمد على الادارة الكلفوية الكفؤة للمؤشرات الكلفوية والمتضمنة (ادارة مؤشرات كلف الارض الحضرية)–ا(دارة مؤشرات كلف الموقع الاسكاني –عددالطوابق–كلف الخدمات للبنى التحتية –مؤشرات التنظيم الفضائي للارض–ادارة مؤشرات الخدمات الاجتماعية –ادارة مؤشرات الافراز السكني والكثافة الاسكانية –ادارة مؤشرات الوحدة السكنية).

اعتماد المؤشرات الكلفوية ستراتيجية كفؤة في الادارة التخطيطية والتصميمية من خلال القراءة الرقمية للمؤشرات التي تحدد مدى كفاءة الانشطة التخطيطية والتصميمية والاستراتيجيات التخطيطية المنتخبة في ادارة المؤشرات الكلفوية للمشاريع الاسكانية على مستوى الموقع السكني الاجمالي او على مستوى الوحدة السكنية، ويمكن وصف المؤشرات الكلفوية لمشاريع الاسكان كما يلي:

- **مؤشر كلفة الارض السكنية = 1/ عدد الطوابق للابنية السكنية.**
- **مؤشر استثمار الارض السكنية = المساحة المخصصة للسكن / مساحة الفضاءات المفتوحة .**
- **مؤشر الكثافات الاسكانية الاجمالية = عددالوحدات السكنية / المساحة الاجمالية .**
- **مؤشر الكثافة المتنامية = الكثافة الاسكانية الاجمالية لمختلف السنيين / الكثافة عند الاشغال .**
- **مؤشر تهيئة الارض الموقع = الكثافة الاسكانية / عدد الطوابق للبناء الافقي والعمودي.**
- **مؤشر الخدمات الفنية = كلف اوطول المسار للخدمات الفنية / عدد المساكن الكلية .**
- **مؤشر التقنية البنائية = الانشاء بالانظمة الحديثة / الانشاء بالنظام التقليدي.**

- **مؤشر التمكين** = $\frac{\text{معدل دخل الفرد}(\$)}{\text{معدل كلفة المتر المربع}}$.
- **مؤشر التمويل السكني** = $\frac{\text{قيمة القسط}}{\text{كلفة البناء الكلية}}$
- **مؤشر كلفة الانشاء** = كلفة البناء لعدد الطوابق

المصادر :

- **" كراس معايير _ الاسكان الحضري "** وزارة الاعمار والاسكان ، الهيئة العامة للاسكان ، العراق _ بغداد _ تشرين الاول _ 2010 .
- أمانة بغداد ، **التعميم (21721/4/2)** في (2004/12/7) .
أمانة بغداد ، **الدراسة الشاملة للنقل لمدينة بغداد** ، مُلخّص التقرير النهائي ، سكوت ولسن كير كباتريك وشركائهم ، 1990، اليابان.
- اميرة جليل احمد **" المؤثرات التخطيطية والتصميمية لمواقع المجمعات السكنية المحلية واطئة الكلفة "** رسالة ماجستير ، الجامعة التكنلوجية _ كلية الهندسة _ قسم الهندسة المعمارية _ 2004 .
- الحساني، صلاح مهدي.**انظمة وتقنيات البناء الحديثة**، كتاب منشور في شركة الغدير للطباعة والنشر المحدودة ، رقم الايداع في دار الكتب والوثائق في بغداد (2245)، بغداد/العراق ، 2010.
الربيعي، هالة جاسم. **الاقتصاديات المعمارية في المشاريع الإسكانية المحلية"** رسالة ماجستير غير منشورة ، قسم الهندسة المعمارية، كلية الهندسة، جامعة بغداد، العراق ، 2009.
- ساجدة كاظم **مؤشرات الاسكان الاقتصادي المستدام ،مجلة الهندسة والتكنلوجيا المجلد33،الجز(A)العدد10،2015**
- العيساوي كاظم ، **" تأثير المعايير السكنية في تحديد مستوى الاسكان منخفض الكلفة في العراق "** رسالة ماجستير _ جامعة بغداد ، مركز التخطيط الحضري و الاقليمي _ 1996.
- القريشي ، انتصار قدوري جمعة **"التخطيط الاسكاني في العراق وفق الكلفة والمنفعة الاجتماعية "** اطروحة دكتوراه ، المعهد العالي للتخطيط الحضري و الاقليمي / جامعة بغداد ، تشرين الاول ، 2006 .
- المرجع الاساس في ادارة المشاريع – 2011.
- الملا وسام سهام **"النمط الافضل اقتصاديا للاسكان منخفض الكلفة "** رسالة ماجستير ، المعهد العالي للتخطيط الحضري و الاقليمي / جامعة بغداد _ 2008 .
- ميريدث ،صومائيل مانيل **" ادارة المشروعات "** - ترجمة د.م. سرور علي ابراهيم سرور / استاذ كلية الادارة والاقتصاد /جامعة ملك سعود _ القصيم _ الناشر شعاع للنشر و العلوم / سوريا حلب -1999.
- نبيل ناظم جعفر، **الاقتصاديات المعمارية في العراق مشاريع الاسكان** – رسالة ماجستير- كلية الهندسة- جامعة بغداد- 1990.
- هالة صكبان ، **" مبادئ و مؤشرات السكن الاقتصادي في العراق "** ، بحث في مؤتمر الاسكان العربي الثاني سياسات و استراجيات توفير السكن اللائق في الدول العربية -بغداد- العراق- 2012.
- الهيئة الوطنية للاستثمار - شركة بلوم (الجهة الاستشارية عن مشروع ضفاف كربلاء)
- وزارة الإعمار والإسكان ، و برنامج الامم المتحدة للمستوطنات البشرية (UN-HABITAT) ، ومنظمة AECOM للتنمية الدولية، **"سياسة الإسكان الوطنية في العراق"**، المرحلة الثانية، أكتوبر2010، بغداد/ العراق.
اليوسفي ، عبد العزيز سليمان **"ادارة القيمية المفهوم و الاسلوب "** السعودية ، الرياض ، الطبعة الخامسة 2008.
- http://investpromo.gov-2013

- Bonnie j. B **"The dynamic of macro-economic aggregates on housing prices and stock of houses**،"(1998)
- T. Achoff "**Housing cost and affordability** "، center for Housing Research , Aotoearoa NewZealand . kainga, 2004.
- Thomton, M, **"The Economics of Honsing Bubbles** "، Ludwing Von Mises Institute , 2008
- Barry J. Simpson **" Site Costs in housing development'**; New York , London, ,(1983) ch. 4.
- Dakhil , H. Fahid and others (1978).(**housing problems in Developing Countries**), vol. 1. New York: John Wiley and sons.
- Rosser , C, **"Housing and planned Urban change : the Calcutta Experience " in , Dweyer" ,** The city as center of change in Asia " University of Hong kong press , 1974 , Misra, R(ed) , Million cities of India , vikas publishing House , 1978.
- John M .Nicholas , Herman Steyn , **Project Management,** for Business, Engineering ,andTechnology,3rd edition, India, first print -2008.

Direct Shear Behavior of Fiber Reinforced Concrete Elements

Hussein Al-Quraishi
Instructor
Building and Construction Dept.-
University of Technology
hussain.abbas@yahoo.com

Mouhammed Jessam Lafta
Assistant Instructor
Engineering and Technology Journal-
University of Technology
10959@uotechnology.edu.iq

Aseel Abdulazeez Abdulridha
Assistant Instructor
Building and Construction Dept.-
University of Technology
asas_87assafi@yahoo.com

ABSTRACT

Improving the accuracy of load-deformation behavior, failure mode, and ultimate load capacity for reinforced concrete members subjected to in-plane loadings such as corbels, wall to foundation connections and panels need shear strength behavior to be included. Shear design in reinforced concrete structures depends on crack width, crack slippage and roughness of the surface of cracks.

This paper illustrates results of an experimental investigation conducted to investigate the direct shear strength of fiber normal strength concrete (NSC) and reactive powder concrete (RPC). The tests were performed along a pre-selected shear plane in concrete members named push-off specimens. The effectiveness of concrete compressive strength, volume fraction of steel fiber, and shear reinforcement ratio on shear transfer capacity were considered in this study. Furthermore, failure modes, shear stress-slip behavior, and shear stress-crack width behavior were also presented in this study.

Tests' results showed that volume fraction of steel fiber and compressive strength of concrete in NSC and RPC play a major role in improving the shear strength of concrete. As expectedly, due to dowel action, the shear reinforcement is the predominant factor in resisting the shear stress. The shear failure of NSC and RPC has the sudden mode of failure (brittle failure) with the approximately linear behavior of shear stress-slip relationship till failure. Using RPC instead of NSC with the same amount of steel fibers in constructing the push-off specimen result in high shear strength. In NSC, shear strength influenced by the three major factors; crack surface friction, aggregate interlock and steel fiber content if present. Whereas, RPC has only steel fiber and cracks surface friction influencing the shear strength. Due to cementitious nature of RPC in comparisons with NSC, the RPC specimen shows greater cracks width.

It is observed that the Mattock model gives very satisfactory predictions when applied to the present test results with a range of parametric variations; ranging from 0 % to 0.5 % in steel fibers content; from 0 % to 0.53 % in transverse reinforcement ratio; from 15 to 105 MPa in compressive strength of concrete. While it gives a poor prediction for a specimen with 1% steel fiber.

Keywords: direct shear, fiber reinforced concrete, failure modes.

سلوك القص المباشر للاعضاء الخرسانية المسلحة بالالياف

حسين القريشي
مدرس
قسم هندسة البناء والانساءات-الجامعة التكنولوجية

محمد جسام لفتة
مدرس مساعد
مجلة الهندسة والتكنولوجيا-الجامعة التكنولوجية

اسيل عبد العزيز عبدالرضا
مدرس مساعد
قسم هندسة البناء والانساءات-الجامعة التكنولوجية

الخلاصة

لتحسين دقة العلاقة بين القوة والتشوه واشكال الفشل والقوة القصوى للاعضاء الخرسانية المسلحة المعرضة الى تحميل مستوي مثل عضو الساند و حائط متصل باساس، واللوائح يجب تضمين مقاومة القص. طرق تصميم القص للمنشات الخرسانية يعتمد بشكل كبير على انتقال القص خلال التشقق والذي يعتمد على عرض التشقق و تزحلق الازاحة وخشونة سطح التشقق.

هذه الدراسة تتضمن فحوصات عملية لدراسة القص المباشر خلال التشقق للخرسانة المسلحة بالالياف وخرسانة المساحيق الفعالة. الفحوصات اجريت على مستوي قص محدد مسبقا لنموذج الدفع الخارجي. تاثير مقاومة الانضغاط ومحتوى الالياف ونسبة حديد القص على مقاومة القص تم اخذها في هذه الدراسة. اضافة الى اشكال الفشل و علاقة اجهاد القص مع التزحلق وعلاقة اجهاد القص مع عرض التشقق تم ايضا اخذها بنظر الاعتبار.

النتائج اظهرت ان كمية الياف الحديد و مقاومة الانضغاط للخرسانة تلعب دور كبير في تحسين مقاومة القص للخرسانة. كما هو متوقع، تسليح القص له ايضا تاثير كبير في مقاومة اجهادات القص. فشل القص للخرسانة العادية وخرسانة المساحيق الفعالة هو فشل فجائي وقصيف مع علاقة تقريبا خطية بيت اجهاد القص والتزحلق. استعمال خرسانة المساحيق بدلا من الخرسانة العادية ينتج عنه مقاومة قص عالية جدا. في الخرسانة العادية مقاومة القص تتاثر بثلاث عوامل هي: احتكاك سطح التشقق، تداخل الحصى، ومحتوى الياف الحديد. بينما في خرسانة الباودر التفاعلي فقط الياف الحديد واحتكاك سطح التشقق يؤثران على مقاومة القص. نتيجة طبيعة الاسمنتية لخرسانة المساحيق الفعالة عرض الشقق كان كبير مقارنة بالخرسانة العادية.

لقد تم ملاحظة ان موديل ماتوك يعطي نتائج مرضية عند تطبيقه على نتائج فحوصات هذه الدراسة لمدى متغيرات من 0 الى 0.5% محتوى الياف الحديد و من 0 الى 0.53% نسبة حديد القص و من 15 الى 105 مقاومة الانضغاط للخرسانة. بينما اعطت نتائج ضعيفة للنماذج التي تحتوي على 1% الياف حديد.

الكلمات الرئيسية: القص المباشر، الخرسانة المسلحة بالالياف، أشكال الفشل.

1. INTRODUCTION

Concrete is the most widely used for building construction. The concrete failure usually occurs due to the effect of shear and bending. The shear failure is unfavorable modes of failure due to its sudden progression. This rapid type of failure made it necessary to investigate more effective ways to design the reinforced concrete members, **Birkeland** and **Birkeland, 1966**.

In general, the shear failure of the normal strength concrete member is brittle. The inclusion of fibers into concrete matrix increases the tensile strength and adjusted the modes of failure to ductile failure. Consequently, the inclusion of fibers in concrete members enhances the shear strength and increases their shear load capacity, **Birkeland,** and **Birkeland, 1966.** The concrete and the shear reinforcement are the main parts contribute the shear strength of concrete. Shear friction or aggregate interlock represents the concrete shear strength. The shear stiffness decrease as the cracks widen due to contact being lost between the cracks faces.

Assessment the effect of aggregate interlock is complex due to difficulties in calculating the crack roughness and localized stresses around reinforcing bars, tension stiffening, dowel action and time-dependent effects such as creep, **Hofbeck, et al.**, **1969**. The popular way for measuring the direct shear strength of concrete is the push-off specimen. This, essentially prism member comprised of two L-shaped blocks, connected in an inverted position to formulate the shear plane.

In the last decade, models of shear strength were suggested using different approaches, such as distributed stress field model, modified compression field theory and shear strength based on the push-off specimen. This study focuses on shear strength mechanism of fiber reinforced concrete members through crack shear stresses and crack shear slip using push-off specimen.

Many types of research had attained to investigate the shear strength of reinforced concrete members.

Birkeland and **Birkeland, 1966,** investigated the shear friction theory in push-off specimens. **Hofbeck, et al.**, **1969**, **Mattock**, and **Hawkins, 1972**, made a further study on shear transfer mechanism. They studied the effect of concrete strength and distributed of shear reinforcement through the shear plane. The results show that the shear reinforcement extremely improves the shear strength. **Jongvivatsakul**, **et al., 2011**, studied the shear stress-slip behavior of fiber reinforced concrete members. The effectiveness of shear reinforcement ratio, fiber content and concrete compressive strength were studied. They found, the shear strength improved due to increase the steel fiber content and shear reinforcement. **Rahal, et al., 2013**, tested fifteen push-off specimens to study the shear strength of high and normal self-compacted concrete. The results indicated that the compressive strength of concrete had a significant role in improving the shear strength of concrete while, had a minor influence on the crack slip and crack width. **Xiao, et al., 2012,** tested 32 push off the specimen to study the shear strength of recycled aggregate concrete. The recycled coarse aggregate replacement ratio, the compressive strength of recycled aggregate, water to cement ratio and shear reinforcement was studied as variables. The test results showed that the mechanism of shear transfer in recycled aggregate is the same as in natural aggregate. The compressive strength and lateral reinforcement had the major role affect the shear strength of recycled aggregate. **Waseem, et al., 2016**, tested push off the specimen to study the shear strength of recycled aggregate concrete with several compressive strength and replacement ratio of recycled aggregate were the variables. The results indicate that the compressive strength of recycled concrete had the most significant variable in shear strength.

It is very important to be addressed that, the concept of shear failure is tensile failure accompanied by aggregate interlock or fiber bridging.

The use of; a micro cementitious material such as silica fume, quartz sand, superplasticizers to reduce water to cement ratio led to a new generation of concrete named reactive powder concrete (RPC).

Review of the above studies addressed the subject of shear strength of normal strength concrete (NSC) and the effectiveness variables that effects on it. However, few studies have focused on the comparisons on the shear strength between NSC and the RPC.

Hence, these paper reports test results of experimental work which aimed to better understanding the shear strength of a non-precracked push-off for NSC and RPC specimens.

2. RESEARCH SIGNIFICANT

The goal of this investigation is to study the shear strength and failure modes for NSC and RPC using the push-off specimens. The tests were performed along the certain shear plane of the push-off specimens prior to 6 mm crack shear slip. The influences of compressive strength of concrete, steel fiber content and shear reinforcement ratio on shear transfer capacity were studied. Finally, it compared between the present test results and the previous Mattock model of the shear strength was carried out.

3. PUSH-OFF TEST SPECIMENS

The push-off specimen consists of two L-blocks connected together in inverted position to produce a plane of pure shear (shear plane). The axial compression force must be applied at the top and bottom of the specimen to produce a pure shear in the adjacent area between two blocks. It is very important to note that the axial compression force must coincide with the shear plane direction. A sketch representation of push-off specimen is shown in **Fig. 1**.

From **Fig. 1** the shear stress and normal stress σ are uniformly distributed in the pre-selected shear plane according to:

$$\sigma = (P / b.L) \quad .....(1)$$

$$\tau = (P / b.h) \quad .....(2)$$

Where; P: axial compressive force, b: width of shear plane, L: total length of the specimen, and h: height of the shear plane.

To make sure that the failure of the specimen in pure shear across the pre-selected plane and to avoid other unwanted modes of failure, reinforcing longitudinal and lateral steel bars were designed and placed away from the shear plane to prevent the flexural failure. The dimensions detail with reinforcement of push-off specimen is presented in **Fig. 2**. It may be noted that the main reinforcement was 6-ϕ10 and transverse reinforcement was 4-ϕ6 were provided in all specimens for each L block to prevent flexural failure. The plywood molds with reinforcing bars are shown in **Fig. 3**.

The push-off specimens of one batch were cast in the laboratory using a concrete mixer. The cast of the concrete in formwork plywood was horizontally along the thickness of the specimen. Two plywood of 150 mm long and 25 mm thickness was used to make the slots.

After casting the concrete, the specimens were covered with plastic sheet to avoid the excessive evaporation. The specimens were de-molded after 24 h for NSC and 48 for RPC specimen respectively. The push-off specimen was ready for testing after 28 days of curing at a room temperature. **Fig. 4** shows the specimen after casting of concrete was completed.

4. MATERIALS PROPERTIES AND MIX PROPORTIONS

Two types of concrete were used in this investigation; NSC and RPC. The material used in constructing the NSC was: Ordinary Portland cement –type I; Coarse aggregate, 5-20 mm in size; fine aggregate and potable water. The mix proportion of NSC is presented in Table 1 and the target compressive strength for cubes was 15 and 30 MPa. The slump test for the two of normal concrete was presented in Table 2.

To improve the concrete compressive strength beyond the value of NSC, the present study used RPC as a matrix which consists of silica fume, Portland cement and quartz sand with a maximum size of 0.5 mm. Glenuim 54 is used as superplasticizer to reduce the water to cement ratio and to increase the workability due to the inclusion of steel fiber in a matrix. The steel fiber of 15 mm long, 0.2 mm in diameter and the aspect ratio of 75 was used. A mix proportions of RPC proposed by **Hirschi** and **Wombacher, 2012,** was adopted in this study and the target compressive strength of cubes was 105 MPa, as in **Table 3**.

The chemical and physical properties of Portland cement were tested according to the provisions of Iraqi specification No.5/1984 as shown in **Table 4** and **5** respectively.
The properties of fine and coarse aggregate were tested according to the provisions of Iraqi specification No.45/1980 as shown in **Table 6** and **7** respectively.
The yield strength of 10 mm and 6 mm reinforcing bars used in constructing the specimen was 420 MPa and 580 MPa respectively.
At least three cubes of 15 x 15 x 15 cm were used to measure the compressive strength of concrete and three cylinders of 150 x 300 mm was used to measure the tensile strength of concrete at 28 days for NSC and for RPC.
The compressive strength of concrete was tested according to BS1881-116 and the tensile strength of concrete was tested according to ASTM C496. The test results are presented in Table 8. **Fig. 5 and 6** show the concrete cubes and cylinders after failure.

5. EXPERIMENTAL PROGRAM

The experimental work was conducted in the Materials and Structural Laboratories – Building and Construction Engineering Department - University of Technology. The experimental program can be described as follows:
A total of six push-off specimens were tested. The influence of steel fiber content on the shear strength was studied on three specimens (L1-Ref, L2-fib0% and L3-fiber1%). The concrete compressive strength was studied on three specimens (L1-Ref, L6-fc15, and L5-RPC). The effect of shear reinforcement ratio on the shear strength was studied by comparisons of two specimens (L1-Ref and L4-Rei0.53%). The characteristics of the tested push-off specimens with reinforcement details are summarized in **Table 9**.

In **Table 9**, each specimen is given a unique name with a letter and digits. The letter and the digits before the hyphen sign identify the push-off specimen. Ref means the reference push-off specimen with properties indicated in **Table 9**. fib0% and fib1% means the specimen has 0% and 1% steel fiber content respectively. Rei0.53% means the specimen has 0.53% shear reinforcement ratio. Finally, RPC means the specimen constructed from reactive powder concrete.

6. MEASUREMENTS

The applied axial compression force was measured using an accurately calibrated load cell. The shear crack slip (s) which represents the relative movement between two L blocks of the push-off specimen was measured using the dial gauge 1 installed at bottom of the specimen. The shear crack opening (w) was measured using dial gauges 2 and 3 installed at the beginning and at end of a middle-third length of the shear plane. The locations of dial gauges are described in **Fig. 7**.

7. TESTING PROCEDURE

In Structural Laboratory of Building and Construction Engineering Department, a shear test of the push-off specimen was carried out. The hydraulic machine of 2500 kN was used to test the specimen and 10 mm thick steel plate stranded at the top and bottom of the specimen to freely permit the horizontal movement.

The specimens were tested under load-control applied in a vertical direction at a rate of 5 kN. In all tests, loading was continued till clearly the whole shear failure was seen. After the mode of failure was completed, the gauges and steel plates were removed to allow more photographs of final shear cracks to be taken. The time spent in testing one push-off specimen was about 20 minutes. **Fig. 8** shows the push-off specimen under test.

8. TEST RESULTS AND DISCUSSION

This section presents test results of:

- The ultimate shear strength of tested specimen.
- The effect of steel fiber content, the compressive strength of concrete and transverse reinforcement ratio on the shear strength of concrete.
- The shear stress-slip behavior and shear stress-crack width behavior.
- Modes of Failure.

8.1 Ultimate Shear Strength

The load at failure is recorded directly from the calibrated load cell. The loads at failure and shear strength are listed in **Table 10**. In which, the ultimate shear strength is calculated by dividing the axial compression force at the failure by the shear plane area (length of the shear plane which is 200 mm by the width of the shear plane which is 150 mm).

The maximum shear strength occurred at the specimen constructed from RPC with 0.5% steel fiber (L5-RPC), this is due to the high compressive strength of RPC, and minimum shear strength occurred in NSC specimen without steel fiber (L2fib0%), this is due to the low compressive strength of concrete. Further, the shear reinforcement, compressive strength of concrete, steel fiber content have important factors that influence the shear strength of concrete as will discuss in the following sections.

8.2 The Effect of Steel Fiber Content

As pointed before, the tested specimens have three percentages of fibers content; the specimen L2-fib0% has 0% steel fiber content, the specimen L1-Ref has 0.5% steel fiber content and the specimen L3-fib1% has 1% steel fiber content.

According to **Table 11**, the shear strength of concrete enhancement is increased by 34.6% and 76.9% when the steel fiber content is increased from 0% to 0.5% and from 0% to 1% respectively.

As mentioned before, the failure mechanism of shear in concrete is the tensile strength in a direction perpendicular to the applied load. Therefore, the steel fiber content plays major role in improving the tensile strength and consequently the shear strength.

8.3 The Effect of Compressive Strength of Concrete

To study the effect of compressive strength of concrete on direct shear strength, a three push-off specimen were tested. L6-fc15 specimen from NSC has a compressive strength of 15.6 MPa, L1-Ref specimen from NSC has a compressive strength of 31.5 MPa and L5-RPC specimen from RPC has a compressive strength of 105.1 MPa. The loads at failure and shear strength are listed in **Table 12**. Increasng the compressive strength of concrete from 15.6 to 31.5 MPa increased the

shear strength of concrete by 118.7%, and increasing the compressive strength from 15.6 to 105.1 MPa increased the shear strength of concrete by 568.7%. These findings indicate that the shear strength of concrete significantly affected by the compressive strength of concrete.

8.4 The Effect of Transverse Reinforcement Ratio

To investigate the effect shear reinforcement on the concrete shear strength, deformed horizontal bars passing through the plane of shear were used to represent the lateral constraint. The comparison is made between the specimen L4-Rei0.53% which has transverse reinforcement of two horizontal deform bars of 10 mm in diameter (shear reinforcement = 0.53%) with L2-Ref specimen without transverse reinforcement.

According to test results listed in **Table 13**, the shear strength was increased by 57.1% when the shear reinforcement was increased from 0% to 0.53%. This expectedly due to the major role of shear reinforcement to resist the applied axial force due to dowel action.

8.5 The shear stress-slip behavior

In this section, the behavior of shear stress-slip is studied. The shear stresses were calculated as mentioned before by dividing the vertical axial compression force on the shear plane area. The shear slip means the relative displacement between the two parts of L blocks in the push-off specimen which was measured using dial gauge installed at the end of the specimen. **Fig. 9** shows the shear stresses and slip relationship.

The test results indicate that the specimen with shear reinforcement (L4-Rei0.53%) has the significantly lesser shear slip than the specimen without shear reinforcement (L1-Ref). Further, the specimen with low compressive strength (L6-fc15) or specimen without steel fiber (L2-fib0%) shows a higher shear slip in comparisons with the reference specimen (L1-Ref).

Using RPC (L5-RPC) instead of NSC (L1-Ref) in constructing the push-off specimen results in an increase in the shear slip, this is due cementitious nature of RPC.

It was remarkable, that the specimen L4-Rei0.53% with lateral constraint has rapid progression failure after yielding of transverse reinforcement.

The stiffness of L4-Rei0.53% specimen constructed with shear reinforcement was greater than the other specimens; this is due to lateral constrained. Further, the stiffness of RPC (L5-RPC) was greater than specimens constructed from NSC (L1-Ref).

The brittle nature of shear failure in concrete member results in the approximately linear behavior of shear stress-slip relationship of NSC as well as in RPC.

8.6 Shear Stress-Crack Width Behavior

An average crack width in the transverse direction to the applied axial compression force during load increments were recorded using two dial gauges installed at begging and end of the middle-third length of the shear plane. The shear stress, in contrast, to crack width for tested specimens is illustrated in **Fig. 10**. One can see from **Fig. 10**, the crack width of the RPC specimen was greater than NSC specimens. This is due to the cementitious nature of RPC. Also, the specimen with shear reinforcement (L4-Rei0.53%) has the less crack width till the peak load and sudden large crack width after ultimate load.

Comparison between the crack width in L1-Ref and L3-fib1% specimen shows that the increase in steel fiber content decreases the crack width as the steel fiber restraint the widening of crack through bridging effect,

It was also remarkable, that the absence of steel fiber or decrease the compressive strength of concrete from 28.5 MPa to 15.6 MPa as in L2-fib0% and L6-fc15 specimen respectively in comparisons with the reference specimen L1-Ref, increased the value of crack width. This, due to constrained of crack width occurred from the presence of steel fiber or higher value of compressive strength used.

In particular, in NSC the crack width in direct shear test influenced by the three major factors; crack surface friction, aggregate interlock and steel fiber content if present. Whereas, in RPC has only steel fiber and crack surface friction influence the crack width. This, due to cementitious nature of RPC in comparisons with NSC, therefore, the RPC specimen (L5-RPC) shows the highest value of crack width in compares with NSC specimens.

8.7 Modes of Failure

In the direct shear test, there are no flexural cracks in the horizontal arms of the push-off specimen were observed, this, due to sufficient main reinforcing bars had been provided to resist the flexural failure.

The shear cracks generally developed along the interface between coarse aggregate and mortar. In this surface, due to shear deformation, the frictional force will develop namely aggregate interlock which represents the shear strength of concrete. The amount of coarse aggregate in unit volume of concrete had the predominant factor in shear strength of concrete. The concrete compressive strength and lateral constraint also had a significant influence on the shear strength of concrete members.

In the RPC, no coarse aggregates in the unit volume are used and presence of steel fiber has the dominant role of shear transfer capabilities.

The failure of push-off specimens occurred suddenly with a loud noise due to the brittle manner of failure.

According to **Fig. 11**, the mode of failure for NSC and RPC are identical; started with a crack at or near the junction line between two L blocks (at shear plane). By load increments, the crack widening and moves along the shear plane. This type of failure is the typical failure in direct shear tests.

9. PREDICTION OF SHEAR STRENGTH CAPACITY

From the observation of test results, the push-off specimen fails in two stages: (1) the shear stress controlled by the concrete alone (cohesive of concrete plus aggregate interlock) till the concrete shear friction capacity is reached; and (2) additional shear stress is resisted by the shear reinforcement (dowel action).

A general model of ultimate shear strength can be written as:

$$v_u = v_c + v_{bar} \qquad \text{.....(3)}$$

Where; v_c is the shear friction of concrete; v_{bar} is the shear stress resisted by the shear reinforcement.

According to experimental work presented by **Mattock, 2001,** Equation 8 is presented in the form of:

$v_u = 0.117 f_c^{'} + 0.8\, \rho_b\, f_y$ .....(4)

Where; 0.117 is the shear friction factor of concrete; $f_c^{'}$ is the compressive strength of concrete cylinders; ρ_b is the shear reinforcement ratio; and f_y is the yield stress of reinforcing bar.

This equation is similar to the models proposed by **Birkeland** and **Birkeland**, **Hofbeck, et al.**, **1966**, **Mattock** and **Hawkins, 1972**, and **Kahn** and **Mitchell**, **2002**.
The present test results were compared with the Mattock model to check the applicability of this model in NSC and RPC, with and without shear reinforcement, with and without steel fiber. The comparisons are presented in **Table 14**.
It is observed that the Mattock model gives very satisfactory predictions when applied to the present test results with a range of parametric variations; ranging from 0 % to 0.5 % in steel fiber content; from 0 % to 0.53 % in shear reinforcement ratio; from 15 to 105 MPa in compressive strength of concrete. While it gives a poor prediction for a specimen with 1% steel fiber.

10. CONCLUSIONS

- The shear strength of concrete was significantly affected by the compressive strength of concrete and steel fiber content.
- The shear reinforcement is the predominant factor in resisting the shear stress due to dowel action.
- The shear failure of NSC and RPC has the sudden mode of failure (brittle failure) with the approximately linear behavior of shear stress-slip relationship till failure.
- Using RPC instead of NSC with the same amount of steel fibers in constructing concrete specimens result in significantly higher shear strength of concrete.
- In NSC the shear strength influenced by the three major factors; crack surface friction, aggregate interlock and steel fiber content if present. Whereas, in RPC has only steel fiber and crack surface friction.
- Due to cementitious nature of RPC in comparisons with NSC, the RPC specimen shows the higher value of crack width in compares with NSC specimens.
- In NSC, increase the compressive strength of concrete or increase the steel fiber content results in a smaller shear slip and smaller crack width.
- The shear stiffness of RPC specimen was 205.7% greater than that of NSC specimen.

REFERENCES

- Birkeland P. and Birkeland H., 1966, *Connections in precast concrete construction*, ACI journal, Vol. 63, No.3, P.P 345-368.
- Hofbeck J., Ibrahim O., Mattock A., 1969, *shear transfer in reinforced concrete*, ACI Journal, Vol. 66, No.2, P.P. 119-128.
- Mattock A., Hawkins N., 1972, *Shear transfer in reinforced concrete recent research*, PCI Journal, Vol. 17, No. 2, p.p. 55-75.

- Jongvivatsakul P., Watanabe K., Matsumoto K. and Niwa J., 2011, *Evaluation of shear carried by steel fibers of reinforced concrete beams using tension softening curves*, Journal of Materials Concrete Structures and Pavements JSCE, Vol. 67, No. 4, p.p. 507-493.
- Rahele N., 2013, *Assessment of shear transfer capacity of non-cracked concrete strengthened with external GFRP strips*, Journal of construction and building material, Vol. 45, No. 1, p.p. 224-232.
- Xiao J., Xie H., Yang Z., 2012, *Shear transfer across a crack in recycled aggregate concrete*, Cement and Concrete Research, Vol. 42, No. 5, p.p. 700–709.
- Waseem S., 2016, *Shear transfer strength of normal and high-strength recycled aggregate concrete – An experimental investigation*, Construction and Building Materials, Vol. 125, No. 1, p.p. 29-40.
- Mattock A., 2001, *Shear friction and high strength concrete*, ACI structural journal, Vol.98, No.1, P.P. 50-59.
- Fardis M. and Buyukozturk O., 1979, *Shear transfer model for reinforced concrete*, journal of the engineering mechanics division, ASCE, Vol. 105, No. EM2, p.p. 255-276.
- Hirschi T. and Wombacher F., 2012, *Influence of different superplasticizer on UHPC*, HiperMat conference, Kassel University, Germany.
- Hsu T., Mau S., Chen B., 1987, *Theory of shear transfer strength of reinforced concrete*, ACI structural journal, Vol. 84, No.2, P.P. 149-160.
- Kahn F., Mitchell A., 2002, *Shear friction tests with high strength concrete*, ACI structural journal, Vol. 99, No.1, P.P. 98-103.
- Mattock A., Li W., Wang T., 1976, *Shear transfer in lightweight reinforced concrete*, PCI Journal, Vol. 21, No. 1, P.P. 20-39.
- Reinhardt H., Walraven J., 1982, *Cracks in concrete subject to shear*, Journal of structural division, ASCE, Vol. 106, St1, p.p. 207-224.
- Shariatmadar H., Khatamirda M., and Zamani E., 2013, *Pre-cracked concrete shear strengthened with external CFRP strips*, Journal of rehabilitation in civil engineering, P.P. 29-38.

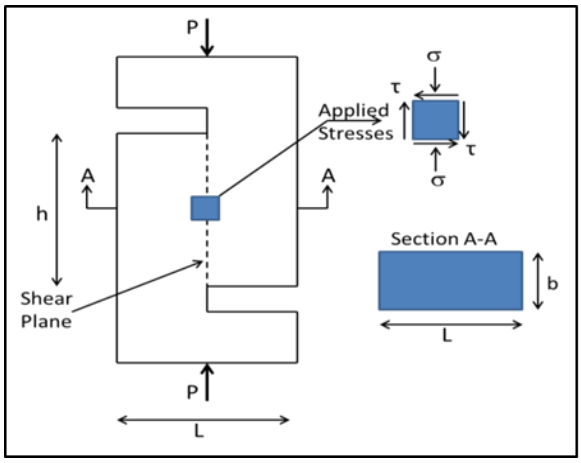

Figure 1. Push-off specimen.

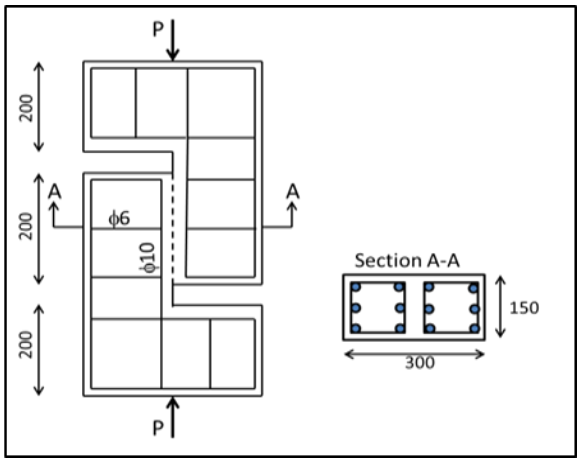

Figure 2. Steel reinforcement details.

Figure 3. Typical mold with reinforcement.

Figure 4. Casting the concrete into specimen.

Figure 5. Concrete cubes at failure.

Figure 6. Concrete cylinders after failure.

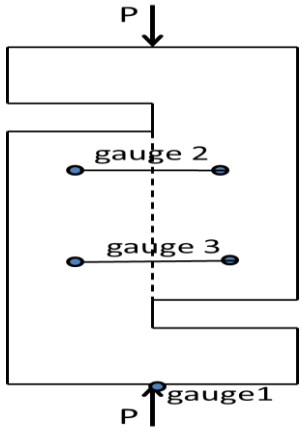

Figure 7. Locations of dial gauges.

Figure 8. The push-off specimen under test.

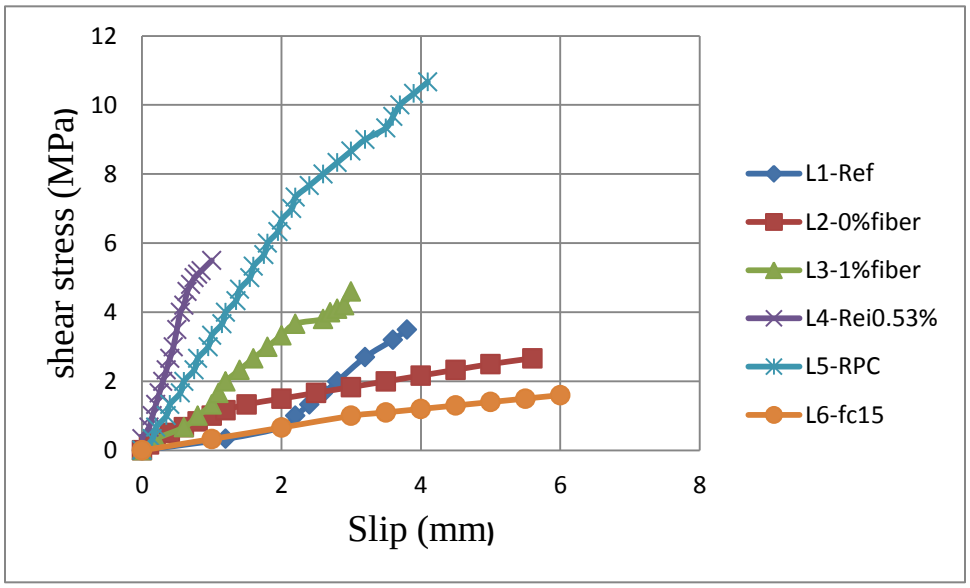

Figure 9. Shear stress-slip relationship.

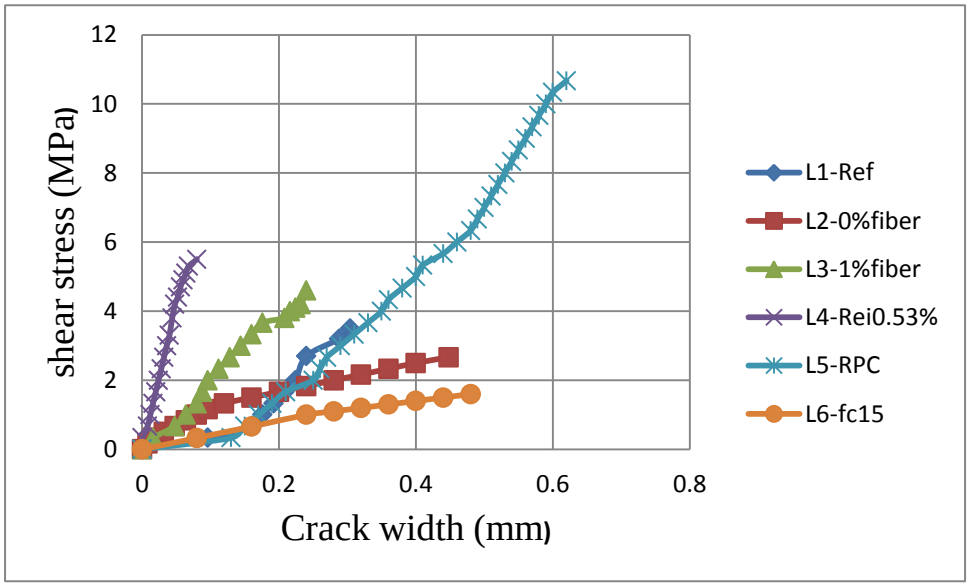

Figure 10. Shear stress-crack width behavior.

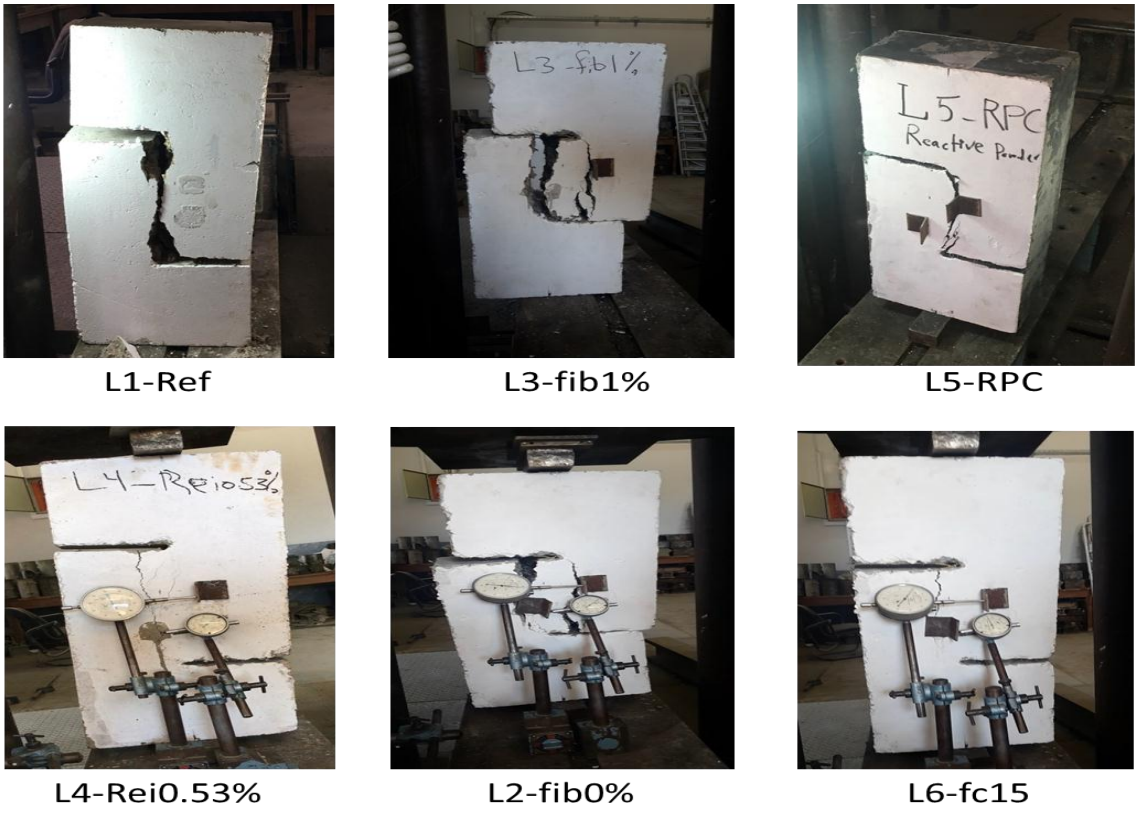

Figure 11. Modes of failure of tested specimen.

Table 1. Mix proportion of NSC.

Material	Weight (kg/m^3) for NSC1	Weight (kg/m^3) for NSC2
Cement (Kg/m3)	375	360
Gravel	1130	1080
Sand	660	775
Water	195	183.6
Water/Cement	0.52	0.51

Table 2. Slump test.

Type of Concrete	Slump (mm)
NSC1	50
NSC2	45

Table 3. Mix proportion of RPC.

Material	Weight (kg/m^3)
Cement	810
Silica Fume	186.3
Quartz Sand	631.8
Superplasticizer	36.4
Steel fiber (0.5%)	39.25
Water	170.1
Water/Cement	0.21
Water/Cementitious	0.170

Table 4. Physical properties of Portland cement**.**

Physical properties	Test results	Limits of Iraqi specification No.5/1984
Specific surface area m2/kg	372	≥230
Soundness (Autoclave) %	0.01	≤0.8
Setting time (Vicat′s apparatus) Initial setting time, hrs: min Final setting time, hrs: min	 3:58 4:50	 ≥45 min ≤10 hrs
Compressive strength 3 days (MPa) 7 days (MPa)	 29.80 34.84	 ≥15 ≥23

Table 5. The chemical composition of Portland cement.

Oxide composition	Abbreviation	Content (%)	Limit of Iraqi specification No.5/1984
Lime	Cao	62.44	-
Silica Dioxide	SiO2	20.25	-
Alumina Trioxide	Al2O3	4.73	-
Iron Oxide	Fe2O3	4.32	-
Magnesia Oxide	MgO	1.5	≤5.0%
Sulphate	SO3	1.88	≤2.8% if C3A>5%
Loss on Ignition	L.O.I	3	≤4.0%
Insoluble residue	I.R.	0.8	≤1.5%
Lime saturation factor	L.S.F.	0.93	0.66-1.02
Main compounds (Bogue′s equation)			
Tricalcium Silicate	C3S	56.9	-
Dicalcium Silicate	C3S	15.21	-
Tricalcium Aluminate	C3A	5.23	-
Tetracalcium alumino-ferrite	C4AF	13.13	-

Table 6. Fine aggregate properties**.**

Sieve size (mm)	Cumulative passing %	Limits of Iraqi specification No.45/1980, zone 2
4.75	100	90-100
2.36	90.15	75-100
1.18	74.22	55-90
0.6	51.37	35-59
0.3	19.3	8-30
0.15	3.79	0-10
Fineness modulus=2.61		
Specific gravity=2.65		
Sulfate content=0.08% (Iraqi specification requirement ≤0.5%)		
Absorption=0.75%		

Table 7. Coarse aggregate properties**.**

Sieve size (mm)	Cumulative passing %	Limits of Iraqi specification No.45/1980, zone 2
14	100	100
10	100	85-100
5	15.3	0-25
2.36	0.53	0-5
Specific gravity=2.66		
Sulfate content=0.08% (Iraqi specification requirement ≤0.1%)		
Absorption=0.52%		

Table 8. The compressive and tensile strength of concrete.

Type of concrete	Average compressive strength of cubes (MPa)	Average tensile strength of cylinders (MPa)
NSC1	15	2.2
NSC2	30	4.1
RPC	105	9.8

Table 9. Characteristics of tested specimens.

Specimen	Type of concrete	Fiber Content (%)	f_{cu} (MPa)	Shear Reinforcement ratio (%)
L1-Ref	NSC	0.5	30.2	0
L2-fib0%	NSC	0	28.5	0
L3-fib1%	NSC	1	35.6	0
L4-Rei0.53%	NSC	0.5	30.3	0.53
L5-RPC	RPC	0.5	105.1	0
L6-fc15	NSC	0.5	15.6	0

Table 10. Shear strength of push-off specimens.

Specimen	Type of concrete	Fiber Content (%)	f_{cu} (MPa)	Shear Reinforcement ratio (%)	Failure load (kN)	Ultimate shear strength (MPa)
L1-Ref	NSC	0.5	30.2	0	105	3.5
L2-fib0%	NSC	0	28.5	0	80	2.6
L3-fib1%	NSC	1	35.6	0	140	4.6
L4-Rei0.53%	NSC	0.5	30.3	0.53	165	5.5
L5-RPC	RPC	0.5	105.1	0	320	10.7
L6-fc15	NSC	0.5	15.6	0	50	1.6

Table 11. Effect of steel fiber content on shear strength.

Specimen	Fiber content (%)	Load at failure (kN)	Ultimate shear strength (MPa)
L2-fib0%	0	80	2.6
L1-Ref	0.5	105	3.5
L3-fib1%	1	140	4.6

Table 12. Effect of compressive strength of concrete on shear strength.

Specimen	Compressive strength (MPa)	Load at failure (kN)	Ultimate shear strength (MPa)
L6-fc15	15.6	50	1.6
L1-Ref	31.5	105	3.5
L5-RPC	105.1	320	10.7

Table 13. Effect of shear reinforcement on the shear strength of concrete.

Specimen	Transverse reinforcement ratio (%)	Load at failure (kN)	Shear strength (MPa)
L1-Ref	0	105	3.5
L4-Rei0.53%	0.53	165	5.5

Table 14. Comparison between the present and Mattock ultimate shear strength.

Specimen	Type of concrete	Fiber Content (%)	f_{cu} (MPa)	Shear Reinforcement ratio (%)	Exprimental shear stress (MPa)	Mattock shear stress (MPa) [10]	Ratio of present and Mattock shear strength
L1-Ref	NSC	0.5	31.5	0	3.5	2.95	0.84
L2-fib0%	NSC	0	28.5	0	2.6	2.66	1.02
L3-fib1%	NSC	1	35.6	0	5.3	3.33	0.62
L4-Rei0.53%	NSC	0.5	30.3	0.53	5.5	4.6	0.84
L5-RPC	RPC	0.5	105.1	0	10.7	9.83	0.92
L6-fc15	NSC	0.5	15.6	0	1.6	1.46	0.92

Regression Analysis Models to Predict the 28 -day Compressive Strength Using Accelerated Curing Tests

Dr. Suhair K. Al-Hubboubi
Building Research Directorate
Ministry of Construction and Housing
suhairkah@yahoo.com

Ass. Prof. Dr. Zena K. Abbas
Assistant Professor
Baghdad University-Civil Engineer Department
zka_abbas@yahoo.com

ABSTRACT

Regression analysis models are adopted by using SPSS program to predict the 28-day compressive strength as dependent variable and the accelerated compressive strength as independent variable. Three accelerated curing method was adopted, warm water (35ºC) and autogenous according to **ASTM C C684-99** and the British method (55ºC) according to **BS1881: Part 112:1983**. The experimental concrete mix design was according to ACI 211.1. Twenty eight concrete mixes with slump rang (25-50) mm and (75-100)mm for rounded and crushed coarse aggregate with cement content (585, 512, 455, 410, 372 and 341)Kg/m^3.

The experimental results showed that the accelerated strength were equal to about (0.356), (0.492) and (0.595) of the 28-day compressive strength for warm water, autogenous and British curing methods respectively. A statistical regression analysis using SPSS program is implemented for the experimental results of the 28-day compressive strength ranging from (16 to 55.2)Mpa and accelerated strength for different curing methods. The linear models with high R^2 and F-value are adopted for different curing methods while the Power model with constant is the best model for non parametric analysis.

Key words: accelerated compressive strength, regression analysis models

موديلات تحليل الانحدار لتوقع مقاومة الانضغاط بعمر 28 يوم باستخدام فحوص الانضاج المعجل

د. سهير كاظم الحبوبي
دائرة بحوث البناء
وزارة الاعمار و الاسكان

أ.م.د. زينة خضير عباس
جامعة بغداد –كلية الهندسة

الخلاصة

تم أعتماد موديلات تحليل الانحدار بأستخدام برنامج SPSS لتوقع مقاومة انضغاط الخرسانة لعمر 28 يوم كمتغير ومقاومة الانضغاط للانضاج المعجل كمتغير معتمد .تم اعتماد ثلاثة طرق وهي طريقة الماء الدافئ (35°م) وطريقة الانضاج الذاتي المعتمدة في المواصفة الامريكية ASTM C684-99 والطريقة البريطانية(55°م) المعتمدة في الطريقة البريطانية BS 1881:Part 112:1983 .تم تصميم الخلطات الخرسانية وفق ACI 211.1. تم تحضير 28 خلطة خرسانية بمدى هطول (25-50) ملم وكذلك (75 -100) ملم لركام خشن مدور ومكسر على التوالي وبمحتوى سمنت (410،372،341،585،512،455) كغم /م^3 .

النتائج العملية لمقاومة الانضغاط المعجل تساوي حوالي (0.356) ، (0,492) و(0,595) من مقاومة الانضغاط بعمر 28 يوما لطريقة الماء الدافئ، الانضاج الذاتي والطريقة البريطانية على التعاقب . تم تنفيذ تحليل الانحدار الخطي بأستخدام برنامج SPSS للنتائج العملية بين مقاومة الانضغاد الاعتيادية بعمر 28 يوم و المقاومة المعجلة . تم تبني الموديلات الخطية و لمختلف طرق الانضاج وبقيم عالية لـR^2 وF-value بينما الموديل الاسي و بوجود الثابت هو الموديل الافضل في التحليل اللاخطي للبيانات.

الكلمات الرئيسيه : مقاومة الانضغاط المعجل ، موديلات تحليل الانحدار.

1. INTRODUCTION

The predicted 28-day compressive strength of a concrete can be estimated in lesser time by accelerating methods mentioned in ASTM C684 and BS1881: Part 112.

Abbas and Auad, 2011 studied the accelerated strength testing method using the British standard methods was performed to predict the strength at later ages. Four different chemical compositions were used with two mean compressive strength equals to 35 and 45MPa. Comparison between the three methods adopted by the British standard refers to despite the fact that the 35 ºC method is the simplest and most convenient of the three; the correlations for a range of different concretes may be somewhat more widely dispersed than for the 55 ºC method. The third way of 82 ºC method is more complex and it needs high water temperature. The percent of accelerated strength test (35 ºC, 55 ºC and 82 ºC methods) of 7-day normal curing strength approximately were 0.4, 0.6 and 0.7 respectively.

Atwan, 2012 studied the effect of accelerated curing methods on mechanical properties of superplasticized and retarding concrete. The adopted accelerating tests are warm water and boiling water method according to the ASTM C684-99.

Two concrete mixes with ordinary and crushed gravel were studied. The effect of surface texture of gravel, curing test methods and admixture doses were studied. The main conclusions that the accelerated strength for both methods was larger than the compressive strength of normal cured concrete specimens at the same age and the specimen's strength for boiling water method were higher than the warm water method.

Fawzi and Tawfeeq, 2012 investigated the effect of curing temperatures (30, 40, and 50˚C) on compressive strength development of high performance concrete and standard conditions at curing temperature (21˚C). The experimental results showed that at early ages, the rate of strength development at high curing temperature is greater than at lower curing temperature, the optimum increasing percentage in compressive strength is 10.83% at 50˚C compared with 21˚C in 7days curing age.

Abbas, 2013 studied the lightweight concrete- no fine concrete. The specimens concrete mixes were (cement: porcelinite coarse aggregate) ratios (1:4), (1:5) and (1:6). The cement content were (200, 300 and 400) kg/m^{3}for each mixes. The tests of density, absorption, porosity, ultrasonic pulse velocity and compressive strength at 7, 28 and 90-day were studied. The correlation between accelerated compressive strength at 1- day and normal compressive strength at 28-day are approximately (0.245 ±0.005) for water bath (55°C) and (0.335±0.05) for water bath (82°C).

2. PREVIOUS MODELS OF THE ACCELERATED STRENGTH TEST AND THE NORMAL CURING TEST

Al- Qassab, 2006, models adopts the linear regression analysis equations of an ordinary Portland cement and sulfate resisting cement respectively:

$$Y_{7\text{-day}} = 2.45 + 1.17X \quad R^2 = 0.97 \qquad (1)$$

$$Y_{7\text{-day}} = 2.17 + 0.88X \quad R^2 = 0.97 \qquad (2)$$

Regression analysis shows the relationship as a second equation of an ordinary Portland cement and sulfate resisting cement respectively:

$Y28\text{-}day = 5.39 + 2.24X - 0.03X^2 \quad R^2 = 0.95$ (3)

$Y28\text{-}day = 4.38 + 1.91X - 0.02X^2 \quad R^2 = 0.95$ (4)

The correlation for all cements as presented equation:

$Y28\text{-}day = 6.06 + 2X - 0.03X^2 \quad R^2 = 0.91$ (5)

The **ASTM C684 -99** for method B, illustrate the procedure, considered the 12 pairs of accelerated and standard-cured at 28-day strengths.

Therefore, the equation of the relationship between the accelerated strength (X) and the standard-cured strength (Y) is as follows:

$Y = 19.50 + 1.19X$ (6)

Abbas, et al., 2012 adopted three accelerated curing test methods which are warm water, autogenous and the proposed method. A good correlation was presented between the accelerated strength and normal strength at ages 7 and 28 day. Five different chemical composition of cement in concrete mixes and different water to cement ratios equal to 0.45, 0.55, and 0.65 and 0.75 were studied.

The regression models for linear relationship between accelerated strength (warm water and autogenous method) and 28-day compressive strength are presented respectively:

7-day Comp. strength = 1.797+ 1.744x accelerated strength-warm $R^2 = 0.942$ (7)

28-day Comp. strength = 2.357+ 2.540x accelerated strength-warm $R^2 = 0.969$ (8)

7-day Comp. strength = -0.171+ 1.677x accelerated strength-autogenous $R^2 = 0.987$ (9)

28-day Comp. strength = 0.062+ 2.398x accelerated strength-autogenous $R^2 = 0.979$ (10)

3. EXPERIMENTAL PROGRAM

3.1 Material

3.1.1 Cement

Sulfate resistance Portland cement (Abu Al Jasser) conforming to the IQS 5/1984 and ASTM C150 was used. The chemical and physical properties are listed in **Tables 1 and 2** respectively.

3.1.2 Fine Aggregate (sand)

The sand from Al-Ukhaider region with grading conforms to the Iraqi specification IQS 45/1984-zone two and the ASTM C33-03. The physical properties and sulfate content are shown in **Table 3**.

3.1.3 Coarse Aggregate

Natural crushed and rounded coarse aggregate with maximum size of 20mm from Al-Niba`ee quarry was used. The aggregate conform to the Iraqi specification IQS 45/1984. The sulfate content and the physical properties are presented in **Table 4**.

3.1.4 Mixing Water

Tap water is used for mixing and curing of concrete mixes, conforming to the IQS 1703/1992.

3.2 Mix Proportions

The concrete mix design was according to ACI 211.1. Twenty eight concrete mixes with slump rang (25-50) mm and (75-100)mm for rounded and crushed coarse aggregate and cement content (585, 512, 455, 410, 372 and 341)kg/m^3as presented in **Table 5**.

3.3 Mixing and Curing of Concrete

The dry constituents of mix were initially mixed for 1.5 minutes using a rotary mixer. The required amount of water was then added, and the whole mix constituents were re-mixed for further 1.5 minutes. The molds, with dimensions of (100) mm are used.

The molds were covered with thick nylon bag for normal curing for 24hrs and then the specimens were transformed to the curing tank with water till the time of testing (7 and 28-day). The procedure is mentioned in the curing methods for the specimens of accelerated curing test.

3.4 Tests Performed

3.4.1 Fresh Concrete- Slump Test

The fresh concrete is illustrated by slump test according to ASTM C143M– 00. The adopted slump range (25-50mm) and (50-75mm) for both mixes using crushed and rounded coarse aggregate.

3.4.2 Compressive Strength Test

The compressive strength test was carried out according to the BS 1881: Part 116: 1983 for concrete cubes of (100) mm.

4. RESULTS AND DISCUSSION

The accelerated strength methods (warm water (35ºC), autogenous and (55ºC)) and normal curing (7 and 28-days) results are presented in **Table 6**.

The effect of cement content (C-585, C-512, C455, C410, C372, C341 andC-315) for crushed and rounded cores aggregate and slump (S25 and S75) on accelerated and normal curing are shown in the **Figs. 1** to **4**. The figures indicated that as cement content increase the compressive strength for accelerated and normal curing and it is conforms to the literatures, **Abbas, 2012** and **Al-marsomy, 2010**.

For the same cement content (C-585) and the slump (S25) and (S75) as shown in the **Figs. 5** and **6** for crusted and rounded coarse aggregate respectively. The accelerated strength with different method and (7 and 28-days) for normal curing strength, concrete mixes with crushed coarse aggregate is more than rounded and that is may be attributed to natural rounded uncrushed gravel

has lower specific surface area and smoother texture than crushed gravel so the bond strength is increase led to increase the compressive strength, **Al Attar, 2008**. **Figs. 7** and **8** shows the accelerated and normal curing concrete (7 and 28-days) for the same cement content (C-315) and the slump (S25) and (S75).

The **Figs. 9** to **12** shows the cumulative compressive strength for different curing methods with different W/C ratio for crushed and rounded cores aggregate and slump (S25 and S75) on accelerated and normal curing. The compressive strength decreased with the increase w/c ratio and that is conforms to the literatures, **Abbas, 2012**.

5. REGRESSION ANALYSIS MODELS

5.1 Descriptive Statistics

The objective is to develop statistical models to predict the 28 –day normal strength as a function of independent variable. It is necessary to examine the existence of the required range of variation in the data. This is achieved by performing a preliminary (descriptive) statistical analysis as presented in **Table 7**.

1. Mean, median and mode (central tendency)
2. Minimum and maximum, range and standard deviation (dispersion).

5.2 Regression Models of Warm Water Method (35ºC),Autogenous and British Curing Method (55ºC)

Using SPSS program version 17.1 for linear and non parametric analysis are presented in **Table 8** and **Figs. 13** and **14** for warm water method, while **Table 9** and **Figs. 15** and **16** for autogenous and **Table 10** and **Figs 17** and **18** for British curing method.

From **Tables 8, 9 and 10** and **Figs. 13 to 18**, it is found that:

1. Model 2-linear is better than model 1-linear with higher R^2 and F-calculated and the experimental data close to the line.
2. The accelerated strength approximately equal to (0.356),(0.492) and (0.595) of 28-day compressive strength of warm water, autojenous and British curing methods respectively for linear regression analysis.
3. For non-parametric regression analysis the models with constant is more convents.
4. The model 5-power is the best with high $R^2$and F-calculated and the experimental data close to the curve.

6. CONCLUSIONS

1. The accelerated curing methods (warm water and autogenus) according to ASTM C and 55ºC according to BS can be adopted to predict the 28-day compressive strength.
2. The accelerated strength approximately equal to (0.356),(0.492) and (0.595) of 28-day compressive strength of warm water, autojenous and British curing methods respectively for linear regression analysis.
3. Statistical linear analysis models presents the best correlation between accelerated strength with different curing methods and 28-day compressive strength ranging (16 to 55.2)Mpa with high (R^2).

4. For non-parametric regression analysis the models (power) with constant for different curing methods is the best with high $R^2$and F-calculated.

7. REFERENCES

- Abbas Z.K. and Auad H.K., 2011, *Effect of accelerated testing methods in British standard on strength of concrete*, 4th International Scientific Conference of Salahaddin University-Erbil
- Abbas Z.K. et al, 2012, *Estimation the 7 and 28- day Normal Compressive Strength by Accelerated Test Methods in Concrete*, Journal of Engineering, Volume 17, Number 6.
- Abbas Z.K., 2013, *Some properties of accelerated cured no fine Lightweight concrete*, Engineering and Technology Journal, Volume (31), Number (13(A)).
- Atwan D. S., 2012, *Some Properties of Superplasticized and Retarding Concrete underEffect of Accelerated Curing Methods*, Journal of Engineering, Volume (18), Number (5).
- Al-Attar, T. S., 2008, *Effect of Coarse Aggregate Characteristics on Drying*, Engineering and Technology, Vol.26, No.2,
- Al Qassab , F.F.,2006,*Development of concrete mix design method with reference to Iraqi conditions*, Ph.D. Thesis, University of Baghdad , College of Engineering, Iraq,.
- Al-marsomy M. H. H.,2010, *Insulating LightWeight Aggregate Concrete*, Engineering and Technology Journal, Volume (28), Number (13).
- Fawzi N.M. and Tawfeeq Agha A.S., 2012, *The Effect of Curing Types on Compressive Strength of High Performance Concrete*, Journal of Engineering, Number (7), Volume (18).

Table 1. Chemical composition of SRP cement*.

Abbreviation	Percentage by weight	Limit of Iraqi Specification No. 5/1984	Limit of ASTM Specification C150-12
CaO	61.74	-	
SiO_2	20.84	-	
Al_2O_3	3.82	-	
Fe_2O_3	5.24	-	
SO_3	2.15	≤ 2.5 %	≤3.0 if C_3A≤8% ≤3.5 if C_3A≤8%
MgO	3.38	≤ 5.0 %	≤ 6.0 %
L.O.I.	2.47	≤ 4.0 %	≤ 3.0 %
I.R.	0.72	≤ 1.5 %	≤ 0.75 %
L.S.F	0.9	0.66-1.02	
Main Compounds (Bogue′s equations)			
C_3S	49.86	-	-
C_2S	22.38	-	-
C_3A	1.26	≤ 3.5	-
C_4AF	15.92	-	-

* The test was carried out in Building Research directorate / ministry of construction and Housing

Table 2. Physical properties of SRP cements*.

Physical properties	Test results	Limits of Iraqi Specification No. 5/1984	Limits of ASTM Specification C150-12
Specific surface area (Blaine method) (m^2/ kg)	325.9	≥ 230	≥ 280
Setting time (Vicat′s method) Initial setting (hrs. : min) Final setting (hrs. : min)	 110 4:30	 ≥ 45 min ≤ 10 hrs.	 ≥ 45 min ≤375min
Compressive strength (MPa) 3 days 7 days	 20 29	 ≥ 15 ≥ 23	 ≥ 12 ≥ 19

* The test was carried out in Building Research directorate / ministry of construction and Housing

Table 3. Physicals properties and sulfate content of fine aggregate*.

Sieve size (mm)	% passing by weight	Iraqi specifications No.45/1984 (Zone 2)	ASTM specification C33-03
10	100	100	100
4.75	95.6	90-100	95 -100
2.36	80.4	75-100	80 – 100
1.18	59.9	55-90	50 - 85
0.6	37	35-59	25 - 60
0.3	9.3	8-30	5 - 30
0.15	1.3	0-10	0 - 10
Material finer than 0.075 mm	3.8	Max. 5	Concrete subject to abrasion (Max. 3) All other concrete(Max.5)
Fineness modulus =2.148 , Specific gravity=2.58			
Sulfate content (%)	0.1	Max. 0.5	-

*The test was carried out in Building Research directorate / ministry of construction and Housing

Table 4. Physical properties and sulfate content of coarse aggregate*.

Sieve size (mm)	Passing by weight (%) Crushed	Passing by weight (%) Rounded	Iraqi specification No. 45/1984 (5-20)mm	ASTM specification C33-03
37.5	100	100	100	-
25	100	100	-	100
20	99.3	99.0	95-100	90-100
10	30	30	30-60	20-55
5	0.05	1.0	0-10	0-10
Material fine than 0.075 mm	0	1.0	Max. 3	-
Sulfate content (%)	0.002	0.001	Max. 0.1	-
Specific gravity	2.6	2.6	-	-

* The test was carried out in Building Research directorate / ministry of construction and Housing

Table 5. Mix proportion for different concrete mixes.

Mix	Number	Cement (kg/m^3)	Water (kg/m^3)	Fine agg. (kg/m^3)	w/c	Mix
C.A-S25	1	585	190	603	0.32	1:1.031:1.735
C.A-S25	2	512	190	663	0.37	1:1.294:1.982
C.A-S25	3	455	190	710	0.42	1:1.560:2.23
C.A-S25	4	410	190	747	0.46	1:1.821:2.475
C.A-S25	5	372	190	778	0.51	1:2.091:2.728
C.A-S25	6	341	190	803	0.55	1:2.354:2.976
C.A-S25	7	315	190	825	0.60	1:2.619:3.222
C.A-S75	8	585	205	514	0.35	1:0.878:1.735
C.A-S75	9	512	205	573	0.4	1:1.119:1.982
C.A-S75	10	455	205	620	0.45	1:1.362:2.23
C.A-S75	11	410	205	661	0.5	1:1.612:2.475
C.A-S75	12	372	205	687	0.55	1:1.846:2.728
C.A-S75	13	341	205	714	0.6	1:2.173:2.976
C.A-S75	14	315	205	735	0.65	1:2.333:3.222
R.A-S25	15	585	190	603	0.32	1:1.031:1.735
R.A-S25	16	512	190	663	0.37	1:1.294:1.982
R.A-S25	17	455	190	710	0.42	1:1.560:2.23
R.A-S25	18	410	190	747	0.46	1:1.821:2.475
R.A-S25	19	372	190	778	0.51	1:2.091:2.728
R.A-S25	20	341	190	803	0.55	1:2.354:2.976
R.A-S25	21	315	190	825	0.60	1:2.619:3.222
R.A-S75	22	585	205	514	0.35	1:0.878:1.735
R.A-S75	23	512	205	573	0.4	1:1.119:1.982
R.A-S75	24	455	205	620	0.45	1:1.362:2.23

R.A-S75	25	410	205	661	0.5	1:1.612:2.475
R.A-S75	26	372	205	687	0.55	1:1.846:2.728
R.A-S75	27	341	205	714	0.6	1:2.173:2.976
R.A-S75	28	315	205	735	0.65	1:2.333:3.222

The aggregate content =1015kg/m^3 for all concrete mixes

Table 6. Compressive strength for accelerated and normal curing methods.

Number	Mix	Accelerated curing (MPa)			Normal curing (MPa)	
		Warm (35ºC)	Aut.	55ºC	7-day	28-day
1	C.A-S25	20.8	28.0	33.8	44.5	55.2
2	C.A-S25	18.1	24.5	30.0	39.2	48.5
3	C.A-S25	17.2	23.6	27.8	36.5	46.8
4	C.A-S25	15.8	22.8	26.5	34.2	44.8
5	C.A-S25	15.0	22.0	25.8	32.9	43.1
6	C.A-S25	14.7	21.3	25.0	31.2	42.2
7	C.A-S25	13.2	19.2	24.1	30.0	40.6
8	C.A-S75	17.8	22.0	26.5	33.5	43.3
9	C.A-S75	12.6	16.8	21.2	25.2	33.1
10	C.A-S75	11.0	15.2	18.2	24.2	30.6
11	C.A-S75	10.0	12.2	16.0	20.6	27.1
12	C.A-S75	8.6	11.8	15.1	18.8	24.5
13	C.A-S75	7.4	10.8	13.2	16.5	20.8
14	C.A-S75	6.5	8.5	10.8	14.0	17.8
15	R.A-S25	18.6	26.1	31.6	41.8	51.8
16	R.A-S25	16.2	22.8	28.1	37.1	45.1
17	R.A-S25	15.5	21.6	26.0	33.6	44.8
18	R.A-S25	14.2	20.7	24.5	31.2	43.2
19	R.A-S25	13.5	19.0	23.2	29.7	42.2
20	R.A-S25	13.2	18.2	22.0	28.0	40.8
21	R.A-S25	11.7	17.0	21.5	27.2	37.5
22	R.A-S75	16.0	20.2	24.1	30.0	41.0
23	R.A-S75	11.1	16.1	20.1	23.1	32.0
24	R.A-S75	9.6	14.2	16.0	22.6	28.1
25	R.A-S75	8.8	11.3	14.1	18.8	26.0
26	R.A-S75	7.6	10.5	12.8	16.5	22.1
27	R.A-S75	6.4	9.2	11.2	14.2	18.5
28	R.A-S75	5.2	7.5	9.0	11.8	16.0

Table 7. Descriptive statistics for experimental data

Curing type		Accelerated curing methods			Normal curing	
Statistics		warm(35ºC)	Autogenic	55ºC	7-days	28-days
N	Valid	28	28	28	28	28
	Missing	0	0	0	0	0
Mean		12.72	17.61	21.36	27.38	35.98
Std. Deviation		4.185	5.718	6.737	8.822	11.092
Minimum		5.20	7.50	9.00	11.80	16.00
Maximum		20.80	28.00	33.80	44.50	55.20

Table 8. Regression models summery for warm water curing method (35ºC)

Model No.	Regression models	R^2	F-tabulated
1-linear	3.02+2.59x acce. str.(35ºC)	0.955	556.08
2-linear	2.805x acce. str.(35ºC)	0.996	6167.3
3-Logarithmic	-37.441+29.562 x log[acce. str.(35ºC)]	0.956	563.3
4-Logarithmic	14.798xlog[acce. str.(35ºC)]	0.976	1091.5
5-Power	$3.291x \text{ acce. str.}(35ºC)^{0.941}$	0.971	878.04
6-Power	$\text{acce. str.}(35ºC)^{1.411}$	0.997	10371.7
7-Exponential	12.264+ exp[0.08x acce. str.(35ºC)]	0.921	303.3
8-Exponential	Exp[0.259 x acce. str.(35ºC)]	0.952	536.03

Table 9. Regression models summery for autogenous curing method.

Model No.	Regression models	R^2	F-tabulated
1-linear	2.16+1.921x acce. str.(Aut.)	0.98	1290.4
2-linear	2.032x acce. str.(Aut.)	0.998	13729.8
3-Logarithmic	-48.113+29.933 x log[acce. str.(Aut.)]	0.97	832.3
4-Logarithmic	13.082xlog[acce. str.(Aut.)]	0.971	911.79
5-Power	$2.351 \text{ x acce. str.}(\text{Aut.})^{0.952}$	0.983	1491.3
6-Power	$\text{acce. str.}(\text{Aut.})^{1.251}$	0.999	24704.4
7-Exponential	11.935+ exp[0.06x acce. str.(Aut.)]	0.946	455.2
8-Exponential	Exp[0.187x acce. str.(Aut.)]	0.954	564.6

Table 10 . Regression models summery for British curing method (55ºC).

Model No.	Regression models	R^2	F-tabulated
1-linear	1.147+ 1.631 x acce. str.(55ºC)	0.981	1329.1
2-linear	1.68x acce. str.(55ºC)	0.998	15929.6
3-Logarithmic	-56.428+30.742 x log[acce. str.(55ºC)]	0.967	750.9
4-Logarithmic	12.2x log[acce. str.(55ºC)]	0.967	799.7
5-Power	$1.793x \text{ acce. str.}(55ºC)^{0.98}$	0.984	1585.2
6-Power	$\text{acce. str.}(55ºC)^{1.171}$	0.999	52758.6
7-Exponential	11.544+ exp[0.051x acce. str.(55ºC)]	0.95	492.6
8-Exponential	Exp[0.155 x acce. str.(55ºC)]	0.958	614.0

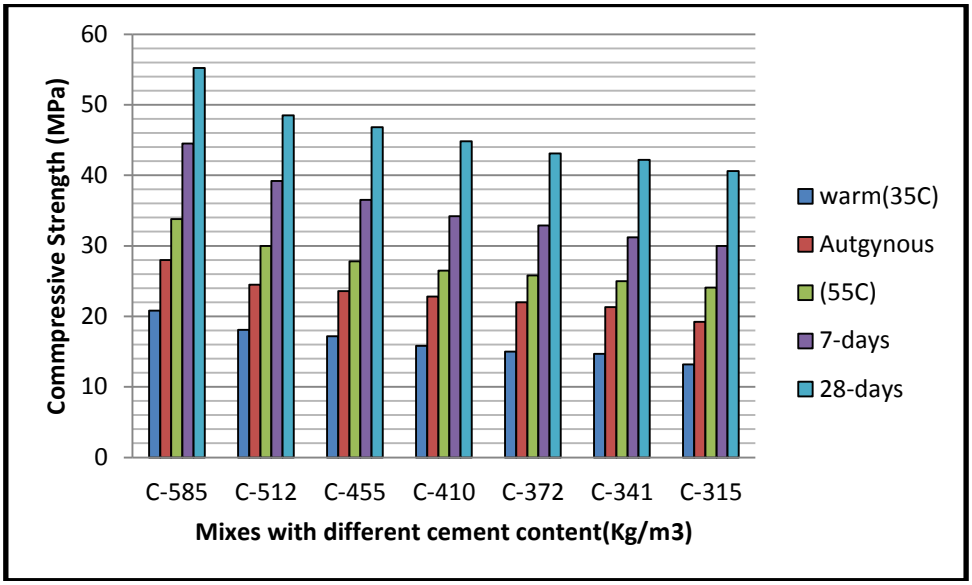

Figure 1. Compressive strength for concrete mixes with different cement content (C.A –S25) for accelerated and normal curing methods.

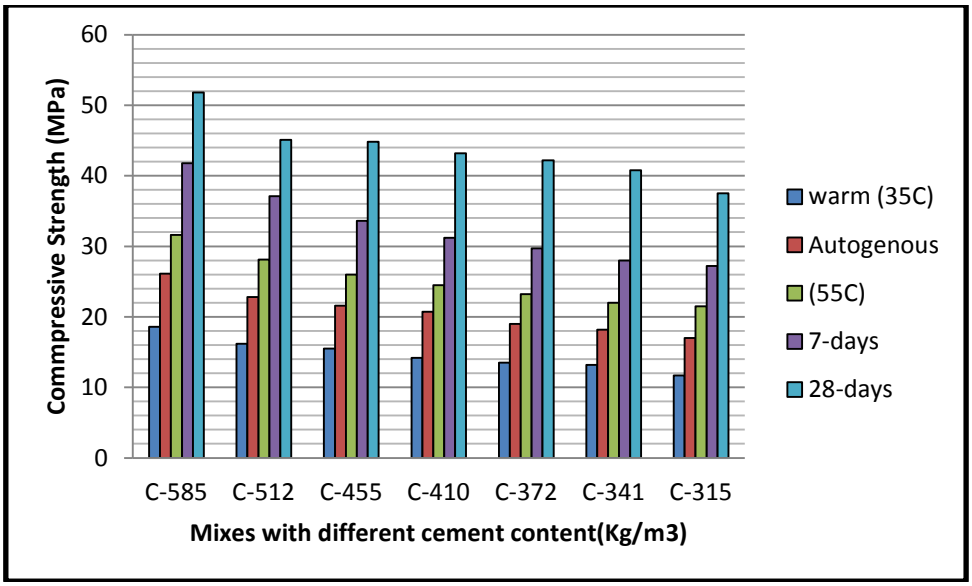

Figure 2. Compressive strength for concrete mixes with different cement content (R.A –S25) for accelerated and normal curing methods.

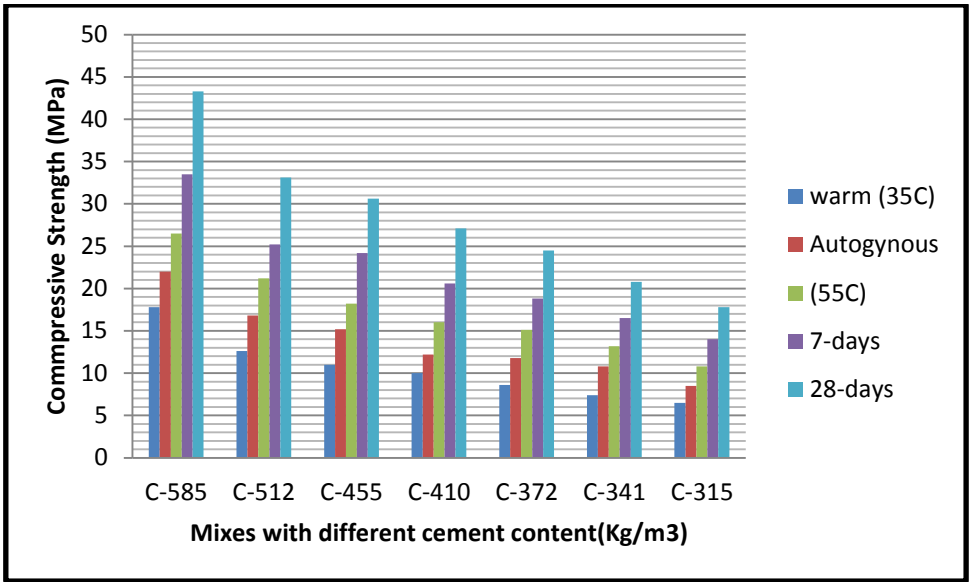

Figure 3. Compressive strength for concrete mixes with different cement content (C.A –S75) for accelerated and normal curing methods.

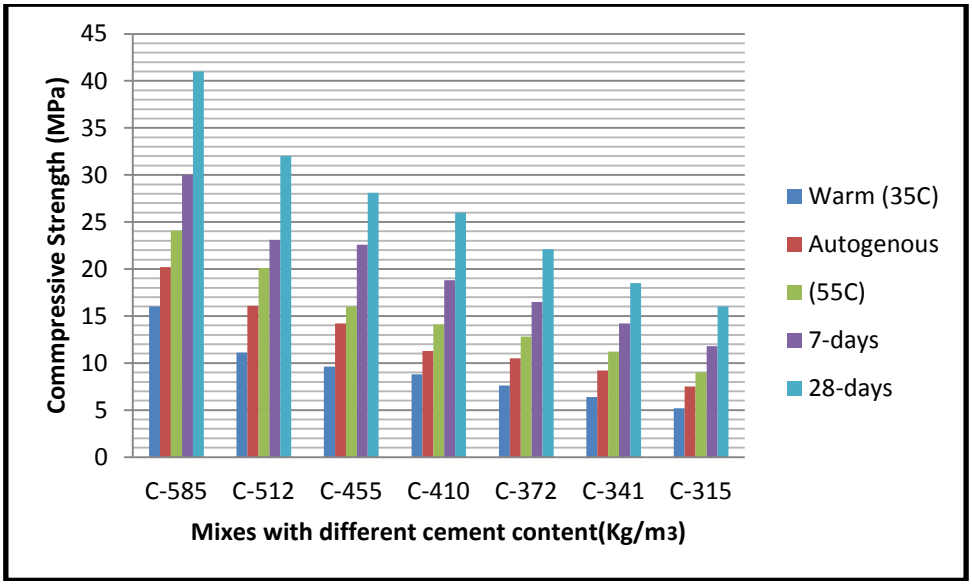

Figure 4. Compressive strength for concrete mixes with different cement content (R.A –S75) for accelerated and normal curing methods.

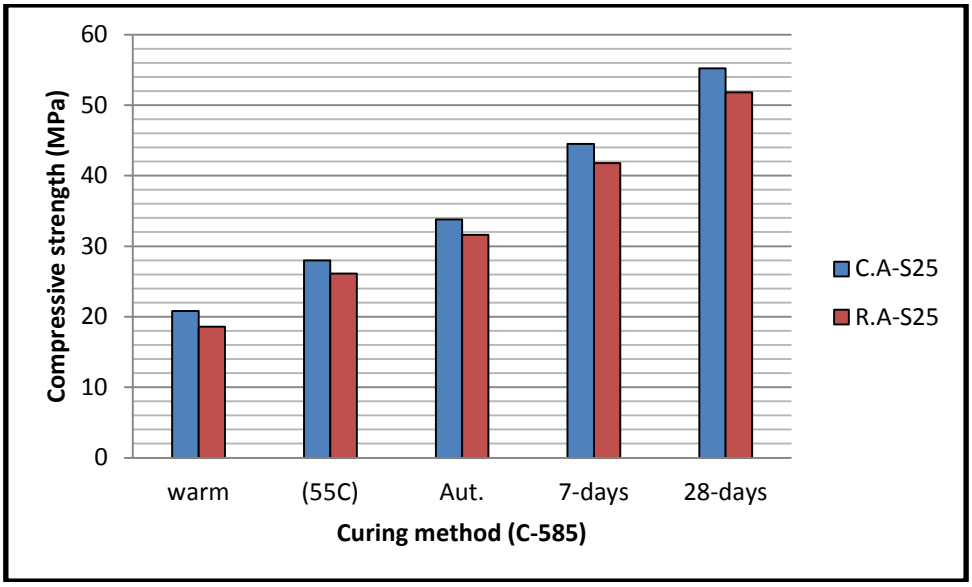

Figure 5. Compressive strength with different curing method for crushed and rounded coarse aggregate with cement content (C-585)kg/m^3 and S25.

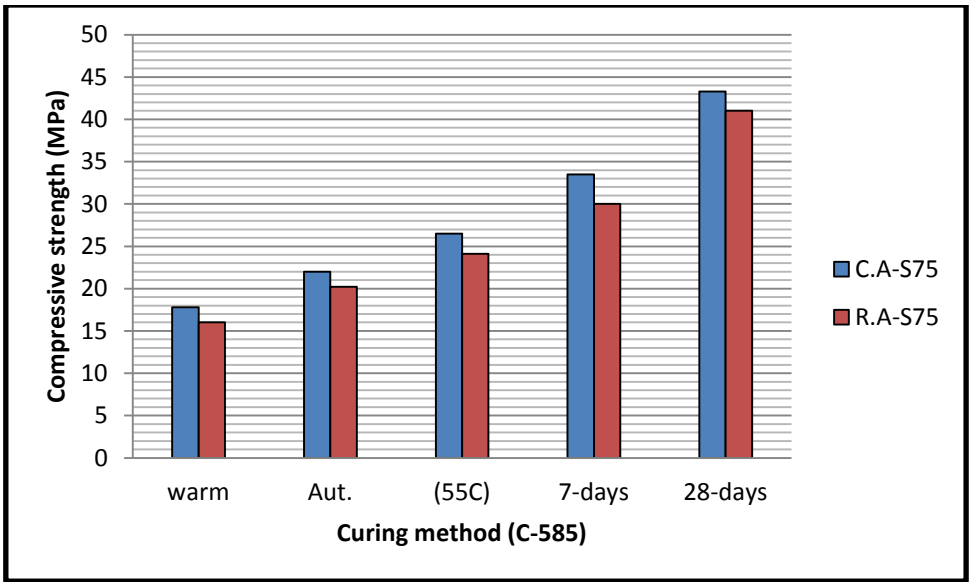

Figure 6. Compressive strength with different curing method for crushed and rounded coarse aggregate with cement content (C-585)kg/m^3 and S75.

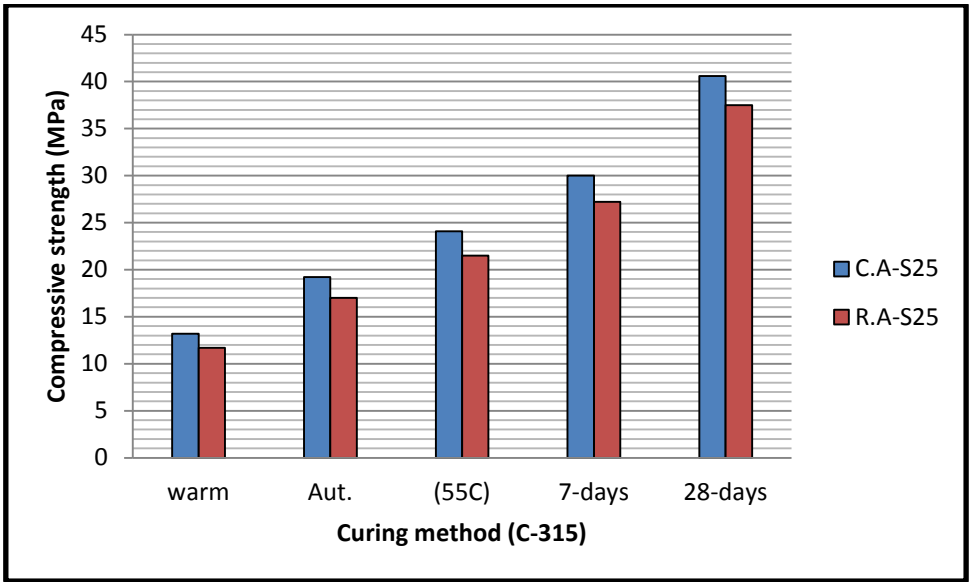

Figure 7. Compressive strength with different curing method for crushed and rounded coarse aggregate with cement content (C-315)kg/m^3 and S25.

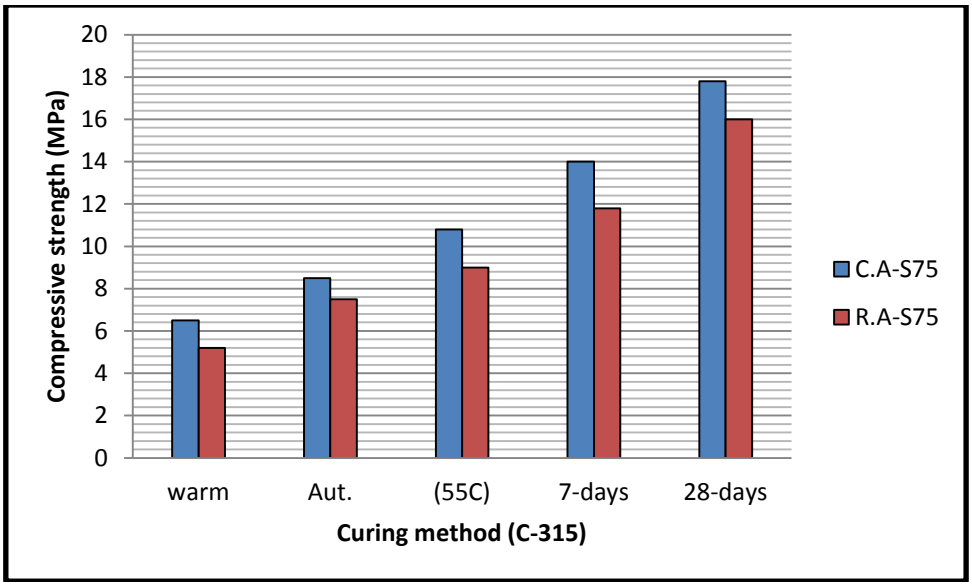

Figure 8. Compressive strength with different curing method for crushed and rounded coarse aggregate with cement content (C-315)kg/m^3 and S75.

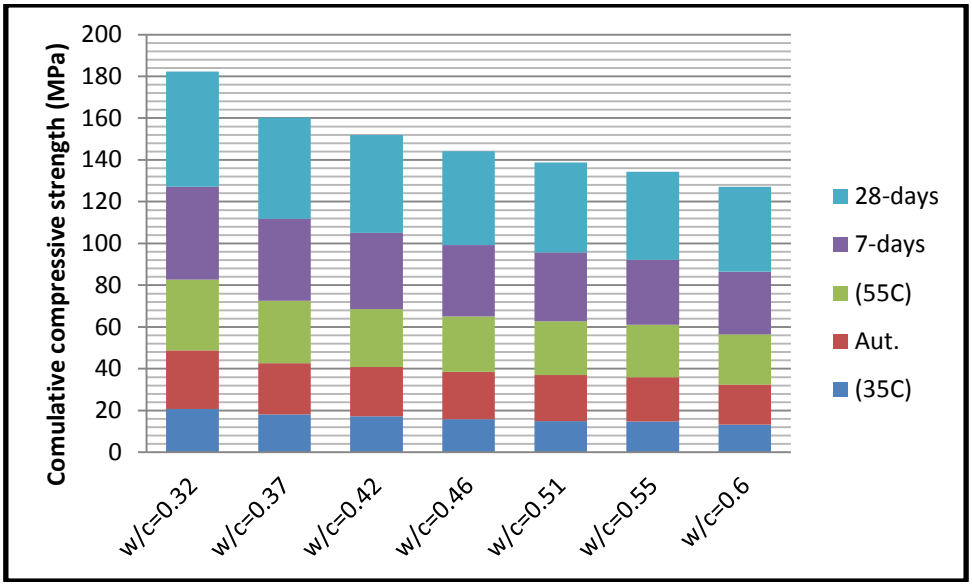

Figure 9. Cumulative compressive strength for different curing methods with W/C ratio for C.A-S25 concrete mixes.

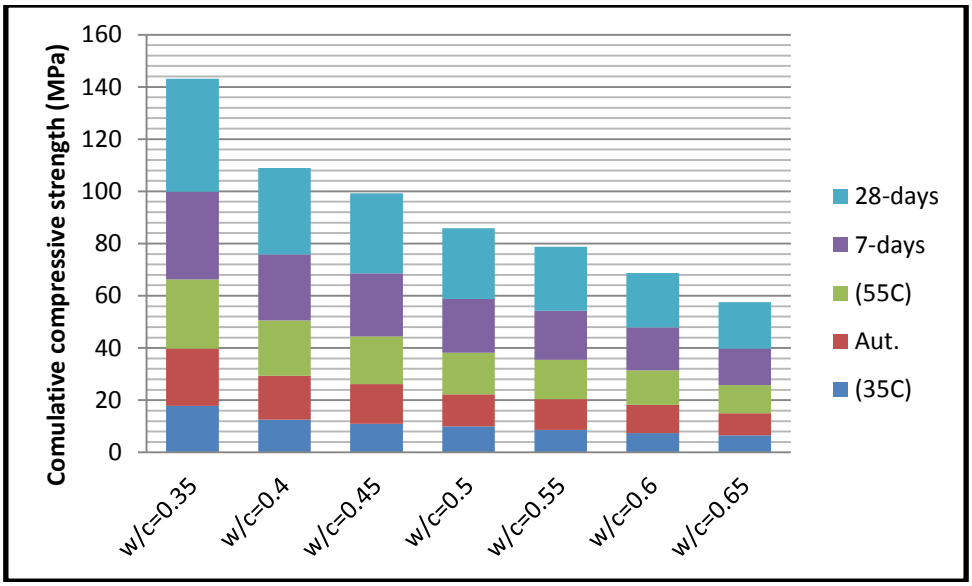

Figure 10. Cumulative compressive strength for different curing methods with W/C ratio for C.A-S75 concrete mixes.

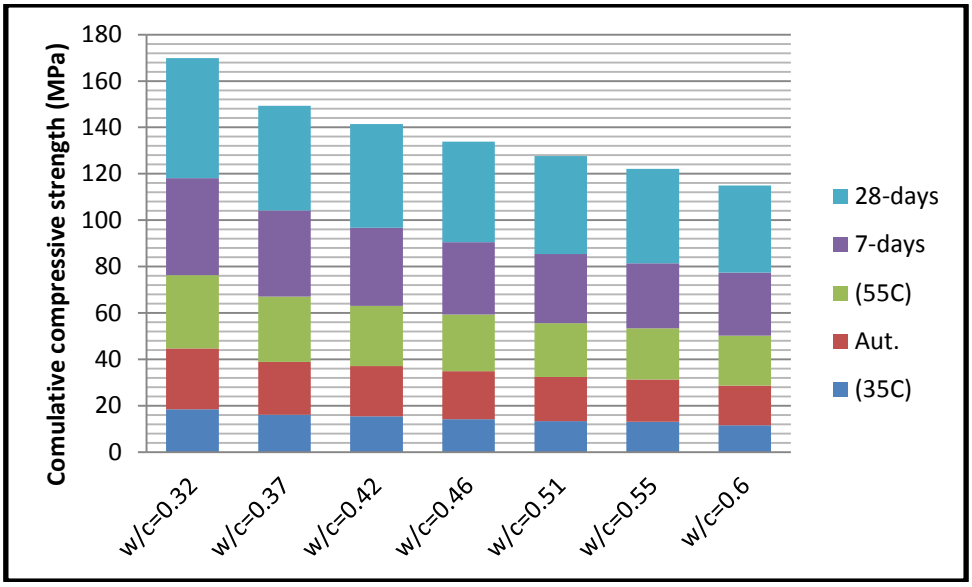

Figure 11. Cumulative compressive strength for different curing methods with W/C ratio for R.A-S25 concrete mixes.

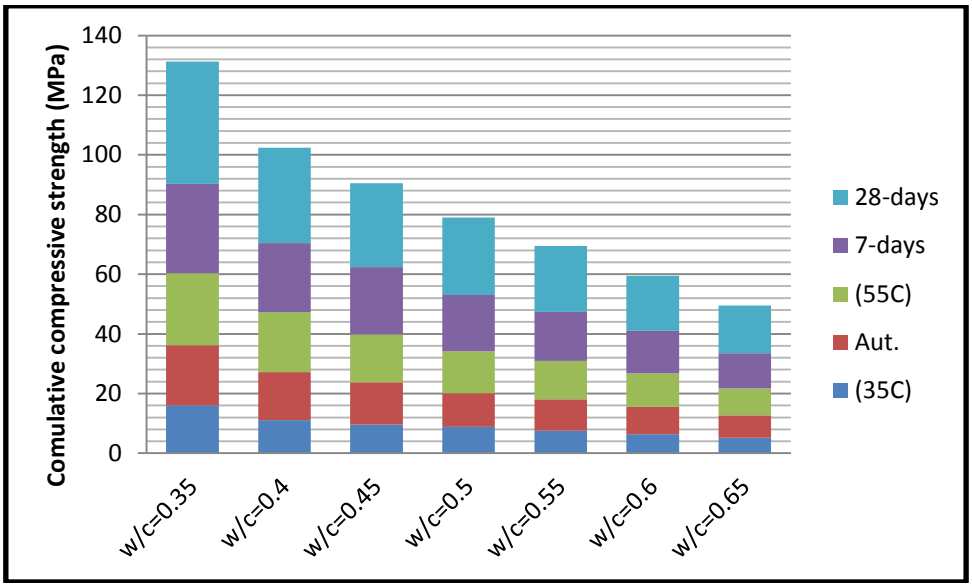

Figure 12. Cumulative compressive strength for different curing methods with W/C ratio for R.A-S75 concrete mixes.

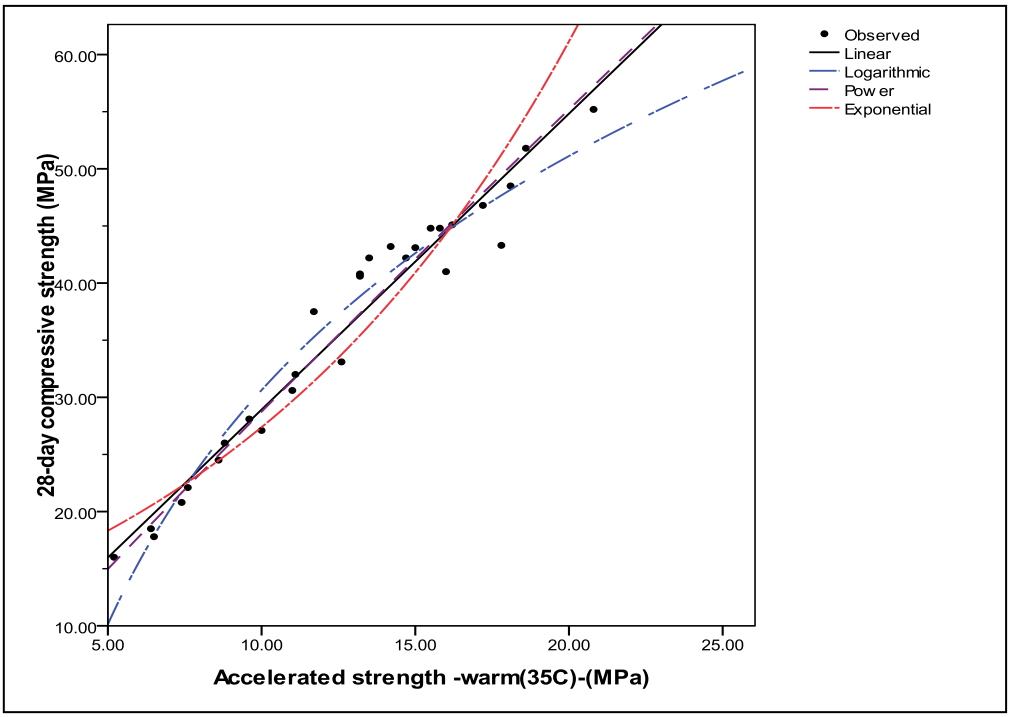

Figure 13. Relationship between 28-day compressive strength and accelerated strength (warm water method) for models with constant.

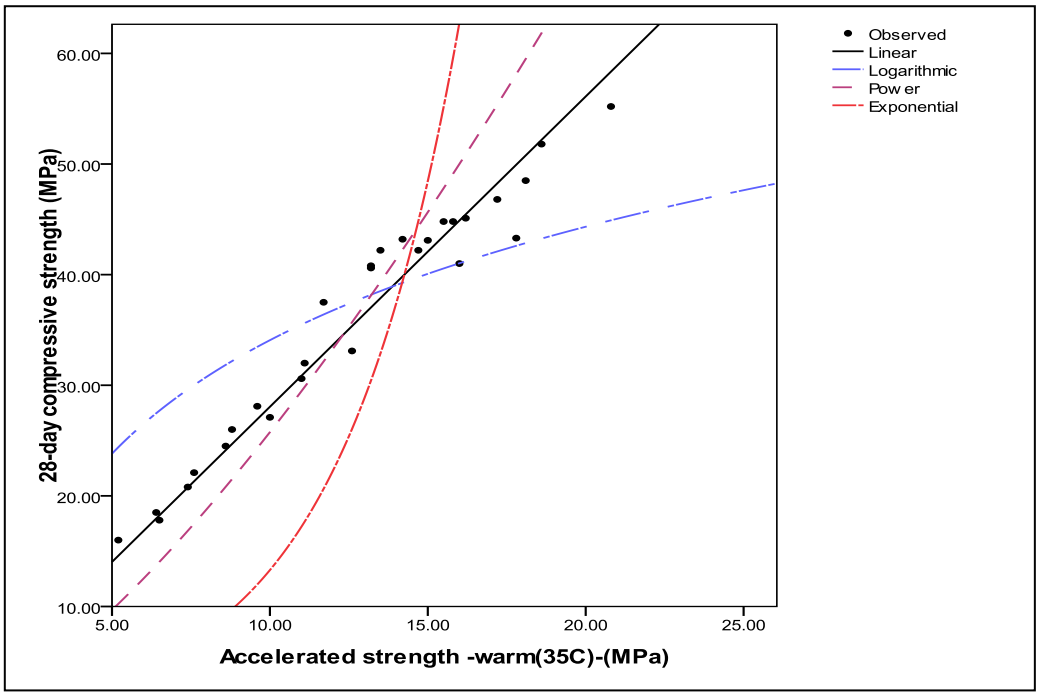

Figure 14. Relationship between 28-day compressive strength and accelerated strength (warm water method) for models without constant.

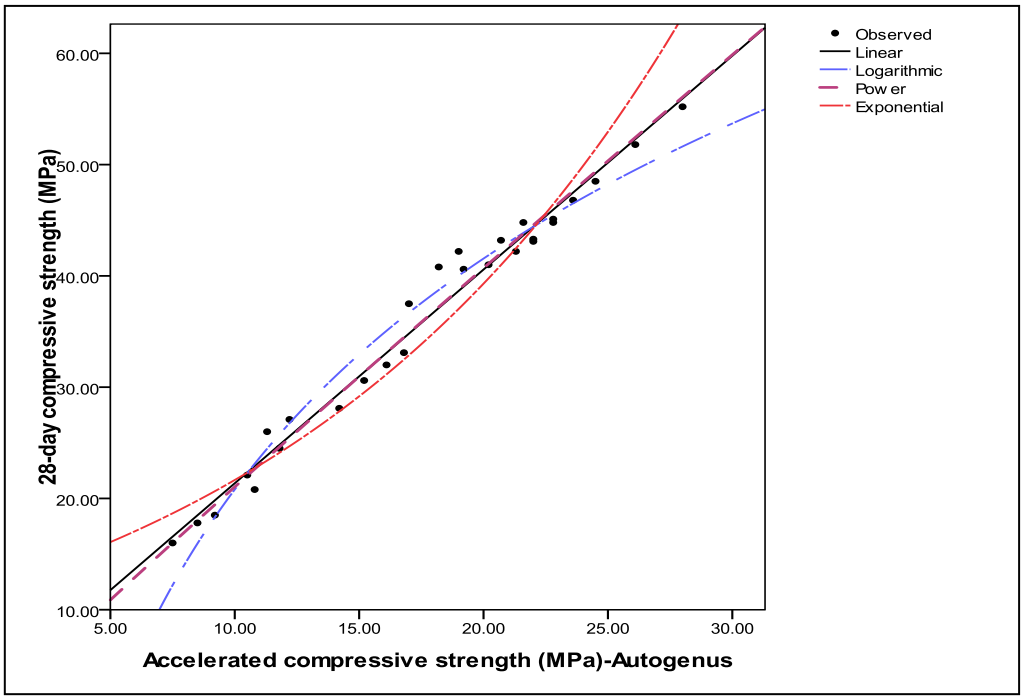

Figure 15. Relationship between 28-day compressive strength and accelerated strength (Autogenous method) for models with constant.

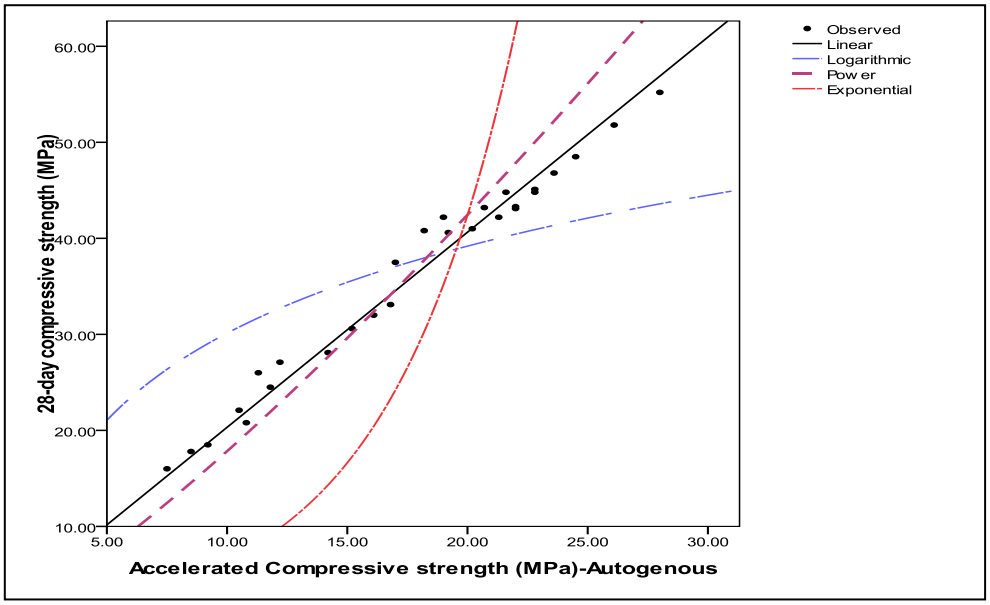

Figure 16. Relationship between 28-day compressive strength and accelerated strength (Autogenous method) for models without constant.

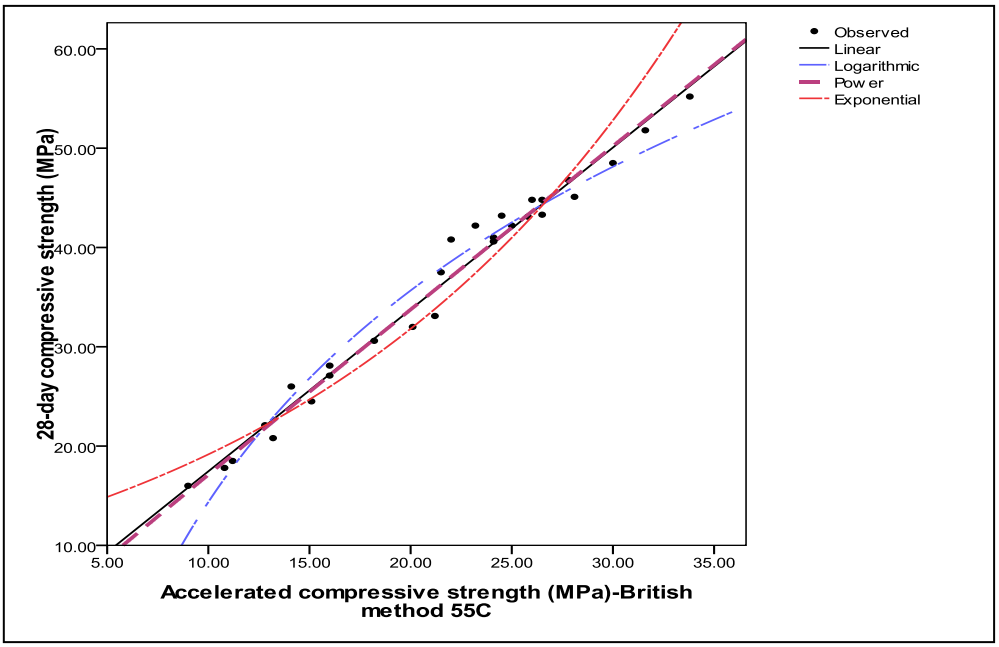

Figure 17. Relationship between 28-day compressive strength and accelerated strength (British method) for models with constant.

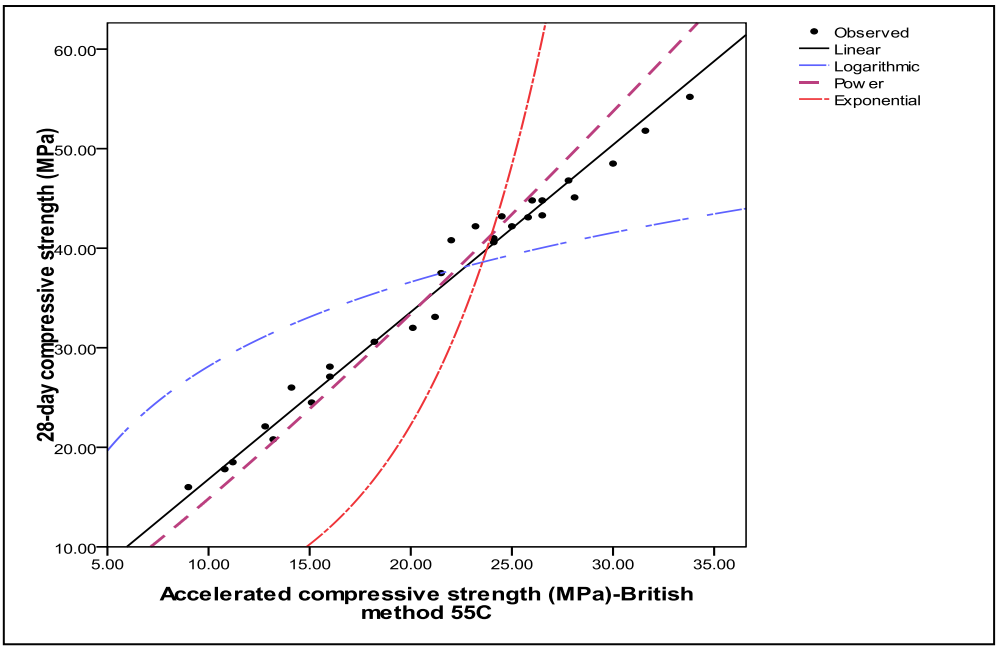

Figure 18. Relationship between 28-day compressive strength and accelerated strength (British method) for models without constant.

Statistical Analysis of Mortality and Morbidity Due to Traffic Accidents in Iraq

Amjad Hamad Albayati
Assistant Professor
Engineering College-University of Baghdad
E-mail: a.khalil@uobaghdad.edu.iq

Roaa Hamed Lateif
Assistant Lecturer
Engineering College-University of Baghdad
E-mail: roaa.hamed@coeng.uobaghdad.edu.iq

ABSTRACT

Undoubtedly, Road Traffic Accidents (RTAs) are a major dilemma in term of mortality and morbidity facing the road users as well as the traffic and road authorities. Since 2002, the population in Iraq has increased by 49 percent and the number of vehicles by three folds. Consequently, these increases were unfortunately combined with rising the RTAs number, mortality and morbidity. Alongside the humanitarian tragedies, every year, there are considerable economic losses in Iraq lost due to the epidemic of RTAs. Given the necessity of understanding the contributory factors related to RTAs for the implementation by traffic and road authorities to improve the road safety, the necessity have been a rise for this research which focuses into two objectives; the first objective is a descriptive analysis for the RTA based on a retrospective analysis during the period of 2002–2015 with the aids of the data obtained from the reports of Iraqi Central Statistical Organization whereas the second objective is to conduct a statistical analysis for RTAs to correlate the criterion variable of accident number, mortality or morbidity to predictor variable which include motorization level or population using traditional statistical regression approach and Artificial Neural Network (ANN) approach.

Key words: road traffic accidents, mortality, morbidity, motorization level.

التحليل الإحصائي للوفيات والجرحى بسبب الحوادث المرورية في العراق

امجد حمد البياتي
استاذ مساعد
كلية الهندسة-جامعة بغداد

رؤى حامد لطيف
مدرس مساعد
كلية الهندسة-جامعة بغداد

الخلاصة

حوادث الطرق المرورية (RTAs) هي معضلة رئيسية من حيث الوفيات والجرحى التي تواجه مستخدمي الطرق والجهات المسؤولة عن سلامة المرور والطرق. ومنذ عام 2002، زاد عدد السكان في العراق بنسبة 49 في المئة وعدد المركبات بمقدار ثلاثة أضعاف. ونتيجة لذلك، فإن هذه الزيادات ترافقت مع ارتفاع عدد الحوادث المرورية والوفيات والجرحى. إلى جانب المآسي الإنسانية، فإن هناك خسائر اقتصادية كبيرة في العراق كل عام بسبب وباء الحوادث المرورية. ونظرا لضرورة فهم العوامل المساهمة في الحوادث المرورية من قبل الجهات المسؤولة عن سلامة المرور والطرق من اجل تحسين السلامة المرورية في العراق، فقد برزت الحاجة لهذا البحث الذي يركز على هدفين؛ الأول هو تحليل وصفي للحوادث المرورية استنادا إلى تحليل بأثر رجعي خلال الفترة 2002-2015 بمساعدة المعطيات التي تم الحصول عليها من تقارير منظمة الإحصاء المركزية العراقية في حين أن الهدف الثاني هو إجراء تحليل إحصائي للحوادث المرورية لربط المتغير المعتمد لعدد الحوادث و الوفيات و الجرحى بمتغير مستقل بما في ذلك مستوى امتلاك المركبات أو السكان باستخدام الانحدار الإحصائي التقليدي و الشبكة العصبية الصناعية (ANN).

الكلمات الرئيسية: حوادث الطرق المرورية، الوفيات، الجرحى، مستوى امتلاك المركبات.

1. INTRODUCTION

Although the road traffic accident (RTA) defined as an event suddenly, inadvertently and unexpectedly occurred under unforeseen circumstances, but identifying the contributory factors as well as circumstances that affect the occurrence of traffic accidents could be helpful in reducing them to its barest minimum through the attraction attention of the traffic agencies to enact an efficient traffic safety regulations to lessen the influence of this dilemma.

Globally, according to the world health organization (WHO), About 1.25 million people die each year as a result of RTA, around 85 percent of these deaths occur in developing countries. Furthermore, up to 50 million people suffer non-fatal injuries, with many incurring a disability as a result of their injury. RTA caused 500 children lose their lives every day. It is the leading cause of death for young people aged 15 to 29 years, and the eighth leading cause of death globally. Alongside the humanitarian tragedies, every year, USD 500 billion is lost due to the epidemic of RTA that represents approximately 3 to 5 percent of the gross national product of the countries. In view of the aforementioned facts, a global target was adopted by the United Nations (UN) framework of Sustainable Development Goals (SDGs) in 2016 to halve deaths and injuries caused by road crashes by 2020.

Locally, according to the WHO report 2015, Iraq is ranked 18th out of the 180 countries in the total number of deaths due to traffic accidents in 2013 (5789 deaths) in which India occupies the top rank (137572). Within the Eastern Mediterranean Region (EMR), Iraq has the 2nd highest road traffic mortality rate based on the report of the WHO in 2013. The highest numbers of mortality due to traffic accidents were among children and young people. Approximately half of mortality in Iraq were pedestrians, a ratio almost double that of any neighboring country, **Leidman, et al., 2016**.

Based on the aforementioned preface, the necessity has been arise for this research which aims two main objectives; analysis the RTAs based on a retrospective analysis during the period of 2002–2015 considering accidents number, accidents types, mortality, morbidity, driver age group, cause of accidents, light condition, monthly distribution of accidents, vehicle type involved in accident, and functional class of highway. The second objective is to conduct a statistical analysis for RTA to correlate the criterion variable of accident number, mortality or morbidity to one or more predictor variables which include motorization level or population, using traditional statistical regression and ANN approaches.

2. BACKGROUND

Road safety is a main concern and aim of highway and traffic engineers. In 1949, **Smeed** has been developed the first statistical model which relates the mortality rate (road death per vehicle) with exposure variable of motorization level (vehicle per capita), the model was based on the analysis of RTAs data that dating back to the year of 1938 for 20 courtiers from different continent of the world. The suggested model which was later known as Smeeds Law has the following hyperbola form:

$$D/N = 0.0003\ (N/P)^{-2/3} \quad (1)$$

where D is annual road deaths, N is number of registered vehicles, and P is population. The main theme which can be abstracted from the Smeeds Law is that the increase of motorization level leads to a decrease in mortality rate.

Although, there was some contradictions existed among the researchers about the Smeed formulas, **Anderson, 1985** and **Adams, 1987**. However, researchers from developed as well as developing countries still use the Smeed laws but with some modification for either the power or intercept of the exposure variable, **Bener,** and **Ofsu, 1991, Ghee, et al., 1997, Koren,** and **Borsos, 2010, Al-Omari, et al., 2013, Hesse,** and **Lamptey, 2014**.

Islam, and **Ahmed, 2012** examined the RTA data of Oman for a period between 2000 and 2009, they stated that the number of accidents fell down from 13,040 cases in 2000 to 7,253 in 2009 with a drop of 44 percent over the study period despite the fact that motorization level has increased over the study period by 26 percent and reach approximately 230 vehicle per 1,000 population in 2009. They finally conclude that 70 percent of the RTA happened to drivers aged 17-36 years.

Al-Omari, et al., 2013 investigated the RTA data of Jordan (1998-2010), they stated that a total of 1,040,112 accidents have occurred over the study period with an average of 80,008 accidents/year. They attributed the increments of RTA which was 223 percent during the study period to the development of motorization level from 82 vehicle/1000 population in the year 1998 to 176 vehicle/1000 population in the year 2010 with an increment of 114.6 percent. Also they stated that majority of RTA have occurred during the summer months with the highest during the month of August in Sundays and Thursdays (the first and last working days in Jordan).

Ghaffar, and **Ahmed, 2015** stated that 19 deaths occur daily and approximately 4 peoples injured every hour in the kingdom of Saudi Arabia due to RTA in the past 10 years (2006-2015), the annual cost for these RTA was about 7 billion US dollars.

Wang, and Chan, 2015 stated that road traffic fatalities (RTF) has increased substantially (134 percent) in china over the period 2002–2012. They believed that the main reason for this increment was the rapid development in motorization level, The number of private vehicles in China has increased from7.7 million in 2001 to 73.2 million in 2011, and the total number of registered vehicles has increased from 65.2 million in 2001 to 209.1 million in 2011. Also, they demonstrated that 57 percent of RTFs occurring among individuals aged 45 and above during 2011–2012.

Bashar, et al., 2013 utilized the traffic accidents data in Jordan for thirteen years period 1998 to 2010 to develop the following power model that correlate number of traffic accident per year (ACC) with motorization level (number of registered vehicles per 1000 population (M):

$$ACC = 56.47\, M^{1.57} \quad (2)$$

Also, they suggested the following polynomial model that predicts the traffic accidents fatalities per year (F) using motorization level (M) as independent variable:

$$F = -9.109\, M^2 + 2847M - 9879 \quad (3)$$

Ibrahim, 2014 utilizes time series methods to fit and forecast rates of traffic fatalities in the United Arab Emirates (UAE) , the accident fatality data were divided into two parts, A training dataset, 1977 to 2003, which is used to describe trend and to develop traffic fatality prediction models, and a validation dataset, 2004 to 2008, which is used to validate the developed models. ARMA like model with an autoregressive component (AR) of order 1 was applied by the author and the following best fit model was suggested:

$$Log(F/V)_t = 0.7425 - 0.7675t + 0.66641 log\,(F/V)_{t-1} \quad (4)$$

Where F is the number of traffic fatalities, V is the number of vehicles and t is the time in years. The author concluded that there is a downward trend in the UAE traffic fatality rates, forecasts of traffic fatalities per 1000 registered vehicles for 2013 is 0.4847 with a reduction approximately 30 than that of 2008 rate.

With the abundance of global scientific research in the RTA field, the number of local researches does not exceed the fingers of hand in this field, **Al-Jameel, 2016** was developed an Expert system for RTA that provides expert consultation in the domain of highway safety in Iraq. The system consisted of two phases. The first one is the diagnostic phase and the second one is the remedy phase. The objective of the developed expert system was to reduce the number of RTA.

Aljoborae, and **Al Humairi, 2014** conducted a hospital based cross sectional study in Hillah city based on the data obtained from the central hospital within the city for five months' time period (May- November 2013). The aim of the study was to investigate some the socio-demographic characteristics of the RTA victims, the authors concluded about half of the drivers had no driving permits and 59 percent of the victims had a history of previous exposure to RTA, Also 83 percent of victims were male, 76 percent came from urban areas and 69 percent of victims were exposed to RTA during daytime. **Leidman, et al., 2016** investigated the fatalities RTA that occurred between January 2010 and 31 December 2013 in eight governorates of Iraq (out of 18 governorates): Baghdad, Al-Anbar, Basrah, Erbil, Kerbala, Maysan, Ninevah, and Al-Sulaimaniya. The data were obtained from the Iraqi Ministry of Health (MoH). The authors concluded that the highest numbers of road traffic fatalities were among males 15 to 34 years of age and children of both sexes under 5 years of age, approximately eight out of ten road traffic fatalities in Iraq were males, and rates of road traffic fatalities ranged from 8.6 to 10.7 per 100,000 population.

3. DATA SOURCE

This study is based on the RTAs data obtained from Central Statistical Organization (CSO) in the ministry of planning. CSO were collected the accidents data from the police affairs agency in the ministry of interior that receive the data from the police stations distributed within each city in Iraq. The accidents data were available from 2002 to 2015 for Iraq (except Kurdistan region, the northern three governorates).

4. ANALYSIS OF ACCIDENTS DATA

4.1 Number of Accidents

The annual distribution of the 109067 RTAs occurred during 2002-2015 is presented in **Fig. 1** with the annual average RTAs of 7790, as well. It's obvious there was a small drop in RTAs in 2003 (outbreaks of the war) then raised gradually in the next three years to reach 9010 in 2005. The maximum downward divergence from the annual average RTAs was recorded in 2007, the RTAs dropped to 3135. the matter which can be attributed to the "even and odd policy" which was followed in Iraq to improve the traffic operational conditions of the highways network, the vehicles that end with an even plate number are permitted to drive in even calendar days whereas those end with an odd plate number can drive in odd calendar days. The application of this policy was terminated in 2008. Then, between 2007 and 2012 there was a noticeable rise in RTAs which finally peaked at 10709 in 2012. This increment associated with the improved level of average annual income for the people. The Gross Domestic Product (GDP) reached to 6,619 USD per capita as

compared to 3,125 USD in 2007. In June 2013, the Iraqi governorates reactivated the "even and odd policy" and the RTAs steadily decrease until 2014 then the RTAs stagnated and leveled off at 8836 in 2015.

Although the fluctuation of the RTAs data presented in **Fig.1** is graphically obvious, further investigation was carried out using Mann-Kendall test to explore any statistically significant trend in the data. The null hypothesis H0 represents no trend. At significance level (α) = .05, 2-tailed test. The obtained Z statistic is z = 1.53 which is lower than 1.96, therefore the null hypothesis is accepted since there is not enough evidence to determine that there is a downward or upward trend in the data.

4.2 Type of Accidents

When the RTA data sorted according to the type of accidents, it is obvious that the most common type of accident during the period 2002 to 2015 is run over which accounted for 45.7 percent of the total number of accidents that have been occurred as shown in **Fig. 2**. This type of accident is the most dangerous type due to the direct contact between the vehicle and the pedestrian involved in the accident. The high mortality rate is belonged to this type of accident, for example, in 2014, the mortalities resulting from the run over constituted approximately 44.3 percent of the total number of mortalities due to the RTA which is the highest mortality rate whereas the morbidities from the same type of accidents composed approximately 36.9 percent of the total number of morbidities representing the second highest morbidity rate after that recorded due to the collision. The collision is the second most common type of RTA, 47226 accidents of this type have been recorded out of 109067 total accident numbers during 2002-2015, this figure represent approximately 43.3 percent which is slightly lesser than the percentage of the first type. Collectively, run over and collision scored together approximately 89 percent of the total number of accidents. As an annual mean, 2101 persons lost their lives and 7590 persons suffered from the morbidities due to these types of accident. In the third rank of RTA there is the turnover; with a rate of 10 percent which is considered low when compared with run over or collision. Finally, 1 percent of RTA was recorded as “others” which denoted the accident like vehicles fire or falling downhill in river.

4.3 Mortality and Morbidity

RTAS have an awful influence on humans, societies and countries. In Iraq around 29415 persons were lost their lives during the period from 2002 to 2015, beside 106259 persons suffered from morbidities due to the RTA. Based on the victims data presented in **Fig. 3** below, the annual average numbers of mortalities and morbidities during 2002-2015 are 2101 and 7590, respectively. Recalling to the mind that the number of accident within this period has an annual average of 7790, it can be easily concluded in each one accident the mortality rate was 0.27 (each 3.7 accidents resulted in one death) whereas the morbidity rate was 0.97.

During 2002 to 2015, both the number of mortality and morbidity reached a low of 1151 for the first and 3033 for the later in 2006, then the mortality rised gradually and morbidity goes up drastically, both of them reached the peak in 2012, the same year that witnessed the highest level of RTAs in Iraq, the recorded mortality and morbidity are 3132 and 11009, respectively.

In order to inspect the existence of any statically useful trend in both the mortality and morbidity data, Mann-Kendall tests were used with a significance level (α) = .05, 2-tailed test. The null hypothesis H_0 represents no trend whereas Ha refers to the existence of an upward trend in the data.

The obtained Z statistic is z = 3.06 for mortality and z = 2.62 for the morbidity, both values more than 1.96. Therefore, the null hypothesis H_0 is rejected for both cases and the evidence is enough to determine that there is an upward trend in both mortality and morbidity data.

The analysis of the accidents data based on the age group of deaths presented in **Fig. 4** shows that about 61 percent of mortality due to RTAs are within the age group range of (18-47) years. It is evident that the youth is the most vulnerable to traffic accidents; therefore the problem becomes catastrophic since most of mortality represents the labor force of the Iraqi community.

Globally, nearly three times more male than female died due to road traffic accidents (WHO, 2013). In Iraq, the death possibility for male due to traffic accidents more than female by approximately four times as illustrated in **Fig. 5**, the same figure shows that the exposure for morbidity due to traffic accidents for male is higher than that for female by 62 percent.

4.4 Drivers Age

The distribution of RTAs based on the drivers age group is presented in **Fig. 6**, it is evident from the exhibited data that the RTAs distribution is skewed towards the younger age group with a mean of 26 years old and maximum occurrences of 24 percent in the age group 24-29 years. followed by those in the age group 30-35 with 21 percent , and 18-23 with 19 percent. Collectively, these three age groups are involved in around two thirds of total RTAs during the period 2002-2015, this result can be attributed to the fact that the drivers within these age groups are young adults, active and have more tendencies for making trips for educational, work and social purposes than other age groups, the matter which increase the probability to exposure for RTA. The teenage drivers with age less than 17 years old accounting for only 5 percent RTAs since the drivers within this age group are not permitted to have driving license according to Iraqi rules that stated the minimum age for obtaining a driving license is 18 years. The RTAs reached a minimum of 2 percent for elderly drivers with age more than 60 years as compared to other age groups due to the facts of limited trips that they need.

4.5 Causes of Accidents

RTAs distribution according to the contributory causal factors is presented in **Fig. 7**. The factors are classified into the following categories; drivers, vehicle, road, pedestrian, passengers and other factors (i.e., animal or obstruction). Based on the presented data, the drivers are the major contributor factor for the RTAs in Iraq with a percentage rate of 72 because many of them do not abide the principle driving rules and safety regulations. For instance, although the local regulations stated that the speed limits for the urban and rural road are 60 km/hr and 100 km/hr, respectively, the enforcement level for this regulation is just 3 out of 10 degree, **WHO, 2015**. The same matters are also applicable for the helmet use for motorcycle drivers and seat belt wear for the vehicle drivers, the enforcement level for the former is just 2 whereas for the latter is 5.

Following the drivers, the vehicle is the second main cause for the RTAs with 11 percent. Poor roadway conditions, structurally presence of sever rutting (loss of steering control) as well as functionally improper geometric design features, are responsible for about 6 percent of traffic accidents in Iraq. The crossing of pedestrian from the undesignated crossing lines in highways other than using the crossing lines or footing bridge resulted in about 7 percent of RTAs. The remaining

causes for RTAs consist of passengers and the "other factors", each of them had 2 percent, denoting the lowest involvement rate as compared to the other causes.

4.6 Light Conditions

One of the major environmental non-behavioral factors which considerably affect RTAs is lighting conditions due to the visibility restrictions in darkness. Based on the availability for data, the numbers of RTAs for four light conditions within the day were recorded. The light conditions consisted; daylight, dark, sunrise and sunset. The total number of RTAs for each light condition (at the time of accident) is shown graphically in **Fig. 8**. Although it was expected that the number of RTAs in the darkness be more than that at under daylight condition, the result showed the contrast. The majority of RTAs in Iraq, 69 percent, happened under the day light condition whereas just 10 percent of RTAs occurred during darkness. This discrepancy could be attributed to the existed vehicles curfew in night (12 am – 5 am) for the period 2007 to 2015 in Baghdad (capital) as well as some other Iraqi governorates. Other light conditions, sunset and sunrise, account for about 10 percent of the RTAs, for each one of them.

It was found that around 69% of the road traffic incidents happened under the day light condition, and all other light conditions had same percentages with a rate of (10 %) for each one of them. In other words, the majority of road traffic crashes revolving in Iraq are taking place during the day light condition because imposed a curfew in night (12 am – 5 am) due to security situation in Iraq at the period from 2003 to 2015.

4.7 Monthly Distribution

Fig. 9 shows how the average number of RTAs for each month changed over the period of 2002 to 2015. January has the lowest number of RTAs; it contributes to about 7 percent from the total number of the RTAs that occurred during the year. Thereafter, slight differences in RTAs monthly distribution can be observed until august. During the last third of the year, the RTAs show detectable fluctuation in the monthly distribution as compared to the first two thirds of the year. The RTAs increase steadily during September and October; the peak number of RTAs occurred in October, within this month there is 753 RTAs which represent 10 percent from the total number of RTAs in the year, this could be attributed to the beginning of the academic year in the colleges as well as all types of schools. Following October, the RTAs decrease in November and then slightly increase in December.

However, the visual inspection for the monthly distribution of RTAs may be considered not enough to conclude either there is significant differences in the average number of RTAs between the months of year or not. Statistics can be serves as a good tool to ascertain the truth. For this purpose, Poisson mean analysis was performed using Minitab V16 software.

For $\alpha = 0.05$, the result is shown in the **Fig. 10**, below. It is evident that the mean number of RTAs in each month is 627 and the LDL and UDL are 558 and 695, respectively. Also, the figure pointed out that there are no significant differences in the mean number of RTAs for all the months of the year, since they are all laying within the limits of decision, except January and October, the former fall below the LDL indicating the month with minimum number of RTAs whereas the latter fall above the UDL referring to the month with the maximum number of RTAs in the year.

4.8 Vehicle Type

The transport system in Iraq is mainly based on the passenger car. For example, the distribution of the registered vehicle in 2015 which is presented in **Fig. 11** revealed that 84 % of registered vehicle is passenger car followed by 9% trucks and 3 % buses beside 3 % motor cycle and pedal cycle as well as 1 % for other types of vehicles (a.e., construction and agricultural).

Based on the aforementioned facts, passenger car was expected to be over-represented in the occurrences of RTAs in Iraq. The inspection of the data presented in **Fig. 12** which exhibits the contribution of each type of vehicle in the RTAs agreed with this expectation. About two thirds of RTAs are caused by passenger car followed by motor cycle which accounted for 11 percent of the total number of accidents. The trucks and buses shared in RTAs with 9 percent for each one whereas the contribution of pedal cycle and other types of vehicles were 3 and 1 percent, respectively.

4.9 Highway Functional Class

Based on the functional classification of highways and their effect on the geometric characteristics as well as traffic characteristic (speed and volume) of the highways, the contribution of each type of highways in RTAs is differ than the others. Obviously in **Fig. 13**, about 59 percent of RTAs occurred in arterial roads, perhaps this class of highway has a high geometric design characteristic that allows high speed and carry high volume of traffic, the matter which rises the probability of an accident also the majority of transportation network in Iraq consisted from this type of highway. Following the arterial highways, the collector highways accounting for 17 percent from the total number of RTAs whereas the expressway and local road accounting for 10 and 5 percent, respectively.

5. POPULATION AND REGISTERED VEHICLES TRENDS

As the number of vehicle and population increases throughout the world, the number and severity of traffic accidents also increases. Referring to **Fig. 14**, the population in Iraq has increased by 49 percent during the period from 2002 to 2015 and approximately the number of registered vehicles in 2015 has more than that in 2002 by three folds.

Furthermore, the high motorization level (number of vehicle per 1000 populations) is a major factor which responsible for the increased number of mortality and morbidity rates due to traffic accidents in Iraq. The motorization level has increased approximately from 54 in 2002 to 141 in 2015 as illustrated in **Fig. 15**. In other words, the vehicle ownership (persons per vehicle) has changed from 18 in 2002 to 7 in 2015.

The use of mortality rate (deaths per 100,000 populations or per 10,000 vehicles) or morbidity rate (injuries per 100,000 populations or per 10,000 vehicles) is more useful to evaluate the severity of the traffic accidents problems than the absolute number. Use of the total number of mortality or morbidity alone can be deceptive, because it neglects the effect of population size for countries, **WHO, 2013**. Also, in the period from 1995 to 2009, the mortality rates in road traffic accidents ranges between (4-7) deaths per 100,000 populations in Iraq. The current data analysis concluded that the mortality rate in road traffic accidents has risen to 9 deaths per 100,000 in the early 2010 and reached a peak of 11 deaths per 100,000 in 2012 which consider the highest rate of mortality due to traffic accidents over the last 30 years. Furthermore, the same year of 2012, has witnessed the highest morbidity rate during the last 30 years of (3.7).

6. ECONOMIC COSTS OF TRAFFIC ACCIDENTS

The RTAs cost countries approximately 3 to 5 percent of their Gross Domestic Product, **WHO, 2015**. In USA, the statistics report of the National Highway Traffic Safety Administration (NHTSA) estimated the economic cost of the traffic accidents nearly $242 billion in 2010, **NHTSA, 2016**.
Based on feasibility study for rehabilitation and upgrading the expressway No. 1, **CC, 2013**, the average costs of road accident in Iraq was 250,000 USD per mortality and 70,000 USD per morbidity. The economic costs of traffic accidents accounted for 14.8 billion USD over the study period (14 years, 2002-2015), representing about 2.9 million USD per day as listed in table (1). The presented cost components cover productivity of casualties, possessions damage, medical bills costs, and emergency services such as ambulance, police, and fire services.

7. DEVELOPMENT OF STATISTICAL MODELS

In statistical modeling the overall objective is to develop a predictive equation relating a criterion variable to one or more predictor variables. Three types of models were attempted in the next sections. In the first type the criterion variable is the number of traffic accident per 10,000 registered vehicles whereas in the second and third types the criterion variables are the mortality per 10,000 registered vehicles and morbidity per 10,000 registered vehicles, respectively. Motorization level or population is the predictor variable in all types of models. Using the data presented in table (2), MINITAB V16 software was adopted to perform the necessary analysis.

7.1 Accidents Models

Different model structures are attempted to improve the explained variation (R^2) which assess the adequacy of the proposed regression models. Due to its simplicity, first it was decided to examine the linear relationship between the criterion variable accidents per 10,000 registered vehicle (A/10,000 V) and the predictor variable motorization level (M) the adopted linear model presented in table (3) yields an R^2 of 0.49, this value is substantially low. Alternatively, polynomial regression models, second and third order, were attempted to improve the explained variation. As shown in table 2, the obtained R^2 for the second order and the third order polynomial models are 0.711 and 0.723, respectively. Accordingly, the replacement of the predictor variable population (P) instead of M in the third order polynomial regression model yields improves the R^2 value to 0.817 which has the implication that only 18.3 percent of the observed variation is unexplained by the developed model.

7.2 Mortality Models

As shown in table (4) are the models examined for the prediction of mortality. The first one is linear model with criterion variable mortality per 10,000 registered vehicles and predictor variable motorization level. Unfortunately, the explained variation by this model is 0.365. The second and the third model are polynomial with second and third order, respectively. The R^2 duplicated in case of using third order polynomial model as compared to the linear model. The use of Population (P) as predictor variable in the third order polynomial model results in some improvement in the explained variation ($R^2 = 0.78$).

7.3 Morbidity Models

The attempted models for the prediction of the morbidity per 10,000 registered vehicles as well as the obtained R^2 are found to be similar into large extent to those models listed above for the prediction of mortality. From the model presented in table 5 below, it can be concluded that the criterion variable morbidity per 10,000 registered vehicles, at best can be predicted with a correlation to the criterion variable of population (P), the resulted R^2 was 0.775.

8. ARTIFICIAL NEURAL NETWORK (ANN)

Artificial Neural Network (ANN) is considered as an effective tool to solve complex wide variety of civil engineering problems. The ANN was used in this research with an aim of improving the adequacy of the prediction models and to achieve better accuracy than those models obtained using the traditional statistical regression approach. The structure of the network used consists of 1 layer of input with 1 nodes (predictor variable), 1 output layer with 1 node (criterion variable), and one hidden layer with 3 nodes, as shown in **Fig. 16**.

The training algorithm used was the Levenberg-Marquardt back propagation algorithm (named trainlm) which is considered one of the most efficient and fastest algorithms, and 85 percent of the data were selected for training and 15 percent for testing for 14 data point. The ANN code was produced using an academic version of MATLAB 2015.

Three ANN models were developed in this research, the output of model no.1, no.2 and no.3 represent accident per 10,000 vehicles, mortality per 10,000 vehicle and morbidity for per 10, 000 vehicles, respectively. Whereas the input of these models was the motorization level. The results of ANN prediction models are shown in **Fig. 17, 18** and **19** for the models no.1, no.2 and no.3, respectively.

The performance of the proposed ANN models were evaluated by using the explained variation (R^2) which represent the square of R value (correlation coefficient between the actual and the predicted values) existed in **Fig. 17, 18** and **19**. The R^2 values for the model no. 1, no.2 and no.3 were 0.978, 0.981 and 0.997, respectively. These R^2 values prove that ANN models has superior abilities in the prediction of the RTAs as well as mortality and morbidity as compared to those models obtained using the traditional statistical regression approach.

9. CONCLUSIONS

Based on the findings of the investigations for the RTAs data over the study period 2002-2015, the following salient conclusions can be drawn:

1. A total of 109067 RTAs has been occurred during the study period with an annual average of 7790. The maximum downward and upward divergence from the annual average RTAs recorded in 2007 and 2013, respectively. The corresponding RTAs were 3135 and 10709.

2. The most common type of accidents was run over which accounted for 45.7 percent of the total number of RTAs, followed by 43.3 percent collision accident type and 10 percent turnover accident type.

3. 29415 persons lost their life beside 106259 persons suffered from morbidity due to RTAs. In each one accident the mortality rate was 0.27 (each 3.7 accidents resulted in one death) whereas the morbidity rate was 0.97 (each 1.03 accidents resulted in one injury).

4. Most of the mortality represents the labor force of the Iraqi community. Based on the age group of deaths, about 61 percent of mortality due to RTAs is within the age group range of (18-47) years.

5. Due to RTAs, the death possibility for male more than female by approximately four times whereas the exposure for morbidity of male is higher than that for female by 63%.
6. Based on the age of drivers that cause RTAs, the RTAs distribution is skewed towards the younger age group with a mean of 26 years old and maximum occurrences of 24 percent in the age group 24-29 years followed by those in the age group 30-35 with 21 percent , and 18-23 with 19 percent.
7. The drivers are the major contributor factor for the RTAs in Iraq with a percentage rate of 72 followed by vehicle with 11 percent then by pedestrian with 7 percent and road by 6 percent.
8. The majority of RTAs in Iraq, 69 percent, happened under the day light condition whereas just 10 percent of RTAs occurred during darkness.
9. January has the lowest number of RTAs; in average it contributes to about 7 percent from the total number of the RTAs that occurred during the year whereas peak number of RTAs occurred in October with an average of 10 percent.
10. About two thirds of RTAs are caused by passenger car followed by motor cycle which accounted for 11 percent of the total number of accidents. The trucks and buses shared in RTAs with 9 percent for each one.
11. About 59 percent of RTAs occurred in arterial roads. The collector highways accounting for 17 percent from the total number of RTAs whereas the expressway and local road accounting for 10 and 5 percent, respectively.
12. Alongside the humanitarian tragedies, the economic costs of traffic accidents accounted for 14.8 billion USD over the study period representing about 2.9 million USD per day.
13. The models obtained by ANN technique showed superior abilities in the prediction of the RTAs as well as mortality and morbidity as compared to those models obtained using the traditional statistical regression approach.

10. REFERENCES

- Adams, J. G., 1987, *Smeed's Law: Some Further Thoughts*, Journal of Traffic engineering and Control, Vol.28, No.2, PP. 70-73.
- Al-Jameel, H. A., 2016, *Reducing the Number of Accidents in Iraq by Using Expert System*, Journalof Babylon University, Engineering Science, Iraq Vol. 24, No.5, PP. 54-65.
- Aljoborae, S. F., and Al Humairi, A., 2014, *A Study of Road Traffic Accidents in Babylon Province*, Medical Journal of Babylon, Iraq Vol.11, No.4, PP. 912-922.
- Al-Omari, B., Ghuzlan, K., and Hasan, H., 2013, *Traffic Accidents Trends and Characteristics in Jordan*, International Journal of Civil and Environmental Engineering, Vol.13, No.5, PP. 9-16.
- Andreassen, D., 1991, *Population and Registered Vehicle Data vs. Road Deaths*, Accident Analysis and Prevention, Vol.23, No.5, PP. 343-351.
- Andreassen, D. C., 1985, *Linking Deaths with Vehicles and Population*, Traffic Engineering and Control, Vol.26, No.11, PP. 547-549.
- Bashar, A. L., Ghuzlan, K., and Hasan, H., 2013, *Traffic Accidents Trends and Characteristics in Jordan*, International Journal of Civil and Environmental Engineering, Vol.13, PP. 9–16.

- Bener, A., and Ofosu, J. B., 1991, *Road Traffic Fatalities in Saudi Arabia*, IATSS research, Vol.15, No.1, PP.35-38.
- Consolidated Consultants (CC), 2013, *feasibility study for rehabilitation and upgrading the expressway No.1*, Ministry of Construction and Housing, Republic of Iraq.
- Ghaffar, U. B., and Ahmed, S. M., 2015, *A Review of Road Traffic Accidents in Saudi Arabia: the Neglected Epidemic*, Indian journal of forensic and community medicine, Vol.2, No.4, PP. 242-242.
- Ghee, C., Silcock, D., Astrop, A., and Jacobs, G. D., 1997, *Socio-Economic Aspects of Road Accidents in Developing Countries*, TRL Report, Vol.247, No.1999.
- Hesse, C. A., Ofosu, J. B., and Lamptey, B. L., 2014, *A Regression Model for Predicting Road Traffic Fatalities in Ghana*, Open Science Repository Mathematics, (open-access), e23050497.
- Ibrahim, M. A. A., 2014, *Forecasting Trend of Traffic Fatalities in the United Arab Emirates*, Proceedings of the 2014 International Conference on Applied Mathematics and Computational Methods in Engineering (AMCME 14), April 2nd-4th. Prague, Czech Republic, PP. 81-86.
- Islam, M. M., and Al Hadhrami, A. Y., 2012, *Increased Motorization and Road Traffic Accidents in Oman*, Journal Emerging Trends in Economics and Management Sciences, Vol.3, No.6, PP. 907.
- Koren, C., and Borsos, A., 2010, *Is Smeed's Law Still Valid? A World-Wide Analysis of the Trends in Fatality Rates*, Journal of Society for Transportation and Traffic Studies, Vol.1, No.1, PP. 64-76.
- Leidman, E., Maliniak, M., Sultan, A. S. S., Hassan, A., Hussain, S. J., and Bilukha, O. O., 2016, *Road Traffic Fatalities in Selected Governorates of Iraq from 2010 to 2013: Prospective Surveillance*, Conflict and Health, Vol.10, No.1, PP. 2.
- Smeed, R. J., 1949, *Some Statistical Aspects of Road Safety Research*, Journal of Royal Statistical Society, Series A (General), Vol.112, No.1, PP. 1-34.
- U.S. Department of Transportation, 2006, National Highway Traffic Safety Administration (NHTSA), National Center for Statistics and Analysis Databases, http://www.nhtsa.dot.gov/, Statistics.
- Wang, C. W., and Chan, C. L., 2016, Estimated Trends and Patterns of Road Traffic Fatalities in China, 2002–2012, Traffic injury prevention, Vol.17, No.2, PP.164-169.
- World Health Organization. *Global status report on road safety 2015*: supporting a decade of action. Geneva: World Health Organization.
- World Health Organization. *Global status report on road safety 2013*: supporting a decade of action. Geneva: World Health Organization.

11. NOMENCLATURE

RTAs	road traffic accidents
ICSO	iraqi central statistical organization
ANN	artificial neural network
WHO	world health organization
UN	united nations
SDGs	sustainable development goals

EMR	eastern mediterranean
D	annual road deaths
N	number of registered vehicles
P	population
RTF	road traffic fatalities
ACC	number of traffic accidents per year
M	motorization level
F	traffic accidents fatalities
AR	auto regression component
V	number of vehicles
t	time in Year
MoH	ministry of health
CSO	central statistical organization
GDP	gross domestic product
Ho	null hypothesis
α	significance level
A	accidents
Mt	mortality
Mb	morbidity

Table 1. Cost of mortality and morbidity due to traffic accidents.

Year	Cost of Mortality $	Cost of Morbidity $	Total Cost $
2002	423,250,000	495,040,000	918,290,000
2003	338,750,000	395,990,000	734,740,000
2004	406,500,000	475,160,000	881,660,000
2005	447,250,000	522,690,000	969,940,000
2006	287,750,000	212,310,000	500,060,000
2007	302,500,000	227,640,000	530,140,000
2008	465,750,000	384,930,000	850,680,000
2009	537,750,000	556,850,000	1,094,600,000
2010	627,000,000	629,720,000	1,256,720,000
2011	675,750,000	713,860,000	1,389,610,000
2012	783,000,000	770,630,000	1,553,630,000
2013	737,750,000	748,580,000	1,486,330,000
2014	692,250,000	644,700,000	1,336,950,000
2015	628,500,000	660,030,000	1,288,530,000
Total	7,353,750,000	7,438,130,000	14,791,880,000

Table 2. Populations, vehicles, traffic Accidents, mortalities and morbidities in Iraq.

Year	Population (P)	Registered Vehicle (V)	Accidents (A)	Mortality (Mt)	Morbidity (Mb)
2002	21,200,000	1,152,702	8,535	1,693	7,072
2003	21,700,000	1,652,723	6,826	1,355	5,657
2004	22,404,800	1,842,512	8,191	1,626	6,788
2005	23,010,000	2,028,301	9,010	1,789	7,467
2006	24,993,000	2,386,612	3,389	1,151	3,033
2007	25,740,000	2,471,461	3,135	1,210	3,252
2008	26,508,000	2,491,711	5,502	1,863	5,499
2009	27,296,000	2,527,335	7,452	2,151	7,955
2010	28,102,000	2,662,946	8,861	2,508	8,996
2011	28,500,000	2,763,667	10,082	2,703	10,198
2012	29,207,000	3,043,975	10,709	3,132	11,009
2013	30,095,000	3,527,534	9,725	2,951	10,694
2014	31,004,000	4,239,818	8,814	2,769	9,210
2015	31,634,000	4,458,780	8,836	2,514	9,429

Table 3. Accidents model.

Model No.	Model Equation	R^2	F	P
1	$A/10{,}000V = 81.1 - 0.497\ M$	0.492	11.63	0.005
2	$A/10{,}000V = 186 - 2.66\ M + 0.0107\ M^2$	0.711	13.51	0.001
3	$A/10{,}000\ V = 291.5 - 6.325\ M + 0.0505\ M^2 - 0.0001372\ M^3$	0.723	8.68	0.004
4	$A/10{,}000\ V = 6591 - 734.4\ P + 27.214\ P^2 - 0.33404P^3$	0.817	14.93	0.001

Table 4. Mortality models.

Model No.	Model Equation	R^2	F	P
1	$Mt/10{,}000V = 15 - 0.0682\ M$	0.365	6.91	0.022
2	$Mt/10{,}000V = 27.4 - 0.325\ M + 0.00126\ M^2$	0.486	5.21	0.026
3	$Mt/10{,}000\ V = 85.5 - 2.34\ M + 0.0233\ M^2 - 0.000076\ M^3$	0.629	5.64	0.016
4	$Mt/10{,}000\ V = 1445.5 - 164\ P + 6.16\ P^2 - 0.0767\ P^3$	0.780	11.8	0.001

Table 5. Morbidity models.

Model No.	Model Equation	R^2	F	P
1	Mb/10,000V = 63.6 - 0.337 M	0.376	7.23	0.020
2	Mb/10,000V = 137 – 1.86 M + 0.00748 M^2	0.554	6.84	0.012
3	Mb/10,000 V = 308 – 7.78 M + 0.072 M^2 – 0.000222 M^3	0.600	5.12	0.021
4	Mb/10,000 V = 6244 - 702 P + 26.2 P^2 – 0.324 P^3	0.775	11.47	0.001

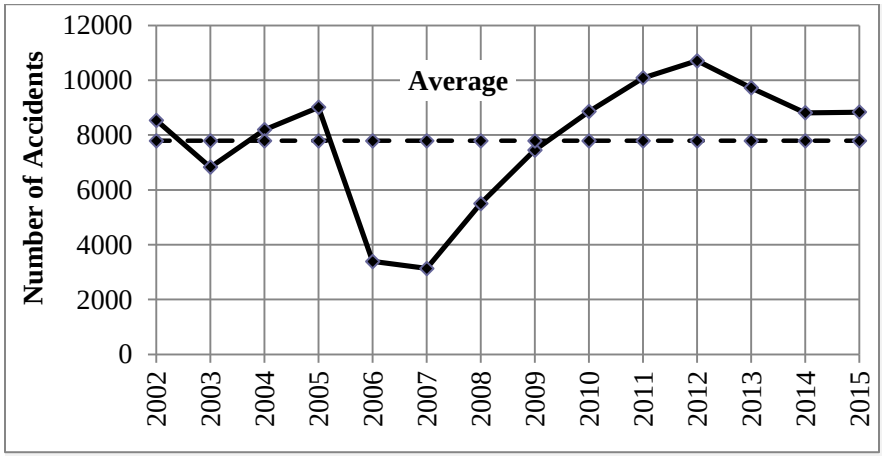

Figure 1. Annual distribution of RTAs.

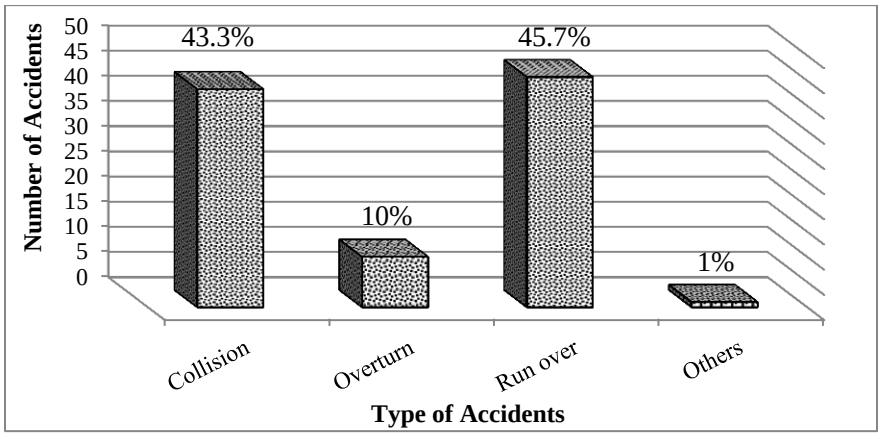

Figure 2. RTA distribution according to the types.

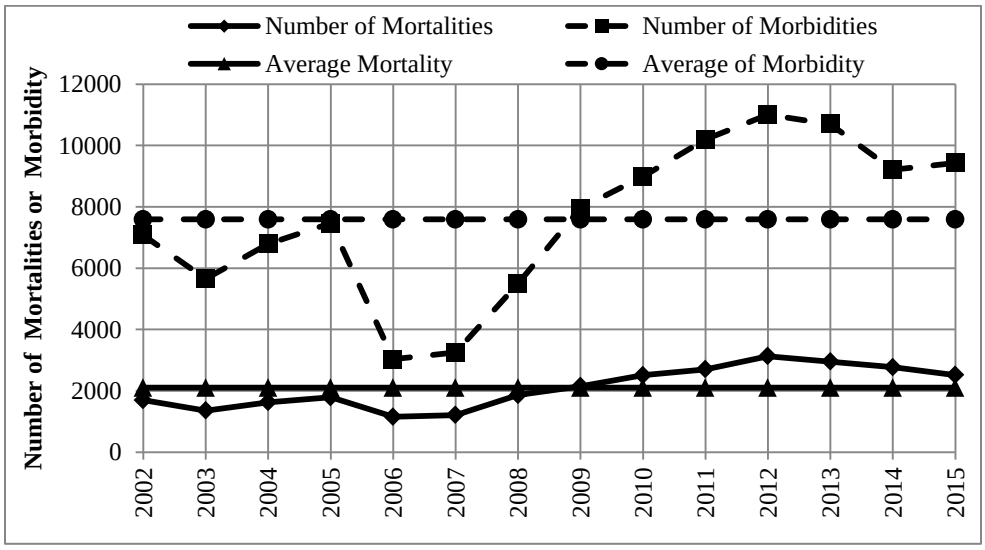

Figure 3. Mortality and morbidity due to RTAs.

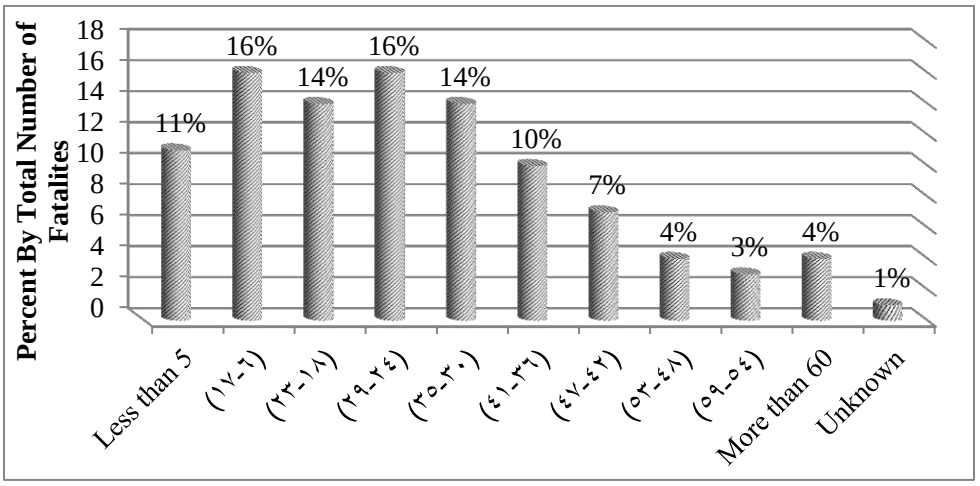

Figure 4. Age group for RTAs mortality.

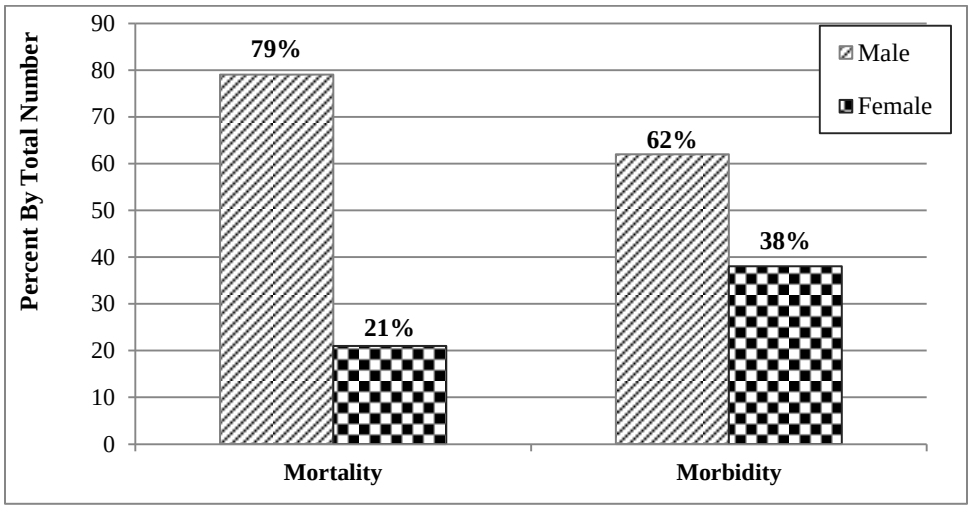

Figure 5. Gender of mortality and morbidity due to RTAs.

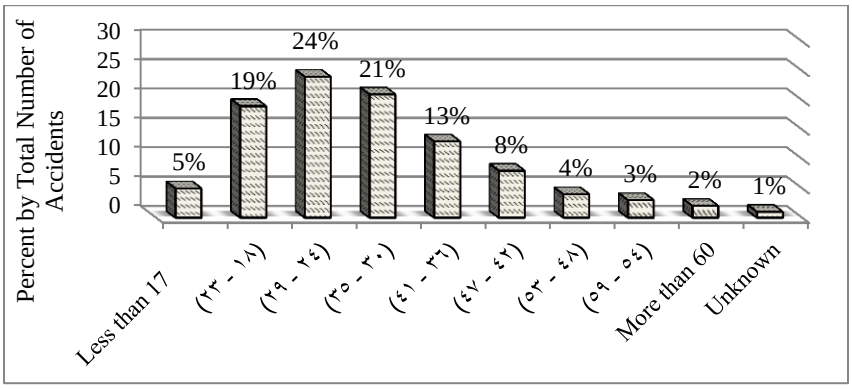

Figure 6. The distribution of RTAs based on driver age.

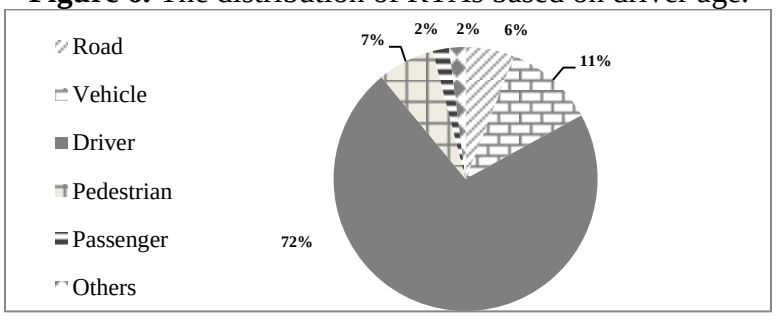

Figure 7. The distribution of RTAs based on causal factors.

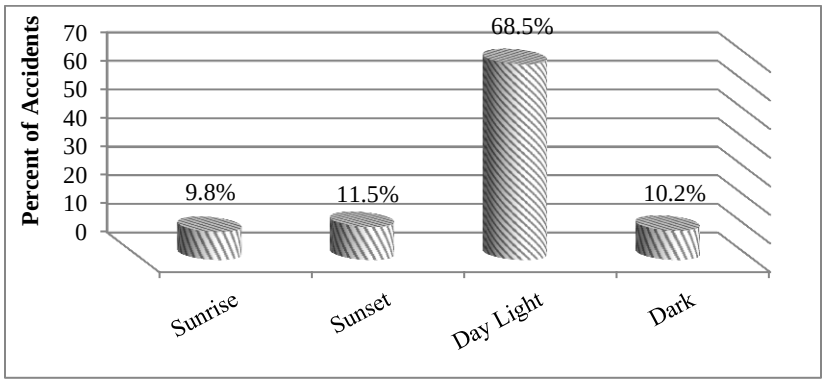

Figure 8. The distribution of RTAs based on light condition.

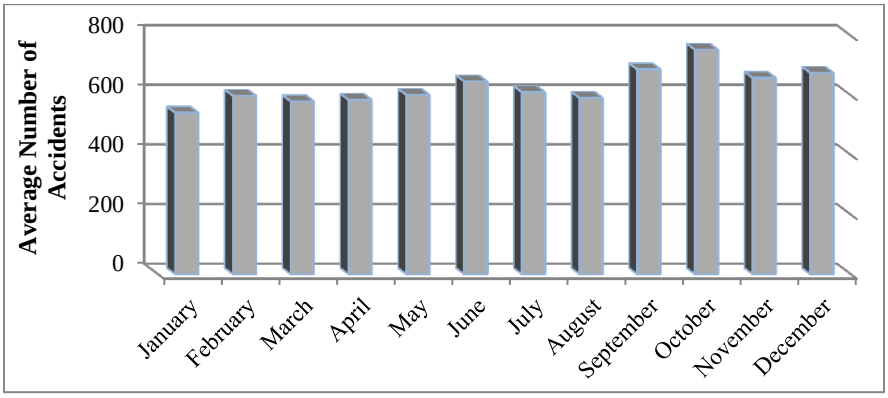

Figure 9. The monthly distribution for RTAs.

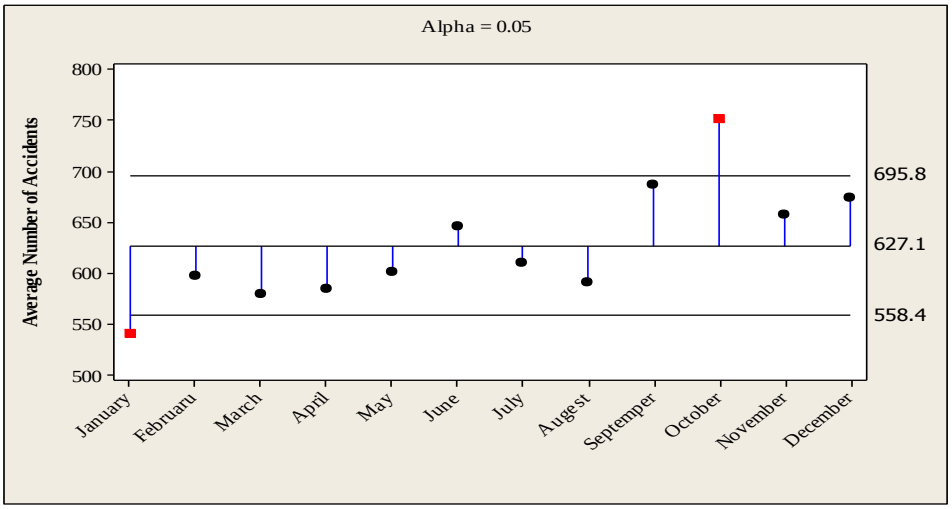

Figure 10. The difference in the mean number of accidents for the months of the year.

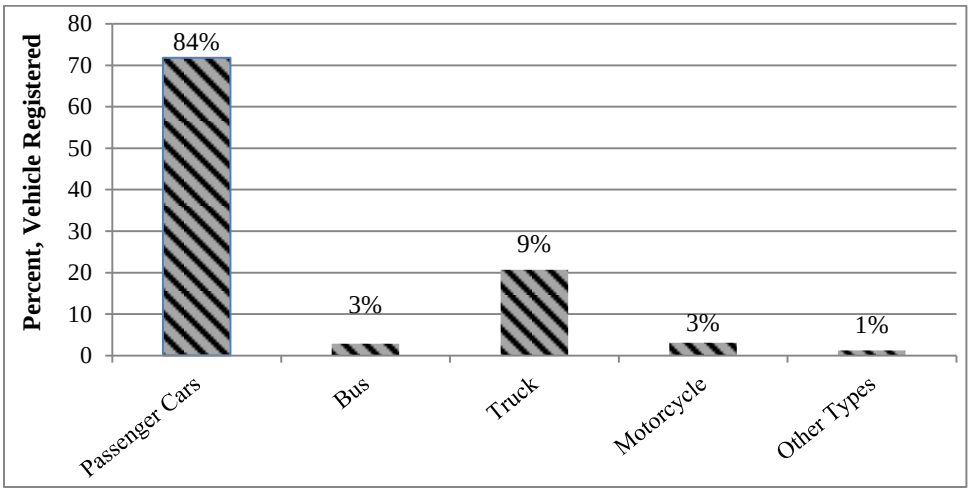

Figure 11. Registered vehicles types in 2015.

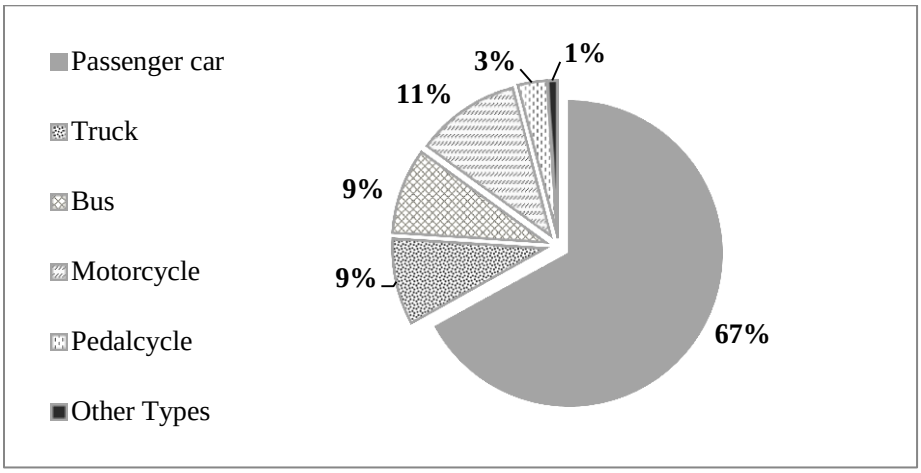

Figure 12. The distribution of RTAs based on vehicle type.

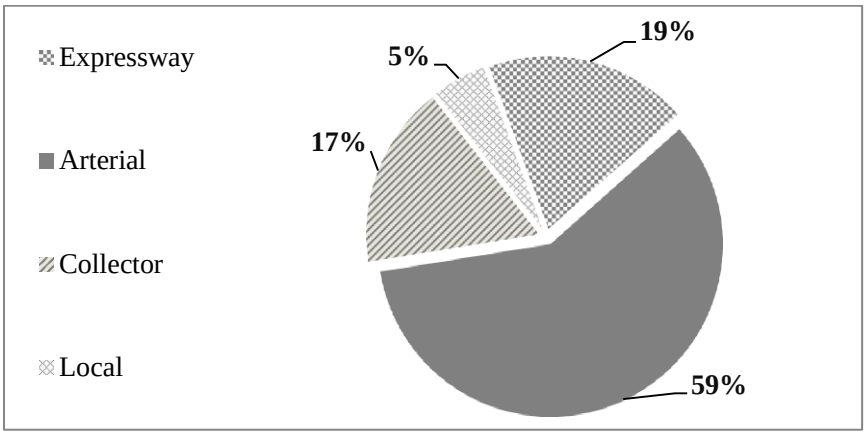

Figure 13. RTAs distribution based on highway functional class.

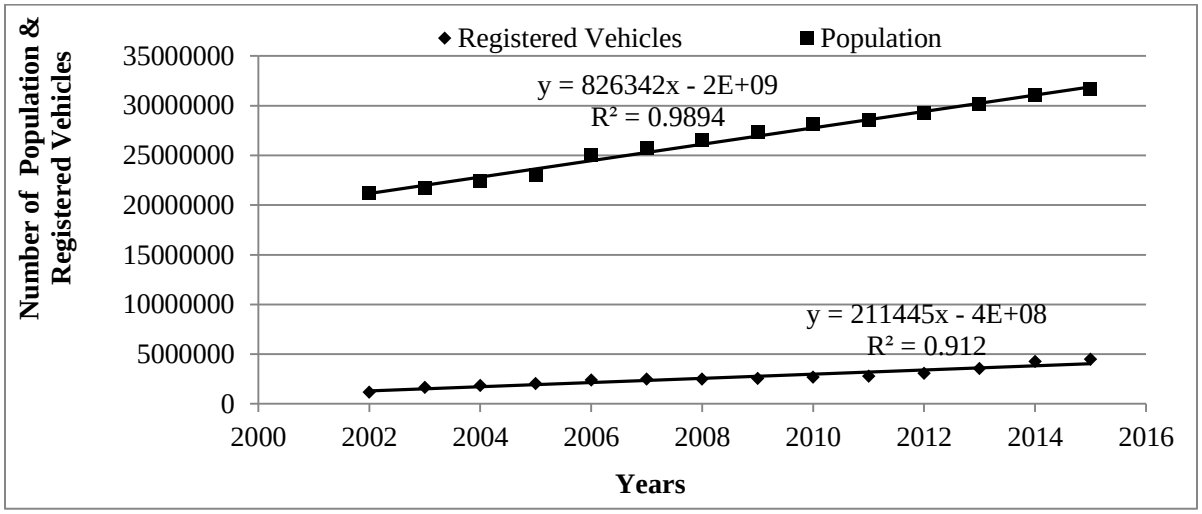

Figure 14. Growth of population and registered vehicles with time.

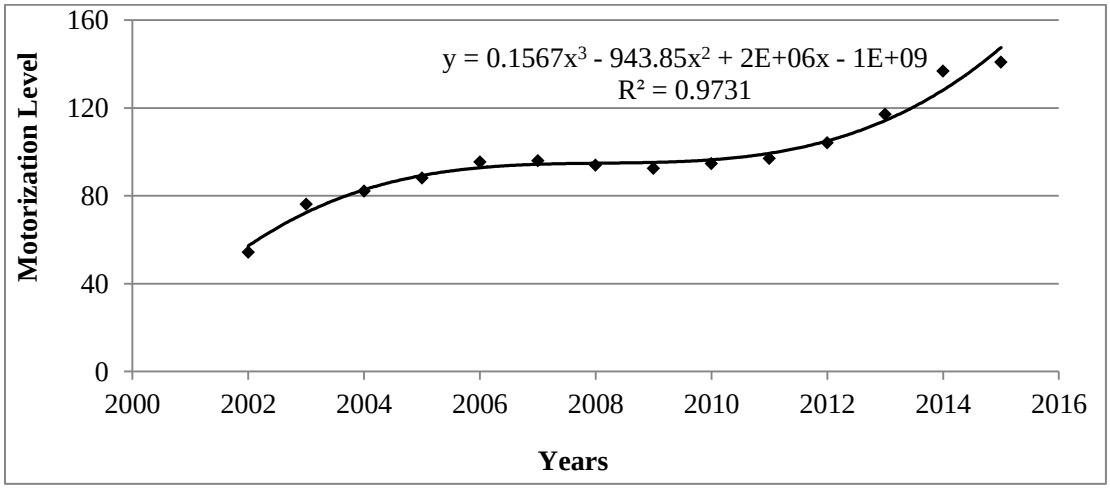

Figure 15. Motorization level with time.

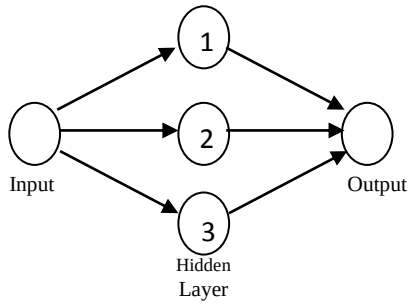

Figure 16. Structure of ANN.

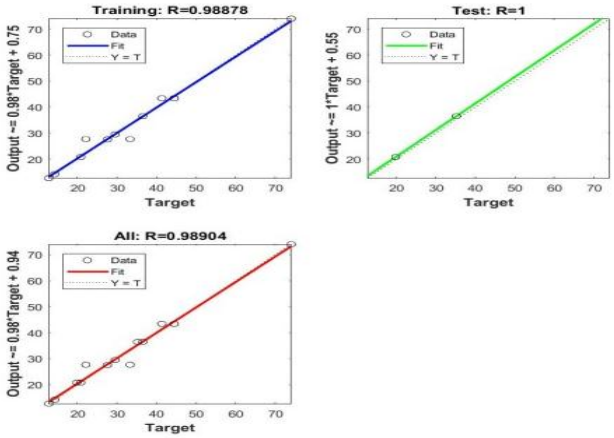

Figure 17. Results of the ANN prediction model no.1 (accident).

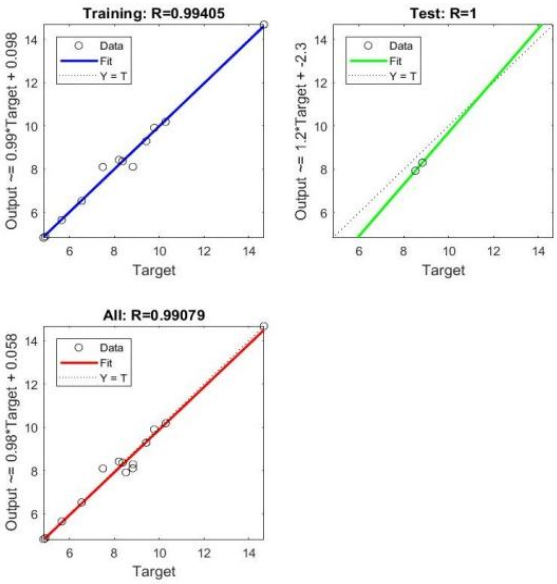

Figure 18. Results of the ANN prediction model no.2 (mortality).

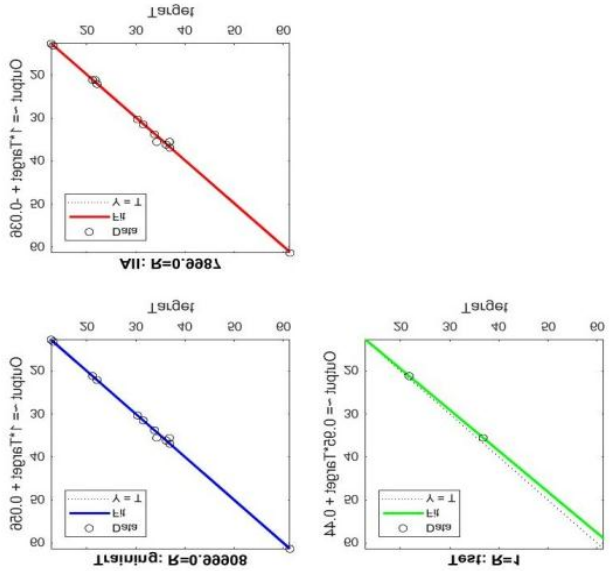

Figure 19. Results of the ANN prediction model no.3 (morbidity).

Zn(II) Removal from Wastewater by Electrocoagulation/Flotation Method using New Configuration of a Split-Plate Airlift Electrochemical Reactor

Saad H. Ammar
Assistance Professor
Chemical Engineering Department
Al-Nahrain University
saad_cheminet@yahoo.com

Fatma Dheif Ali
Assistance Lecturer
Chemical Engineering Department
Al-Nahrain University
fatmadheif@gmail.com

Ruaa Fadhil Shafi
Assistance Lecturer
Chemical Engineering Department
Al-Nahrain University
roaa_fadeel2004@yahoo.com

Alaa Ibrahim Elaibi
Lecturer
College of Engineering
Al-Nahrain University
alaasun2005@yahoo.com

ABSTRACT

In this paper, split-plate airlift electrochemical reactor as an apparatus with new configuration for wastewater treatment was provided. Two aluminum plates were fixed inside the reactor and present two functions; first it works as split plates for internal loop generation of the airlift system (the zone between the two plates acts as riser while the other two zones act as downcomer) and second it works as two electrodes for electrocoagulation process. Simulated wastewater contaminated with zinc ions was used to test the performance of this apparatus for zinc removal by studying the effect of different experimental variables such as initial concentration of zinc (50-800 ppm), electrical current density (2.67-21.4 mA/cm^2), initial pH (3-11), air flowrate (12-50 LPH), and implicitly the electrocoagulation time. The results have shown the applicability of this split-plate airlift reactor as electrocoagulation cell in the treatment of wastewater such as wastewater containing Zink ions. The Zink removal percent was shown to increase upon increasing the current density and the electrolysis time. Also best removal percent was achieved in the initial pH range between 7 and 9. The minimum electrocoagulation time required for removal of ≥ 90% of Zn(II) decreases from 90 to 22 min when operating current density increases from 2.67 to 21.4 mA/cm^2.

Key words: wastewater treatment, zinc ions, electrocoagulation/flotation, split-plate, airlift reactor.

ازالة ايونات الزنك من المياه الصناعية بواسطة طريقة التخثير/التطويف الكهربائي وباستخدام شكل جديد لمفاعل الرفع الهوائي ذو الصفائح الفاصلة

د. سعد حنش عمار
استاذ مساعد-قسم الهندسة الكيمياوية
جامعة النهرين

فاطمة ضيف علي
مدرس مساعد-قسم الهندسة الكيمياوية
جامعة النهرين

رؤى فاضل شافي
مدرس مساعد-قسم الهندسة الكيمياوية
جامعة النهرين

د. الاء ابراهيم العيبي
مدرس-كلية الهندسة-جامعة النهرين

الخلاصة

تم في هذا البحث توفير شكل جديد لمفاعل كهروكيمياوي وهو مفاعل الرفع الهوائي ذو الصفائح الفاصلة Split-plate airlift reactor في معالجة النفايات السائلة. استخدمت صفيحتين من الالمنيوم مثبتة داخل المفاعل من جهة تعمل على توفير نظام الرفع الهوائي ذو التدوير الداخلي (بحيث ان المنطقة مابين الصفيحتين تتصرف كجزء ناهض riser والمناطق الاخرى تعمل كجزء هابط

downcomer ومن جهة اخرى تعمل هذه الصفيحتين هي نفسها كأقطاب كهربائية لعملية التخثير الكهربائي. تم اختبار هذه المفاعل في معالجة وازالة ايونات الزنك من المياه الملوثة والمحضرة مختبريا عن طريق دراسة تأثير المتغيرات التالية على كفائة ازالة ايونات الزنك وهي التركيز الابتدائي للزنك (من 50 الى 800 جزء بالمليون)، كثافة التيار الكهربائي المسلط (من2,67 الى 21,4 ملي امبير/سم^2)، الاس الهيدروجيني الابتدائي للمحلول (من 3 الى 11)، معدل جريان الهواء (من 12 الى 50 لتر/ساعة) وزمن التخثير الكهربائي. بينت النتائج نجاح وامكانية تطبيق هذا المفاعل ذو الرفع الهوائي والصفائح الفاصلة كخلية تخثير كهروكيمياوية في معالجة المياه الملوثة بايونات الزنك. تزداد نسبة الازالة بزيادة كثافة التيار الكهربائي وزمن التخثير وكانت افضل نسبة ازالة لايونات الزنك تتحقق بحدود اس هيدروجيني بين 7 و9. اقل زمن تخثير لتحقيق اكبر او يساوي 90% نسبة ازالة لايونات الزنك ينخفض من 90 الى 22 دقيقة عند استخدام كثافة تيار كهربائي من 2,67 الى 21,4 ملي امبير/سم^2 على التوالي.
الكلمات الرئيسية: معالجة المياه الملوثة، ايونات الزنك، التخثير/التطويف الكهربائي، الصفائح الفاصلة، مفاعل الرفع الهوائي.

1. INTRODUCTION

Nowadays, environmental pollution by heavy metals has become one of the most serious environmental problems. Many industrial activities generate various wastewater contain several danger heavy metals disposed in the environment which have negative effect on humans, plants and animals, **Srivastava** and **Majumder, 2008**.

With the fast development of industrial activities such as mining industries, metal plating, fertilizer, batteries, tanneries, paper and insecticides industries, wastewaters containing high concentrations of toxic heavy metals include copper, zinc, nickel, mercury, lead, cadmium and chromium may be disposed into the environment increasingly. Heavy metals are not biodegradable and inclined to accumulate in living organisms. Many heavy metal ions are known to be carcinogenic, **Fu** and **Wang, 2011**.

Zinc is important for human health as a trace element. It is essential for the physiological functions of living tissue and regulates many biochemical processes. However, the excessive intake of zinc can cause notable health problems, such as stomach cramps, skin excitement, puke, nausea and anemia, **Oyaro et al., 2007**.

The electrocoagulation (EC) method is one of the most successful processes used for treatment of different type of soluble or colloidal pollutants in the industrial wastewater. Such pollutants as emulsion oils, dyes in textile wastewater, heavy metals, and organics such as phenolic compounds. Because of the simple and low cost operation, excellent removal efficiency, and low sludge production EC process therefore has wide applications and replaces the traditional chemical-coagulation process which uses expensive chemicals, **Emamjomeh, et al., 2009**.

EC includes applying direct electric current to two metal electrodes anode and cathode inside an electrochemical reactor tank. The two electrodes may be made of same or different metal. The coagulants were generated by electrolytic oxidation of the electrode in the first stage then in the second stage the contaminants or pollutants become unstable and aggregate together because of the attraction between the formed coagulants and these contaminants. The aggregated contaminants then either settle or float to be easily separated, **Heidmann** and **Calmano, 2008, Chen, 2004**.

The electrodes are made from either aluminum or iron. In case of aluminum cations dissolve from the anodes according to, **Rincon** and **La Motta, 2014.**

$Al_{(s)} \rightarrow Al^{3+}_{(aq)} + 3e^-$ *and/or*
$Al_{(s)} \rightarrow Al^{2+}_{(aq)} + 2e^-$

Also the following water electrolysis reaction may take place:

$2H_2O_{(l)} \rightarrow 4H^+ + O_{2(g)} + 4e^-$

Simultaneously, at the cathode water is reduced to hydrogen gas and hydroxyl ion OH^- according to:

$2H_2O_{(l)} + 2\,e^- \rightarrow H_{2(g)} + 2OH^-$

Aluminum cations are reacting with hydroxyl to form various aluminum hydroxides:

$Al_3 + + 3OH^- \rightarrow Al(OH)_{3(s)}$

Also hydroxides polymers can be built up according to:

$nAl(OH)_{3(s)} \rightarrow Al_n(OH)_{3n(s)}$

Other dissolved ionic species, like $Al(OH)^{2+}$, $Al_2(OH)_2{}^{4+}$, $Al(OH)_2{}^+$, $Al(OH)_4{}^-$, $Al_6(OH)_{15}{}^{3+}$, $Al_7(OH)_{17}{}^{4+}$ … etc. may also occurr in the system. These ionic hydroxides have very strong attraction force toward destabilized pollutants caused removal of these substances from the system by electrostatic attraction and then coagulation. The continually small bubbles of hydrogen and oxygen gases generated in the EC process make the pollutants floats to the wastewater surface in the reactor tank, **Balla, 2010**. **Fig.1** shows a representation of the electrocoagulation/flotation process.

The interaction between the two phenomena; electrocoagulation (EC) and electroflotation (EF) gives unique technique for removal of several pollutants from wastewater before disposal or reuse, **Deghles** and **Kurt, 2016**.

Airlift reactors have been widely utilized in the wastewater treatments to implement many applications including two or three phase. Airlift reactors are a special case of bubble column. It consists of two distinctive zones the riser and the downcomer. The air or gas may be sparged in the riser zone which leads to a difference in gas holdup between riser and downcomer. As a result of the gas holdup differences and thus densities differences between the two sections, there will be a static pressure difference between the riser and downcomer, therefore this leads the liquid circulation between them. There are two main configurations for airlift: internal loop and external loop airlift reactors, **Chisti, 1989**.

The objective of this research is to utilize internal-loop with two split plates airlift reactor as electrocoagulation/flotation cell. Several experimental parameters were studied on the zinc removal

efficiency from water such as initial Zn concentration, electrical current density, and initial pH of the wastewater, contact time and air pumping effect.

2. EXPERIMENTAL WORK

2.1 Materials

Stock solution of 800 mg/L Zn(II), was prepared by dissolving the required amounts of zinc sulfate ($ZnSO_4 \cdot H_2O$, 99.0% purity supplied by Merck) in deionized water. Other required lower initial concentrations were prepared by suitable dilution. Sodium nitrate (NaCL, ≥ 99.0% purity, supplied by Sigma-Aldrich) was added if necessary to increase the solution conductivity. Initial pH of the reactor content was adjusted by adding 0.1 M solutions of HCl and NaOH as needed.

2.2 Experimental setup and procedure

The experimental setup mainly consists of the airlift electrochemical reactor. The reactor designed as an airlift reactor with internal loop with capacity of 2.5 L includes two aluminum plates of rectangular shape. These plates act as electrodes (anode and cathode) and split plates for airlift system generation at the same time. The reactor was made from Perspex material with 10 cm diameter and 33 cm height giving a working volume of 1.8 L. The two aluminum plates were fixed inside the reactor, the plate dimensions were (85 mm* 220 mm with 1 mm thickness giving electrode surface area of 187 cm^2) and the distance between electrodes was 4 cm. A digital DC power supply (model HY3002, Hyelec, India) was used to create electrolysis. **Fig.2** shows the schematic representation experimental setup arrangements.

Five parameters were selected to investigate the zinc removal from simulated wastewater, these parameters include initial concentration of metal (50, 100, 200, 400 and 800 mg/L), electrical current 0.5, 1, 1.8, and 4 A (which correspond to current density of 2.67, 5.34, 9.6 and 21.4 mA/cm^2), air flowrate (12, 25, 37, and 50 LPH), electrocoagulation time (5-75 min) and initial pH (3-11). All experiments were performed at a room temperature (about 30^oC). The experimental work was divided into four parts:

- **Part#1 (initial concentration & electrocoagulation time effect studies):** In this set, the prepared wastewater with desired zinc initial concentration varied from 50 to 800 mg/L was poured into the reactor. The air flowrate, electrical current and initial pH, were fixed to the values 0 LPH, 9.6 mA/cm^2, and 7 respectively. The samples were taken according to the prespecified time intervals.
- **Part#2 (Current density study):** In this set, four runs were performed, the current density was varied as 2.67, 5.34, 9.6 and 21.4 mA/cm^2 while other parameters initial copper concentration, air flowrate, and initial pH were fixed at 200 mg/L, 0 LPH, and 7 respectively. The electrocoagulation time in this runs was varied also according to the prespecified time intervals.
- **Part#3 (Initial pH study):** Finally, the initial pH of the solution was varied from 3 to 11, initial pH value was varied by adding small droplets of 1 M NaOH or 1 M HCl solution as needed. The pH was monitored with a pH meter (model HI110, HANNA Instruments Co., India). Other parameters such as current density, air flowrate, initial zinc concentration and

electrocoagulation time were fixed at 21.4 mA/cm^2, 0 LPH, 200 mg/L and 35 min respectively.

- **Part#4: (Air flowrate study):** the flowrate of inlet air was studied from 12 to 50 LPH while the current density, initial pH, initial zinc concentration and electrocoagulation time were fixed at 21.4 mA/cm^2, 7, 200 mg/L and 35 min respectively.

Every electrocoagulation experiment was started with working volume of 1800 ml of zinc solution. The desired current was applied and 2 mL samples were taken from the bulk solution in the downcomer zone every prespecified min. The total outlet concentration of zinc in the treated solution from the reactor was determined with flame Atomic Adsorption Spectrophotometer AAS (model Perkin Elmer 5000, Italy).

The removal efficiency of zinc was calculated as:

$$\text{R}\,(\%) = \frac{C_{in} - C_{out}}{C_{in}} \times 100 \quad (1)$$

where R (%) is the removal efficiency, C_{in} is the initial zinc concentration (ppm) and C_{out} is the residual outlet zinc concentration (ppm) after electrocoagulation time of t.

Also, the specific electrical energy consumption of zinc treatment via electrocoagulation/flotation process in this reactor was calculated by the following equation, **Konstantinos et al., 2011**:

$$E\left(\frac{kWh}{kg\ Zn(II)}\right) = \frac{\mathbf{1000\ UIt}}{\boldsymbol{V\ C_{in}\ R}\%} \quad (2)$$

Where E is the electrical energy consumption ($\frac{kWh}{kg\ Zn(II)}$), U is the voltage (V), I is the applied current (A), t is the electrocoagulation time, and V is the working volume in the reactor.

3. RESULTS AND DISCUSSION

3.1 Effect of initial concentration and electrocoagulation time

Fig.3 shows the removal efficiency of zinc in the reactor with time (electrocoagulation time) at different initial zinc concentration and at current density of 9.6 mA/cm^2 (1.8 A) without air pumping. The removal efficiency increased almost linearly by time during the first 40 min. The removal percent for 50, 100, 200, 400 and 800 ppm initial Zn concentration in 1800 ml reactor working volume were nearly 90% removed after 25, 35, 45, 50 and 75 min respectively as shown in **Fig.4**. Conversely, the removal efficiency of Zn increase with decreasing initial Zn concentration due to the availability of large amount of coagulation agents required for low initial concentration. Almost, the same results of zinc removal were obtained by **Adhoum, et al., 2004** and **Prica, et al., 2015**.

Generally, a considerable formation of H_2 gas micro bubbles was observed at the cathode during all the EC experiments, whereas at the anodes no O_2 gas bubbles were evolved. The main reactions at the anode were aluminum dissolution while at the cathode, H_2 and OH^- ions were formed.

3.2 Effect of current density

Fig.5 shows the effect of electrocoagulation time on the removal efficiency for different current density values. The current density has a significant impact on Zn removal efficiency. Increasing the current density leads to increase the Al^{3+} and OH^- dosage into the system by time and also the bubble H_2 production rate, in contrast the bubble size decreases with increasing current density, **Khosla** and **Somasundaran, 1991** which is advantageous to the removal process. Thus the process of Zn removal can be accelerated. This effect was also observed by other researchers with Zn(II) such as **Adhoum, et al., 2004** and **Meunier, 2004**. The electrocoagulation time required for removal of more than 90% of Zn(II) decreases from 90 to 22 min when operating current density increases from 2.67 to 21.4 mA/cm^2 as shown in **Fig.6**.

In all cases, it was noted that increasing the current density leads to increase the liquid circulation velocity inside the reactor due to the increase the hydrogen micro bubbles generated at the cathode surface. It was noted that the liquid circulation between the riser and downcomer zones was achieved even by small bubbles of hydrogen gas at the cathode electrode when no air bubbled in the riser.

Liquid circulation velocities were determined by calculating the circulation time in the riser and downcomer zones by a method called neutral-buoyancy flow follower. The method depends on using of plastic particle with a distinctive color. The diameter of tracer particle was 2 mm and specific gravity was 1.05. The time which elapsed in the downcomer or riser is the time taken by this particle to travel a vertical distance equal to the riser height plus half distance between top edge of the plates and liquid level plus half distance between bottom edge of the plates and base of the reactor. The procedure was repeated many times and the velocity in each section was calculated from the average of 5 trials, **Lu, et al., 1994.** Increasing hydrogen generation with small bubbles in the riser leads to increase gas holdup in this zone and therefore increasing liquid circulation due to density difference between riser and downcomer. The double effect of current density on the zinc removal efficiency was resulted from two effects: first, the formation more coagulating agents such as $Al(OH)_3$ due to increasing the rate of anodic dissolution and second, good mixing in the reactor which resulted from increasing circulation velocity inside the reactor by more micro bubbles of hydrogen generated at the cathode surface. This means more coagulating agent is being contacted with Zn(II) ions which leads to improve the removal efficiency without using mechanical stirring.

3.3 Effect of initial pH

The initial pH has a notable influence on the performance of electrocoagulation/flotation process, **Chen et al., 2000**. To study this effect, a set of experiments were performed, using solutions of Zn(II) of 200 ppm each, with an initial pH varying in the range (2–11). As shown in **Fig.7**, the removal efficiency, after 35 min of electrocoagulation at 21.4 mA/cm^2, reached value as high as 93%, when pH exceeded 5. Furthermore, it can be seen that the removal efficiency decreased upon

decreasing initial pH. The best removal condition was for the initial pH, which was between 7 and 9. The decrease of removal efficiency of Zn(II) at a pH less than 5 and higher than 9 was attributed to an amphoteric behavior of $Al(OH)_3$ which led to soluble Al^{3+} cations, when the initial pH was low and to monomeric anions such as $Al(OH)_4^-$, when the initial pH was higher than 9, **Do** and **Chen, 1994**. When the initial pH was set in the range between 7–9, all aluminum cations formed at the anode are polymeric species and precipitated $Al(OH)_3$ leading to a more effective treatment, **Kobya** and **Bayramoglu, 2003**.

Fig.8 shows that the pH changed during electrocoagulation process. The treatment induced an increase in the final pH when the initial pH was low as shown in **Fig.9**. This might be attributed to the excess of OH^- ions formed at the cathode in acidic conditions and by the liberation of OH^- due to the occurrence of a partial exchange of Cl^- with OH^- in $Al(OH)_3$, **Chen, et al., 2000**. When the initial pH is above 9, the formation of $Al(OH)_4^-$ species together with parasite attack of the cathode by OH^- ions which led to a slight decrease in the final pH.

3.4 Power consumption

The electrical energy consumption was calculated in terms of *kWh* per kg of *Zn(II)* of treated effluent using **Equation 2** at operation time for which Zn removal was 90%, initial Zn content was of 200 ppm and initial pH was 7. **Fig.9** shows the electrical power consumption at different current density. It was noted that a continuous increase in energy consumption with increasing of the current density. Similar results of power consumption in the electrocoagulation/flotation process were obtained by many researchers such as **Prica, et al., 2015, Fu** and **Wang, 2011**.

3.5 Effect of air pumping

Fig.10 shows the effect air flowrate on the zinc removal efficiency. The air flowrate was studied from 0 to 50 LPH while the current density, initial pH, initial zinc concentration and operation time were fixed at 21.4 mA/cm^2, 7, 200 mg/L and 35 min respectively. The purpose of this study is to check the effect of increasing the liquid circulation velocity when air is pumped in the riser zone of the reactor. Removal efficiency increase slightly with increasing air flowrate, therefore, this type of reactor can be used as electrocoagulation/flotation cell successfully even without using air in the riser.

4. CONCLUSIONS

In this work, the removal of Zn(II) ions from simulated wastewater by the electrocoagulation/flotation process was investigated. The results have shown the applicability of split-plate airlift reactor as electrocoagulation/flotation unit for the treatment of wastewater containing Zn ions without using mechanical stirring and therefore less power consumption. Several experimental variables (initial zinc concentration, current density, operating time and air pumping) were studied. The Zn removal rate was shown to increase significantly upon increasing the current density. Also, it was observed that zinc removal efficiency increased with the increase of electrolysis time. Best removal capacity was achieved in the pH range between 7 and 9.

5. REFERENCES

Adhoum, N., Monser, L., Bellakhal, N., and Belgaied, J. E., 2004, *Treatment of electroplating wastewater containing Cu 2+, Zn 2+ and Cr (VI) by electrocoagulation*, Journal of hazardous materials, 112(3), 207-213.

Balla, W., Essadki, A. H., Gourich, B., Dassaa, A., Chenik, H., and Azzi, M, 2010, *Electrocoagulation/electroflotation of reactive, disperse and mixture dyes in an external-loop airlift reactor*, Journal of hazardous materials, 184(1), 710-716.

Chisti, M. Y., 1989, *Airlift bioreactors*, (Vol. 39). New York: Elsevier Applied Science.

Chen, X., Chen, G., and Yue, P. L., 2000, *Separation of pollutants from restaurant wastewater by electrocoagulation*, Separation and purification technology, 19(1), 65-76.

Chen, G., 2004, *Electrochemical technologies in wastewater treatment*, Separation and purification Technology, 38(1), 11-41.

Do, J. S., and Chen, M. L., 1994, *Decolourization of dye-containing solutions by electrocoagulation*, Journal of Applied Electrochemistry, 24(8), 785-790.

Deghles, A., and Kurt, U., 2016, *Treatment of tannery wastewater by a hybrid electrocoagulation/electrodialysis process*, Chemical Engineering and Processing: Process Intensification, 104, 43-50.

Emamjomeh, M. M., and Sivakumar, M., 2009, *Review of pollutants removed by electrocoagulation and electrocoagulation/flotation processes*, Journal of environmental management, 90(5), 1663-1679.

Fu, F., and Wang, Q., 2011, *Removal of heavy metal ions from wastewaters: a review*, Journal of environmental management, 92(3), 407-418.

Heidmann, I. and Calmano, W.,, 2008, *Removal of Zn (II), Cu (II), Ni (II), Ag (I) and Cr (VI) present in aqueous solutions by aluminium electrocoagulation*, Journal of Hazardous Materials, 152(3), pp.934-941.

Khosla, N. K., Venkatachalam, S., and Somasundaran, P., 1991, *Pulsed electrogeneration of bubbles for electroflotation*, Journal of Applied Electrochemistry, *21*(11), 986-990.

Kobya, M., Can, O. T., and Bayramoglu, M., 2003, *Treatment of textile wastewaters by electrocoagulation using iron and aluminum electrodes*, Journal of hazardous materials, 100(1), 163-178.

Konstantinos D., Achilleas C., and Evgenia V., 2011, *Removal of nickel, copper, zinc and chromium from synthetic and industrial wastewater by electrocoagulation*, International Journal of Environmental Sciences Vol. 1, No. 5.

Lu, W. J., Hwang, S. J., and Chang, C. M., 1994, *Liquid mixing in internal loop airlift reactors*, Industrial & engineering chemistry research, 33(9), 2180-2186.

Meunier, N., Drogui, P., Gourvenec, C., Mercier, G., Hausler, R., and Blais, J. F., 2004, *Removal of metals in leachate from sewage sludge using electrochemical technology*, Environmental technology, 25(2), 235-245.

Oyaro, N., Ogendi, J., Murago, E. N., and Gitonga, E., 2007, *The contents of Pb, Cu, Zn and Cd in meat in nairobi, Kenya*, Journal of Food, Agriculture & Environment Vol.5 (3&4):119-121.

Prica, M., Adamovic, S., Dalmacija, B., Rajic, L., Trickovic, J., Rapajic, S., and Becelic-Tomin, M., 2015, *The electrocoagulation/flotation study: The removal of heavy metals from the waste fountain solution*, Process Safety and Environmental Protection, 94, 262-273.

Rincon, G.J. and La Motta, E.J., 2014, *Simultaneous removal of oil and grease, and heavy metals from artificial bilge water using electro-coagulation/flotation*, Journal of environmental management, 144, pp.42-50.

Srivastava, N.K., and Majumder, C.B., 2008, *Novel biofiltration methods for the treatment of heavy metals from industrial wastewater*, J. Hazard. Mater. 151, 1-8.

6. NOMENCLATURE

C_{in} = initial Zn(II) concentration, ppm
C_{out} = outlet Zn(II) concentration, ppm
E = electrical energy consumption, $\frac{kWh}{kg\ Zn(II)}$
I = electrical current, A
LPM = liter per min.
M = concentration, molarity
R = removal efficiency, %
t = electrocoagulation time, min.
U = voltage, V
V = volume of the liquid in the reactor, L

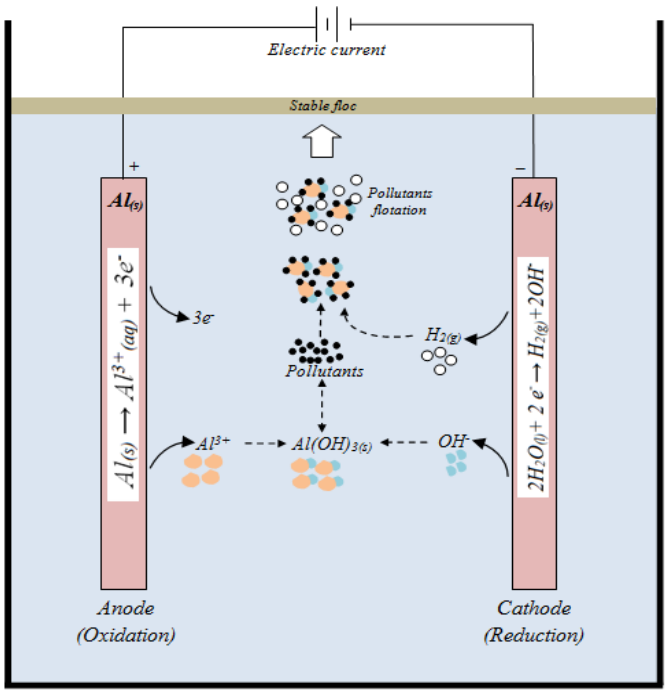

Figure 1. Representation of the electrocoagulation/flotation process.

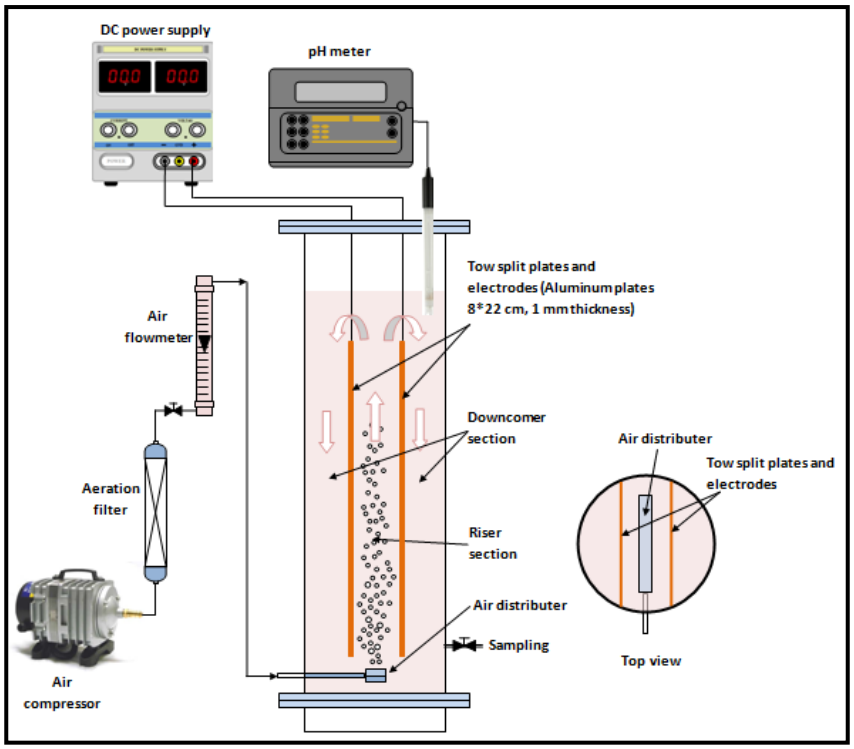

Figure 2. Experimental setup arrangement of the split-plate airlift electrochemical reactor

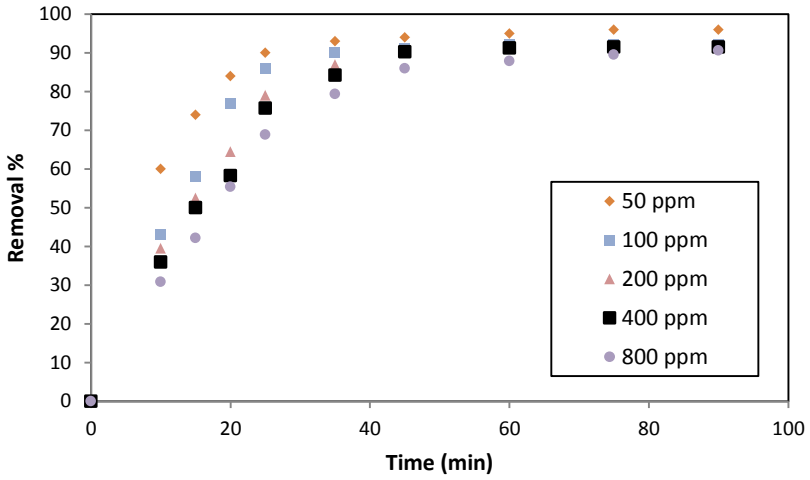

Figure 3. Effect of initial zinc concentration on the removal efficiency (current density: 9.6 mA/cm^2, initial pH: 7).

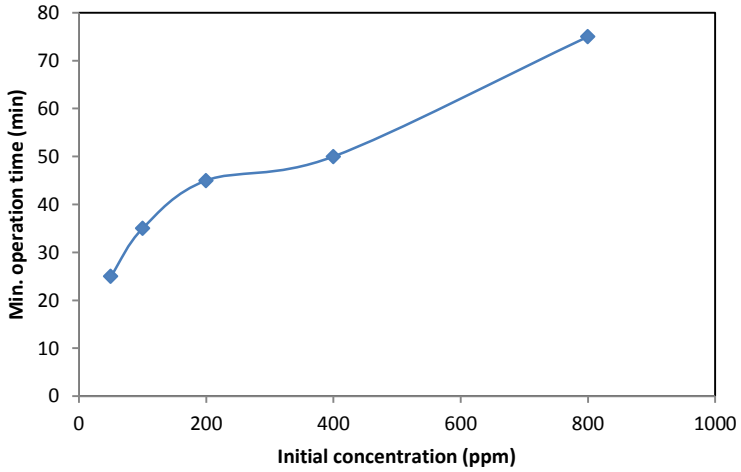

Figure 4. Effect of initial zinc concentration on the minimum operation (electrocoagulation) time value required for ≥ 90% removal efficiency (current density: 9.6 mA/cm^2, initial pH: 7).

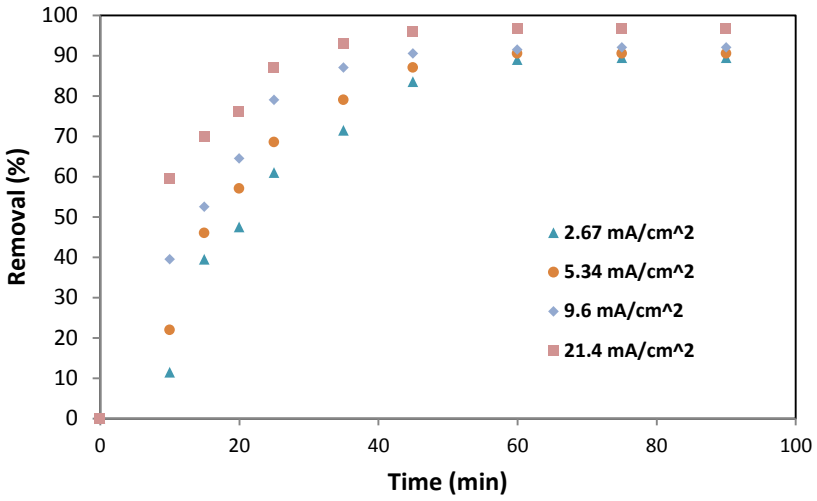

Figure 5. Effect of current density on the removal efficiency (Zn initial concentration: 200 ppm, initial pH: 7).

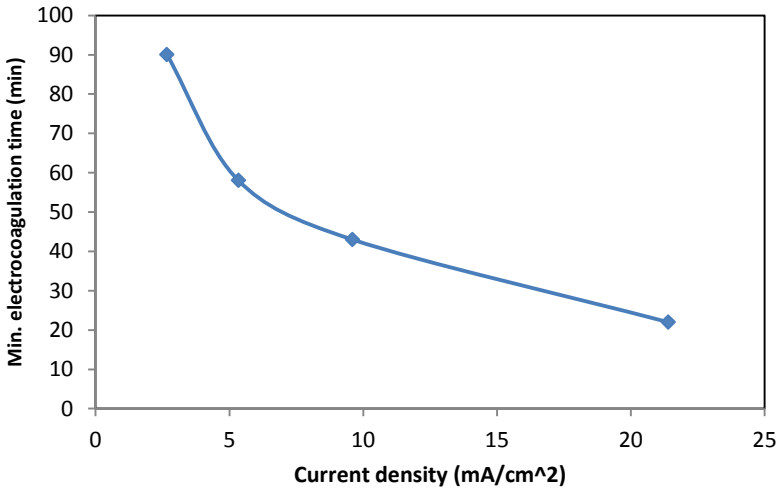

Figure 6. Minimum electrocoagulation time required for ≥ 90% Zn removal at different current density (Zn initial concentration: 200 ppm, initial pH: 7).

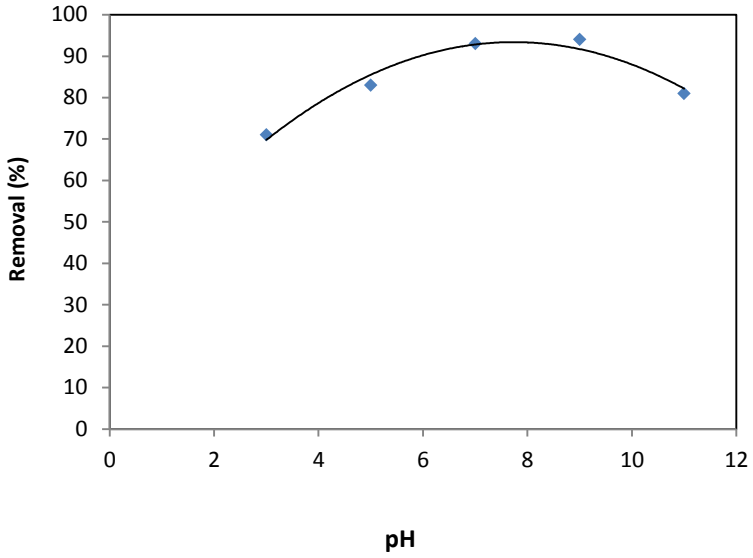

Figure 7. Effect of initial pH on Zn(II) ions removal. (Initial concentrations: 200 ppm, current density: 21.4 mA/cm^2, time of electrocoagulation: 35 min)

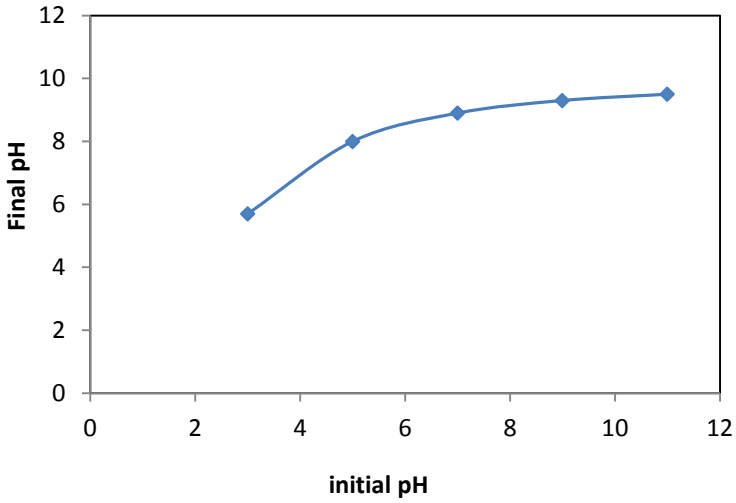

Figure 8. pH variation after electrocoagulation (Initial concentrations: 200 ppm, current density: 21.4 mA/cm^2, time of electrocoagulation: 90 min)

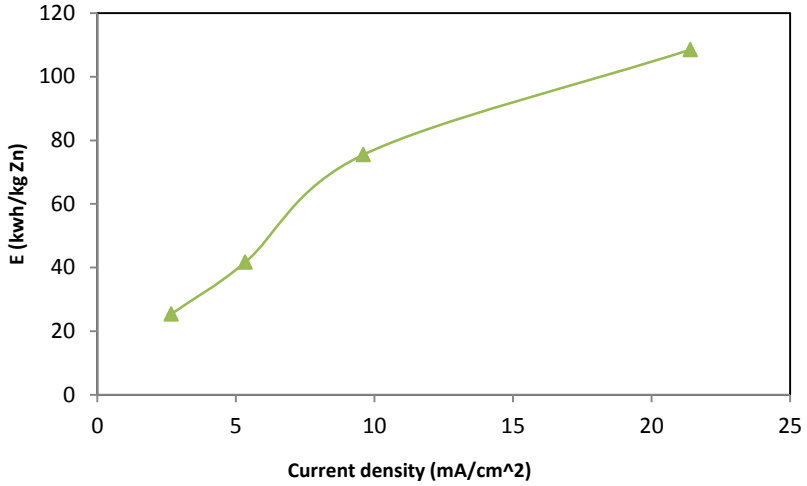

Figure 9. Effect of current density on electrical energy consumption (*E*) at operation time for which Zn removal of 90% (initial Zn concentration: 200 ppm, initial pH: 7)

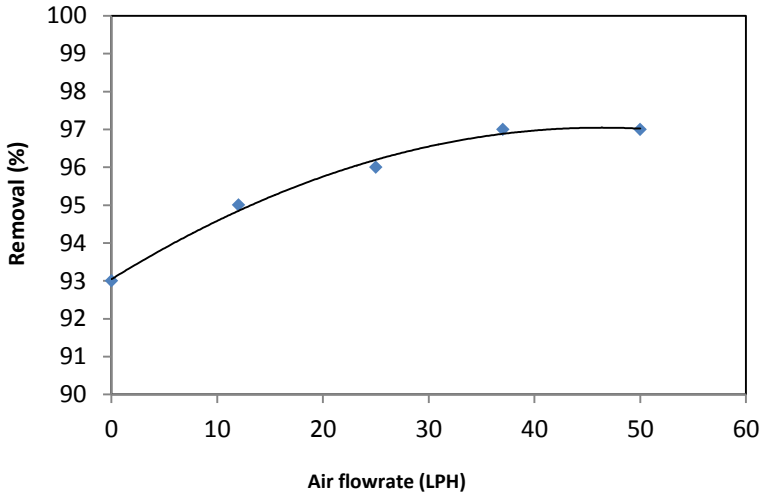

Figure 10. Effect of air flowrate on Zn removal efficiency (operation time: 35 min, initial Zn concentration: 200 ppm, initial pH: 7 and current density of 21.4 mA/cm^2)

Pitting Corrosion Behavior of 304 SS and 316 SS Alloys in Aqueous Chloride and Bromide Solutions

Ibtehal Kareem Shakir
Assistant Professor
College of Engineering-University of Baghdad
ibtehal_27@yahoo.com

Abdul-Kareem Mohammed Ali Alsamurraee
Assistant Professor
College of Science-University of Baghdad
Karim.alsamuraee@gmail.com

Shaymaa Mahdi Saleh
PhD student
College of Engineering-University of Baghdad
Email: shaymaallami@yahoo.com

ABSTRACT

The importance of the present work falls on the pitting corrosion behavior investigation of 304 SS and 316 SS alloys in 3.5 wt% of aqueous solution bearing with chloride and bromide anion at different solutions temperature range starting from (20-50)^{o}C due to the pitting corrosion tremendous effect on the economic, safety and materials loss due to leakage. The impact of solution temperatures on the pitting corrosion resistance at 3.5wt% (NaCl and NaBr) solutions for the 304 SS and 316 SS has been investigated utilizing the cyclic polarization techniques at the potential range -400 to1000 mV vs. SCE at 40 mV/sec scan rate followed by the surface characterization employing Scanning Electron Microscope. The results show that a significant decline in the pitting corrosion potential Ep values of both stainless steel alloys in chloride and bromide solution during temperature increase attributed to the pitting corrosion potential decreased arises from the modification of the passive film properties. The surface examination using optical microscope and scanning electron microscope prove the occurring of higher pitting density over 304 SS in chloride solution than that observed in bromide solution with a non-circular lacy cover pitfall out at the center and falls inside the pits hall in comparison to the isolated circular lacy cover pit formed on 316 SS in 3.5wt% NaBr solution at 50 ^{o}C.

Keywords: 304 and 316 SS alloys, pitting corrosion, Sodium halide salts, temperature effect.

سلوك التأكل النقري لسبائك الفولاذ المقاوم للصدأ 304 و316 في محاليل الكلور والبروم الملحية

ابتهال كريم شاكر
استاذ مساعد
كلية الهندسة-جامعة بغداد

عبد الكريم محمد علي السامرائي
استاذ مساعد
كلية العلوم –جامعة بغداد

شيماء مهدي صالح
طالبة دكتوراه
كلية الهندسة – جامعة بغداد

الخلاصة

يقع الاهتمام الكبير في هذا البحث على دراسة سلوك التأكل النقري لسبائك الفولاذ المقاوم للصداء 304 و316في3.5 نسبة مئوية وزنية لمحاليل مائية محملة بأيونات الكلور والبروم السالبة عند درجات حرا ره مختلفة تبدأ من 20 الى 50 درجه مئوية بسبب التأثير الهائل للتأكل النقري على الاقتصاد والسلامة وفقدان المواد الحاصل بسبب التسرب. قد تم دراسة تأثير درجة حرارة المحلول على مقاومة التأكل النقري لمحلول 3.5 نسبة مئوية وزنية لمحلول كلوريد الصوديوم وبروميد الصوديوم لسبائك الفولاذ 304 و316 باستخدام تقنينة الاستقطاب الحلقي عند معدل جهد يبدأ من -400 ملي فولت الى 1000 ملي فولت متبوعا بدراسة خواص السطح بأستخدام المجهرالالكتروني . لقد اظهرت النتائج ان انخفاض واضح في قيم جهد التأكل النقري للسبائك في محاليل الكلور والبروم بارتفاع درجة حرارة المحلول يعود السبب الى انخفاض مقاومة طبقة الحماية . فحوصات السطوح اثبتت حدوث تأكل نقري عالي الكثافة على سبيكة الفولاذ 304 في محلول كلوريد الصوديوم اعلى منه في محلول بروميد الصوديوم وان نقر كبيرة الحجم ذات غطاء شريطي متساقط من منتصف الغطاء الى داخل قعر الفجوة قد لوحظت

مع سبيكة فولاذ 316 في محلول 3.5 %الكلوريد مقارنة بفجوات معزولة دائرية الشكل في محلول 3.5 % بروميد الصوديوم عند درجة حرارة 50 درجة مئوية.
الكلمات الرئيسية: سبائك الفولاذ المقاوم للصدأ 304 و316، تأكل نقري، املاح هاليدات الصوديوم، تأثير درجه الحرارة.

1. INTRODUCTION

Pitting corrosion is a corrosion mechanism characterized by a highly localized loss of metals particularly passivated materials **Schweitzer, 2007**. Fe-Cr-Ni alloys, for example 304 and 316 Stainless steel, which are the most popular corrosion-resistance alloys used in many different applications due to their excellent corrosion resistance arises from the formation of a thin protective passive film with a thickness of several nm covering the stainless steel alloys surfaces at different environments and different experimental conditions, **Ahmed, 2006, Shreir, et al., 1994**. .

Despite their characteristic properties, these alloys are susceptible to pitting corrosion in halide containing solutions. The 304 SS alloy is susceptible to pitting corrosion attack at 10^{o}C in seawater while 316 SS alloy is more resistance than 304 SS and will suffer the same pitting attack at a temperature higher than that for 304 SS. Numerous studies have demonstrated that increasing the solution temperatures in the presence of halide anion will promote pitting corrosion attack to the Fe-Cr-Ni alloys **Wang, et al., 1988**, **Pardo, et al., 2000**.

Pitting corrosion of SS alloys mostly occurs in an environment bearing with ions such as Cl^{-}, Br^{-}, and I^{-} in perceivable concentration with chloride being the most aggressive one and as well as in marine environments. A shifting in the pitting corrosion potential Ep towards an active direction was associated with increasing the solutions temperature or chloride concentration **Ahmed**, **2006, Talbot, 1998**.

Liu et al., 2014, finds 13Cr Stainless steel is susceptible to severe pitting corrosion attack in heavy brine 1400 g/L KBr solution.

The aim of the present work was to determine the pitting corrosion resistance of 304 and 316 SS alloys in 3.5wt% NaCl and NaBr solution at temperature range (20 -50)^{o}C, with comparing the aggressiveness of halide (Chloride and Bromide) towards pitting corrosion.

2. EXPERIMENTAL PROCEDURE

2.1 Materials

The chemical compounds used for the tested solutions preparation were sodium chloride (NaCl) and sodium bromide (NaBr) with analytical grade product manufactured by BDH. A 3.5wt% NaX^{-} solution at pH5 was prepared by adding a 35 g of halides salt in one liter of deionized water, this concentration represents the synthetic seawater concentration and this value was fixed for the Br^{-} halide to compare the aggressivity of the two halides. The specimens under investigation were an alloy of plate cut from stainless steel sheet (304 and 316)SS alloy with a dimension of 1.5cmx1.5cmx2mm. These alloys and their chemical compositions listed in table 1were supplied by HESSCO / Heavy Engineering Equipments State Company / Ministry of Oil/Iraq.

The specimen were first ground using a series of silicon carbide emery paper starting from 80 up to 2000 surface finishing in order to remove surface scratch or defect, followed by degreasing with acetone and washing with distilled water, finally swabbed with ethanol and dried using a stream hot air supplied by heat gun then kept in the desiccator.

2.2 Electrochemical Measurements

The electrochemical measurement including the cyclic polarization techniques for pitting corrosion studies was performed with Wenking M-lab 200 Electronik Germany Bank potentiostat, in a double glass wall three electrode corrosion cell with a 1 cm^2 surface area. The opening face of the holder was exposed to the tested solution acts as working electrode, a saturated calomel electrode and a high purity platinum rod with 10 cm long were used as reference and counter electrode respectively **Fig. 1** shows the full electrochemical system used for polarization studies. The cyclic polarization measurements were performed at a 10 mV/Sec scan rate starting from -400 mV up to 1000 mV in the anodic direction (forward scan) and back to the starting potential (backward scan). These measurements were done to the tested alloys in the prepared solution (3.5wt% NaCl and NaBr) at different solution temperatures with a heating-cooling circulation unit type HAAKE OOO-3959/ Germany in order to control the desired solutions temperature within ±1 ^{o}f, to estimate the pitting potential values which gives an indication of the potential up with the onset of pitting corrosion surfaces attack, while the protection or repassivation potential Erep which is defined as the potential at which the potential above is with no pit nucleation but allowed propagation of the existing pits and below which occurs of pitting corrosion.
Finally, the samples were subject to the surface examination utilizing the FEI Scanning Electron Microscope SEM, model Inspect S50 made in the Czech Republic.

3. RESULTS AND DISCUSSION

The major goal of this paper is to examine and discuss the pitting corrosion behavior of the 304 SS and 316 SS alloys in 3.5wt% of sodium halides salt NaCl and NaBr at different solution temperature due to the massive presence of sodium chloride and sodium bromide in the industry.

3.1 Stainless steel /Chloride System

3.1.1 304 SS/ Chloride system

The cyclic polarization curves of 304 SS tested specimens in 3.5 wt% NaCl solution at 20,30,40 and 50^{o}C are shown in **Fig. 2**. In general this figure shows that the sample was susceptible to pitting corrosion attack in a solution bearing with chloride halide at different temperature range starting from 20^{o}C up to 50^{o}C from the existence of positive hysteresis loop in cyclic polarization curves, which characterizes the passive film breakdown in the forward scan and subsequent repassivation on the backward scan. Although a decrease in the anodic polarization curves was observed for 304 SS alloy in the chloride halide solutions due to solutions temperature increasing up to 50^{o}C these results coincided with the SEM observation.

According to **Wang, et al., 1988, Malik, et al., 1992, Roy, and Basu**, **1981**, an active shifting of the anodic polarization curves as well as in the pitting potential Ep, with a pronounced increase in the passive current density was observed through solution temperature increases. The same results were observed in this study with a slight influence of temperature on repassivation potentials.

One can notice from **Fig. 2** that the pitting corrosion potential Ep decreased while the pitting current density Ip in mA/cm^2 measured at the Ep values increased with increasing the solution temperature from 20 to 50^{o}C, with no tendency for 304 SS to repassivate in 3.5 wt% NaCl

solution at the studied temperature which indicates that the 304 SS suffers a severe pitting corrosion attack at these conditions. These results are extracted from the cyclic polarization curve **Fig. 2** and illustrated in Table 2**.**

Fig. 3 shows the effect of the temperature on the Ep, Ecorr values as well as on the potential area difference ΔE between the pitting and corrosion potentials for a chance of the metals surfaces affected by pitting corrosion for 304 SS in chloride containing solution versus solutions temperature, both values Ep and ΔE decreased with temperature increase attributed to decreasing the resistance to pitting corrosion with about 200 mV potential of ΔE higher than Ep curve **Munoz, et al., 2006**.

The variation in the Ep, Ecorr, ΔE, and Ip values arises from the fact that the passive film undergoes a degradation in its properties with temperature, and becomes more defective, porous and less resistance to film breakdown with an intrinsic modification of their chemical and physical structures **Hur**, and **Park, 2006, Wang, et al., 1988, Manning,** and **Duquette, 1980**.

Fig.4 (a and b) shows the SEM micrographs of 304 SS at different magnification after testing the alloy with cyclic polarization techniques applying a potential (-400-1000)mVat 10mV/sec scan rate in 3.5wt% NaCl at 50C. These micrographs show a small shallow open mouth circular pits spreading on the alloy surface with another large noncircular lacy cover pit collapse at the cover center and falls inside a pits hall, as well as a salt film deposit inside the cavities showing bright parts indicates salt film deposition, while the dark cavities gives an indication to the deep pit.

The SEM observation also showed that the pits formed in clusters of numbers of the pit and the pits grow rate increase with temperature increase and subsequently the pits grow into one another to form one large irregular lacy pit shape **Tait, 1979**.

3.1.2 316 SS /Chloride system

The cyclic polarization curve of 316 SS in 3.5wt% NaCl solution at temperature range is (20, 30, 40 and 50) ^{0}C is shown in **Fig.5.** A clear sign to pitting corrosion occurring on the 316 SS alloy surface in a chloride containing solution at all temperatures arises from the presence of the positive hysteresis loop with the ability of the 316 SS to repassivate at Erep after pitting corrosion occurs in 3.5wt% NaCl at the studied temperature range. The values of the Ep, Ecorr, Erep and Ip are listed in Table3 which are extracted from the cyclic polarization curves **(Fig.5**) and also is shown in **Fig.6**. A decrease in the characteristic potentials that distinct the pitting corrosion attack on 316 SS alloy illustrated in Ep, Erep, Ecorr, and ΔE values with solution temperature increases up to 50^{o}C towards an active direction, which can be attributed to the impact of halide solution temperature on the protective oxides passive layer that is covering the SS surface with an indication of decreased resistance to pitting corrosion occurrence during temperature increase **Laycock, and Newm , 1998**. Moreover, the Ip values show to be increased with temperature increasing as can be noticed from Table 3.

The SEM micrograph of 316 SS surface shows that this alloy incur a pitting corrosion attack in chloride containing medium with a low-density pit were formed on the 316 SS surface which evinces the higher resistance of this alloy toward susceptibility to pitting corrosion in comparison to the 304 SS behavior in the same halide salt solution as can be shown in **Fig.7.**

3.2 Stainless Steel /Bromide system

3.2.1 304 SS/ Bromide system

To investigate the 304 SS susceptibility to pitting corrosion in a 3.5wt% NaBr solution at different picked temperatures starting from 20^{o}C up to 50^{o}C, a cyclic polarization technique was used to the working electrode (304 SS) from -400 to 1000 mV versus SCE as mentioned previously in the experimental work.

Fig. 8 shows the typical cyclic polarization curves for 304 SS in a solution bearing with 3.5wt% sodium bromide (NaBr) salt over a temperature range (20-50)^{o}C, the results show that bromide halide promotes pitting corrosion to 304 SS at all studied temperature with the metal ability to repassivate under the experimental condition, in addition, a slight decrease in the pitting corrosion potential Ep, Ecorr and the potential area difference ΔE versus the temperature varying was observed. **Fig. 9** and Table 4 illustrate the 304 SS pitting corrosion characteristic parameters in a bromide containing solution. Again the influence of environmental condition temperature (20, 30, 40 and 50)^{o}C on the increasing susceptibility of 304 SS towards pitting corrosion results form the aggressive bromide anion in breaking the passive oxide film which then promotes the pitting corrosion to the 304 SS.

Examination the 304 SS surface confirmed the presence of different pits size widespread over the alloy surface with an interrupted area with no pits denote the remaining of passive film cathodic area in comparison with pit (anodic area). **Fig. 10** depicted the pitting corrosion occurring on the 304 SS surface using SEM microscope, a deep lacy cover pits the surface with an average pit mouth diameter of about 66.30 µm.

3.2.2 316 SS/ Bromide system

The pitting corrosion behavior of 316 SS in a bromide containing solution at different solution temperatures was done utilizing the cyclic polarization techniques and surface microscopic examination. **Fig.11**, **Fig.12** and Table 5 present the pitting and corrosion parameter for 316 SS in a 3.5wt% NaBr solution at temperature increase from 20^{o}C up to 50^{o}C. Pitting potential and ΔE showed to decrease with temperature increasing with more than 100 mV differences between the two values which gives an indication of increased susceptibility to pitting corrosion through decreasing the resistance to pitting corrosion. An open mouth pits with 69.77 µm were formed on 316 SS with a salt film deposition inside the pit favoring pits growth rate towards gravity **Fig.13**.

3.3 Comparison between Cl^- and Br^- anion

It is well known that the presence of aggressive anion would promote the pitting corrosion to SS alloys by penetrating the film which causes breaking the passive film covering the surface of the metal. This can be seen for instance from **Fig. 14**, this figure illustrates a marked difference in the Ep values for the 304 SS in comparison to the two prepared aqueous halide salts versus temperature and a higher reduction in Ep values was observed in chloride than bromide. Moreover, the chloride values (Ep) shows to be a 100 mV more negative than that of bromide associated with the fact that chloride was more aggressive than bromide ion. In addition, the same behavior was obtained for pitting resistance ΔE as can be shown in **Fig.15,** with the same behavior obtained **by Leckie, and Uligh, 1966, Kolotyrkin, 1963, Refaey, et al., 2005**.

Dawood, and Szklarska-Smialowska, 1986 reported that the aggressiveness of halide decreased in the order $Cl^- > Br^-$, in contrast to the anion radius $Cl^- < Br^-$.

Pitting corrosion promotes by the presence of halide anion especially chloride anion which is more mobile in solution, small ion size can easily penetrate the passive film and allowed the formation of pitting corrosion due to the halide properties **Talbot, 1998**, **Jones,1996, Loto, 2015.**

Pardo et al., 2000, observed a decrease in the ΔE values for two high alloys SS in a solution with different chloride concentration and temperature and mentioned that the higher the ΔE values lead to the higher resistance to the pitting corrosion.

The pits were also imaged in SEM microscope. These observations proved that the surface of the alloy was covered with a high density of pits not only around the MnS inclusion but also upon the surface defect especially in bromide- containing solution as well as these formed at the boundary of grains illustrated in the cavity bottom, these results were in accordance with **Tzaneva, et al., 2006**.

Abd El Meguid, 2007, stated that the pits morphology of SS alloys under chloride attack are not hemispherical but grew under the metal surface, growth in a numerous point to make a lacy pattern.

Fig. 16 illustrated the difference in pits formed on 316 SS in bromide compared to chloride solutions; one can see that an isolated circular pit with salt deposition in the pit cavity was pronounced in bromide while a one large pit composed of different pits formed in chloride solution, both pits are of open mouth, which enhances the repassivation process.

4. CONCLUSIONS

1. Stainless Steel grades 304 and 316 are susceptible to pitting corrosion attack in chloride and bromide containing media with different extent depending on the anion aggressivity and size.
2. Pitting corrosion resistance decreased as Ep, Erep, and ΔE decrease with the solution temperatures increase from 20 to 50^oC in both studied halide salt solutions for 304 SS and 316 SS.
3. A 100 mV difference was observed for 304 SS in chloride solution compared to bromide solution (chloride more aggressive than bromide) and this difference increases with solution temperature increase the resistance to pitting corrosion decreased.
4. A non-hemispherical or irregular pit with a lacy cover formed on 304 SS and 316 SS surfaces in chloride containing solution compared to an open mouth isolated circular pits in 3.5 wt% Bromide solution.

REFERENCES

- Abd El Meguid, E.A., and Abd El Latif, A.A., 2007, *Critical Pitting Temperature for Type 254SMO Stainless Steel in Chloride Solutions*, Corrosion science., Vol. 49, PP. 263-275.
- Ahmed, Z., 2006, *Principles of Corrosion Engineering and Corrosion Controls*, Elsevier Science and Technology Books, PP. 149.
- Dawood, N.M., *Corrosion of Stainless Steel 316L in Various Aqueous Salt Solutions*, College of Material Engineering- Babylon, http://uobabylon.edu.iq/uobColeges/fileshare/articles/.
- Hur, D. H., and Park, Y. S., 2006, *Effect of Temperature on the Pitting Behavior and Passive Film Characteristics of Alloy 600 in Chloride Solution*, Corrosion Journal, Vol. 62, No.9, PP.745-750.
- Jones, D. A., 1996, Principles and Prevention of Corrosion, 2nd ed., Prentice Hall, United States of America, PP.199.
- Kolotyrkin, JA.M., 1963, *Pitting Corrosion of Metals*, National Association of Corrosion Engineers NACE, Vol. 19, August, No.8, PP.261t-268t.
- Laycock, N. J., and Newman, R. C., 1998, *Temperature Dependence of Pitting Potential for Austenitic SS above their Critical Pitting Temperature*, Corrosion science., Vol. 40, No.6, PP.887-902.
- Leckie, H. P., and Uhlig, H. H., 1966, *Environmental Factors Affecting the Critical Potential for Pitting in 18-8 Stainless Steel*, Jurnal of The Electrochemical Society, Vol.113, No.12, PP.1262-1267.
- Liu, Y., Xu, L., Lu, M., Meng, Y., Zhu, J., and Zhang, L., 2014, *Corrosion Mechanism of 13Cr Stainless Steel in Completion Fluid of High Temperature and High Concentration Bromine Salt*, Applied Surface Science, Vol. 314, PP. 768-776.
- Loto, R.T., 2015, *Pitting Corrosion Evaluation and Inhibition of Stainless Steel, A Review*, Journal of Materials and Environmental Science, Vol.6, No.10, PP. 2750-27620.
- Malik, A. U., MayanKutty, P. C., Siddiqi, N. A., Andijani, I. N., and Ahmed, S., 1992, *The Influence of PH and Chloride Concentration on the Corrosion Behavior of AISI316L Steel in Aqueous Solution*, Corrosion Science, Vol. 33, No. 11, PP.1809-1827.
- Manning, P. E., and Duquette, D. J., 1980, *The Effect OF Temperature (25°-289°C) on Pit Intiontion In Single Phase and Duplex304L Stainless Steel in 100 ppm C1-Solution*, Corrosion Science, Vol. 20, PP. 597- 610.
- Munoz, A.I., Anton, J. G., Gunion, J. L., and Herranz, V. P., 2006, *Effect of Solution Temperature on Localized Corrosion of High Nickel Content Stainless Steel and Nickel in Chromated LiBr Solution*, Corrosion Science, Vol. 48, PP. 3349-3374.
- Pardo, A., Otero, E., Merino, M. C., Lopez, M. D., Utrilla, M. V., and Moreno, F., 2000, *Influence of pH and Chloride Concentration on the Pitting and Crevice Corrosion Behavior of High-Alloy Stainless Steels*, Corrosion, Vol. 56, No. 4, PP. 411-418.
- Refaey S.A.M, Taha, F., and Abd El-Malak, A. M., 2005, *Corrosion and Inhibition of Stainless Steel Pitting Corrosion in Alkaline Medium and the Effect of Cl^- and Br^- anions*, Applied Surface Science, Vol. 242, No.1-2, PP.114-120.
- Roy, D. L., and Basu, S., 1981, *Pitting Corrosion of Stainless Steel in Chloride Containing Media*, Proceedings of the Indian National Science Academy, Vol. 48, A, No. 4, PP. 400-415.

- Schweitzer, P.A., 2007, *Fundamentals of Metallic Corrosion*, 2nd ed., CRC press, Tylor and Francis group, United States of America, PP. 111.
- Shreir, L.L., Jarman, R. A., and Burstein, G. T., 1994, *Corrosion/ Metal environment*, 3rd ed., Metallurgy, Corrosion, Butterworth-Heinemann, Great Britain, Vol.1, PP. 1:118.
- Simalowska, Z. S., 1986, *Pitting Corrosion of Metals*, National Association of Corrosion Engineering, Houston, PP. 223.
- Tait, W. S., 1979, Effect *of Physical Parameter on the Pitting Corrosion of Mild Steel in Low Total Dissolved Solids*, Oxygen Bearing Waters, Corrosion, Vol. 35, No. 7, PP. 296-300.
- Talbot, J., and Talbot, D., 1998, *Corrosion Science and Technology*, CRC Press L.LC., United States of America, PP. 275.
- Tzaneva, B. R., Fachikov, L. B., and Raicheff, R. G., 2006, *Effect of Halide Anion and Temperature on inhibition of Pitting in Cr-Mn-N and Cr-Ni Steels*, Corrosion Engineering, Science and Technology, Vol.41, No.1, PP. 62-66.
- Uhlig, H. H., and Leckie, H. P., 1966, *Environmental Factors Affecting the Critical Potential in 18-8 Stainless Steel*, Journal of the Electrochemical Society, Vol.113, No. 12, PP.1262-1267.
- Wang, J. H., Su, C. C., and Szklarska-Smialowska, Z., 1988, *Effect of Cl^- Concentration and Temperature on Pitting of AISI 304 Stainless Steel*, Corrosion Science, Vol. 44, No. 10, PP. 732-737.

NOMENCALTURE

Ecorr. = corrosion potential, mV
EDX= Energy Dispersive X-Ray
Ep= pitting corrosion potential, mV
Erep= repassivation potential, mV
Ip= pitting current density at Ep values, mA/cm^2
SCE= standard calomel electrode
Sec= time, second
SEM= Scanning Electron Microscope
SS= Stainless Steel
X^-= Halide type (Cl^- and Br^-)
ΔE= potential area difference = Ep-Ecorr, mV

Table 1. Chemical composition of studied alloys in wt%.

Fe-Cr-Ni. wt%	Ni	Cr	C	Mn	Mo	S	Cu	P	Si	Fe
304 SS	9.7	19.3	0.06	1.37	0.122	<0.005	0.198	<0.005	0.986	Bal.
316 SS	8.67	17.1	0.09	1.5	2.66	<0.005	0.177	<0.005	0.67	Bal.

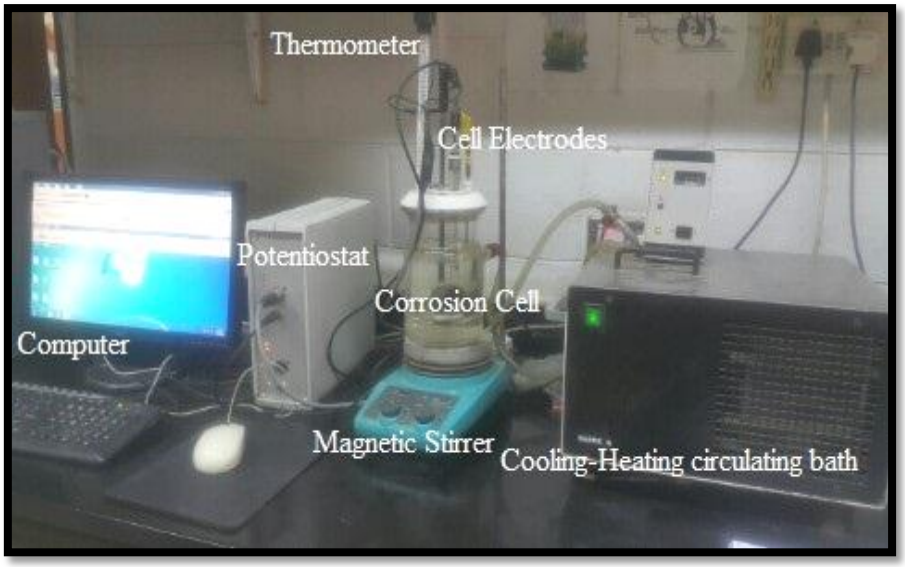

Figure 1. Full electrochemical system for polarization studies.

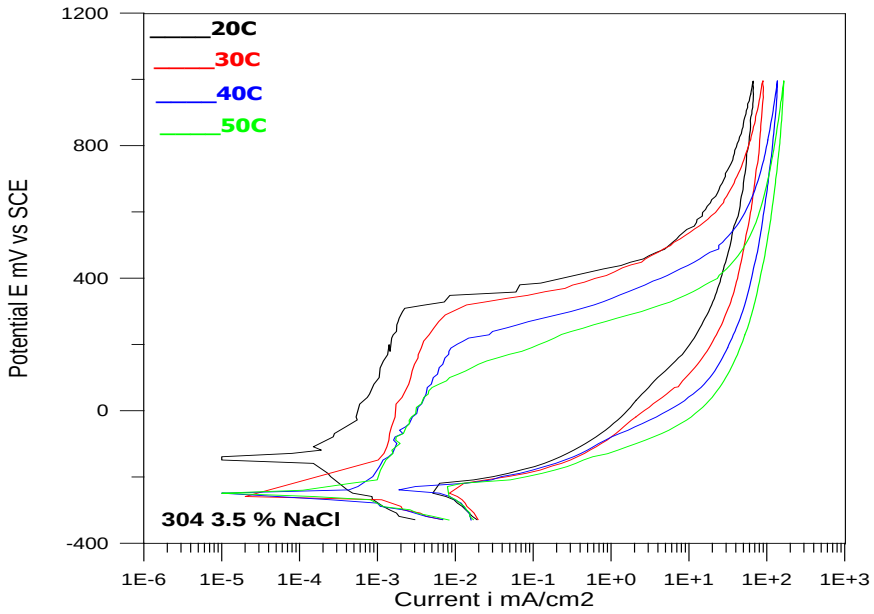

Figure 2. The cyclic polarization curve for 304 SS in 3.5wt% NaCl solution vs. temperature change (20-50)ºC.

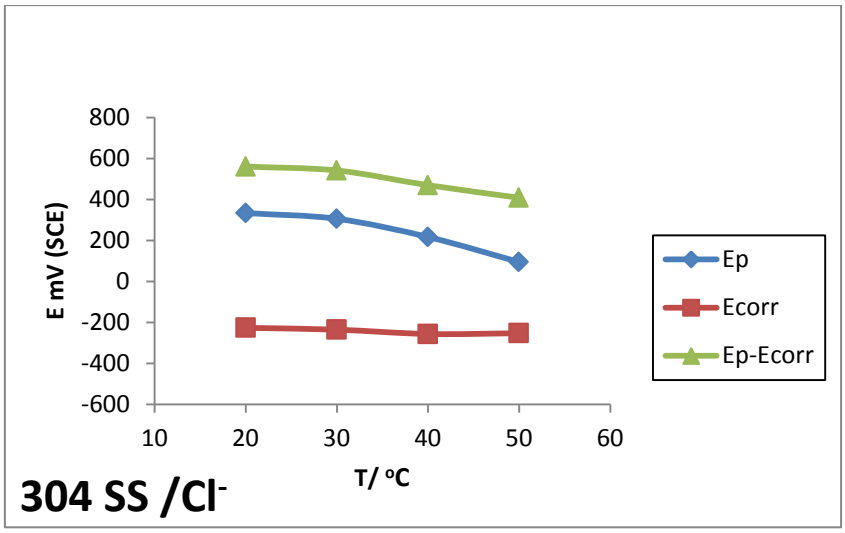

Figure 3. The variation of pitting, corrosion and potential area difference with temperature for 304 SS in 3.5wt% NaCl.

Table 2. Pitting, corrosion and resistance potential characteristic to pitting corrosion for 304 SS at different temperature in 3.5wt% sodium chloride solution.

Temp./ °C	304 SS in 3.5 wt% NaCl			
	Ep mV	Ecorr mV	Current ip µA/cm^2 at Ep	ΔE=Ep-Ecorr mV
20	333.2	-227	4.4	560.2
30	305.1	-236	9.9	541.1
40	216.4	-257	15.5	469.5
50	94.3	-253.3	8.5	407.9

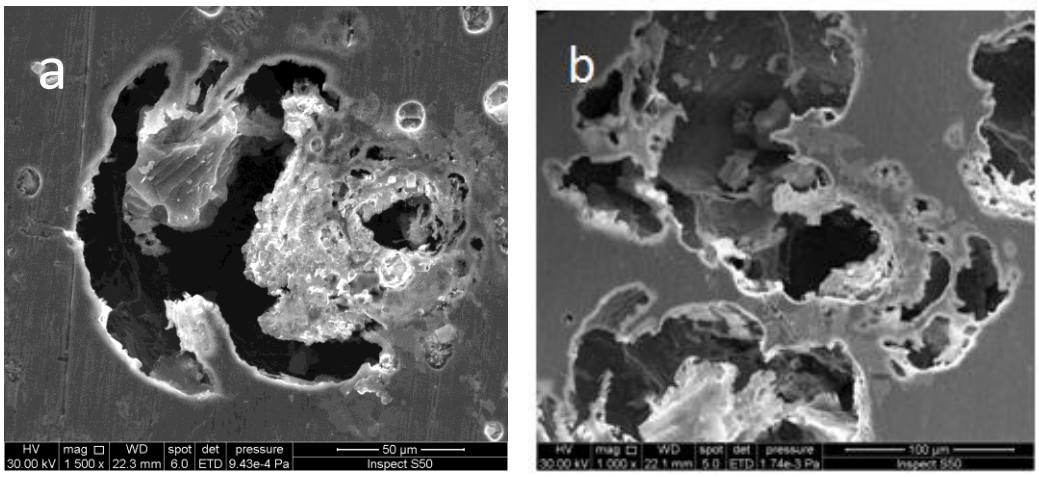

Figure 4. The SEM observation of 304 SS after applying cyclic polarization techniques in 3.5wt% NaCl at 50°C at different locations and at(a 50 and b 100) µm magnification.

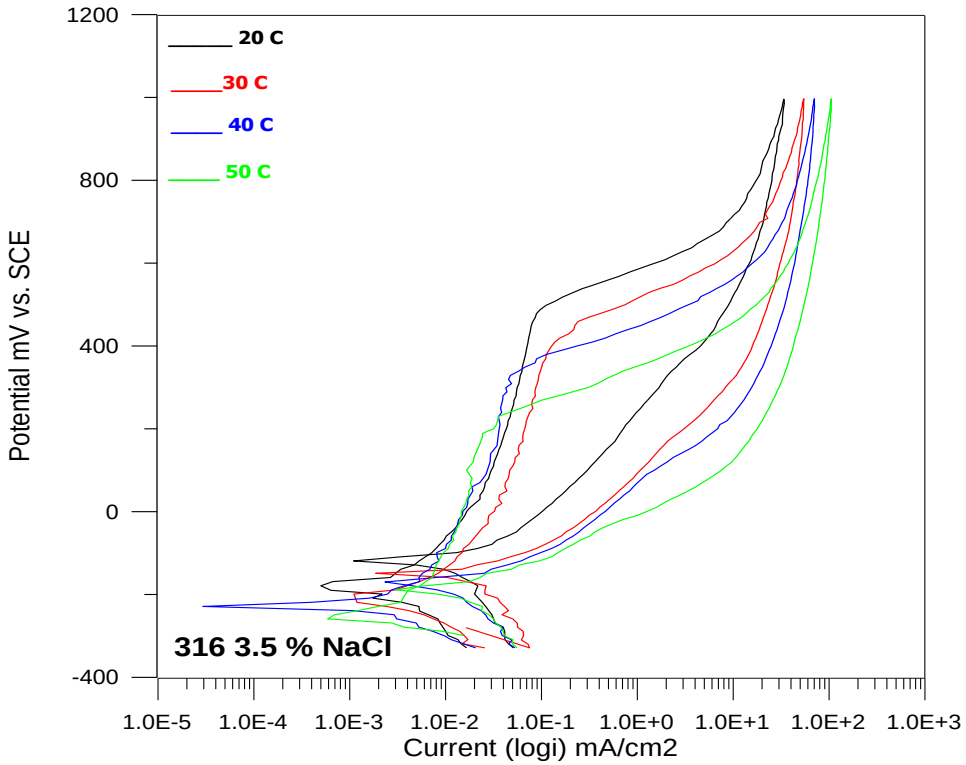

Figure 5. Cyclic polarization curves for 316 SS in 3.5wt% NaCl at temperature (20-50)^{o}C

Table 3. Pitting corrosion, free corrosion, potential area difference and Ip versus Temperature for 316 SS in 3.5wt% NaCl solution.

Temp./ ^{o}C	316 SS in 3.5wt% NaCl			
	Ep mV	Current ip $\mu A/cm^2$ at Ep	Ecorr mV	ΔE=Ep-Ecorr mV
20	496.9	111.7	-182.5	679.4
30	412.2	157.2	-216	628.2
40	350	68.4	-221	571
50	237	35.8	-244.1	481.1

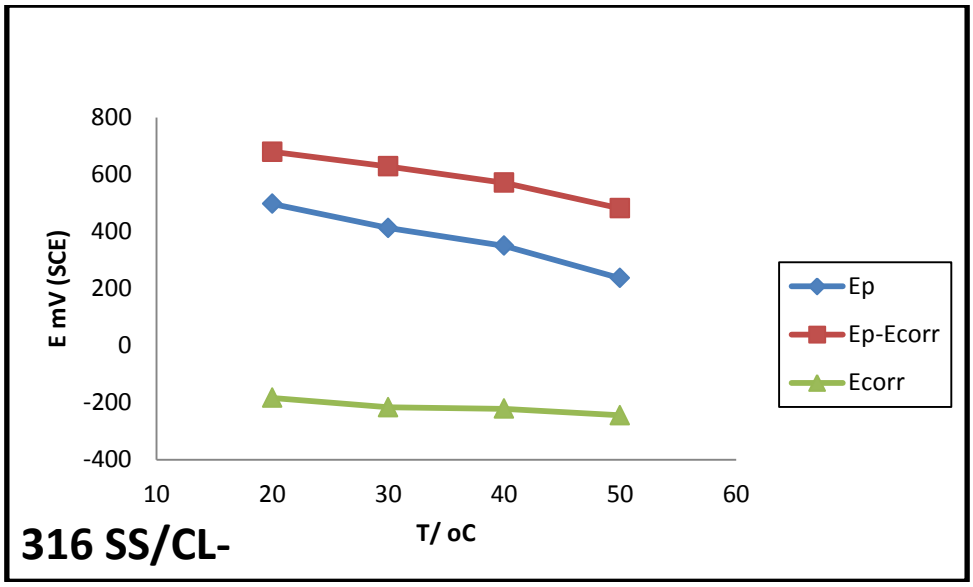

Figure 6. The variation of Ep, Ecorr and potential area difference vs. solution temperature (20-50)^{o}C for 316 SS in 3.5wt% NaCl.

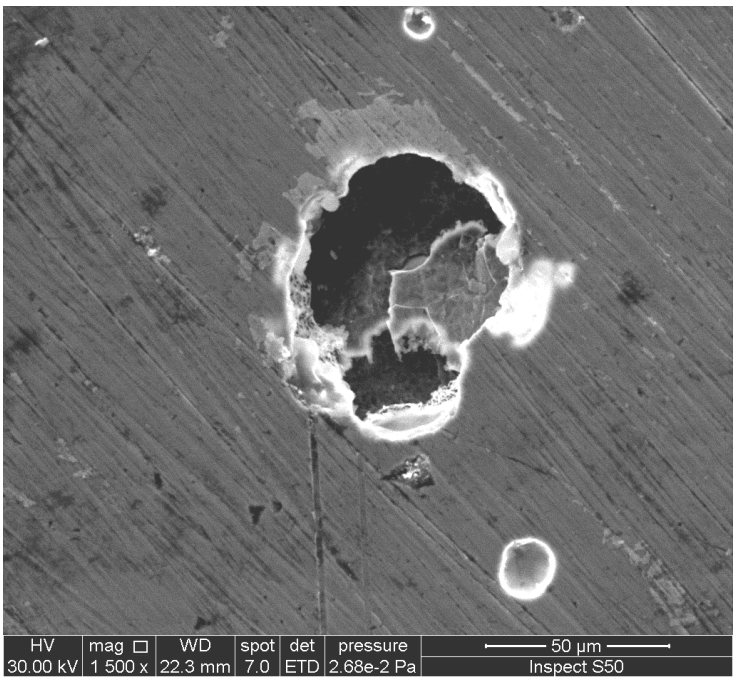

Figure 7. The SEM observation of 316 SS in 3.5wt% NaCl solution at 50^{o}C.

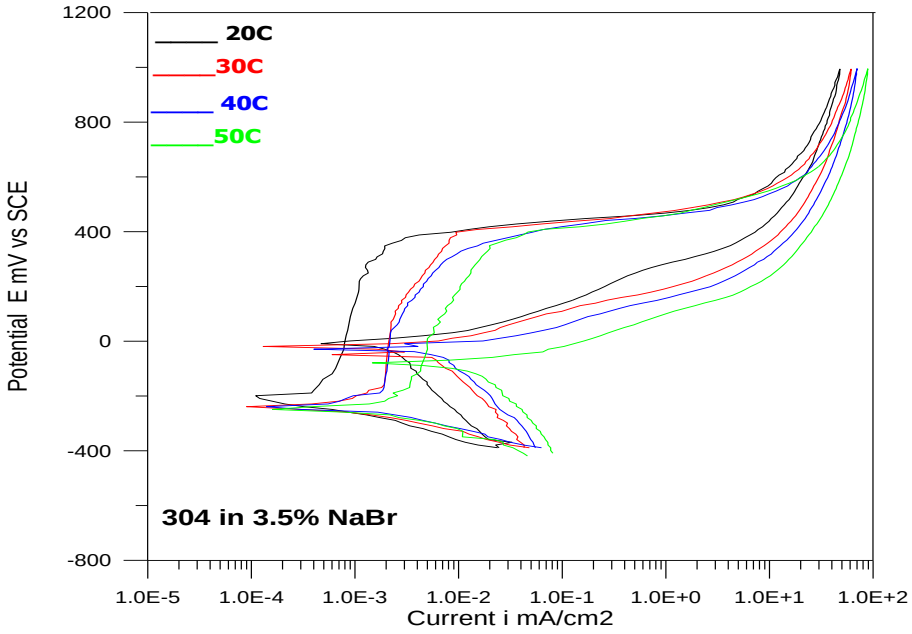

Figure 8. Cyclic polarization curve of 304 SS in 3.5wt% NaBr at varying temperature range (20-50)^{o}C.

Table 4. Pitting potential Ep, corrosion potential Ecorr, Ip pitting current density and potential area ΔE versus solution temperature for 304 SS in 3.5wt% NaBr.

Temp./ ^{o}C	304 SS in 3.5wt%NaBr			
	Ep mV	Ecorr mV	Current ip μA/cm^{2}at Ep	ΔE=Ep-Ecorr mV
20	405	-223.6	10.5	628.6
30	400	-236.8	11.3	636.8
40	362	-241.7	19.8	604.1
50	352	-247	23.1	599

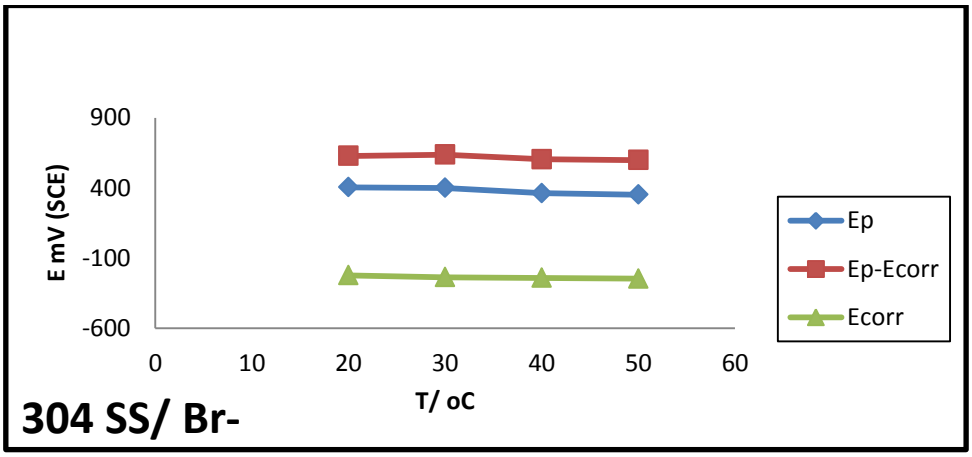

Figure 9. Pitting Ep, corrosion Ecorr, and potential area difference ΔE of 304 SS in 3.5wt%NaBr determined by cyclic polarization test vs. temperature range (20-50)^{o}C.

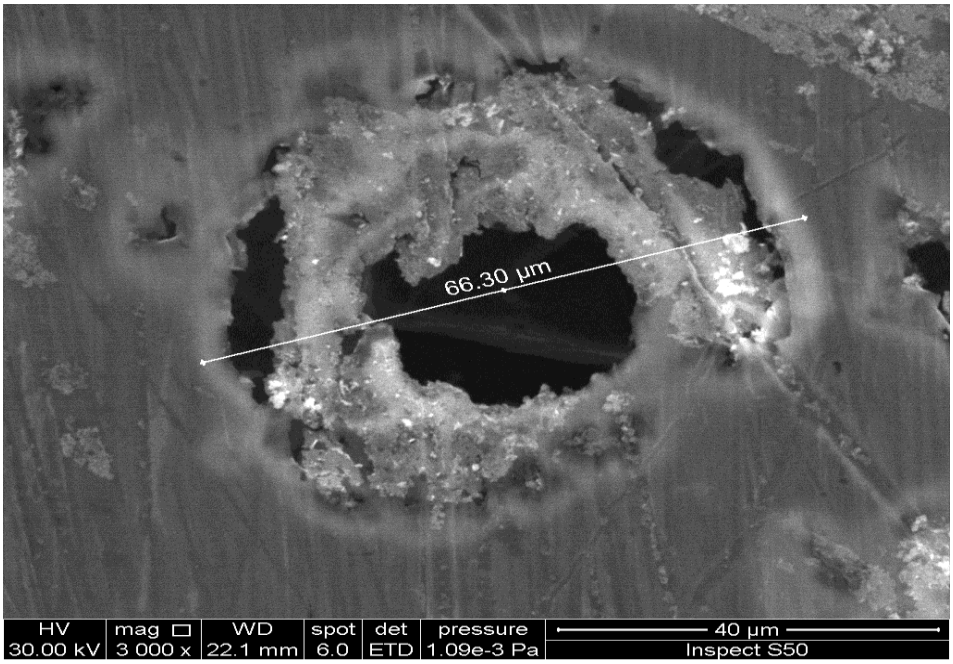

Figure 10. Scanning Electron Microscopy SEM of 304 SS in 3.5wt%NaBr at 50 ^{o}C.

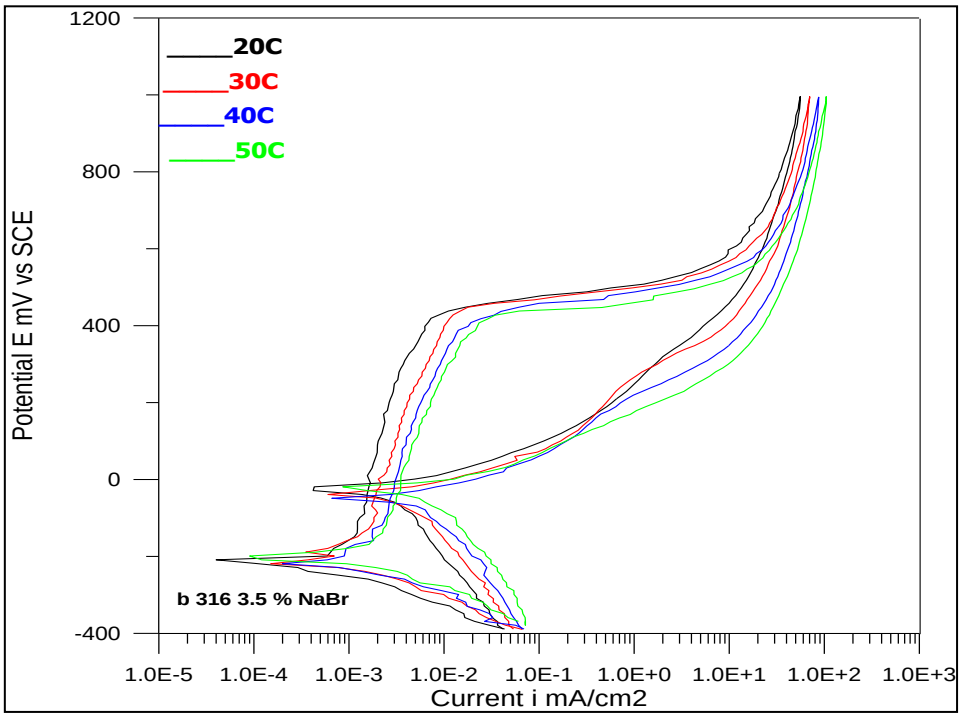

Figure 11. Cyclic polarization curves for 316 SS alloy in 3.5wt% NaBr at temperature (20-50)^{o}C.

Table 5. The pitting potential Ep, Corrosion potential Ecorr, ΔE potential difference vs. temperature in ^{o}C for 316 SS in 3.5wt% NaBr.

Temp./C	316 SS in 3.5wt%NaBr			
	Ep mV	Ecorr mV	Current ip μA/cm^2	ΔE=Ep-Ecorr mV
20	450	-213	11.7	663
30	428	-217	12.8	645
40	391.8	-212	16.9	603
50	380	-202	20.4	582

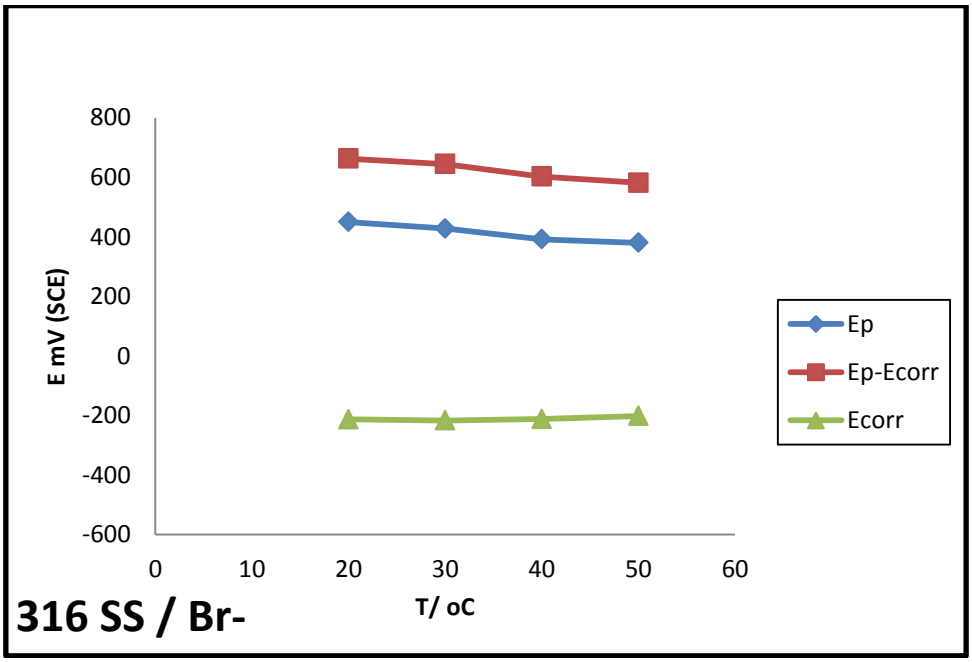

Figure 12. Pitting Ep, corrosion Ecorr, and potential area difference ΔE of 316 SS in 3.5wt%NaBr determined by cyclic polarization test vs. temperature range (20-50)^{o}C.

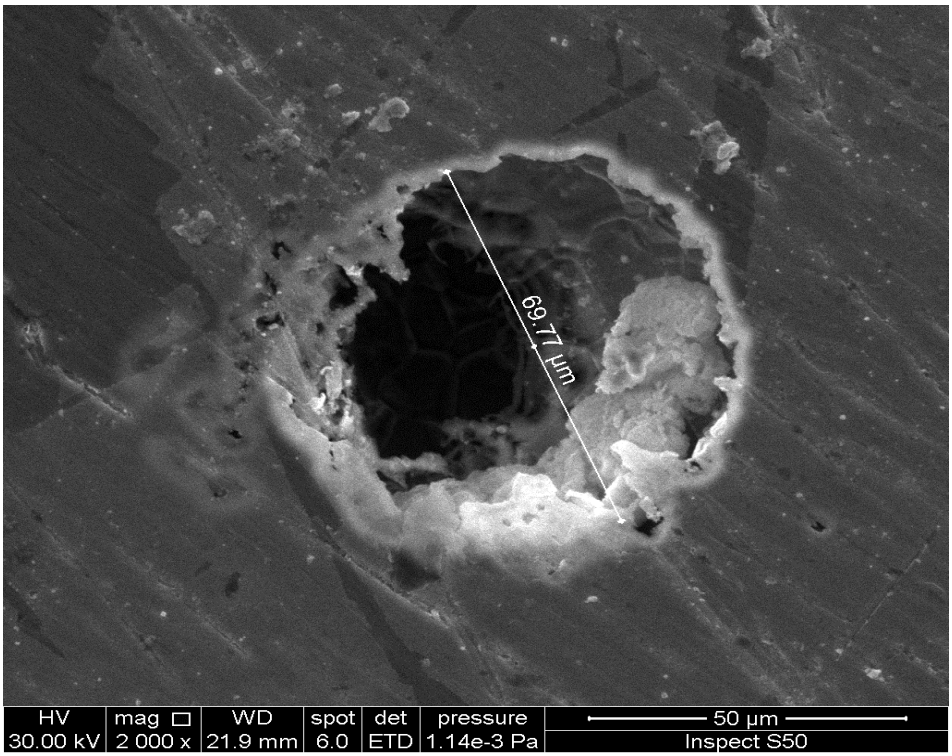

Figure 13. Scanning Electron Microscope SEM for 316 SS after cyclic polarization test in 3.5wt%NaBr.

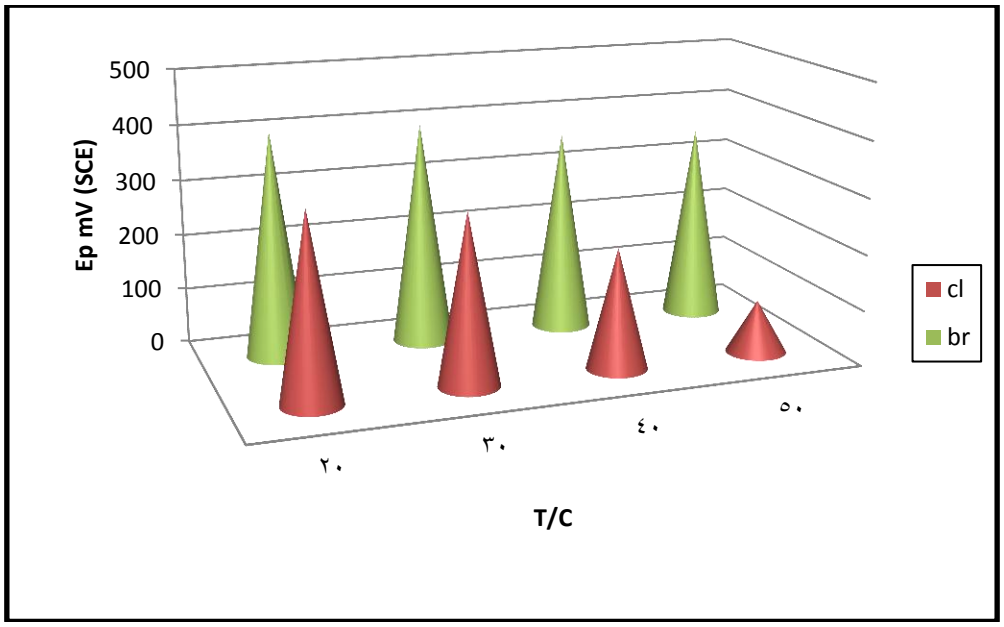

Figure 14. Pitting potential Ep comparison between Cl^- and Br^- halide of 304 SS vs solutions temperature.

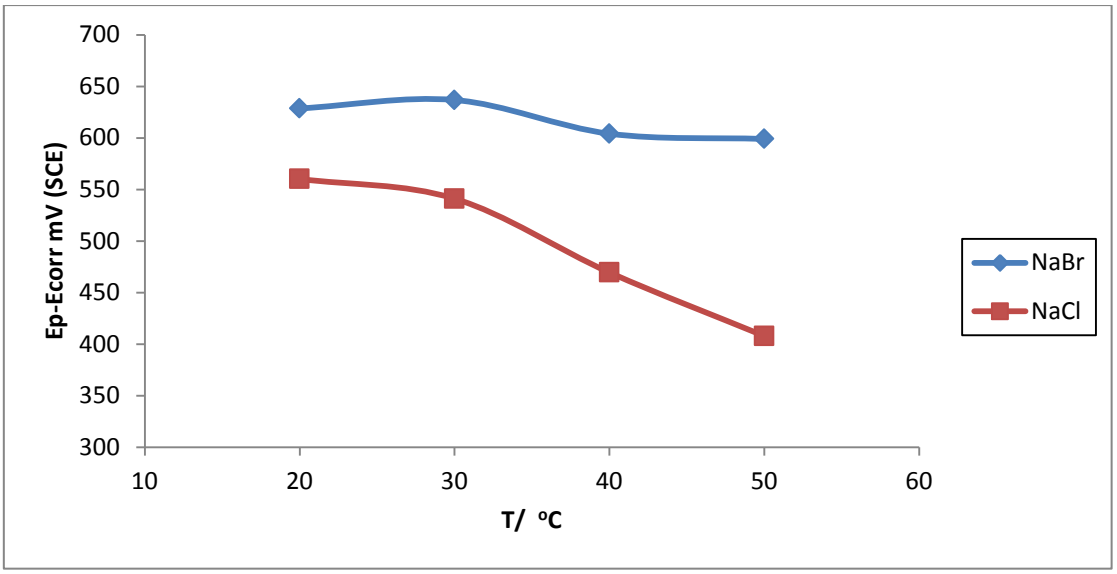

Figure 15. The reduction in ΔE values of 304 SS under halide anion effect at different temperatures.

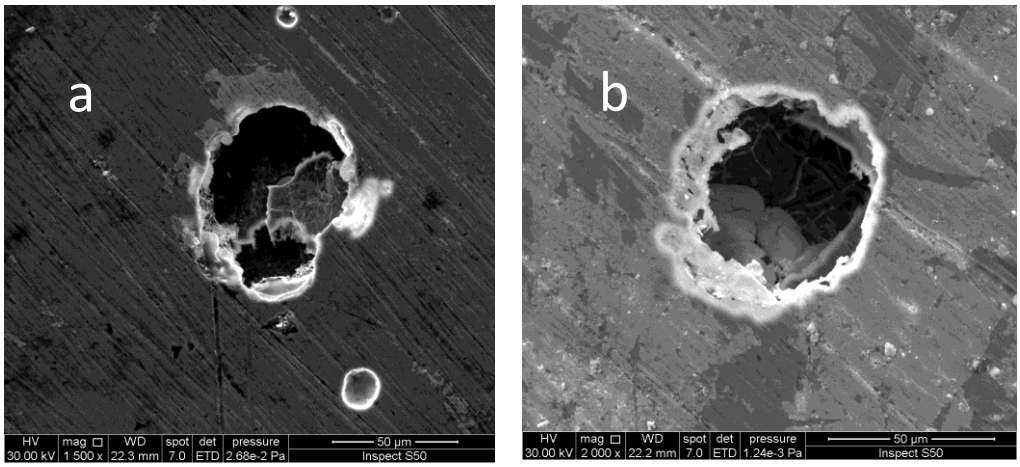

Figure 16. Halide pitting corrosion on 316 SS a for 3.5wt%NaCl while b in 3.5wt% NaBr solution at 50 µm magnification.

Investigating the Influence of the Cerium loading in prepared Y zeolite from Iraqi kaolin on its Catalytic Performance

Lecturer Karim Khalifa Esgair
Department of Chemical Industries
Al-Technology Institute.
Middle Technical University
karimkhalifa70@yahoo.com

ABSTRACT

In this study, the effects of different loading doses of cerium in the prepared NaY zeolite from Iraqi kaolin were investigated. Al-Duara refinery atmospheric residue fluid catalytic cracking was selected as palpation reaction for testing the catalytic activity of cerium loading NaY zeolite. The insertion of cerium in NaY zeolites has been synthesized by simple ion exchange methods. Three samples of modified zeolite Y have been obtained by replacing the sodium ions in the original sample with cerium and the weight percent added are 0.35, 0.64, and 1.06 respectively. The effects of cerium loading to zeolite Y in different weight percent on the cracking catalysts were studied by employing a laboratory fluidized bed reactor. The experiments have been performed with weight hourly space velocity (WHSV) range from 6 to 24 h^{-1}, and the temperature range from 450 to 510 ^{o}C.

The activity of the catalyst with 1.06 wt% cerium has been shown to be much greater than that of the sample parent NaY. Also it was observed that the addition of the cerium causes an increase in the thermal stability of the zeolite.

Key words: cerium exchange NaY, rare earth elements, fluid catalytic cracking.

دراسة تأثير تحميل السيريوم في زيوليت Y المحضر من الكاولين العراقي على أدائه التحفيزي

م.كريم خليفه ازغير
قسم الصناعات الكيمياوية
معهد التكنولوجيا/الجامعه التقنيه الوسطى

الخلاصة

في هذه الدراسه. تم بحث تأثير تحميل السيريوم في الزيولايت Y المحضر من الكاؤلين العراقي . تفاعل التكسير الحفازي المائع لمتبقي التقطير الجوي تم اختياره كمجس لاختبار الفعالية الحفازية للزيولايت المحسن والمحضر نوع NaY . الزيولايت المطور تم تصنيعه بطريقة التبادل الايوني البسيط .ثلاثة نماذج من الزيولايت المطورتم الحصول عليها عن طريق استبدال ايون الصوديوم في النموذج الاصلي بالسيريوم وبالنسب الوزنية المئويه التالية 0.35 , 0.64 ، 1.06 تأثير تحميل السيريوم للزيولايت وبنسب وزنية مختلفة على الفعالية التكسيرية تم بحثه باستخدام منظومه مختبريه تجريبيه لمفاعل الطبقة المميعة . التجارب المختبرية اجريت عند سرع وزنية فراغيه بين 6 الى 24ساعه$^{-1}$ وبدرجة حرارة من 450 الى 510 درجة مئوية.

الفعالية الحفازية للعامل المساعد المحتوي على نسبه وزنية من السيريوم بمقدار 1.06 كانت اكبر بكثير من الفعالية الحفازية للعامل المساعد الاصلي . وكذلك تم ملاحظة ان اضافة السيريوم ادت الى زيادة الثباتية الحرارية للزيولايت .

الكلمات الرئيسية: استبدال السيريوم بالزيولات NaY، عناصر الارض النادرة، التكسير الحفازي المائع.

1. INTRODUCTION

The atmospheric distillation residue oil is gained as a byproduct from the refineries through atmospheric distillation of crude oil to produce light hydrocarbon fraction **Jakob and Peter, 1977** . Approximately half of the crude oil leaving the behind atmospheric distillation is the atmospheric distillation residue. That it is a necessary to find a possible economic process to convert low value product such as residual distillation to high value products such as gasoline and middle distillate**, Pappal, et al., 2003, Gray, 1994..**

The important process in the refinery industry to convert heavy fraction low value product of the crude oil into an assortment of high value, light products is the fluid catalytic cracking (FCC).The operation conditions of this process are preferable achieved with a pressure 1 to 10 bar , weight hour space velocity (WHSV) from 3 to 200 h^{-1} ,and temperature from 400 to 550 ^{o}C, **Chen, and Cao, 2005.** Fluid catalytic cracking process produces a raw material for many petrochemical processes such as light olefins increasing the its importance, in addition to its main purpose of producing of diesel fuel and gasoline, **Biswas and Maxwell, 1990**

The FCC catalyst is a key point in the optimization of FCC unit. Basically , the FCC catalysts could be divided into three main categories based on the refineries objective i) maximization of valuble product ,ii) improving the gasoline quality and, iii)minimization of the residue.In order to achieve those goals ,the FCC catalyst has two components ,the zeolite and the matrix. Besides these components the catalyst can also have other functional ingredients and or /additives for specified function like enhancing gasoline octane , upgrading the conversion of residue feedstock ,enhancing the resistance to metallic poisons ,promoting the CO combustion ,reduction the NOx and SOx emission , among there, **Costa, et al., 2004**.

In the recent years the replacement of rare earth zeolite has become more interesting as stable solid acid catalyst due to the high thermal stability **Magee, et al., 2002.**Modifing zeolites Y by ion exchange of commutable cations provides a beneficial properties to particular application which become an integral portion of the manufacture process catalyst. The performance of cracking catalyst such as catalyst selectivity, hydrothermal stability, catalyst activity has been enhanced when rare earth element was introduced. The faujasite Y zcolites modified process can be achieved by replacing the native sodium ions with rare-earth ions. For example Ce NaY , LaNaY plays an significant part in the production of FCC catalysts, **Nery, et al., 1997 and Thomas, et al., 2006.**

The sodium ions in the zeolite crystal exchange with rare earth element, such as praseodymium , cerium and lanthanum being trivalent which make "bridges" among three or two acid sites in the framework of zeolite, these bridges stabilizes the structure of zeolite and protect acid sites from ejection. The hydrothermal and thermal and activities of zeolite increases with exchange rare earth components due to the "bridge" stabilizes and prevents aluminum atoms from dissociation from the zeolite structure whenever the catalyst exposure to high temperature in the reactor and regenerator. The rare earth element is generally ion exchange with NaY zeolite , **Sadeghbeigi, 2000**.

The aim of present study is to modify the zeolite Na Y prepared from Iraqi kaolin with various weight percents cerium exchange. Also the activity of the resulting catalyst were evaluated by employing a laboratory fluidized bed reactor by using atmospheric distillation residue as a feed , and the influence of the addition of cerium on the thermal stability of the NaY was investigated.

2. EXPERIMENTAL

2.1 Feedstock

Atmospheric residue with boiling range 278^{o}C to 450^{o}C was supplied from atmospheric distillation unit of Al-Duara refinery as a raw material for the catalytic performance of the zeolites synthesized, and its detailed properties are listed in **Table 1**.

2.2 Catalyst

Parent NaY zeolite were prepared from Iraqi kaolin as follows: Kaolin was finely divided to powder and mixed with sodium hydroxide solution was prepared at concentration 45% wt with weight ratio $\left(\frac{Kaolin}{pureNaOH} = \frac{1}{1.5}\right)$. The mixture fused at 850˚C by programmable electrical furnace, then ten grams of powder resulting mixed with twelve point sixty seven gram of sodium silicate and disseminate in one hundred and fifty milliliter of deionizesd water with stirring for one hour. The resultant slurry which has pH 13.6 was subjected to aging at 50 ^{o}C for 24 hr in a programmable electrical furnace, then the gel slurry was subjected to hydrothermal crystallization at 100 ^{o}C for 48 hr in the same furnace. After that the slurry was filtrated to separate the precipitate from mother liquid. The crystalline precipitate washed with deionized water to reduce a pH to 11.5. After that the slurry was filtrated to separate the precipitate from mother liquid. The precipitate subjected to dry at one hundred centigrade for sixteen hours. The dried powder was activated by calcinations in a programmable electrical furnace at five hundred centigrade for one hour. **Htay and Oo, 2008**

2.3 Modified Zeolite Procedure.

Cerium exchanged was obtained by contacting Na-Y with 0.5M cerium nitrate solution (0.025 moles of cerium nitrate / g of zeolite) at 80 ^{o}C for 24 hours ,then filtrate, and was washed to obtained 0. 35 wt% Ce Na-Y . This exchange cycle was repeated two times with fresh cerium nitrate to obtain 0.64 wt% CeNa-Y. Na-Y was mixed with fresh 0.5M cerium nitrate solution four times to obtained 1.06 wt% Ce Na-Y. All samples were calcined after each exchange at a temperature of 150 to 500 ^{o}C with heating rate 12 ^{o}C /minute and at 500 ^{o}C for 5 hours **Thomas, et al., 2006**. The degree of cerium exchange in the zeolite was determined by the analysis of each zeolite sample to determine the sodium weight percent in the starting and those remaining after the cerium exchange. The sodium weight percent loss converted to equivalent cerium

2.4 Catalytic activity test

Catalytic Cracking experiments achieved by employing a laboratory fluidized bed reactor, , shown in **Fig. 1**. This unit was found in the laboratories of Chemical Engineering Department, Baghdad University, it includes four parts: water and atmospheric residue pumping system, catalytic cracking reaction, control of temperature system, and separation and collection system.

Water pumped preheater at specified flow rate; the water was converted to steam by heating system. Steam was used to remove the air from reactor. After that atmospheric residue was pumped to a pre-heater to increase temperature before reaching catalytic reactor

which reactions was occurred. The products from reactor cooled, and then separated to gas and liquid products. Cracking liquid product was transferred to distillation unit for separation catalytic cracking gasoline from heavy stock. The chemical composition of the gases and catalytic cracking gasoline was determined by using gas chromatography.

Coke content on catalysts was measured by the following method. A sample of catalyst from reactor was weighed and dried by electrical programmable furnace at 100 ^{o}C for 16 hr. The dry sample was weighed and returned to electrical programmable furnace to restore catalyst activity by burning off coke deposition on spent catalyst at 650 ^{o}C for one hour. The **c**alcined sample after burring coke was weighed. The differences between weight 1 and weight 2 represents moisture and difference between weight 2 and weight 3 represents delta coke. Delta coke is defined as the difference between coke on the spent catalyst after stripping and on the regenerated catalyst. The catalyst activity was determined by the weight percent of feedstock was converted to products ,the products included gas ,gasoline ,and coke. The part of liquid product which has a boiling point between ambient temperatures and 220 ^{o}C was represented a gasoline.

2.5 Operating Conditions

The experiments of catalytic cracking of atmospheric residue were achieved on parent NaY zeolite and modified zeolite catalysts sampled in the laboratory fluidized bed reactor system. Operating conditions were catalyst weight hourly space velocity was 6 , 12 ,18,and 24 h $^{-1}$, reaction temperature was 450 ,470,490,and 510 ^{o}C. The effect of regeneration number (it refers to restoring catalyst activity after each complete reaction) on the catalyst activity of the parent NaY zeolite and modified zeolite(1.06wt%) was carried out at 510 ^{o}C, WHSV= 6 h^{-1}, and atmospheric pressure.

2.6 Analytical Apparatus

The digital flame analyzer by flame photometer Gallen Kamp in The State Company for Geological Survey and Mining was used to determine the sodium content the parent catalyst and modified catalyst after cerium ion exchange.

The gas chromatograph Agilent Technologies 6890N equipped with flame ionization detector (FID) was used to determine the composition of the gases produced from experiment. The volume data converted to mass data by using equation of state for ideal gases.

The composition of cracked gasoline measured by using simulated distillation gas-chromatography Agilent Technologies 6890N .

Chemical analysis according UOP Method 172- 59 was used to measure the concentration of the hydrogen sulfide.

Gas Chromatograph 373 GASUKURD KDGYO was used to determined the concentration hydrogen gas in the gases mixture produced. All above device was located in Al- Duara Refinery.

3. RESULT & DISCUSSION

3.1 The Effect of Cerium Exchange on the Atmospheric Residue Conversion.

The effects of cerium exchange and WHSV on the atmospheric residue conversion were studied at different reaction temperatures. **Fig. 2** and **Table 2** show the dependence of conversion upon cerium weight percent loading and catalyst hour space velocity when catalytic cracking was over zeolite catalysts containing different weight percent cerium.

At a given catalyst hour space velocity with constant temperature, the zeolite catalysts containing more cerium weight percent loading show greater conversion of atmospheric residue and gives more products (gasoline , gases, and coke) in comparsion with the parent Na-Y zeolite (fig .2 and table 2).This means that the cerium indeed contribute to the conversion, which may be explained as following :the sodium ion reduced the acidity of zeolite then reduced the activity of zeolite due to that the residual sodium ion has poisoning effect on the acidity especially Bronsted type of faujasite zeolites .Low acid amount of Na-Y zeolite might reduce catalyst activity, which is the crucial step in the formation of the desired product.

The total acid amount increased after introducing rare elements (RE) to zeolite sample. There were two possible reasons for the result. Firstly, the hydrothermal stability had been strengthened on account of the addition of the rare elements (RE) cation, which coordinated with the oxygen atoms in the pore channel. Therefore, the dealumination of the framework was restrained during the hydrothermal disposal. So the loss of acidic amounts would reduce. Secondly, silicon hydroxyl and aluminum hydroxyl in the zeolite framework were polarized due to the insertion of the RE cation. Consequently the electron density increases in the framework of zeolite, appeared vigorous acidity of the acidic center. And because of the existence of an empty f orbit RE^{3+}**,** the amount of Lewis acid would also increase, **Xiaoning, et al., 2007**. The zeolite activity comes from these acid sites, **Hayward, and Winkler, 1990**. From the above the increasing cerium exchanged decreases Na^{+} ion in the zeolites and gives more conversion of atmospheric distillation residue.

3.2 The Effect of WHSV on the Atmospheric Residue Conversion.

At a constant temperature with a given cerium weight percent loading **Fig. 3** and **table 2** shows that the atmospheric residue conversion increases with decreasing of WHSV. This means that the conversion of reduced crude is a function of reaction time for all catalysts, when the contact time between particle of catalyst and the feed molecules increases the atmospheric residue conversion increasing in direct proportion to the amount of the catalyst and inversely proportional to the feed flow rate. These results are a good agreement with those obtained by **Ancheyta** and **Sotelo, 2002, Wallenstein, et al., 2002** about the effect of WHSV on the atmospheric distillation residue conversion, gasoline, gases, and delta coke yield.

3.3 The Effect of Temperature on the Atmospheric Residue Conversion.

At a given catalyst hour space velocity with constant cerium weight percent loading **Fig. 2** and **Table 2** show that the atmospheric residue conversion increases with increasing the temperature. This may be imputed to the intermolecular motions accelerated with the increasing of temperature contributing to the conversion of the reactants to new products and consequently increases the chemical reaction rate. Also the increasing of temperature accelerates thermal activation which conjuncts with catalytic activation to increase the conversion of atmospheric residue**.** The feed molecules a better vaporized at the higher temperature that decreased the coke formation from condensation reactions which occurred when poor feed molecules vaporization at low temperature. The diffusion of feed molecules increased at coke decreasing and high temperature which consequently increases the feed conversion as mentioned by **Decroocq, 1984**. These results are a good agreement with those obtained by **Lan, et al., 2009** about the effect of temperature on the atmospheric distillation residue conversion, gasoline, gases, and delta coke yield.

3.4 The Effect of Cerium Exchange on the Gasoline Yield.

Fig. 4 and **Table 2** show that the gasoline produced from the different catalysts when cracking atmospheric residue depends on the conversion, when the catalysts contain more cerium weight percent loading it gives a higher gasoline yield .Also increasing temperatures and decreasing weight hours space velocity shows more gasoline yield obtained. **Table 3** shows chemical composition of cracked gasoline for parent NaY and 1.02 CeNa. This table shows that olefins and naphthenes decrease while paraffins and aromatics increases for 1.06 CeNaY with respect to the parent NaY,due to the hydrogen transfer reactions increases with increasing cerium weight percent loading, In this reaction two molecules reacted (bimolecular reaction) one of them is olefin and the another either naphthenes or also olefin . In case of both molecules reacted being olefin, the reaction is chain reaction and ultimately converts olefins molecules to paraffin's and aromatics molecules. In the reacted olefins molecules with naphthenes molecules, this reaction produces aromatics and paraffin's.

In comparing **Fig. 2 and 4** for the catalyst 1.06 CeNaYat 6 WHSV the reduced crude conversion increases with increasing of temperature at constant WHSV within the limit of study, while, the gasoline yield increases with conversion, with a tendency to reach a maximum (at 490 ^{o}C) and after that the gasoline yield remain approximately constant. This is due to the fact that gasoline yield undergoes the secondary cracking (over cracking) to gaseous products and coke.

From **Table 2** the gases yields and coke yield are dependent on conversion when catalytic cracking of atmospheric residue over different catalysts. This table shows that the coke yields and the gases yield as function of the cerium weight percent loading, temperatures and weight hours space velocity. The composition of the gas produced at a conversion of 82.3 wt %(as a sample), is shown in **Table 4**. The above result agreement with the results obtained by **Al-Khattaf, 2002, Ancheyta** and **Sotelo, 2002** about the relation between WHSV and gasoline yield with occur the phenomenon of secondary cracking (over cracking) of gasoline to gaseous products and coke

3.5 The Effect of Cerium Exchange on the Thermal Stability.

Fig. 5 shows the relation between the conversion of atmospheric residue and the number of regeneration for NaY and 1.06CeNaY catalysts. From this figure the difference in the activity between NaY and 1.06 CeNaY for zero regeneration (fresh catalysts) was about 15 wt%. For first regeneration it was about 37wt%, while for second regeneration it was about 43wt%. This means that the catalyst 1.06 CeNaY decreases the activity less than the catalyst NaY due to the fact that the sodium ion reduces the zeolite hydrothermal stability and reacts with acid sites of zeolite to decrease the activity of catalyst, **Suchuchchai, 2004**. In the regenerator the temperature increases which causes the mobility of sodium and it's neutralizes the stronger acid sites**, Scherzer, 1990** , while the cerium is insensitive to the temperature increase, its immobile component**, Lottermoser, 1992.**

To explain this positive effect of the RE elements on zeolites thermal stability, two aspects may be considered: (i) cation valence, and (ii) formation of RE–O–RE bonds in zeolite cavities. the divalent cations have a more stabilizing influence than monovalent cations, the exchanged trivalent cations with zeolites gives the more stable ones. Moreover, the enhancement on thermal stability has also been attributed to the existence of RE–O–RE bonds in the interior of sodalite cavities, which form bridges with the zeolite tetrahedra, stabilizing the structure, **Trigueiro, et al., 2002.**

4. CONCLUSION

1- The Na–Y modified with cerium increased cracking activity, which show an increasing the gasoline, gas ,and coke yields with increasing cerium weight percent.
2-The secondary cracking of gasoline to gaseous products and coke occur at 6 WHSV and 490^{o}C
3- Cerium substituted zeolite show far best stability toward reaction they lost 12.1 % of the initial activity in 1.06CeNaY whereas, NaY lost 33.6% activity with same condition (6WHSV,510^{o}C) for first regeneration and 21.2 % to 1.06 CeNaY, 50.2% to NaY respectively for second regeneration .

5. REFRENCES

- Al-Khattaf ,S., 2002 *The influence of Y zeolite unit cell size on the performance of FCC catalysts during gas oil catalytic cracking* , Applied Catalysis A: General.231 ,pp. 293– 306.
- Ancheyta , J.,and Sotelo, R., 2002 ,*kinetic modeling of vacuum gas oil catalytic cracking* ,J .Mexican,chem.society Vol.46,PP.38-42.
- Bartholomew, C.H., Oballa, M.C., and Shih ,S.S., 1994. *Catalytic hydroporcessing of petroleum and distillates*. New York: Marcel Dekker.
- Biswas, J.. Maxwell, J.E,1990 ,*Recent process and catalyst-related development in FCC*, Appl. Catal.Vol 63,pp. 197–258
- Chen, J.W., and Cao, H.C., 2005,*Catalytic Cracking Process and Engineering*, China Petrochemical Press,pp. 126.
- Costa.A.F.,Cerqueira.H.S.,Sousa.E.F.,and Ludvig ,W.2004,*Performance of FCC Catalyst Prepared with Sub –Micron Y Zeolite " Studies in Surface Science and Catalysis*, (Vol. 154), Eds. E. van,Steen., L.H. Callanan .,and M.Claeys. Elsevier Science B.V., Amsterdam. pp 2296.
- Decroocq , D., 1984"*Catalytic Cracking of Heavy Petroleum Fractions*", Imprimerir Louis-Jean, Paris,(1984).
- Gray ,M.R., 1994 ,*Upgrading petroleum residues and heavy oils*,. New York: Marcel Dekker.
- Hayward, C. M., and Winkler, W. S. 1990,*FCC: Matrix/Zeolite*, Hydrocarbon Processing, February pp. 55-56
- Htay, M. M., and Oo, M. M., 2008 "*Preparation of Zeolite Y Catalyst for Petroleum Cracking*", Pwaset Vol. 36 ISSN 2070-3740,pp. 859 – 865.
- Jakob , V. K., and Peter, L ,1977, *Process for hydrocarbon conversion* , U.S.patent 4039429

- Lan, X., Xu, C., Wang, G., and Gao, J.,2009 " Reaction performance of FCC slurry catalytic cracking " Catalysis Today Vol.140,iss 3-4 ,pp174-179.
- Lottermoser, B.G,1992, *Rare earth elements and hydrothermal ore formation processes*, Ore Geology Reviews, Vol,7,PP 25-41.
- Magee, J.S., Balzek, J.J., and Rabo J.A., 2002, Zeolite Chemistry and Catalysis, American Chemical Society, Washington, DC, pp.615
- Nery. J. G., Mascarenhas. Y. P.,. Bonagamba . T. J., and Mello. N. C., 1997, Location *of cerium and lanthanum cations in CeNaY and LaNaY after calcinations* , Zeolites Vol,18, pp.44-49.
- Pappal, D.A., Plantenga, F.L., Tracy, W.J., Bradway, R .A., Chitnis, G., and ,Lewis, W.E., 2003 ,*Stellar improvement in hydro processing catalyst activity*,NPRA, Annual Meeting March 23–25, San Antonio (TX).
- Sadeghbeigi, R., 2000,*Fluid catalytic cracking handbook*, Gulf publishing company, pp. 40–48.
- Scherzer. J. ., 1990, *Octane-enhancing, zeolite FCC catalysts*, Marcel Dekker, N.Y.
- Suchuchchai, N. 2004, *Effects of Particle Size and Hydrothermal Treatment of Y-zeolite on Catalytic Cracking of n-Octane*, M.Sc. , University of Chulalongkorn.
- Thomas, B., Bibhuti, B. ,and Sugunan S,2006, *Rare earth exchanged (Ce3+, La3+ and RE3+) H–Y zeolites as solid acid catalysts for the synthesis of linear alkyl benzene*s, Microporous and Mesoporous MaterialsVol. 95,pp 329–338.
- Trigueiro, F.E., Monteiro, D.F.J., Zotin F.M.Z.,and Falabella , E., 2002 ,*Thermal stability of Y zeolites containing different rare earth cations* ,Journal of Alloys and Compounds,Vol. 344, pp 337–341.
- Wallenstein, D., Seese, M., Zhaob, X., 2002 " A novel selectivity test for the evaluation of FCC catalysts" Applied Catalysis A: General .231 ,pp.227–242.
- Xiaoning, W., Zhen, Z ., Li, Z., Guiyuan, Chunming ,J**,** Aijun, D., 2007,*Effects of Light Rare Earth on Acidity and Catalytic Performance of HZSM-5 Zeolite for Catalytic Cracking of Butane to Light Olefins*, Journal of Rare Earths ,Vol,25 ,pp321 –328.

Table 1. Atmospheric residue Properties.

Density (20 ^{o}C ,gm / cm^{3})	0.908
Molecular weight	486
Carbon residue(wt%)	4.67
ASTM distillation (^{o}C)	
IBP	278
10%	291
30%	352
50%	396
70%	417
90%	450

Table 3. A comparison between the chemical compositions of cracked gasoline at 6 WHSV and 490 ^{o}C.

Chemical Composition of cracked gasoline(vol. %)	NaY (C_5-220^{o}C)	1.02 CeNaY (C_5-220^{o}C)
Paraffins	19.4	27.8
Naphthenes	5.7	3.2
Olefins	40.1	32.3
Aromatics	34.8	36.9

Table 4. Chemical analysis of gases at 6 WHSV and 510^{o}C.

Gases	Yield(wt%)from the total product
Hydrogen	0.5375
Hydrogen sulfide	0.7485
Methane	2.4820
Ethane	2.8345
Ethylene	2.0677
Propane	4.3310
Propylene	3.4025
Iso Butane	2.5930
N. Butene	3.4835
N.Butane	3.2690
Iso Pentane	0.4813
N. Pentane	0.1695

Table 2. Cracking experiments results of the atmospheric residue at different cerium weight percent loading.

Catalyst type	Reaction temperature	WHSV (h^{-1})	Conversion	Gasoline(wt%)	Gases(wt%)	Coke(wt%)	Heavy oil(wt%)
NaY	510	24	46.2	20.1	16.0	10.1	53.8
	490		43.8	19.3	15.0	9.5	56.2
	470		42.3	19.1	14	9.2	57.7
	450		41.4	18.3	14.2	8.9	58.6
	510	18	53.7	23.5	18.1	12.1	43.3
	490		52.4	23.1	17.3	12	44.6
	470		50.8	22.2	17.1	11.4	46.2
	450		48.6	21.4	16..2	11	47.4
	510	12	61.9	29.2	18.7	14.1	38.1
	490		59.8	28.4	18.1	13.5	39.2
	470		58.4	28.1	17.9	12.4	41.6

	450		55.9	27.1	17.3	11.5	44.1
	510	6	70.2	33.2	21	16	29,8
	490		68.7	32.4	20.1	15.2	31.3
	470		65.1	31.0	19.1	15	33.9
	450		63.2	30.0	19	14.2	36.8
0.35Ce NaY	510	24	50	24.9	15.1	10	50
	490		47.2	24.1	14	9.1	51.8
	470		45.7	23.0	13.3	8.4	54.3
	450		43.3	22.0	13.1	8.2	56.7
	510	18	57.1	28.2	16.9	13	42.9
	490		55.8	27.8	16.5	12.5	44.2
	470		54.1	26.9	16.2	11	45.9
	450		51.6	26.2	15.3	11.1	48.4
	510	12	64.9	31.2	19.9	13.8	35.1
	490		63.1	30.3	19.1	13.7	36.9
	470		60.8	29.1	18.5	13.2	39.2
	450		59.2	28.3	17.9	13.0	40.8
	510	6	74.1	34.9	23.1	16.1	25.9
	490		71.9	33.8	22.3	15.8	28.1
	470		70.2	33.0	21.9	15.3	29.8
	450		67.5	32.8	20.7	14.0	32.5
0.64Ce NaY	510	24	54.3	24.2	18.0	11.1	45.7
	490		50.5	23.0	17.3	10.2	49.5
	470		48.1	22.2	16.4	9.5	51.9
	450		46.4	21.6	15.7	9.1	53.6
	510	18	60.8	27.5	20.1	13.2	39.2
	490		59.5	27.1	19.6	12.8	40.5
	470		57.3	26.2	19.0	12.1	42.7
	450		55.6	25.7	18.4	11.5	54.4
	510	12	68.7	31.2	22.4	15.1	31.3
	490		66.4	30.1	21.5	14.8	33.6
	470		64.6	29.4	21.0	14.2	35.4
	450		61.1	28.2	20.3	13.6	37.9
	510	6	77.6	36.2	24.0	17.4	22.4
	490		75.8	35.4	23.5	16.9	24.2
	470		73.9	34.6	23.1	16.2	26.1
	450		70.5	32.4	22.2	15.9	29.5
1.06Ce NaY	510	24	58.8	29.1	18.4	11.3	41.2
	490		55.2	27..2	17.1	10.9	44.8
	470		53.6	26.7	16.5	10.4	46.4
	450		51.6	25.8	16.1	9.7	48.4
	510	18	65.8	32.3	20.4	13.1	34.2
	490		63.5	31.2	20.0	12.3	36.5
	470		61.7	30.4	19.5	11.8	38.3
	450		60.1	30.0	18.8	11.3	39.9
	510	12	73..4	35.3	23.0	15.1	26.6
	490		70.6	34.2	22..4	14.0	29.4
	470		68.9	33.3	21.9	13.7	31.1

	450		66.0	31.8	21.1	13.1	33.7
	510	6	82.3	37.1	26.4	18.8	17.7
	490		80.6	37.2	25.6	17.9	19.4
	470		77.8	36.5	24.1	17.3	22.2
	450		75.5	35.1	23.2	16.2	24.5

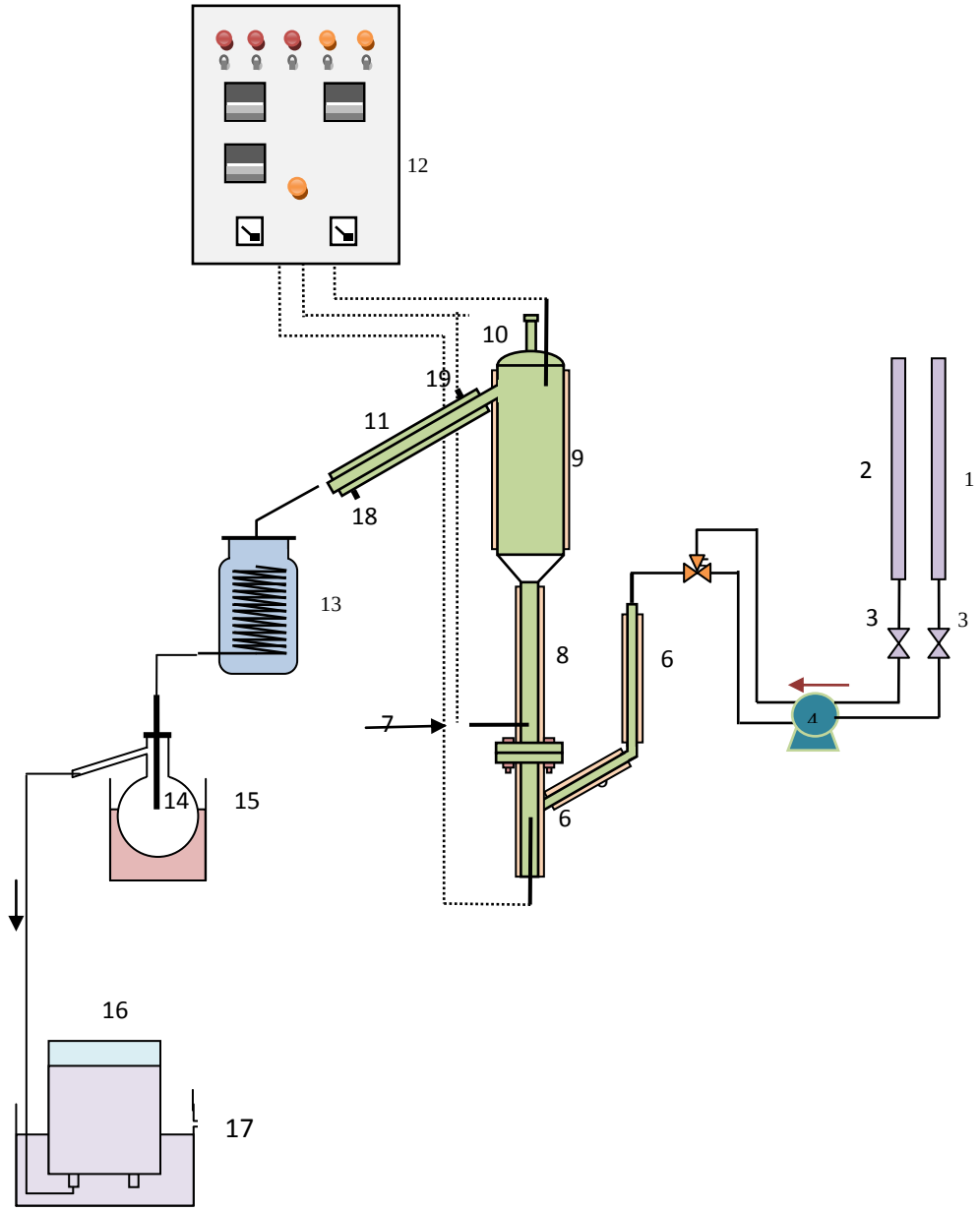

Figure 1. Schematic flow diagram of the fluidized catalytic cracking system:

(1) Burette atmospheric residue supplying; (2) Burette water supplying; (3) Valve; (4) Feeding pump; (5) Three way valve; (6) Preheated part ; (7)Distributor (8)Fluidized bed reactor part; (9)Reactor separation part; (10) Catalyst charge inlet; (11) Double pipe heat exchanger; (12) Control panel; (13) Internal tube ice water bath; (14) Collection and

separation flask; (15) Ice water bath ; (16) Collection of gas ; (17) Water tank; (18) Chilled water in; (19) Chilled water out.

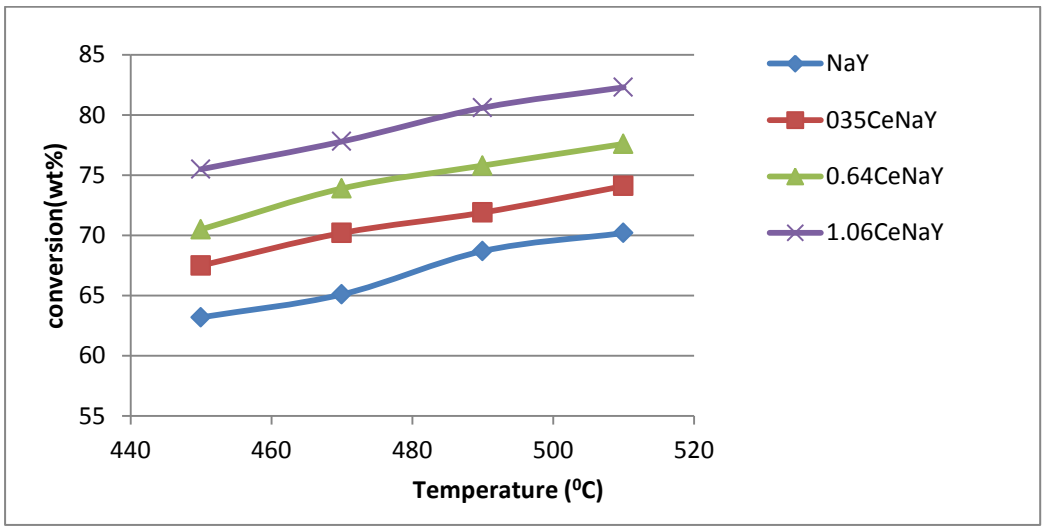

Figure. 2 Effect of cerium weight percent loading on the atmospheric residue conversion at different temperatures and 6 WHSV.

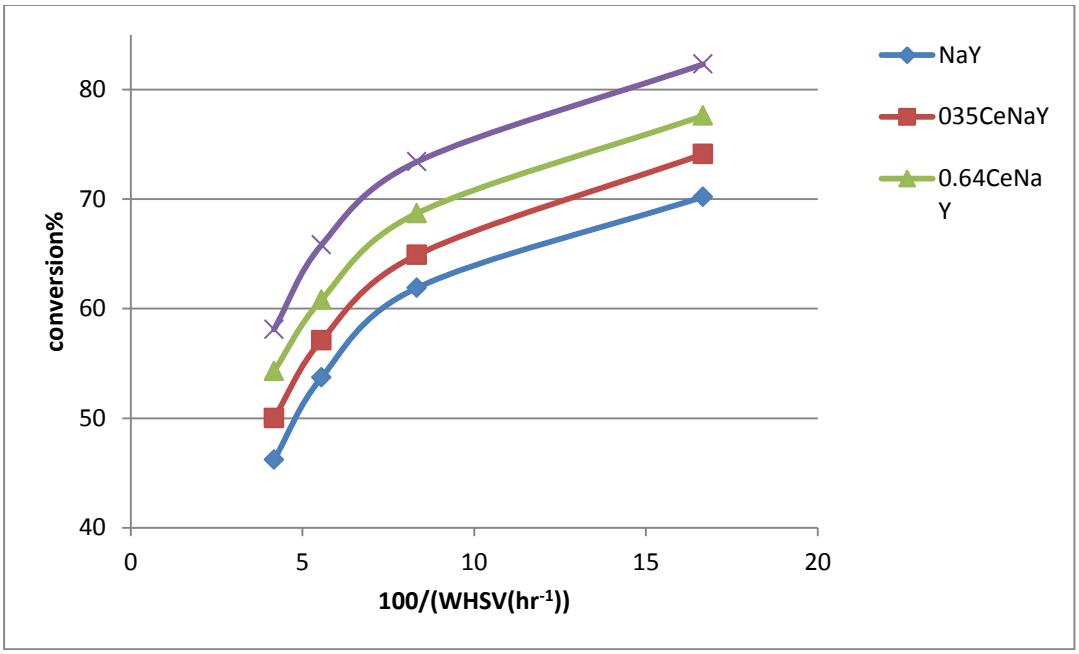

Figure.3 Effect of cerium weight percent loading on the atmospheric residue conversion at different WHSVand temperatures 510°C.

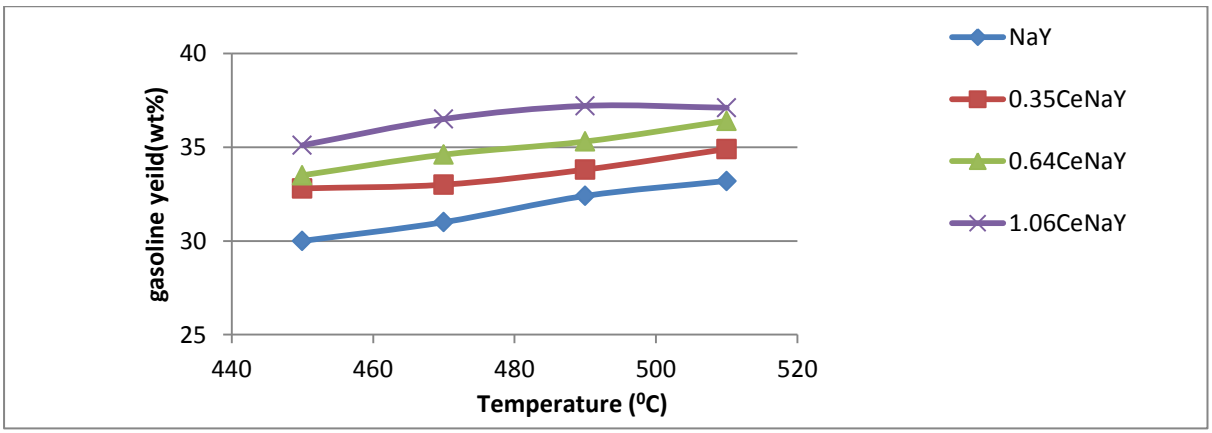

Figure.4 Effect of cerium weight percent loading on the yield of gasoline at different temperatures and 6 WHSV.

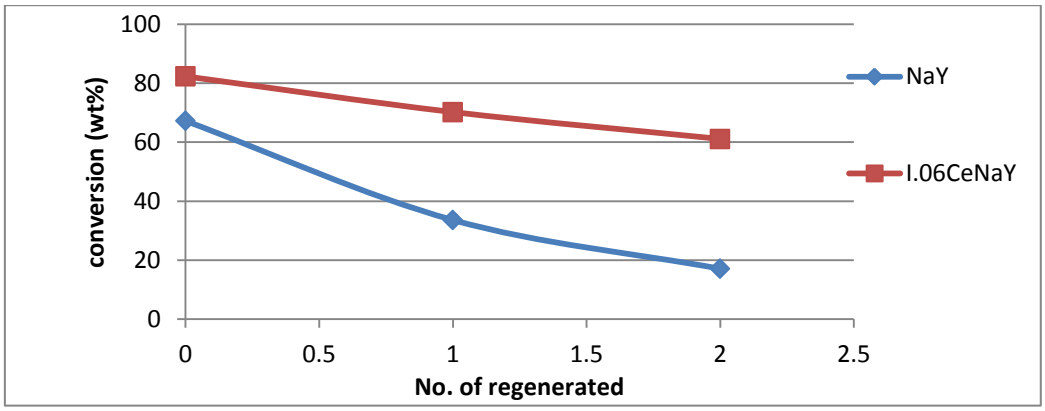

Figure.5 Relation between the conversion and the number of regeneration for NaY and 1.06 CeNaY catalysts.

Performance Evaluation of RIPng, EIGRPv6 and OSPFv3 for Real Time Applications

Sama Salam Samaan
Assistant Lecturer
Computer Engineering Department - University of Technology
samasamaan@yahoo.com

ABSTRACT

In this modern Internet era and the transition to IPv6, routing protocols must adjust to assist this transformation. RIPng, EIGRPv6 and OSPFv3 are the dominant IPv6 IGRP (Interior Gateway Routing Protocols). Selecting the best routing protocol among the available is a critical task, which depends upon the network requirement and performance parameters of different real time applications. The primary motivation of this paper is to estimate the performance of these protocols in real time applications. The evaluation is based on a number of criteria including: network convergence duration, Http Page Response Time, DB Query Response Time, IPv6 traffic dropped, video packet delay variation and video packet end to end delay. After examining the simulation results, a conclusion will be extracted to reveal the findings of which protocol performs the best upon implementation within a IPv6 WAN. OPNET modeler simulator is used to evaluate the accomplishment of these protocols. To get the results, three scenarios are designed, one for each protocol.

Key words: RIPng, EIGRPv6, OSPFv3, routing protocols, OPNET, performance evaluation, IPv6, real time applications

تقييم اداء مجموعة من بروتوكولات التوجيه في تطبيقات الزمن الحقيقي

سما سلام سمعان
مدرس مساعد
قسم هندسة الحاسوب – الجامعة التكنولوجية

الخلاصة

في عصر الإنترنت الحديث والانتقال من IPv4 نحو IPv6، توجب على بروتوكولات التوجيه التي تستخدم لإعادة توجيه البيانات ونقلها من المرسل الى المستلم عبر الشبكة التكيف والتطور لدعم هذا التحول. RIPng، EIGRPv6، ISIS وOSPFv3 هي البروتوكولات الاكثر شيوعاً واستخداما في الشبكات الداخلية. اختيار أفضل بروتوكول بين ما تقدم يعتبر مهمة حاسمة، والتي تعتمد على متطلبات وأداء الشبكة والتطبيقات المطلوبة منها. ان الهدف الرئيسي من هذا العمل المقدم هو تقييم أداء هذه البروتوكولات في ضوء مجموعة من التطبيقات العملية كالفيديو والصوت وقواعد البيانات وصفحات الويب. ويستند هذا التقييم على عدد من المعايير منها: مدة شبكة التقارب، زمن الاستجابة، كم البيانات المفقودة، وتباين وقت وصول بيانات الفيديو والصوت. سيتم دراسة اي من هذه البروتوكولات الثلاثة هو الافضل حسب كل معيار من المعايير المستخدمة لغرض المقارنة.

الكلمات المفتاحية: بروتوكولات التوجيه، تقييم الاداء، تطبيقات الزمن الحقيقي.

1. INTRODUCTION

Routing is choosing the best path from a source to a specific destination. It can be done dynamically using routing protocols that are stand on different routing algorithms. Routing protocols are broadly classifieds as Exterior Gateway Routing Protocols (EGRP) and Interior Gateway Routing Protocols (IGRP), **Odom, 2013.** BGP is an example of EGRPs. IGRP are classified as distance vector, link state and hybrid routing protocol. Most popular IGRPs are RIP, EIGRP, ISIS and OSPF. Elements that distinguish various routing protocols are convergence which means rapidity to adapt to network changes, their ability to choose the optimal route among different paths and the amount of routing traffic produced, **Sankar and Lancaster, 2010.** For the success of a network, routing protocols play a decisive role. Most of the routing protocols developed in IPv4 had been altered to be used for IPv6 addresses with its different header architecture. IPv6 routing protocols have some similarities in functions and configurations to their IPv4 equivalents, but since an IPv6 is longer than an IPv4, routing updates have to carry more information, **Kaur and Singh, 2014**. In this work, three IPv6 routing protocols, RIPng (distance vector routing protocol), EIGRP (hybrid routing protocol), OSPF (link state routing protocol) are analyzed on the basis of convergence time, packet drop, HTTP page response time, DB query response time, video packet end to end delay, video packet delay variation, jitter, voice packet end to end delay and voice packet delay variation. The scheme of this paper is as follows:

- Design the network topology
- Implement the routing protocols
- Setting up performance metrics
- Analysis of simulation results
- Comparison of results.

2. RELATED WORKS

In order to provide an overview of previous work, some researches presented by various authors are reviewed. **Hinds, et al., 2013,** compared two routing protocols; OSPF and EIGRP. The two protocols have been compared according to a number of criteria, including hardware resilience, routing metrics range, fast convergence when topology changes, throughput, scalability, lower routing overhead, difficulty in configuration and routing protocol security. The analysis showed that EIGRP protocol is better than OSPF. **Narula and Aggarwal, 2014,** evaluated the performance of RIP and OSPF for IPv6 using OPNET. Criteria to compare include packet delay variation, end to end delay, response time, jitter, page response time, object response time, traffic dropped for IPv6 Etc. They realized that the combined employment of OSPFv3 and RIPng performs better than RIPng and OSPFv3 when employed separately. **Whitfield and Zhu, 2015,** introduced each routing protocol security techniques and made a comparison of EIGRPv6 and OSPFv3. The principle conclusion was that EIGRPv6 exceeds OSPFv3 relating to start-up and re-convergence speed and is therefore the faster protocol. However, OSPFv3 is an attractive choice to use as a routing protocol since it combines a powerful security technique and runs in a hierarchical topology. **Sirika and Mahajine, 2016,** studied RIP, EIGRP and OSPF and compared their work in a number of applications including VoIP, Video conferencing based on convergence, end to end packet delay, packet delay variation and queuing delay which are considered as real-time applications. They found

that even OSPF is complex to configure, it is considered a common protocol as it is an open standard with rapid convergence.

3. ROUTING PROTOCOLS OVERVIEW

3.1 RIPng

The Routing Information Protocol next generation (RIPng) is heavily built on IPv4 RIPv2. In fact, RIPng is the updated version RIPv2 with small changes desired to allow it to advertise IPv6 paths. Both RIPv2 and RIPng updates are sent at systematic intervals (30 seconds). A metric of 16 hop is still considered infinite. Since IPv6 addresses are longer than its IPv4 counterparts, the RIPng packet format did need change. Few changes have been done **Narula and Aggarwal, 2014:**

- RIPng uses UDP port 521while RIPv2 uses port number 520. The RIPng destination multicast address is FF02::9, while it is 224.0.0.9 in RIPv2.
- With every route entry in RIPv2 packet, there is a next hop field carried. While in RIPng, a particular entry is used to define a next-hop address.
- In RIPng, authentication is not a part of it. It is done by IPv6 IPsec in addition to encryption.
- In RIPng packets, no route tag information is carried.

3.2 OSPFv3

The Open Shortest Path First (OSPFv3) is considered a link state routing protocol which takes its routing decisions according to the links' states that connect source and destination nodes. A link-state protocol uses the Shortest Path First (SPF) algorithm. OSPFv3 is designed to work in IPv6 environment **Whitfield and Zhu, 2015.** OSPFv3 acts very much like OSPFv2 which had been designed to work in IPv4 environment. For example, both use link-state logic and both use the same metric. The biggest differences between OSPFv3 and the older OSPFv2 lay with internals and with configuration. OSPFv3 changes the structure of some OSPF LSAs (Link State Advertisements). OSPFv3 uses a more direct approach to configuration, enabling OSPFv3 on each interface using an interface subcommand, **Odom, 2013.**

3.3 EIGRPv6

The Enhanced Interior Gateway Routing Protocol (EIGRPv6) is considered a hybrid protocol because it has link state protocol properties, **Iqbal and Khan, 2015.** EIGRP runs by taking routing decisions according to a group of cost metrics associated with router interfaces, which are computed using the Diffusing Update Algorithm (DUAL) to determine the best route to a destination. This algorithm is considered faster than algorithms used by other routing protocols like the Distributed Bellman-Ford, while creating less CPU overhead than link state counterparts. Tor each link connected to the router, the metrics are bandwidth, load, reliability, delay and Maximum Transmission Unit (MTU), **Hinds, et al., 2013**. EIGRPv6 which is designed to operate in IPv6 environment behaves much like its EIGRPv4 IPv4 counterpart. Many similarities exist between EIGRPv6 and EIGRPv4 except for a few differences, **Odom, 2013:**

• EIGRPv6 announces IPv6 prefixes, whereas EIGRPv4 announces IPv4 subnets.

• EIGRPv6 routers may become neighbors if they have IPv6 addresses in different subnets, while in EIGRPv4, neighbors must be in the same IPv4 subnet.

• Unlike EIGRPv4, EIGRPv6 does not have an auto summary.

4. STATISTICS DEFINITIONS

1. DB Query response time: it is the time proceeded between sending a request and receiving the response.
2. HTTP Page response time: it is the time needed to restore the complete page with all its objects. In the proposed network, Heavy HTTP application is used by the users.
3. Traffic dropped: the packets are dropped when a router or switch is incapable to receive incoming packets at a specified time.
4. Network convergence duration: within the entire network, the duration of convergence cycles for the routing tables is kept.
5. Packet delay variation in video conferencing: for video packets, it means difference among end to end delays. This type of delay is evaluated from the time it is created to the time it is received.
6. Packet End-to-End delay in video conferencing: it is measured when the packets transmitted from source to destination. When packets take long time to reach destination, it causes delays in the overall process and it has a serious impact on the network performance, **Kaur and Singh, 2014.**
7. Packet delay variation in voice: for voice packets, it is the difference among end to end delays.
8. Packet End-to-End delay in voice: The complete voice packet delay equals to network delay + encoding delay + decoding delay + compression delay + decompression delay + dejitter buffer delay.
9. Jitter: in voice, jitter is the difference in delay times of received packets. This factor should be as small as possible, **Narula and Aggarwal, 2014.**

5. NETWORK TOPOLOGY

The interrelation of network devices is characterized by network topology. **Sethi and Hnatyshin, 2013**, distinguishes between physical and logical network topologies. Physical topology is the actual model of the nodes and the links connecting them, taking considerations like the physical locations of particular nodes and the real areas traversed by the communication links. Otherwise, logical topology affords a conceptual interpretation of the communication links between the nodes regardless for the actual physical positions and distances between nodes in the network.

In this paper, OPNET Modeler academic edition 17.5 Simulator has been used. OPNET is a simulation tool that is used in numerous studies. In a production network, such a topology cannot be created; only simulation is possible because it provides mathematical and graphical model of result and these results can be understood readily. The network topology presented in this paper is composed of the following network devices and configuration utilities:

1. Nine Ethernet IP Router
2. Seven Ethernet Switch
3. Seven 100 BaseT switched LAN
4. Four Ethernet Server
5. PPP DS3 Duplex Link
6. Ethernet 100 Base T Duplex Link
7. Application configuration
8. Profile configuration
9. Failure recovery

The presented network consists of nine routers distributed among nine different districts in Baghdad, the Iraqi capital as shown in **Fig. 1**. Routers are connected together using DS3 Duplex Link (data rate 44.736 Mbps) link model with point to point (PPP) protocol. There are seven Ethernet LANs, each LAN is connected to an Ethernet switch using Ethernet 100 Base T Duplex Link. Each switch is connected to a corresponding router using the same link type (Ethernet 100 Base T). There are four servers: video, voice, HTTP and database server. These servers are connected to a switch located in a central site. There are one application definition and one profile definition. The profile definition is used to create user profiles in the different network nodes to generate application layer traffic. Four profiles are prepared: video, voice, database and HTTP. Table (1) describes each application while table (2) specifies the location and status of the planned failure.

6. SIMULATION RESULTS

The simulation includes three scenarios. Simulation time is 900 seconds for RIPng, EIGRPv6 and OSPFv3 scenarios.

1. DB Query response time:
   In the performance metric of DB Query response time, OSPFv3 is better than RIPng and EIGRPv6 as shown in **Fig. 2.**
2. HTTP Page response time:
   Relating to Http Page response time, EIGRPv6 is better than RIPng and OSPFv3 as shown in **Fig. 3.**
3. Traffic dropped: in traffic drop performance metric, EIGRP is better than OSPFv3 and RIPng as shown in **Fig. 4.**
4. Network convergence duration: in network convergence duration, EIGRPv6 is the best among OSPFv3 and RIPng as shown in **Fig. 5.**
5. Packet delay variation in video conferencing: in packet delay variation performance metric, EIGRPv6 is better than OSPFv3 and RIPng as shown in **Fig. 6.**
6. Packet End-to-End delay in video conferencing: EIGRPv6 is better than OSPFv3 and RIPng as shown in **Fig. 7.**
7. Jitter: in voice jitter, EIGRPv6 is better than OSPFv3 and RIPng as shown in **Fig. 8.**
8. Packet delay variation in voice: in packet delay variation performance metric, EIGRPv6 is better than OSPFv3 and RIPng as shown in **Fig. 9.**

9. Packet End-to-End delay in voice: EIGRPv6 is better than OSPFv3 and RIPng as shown in **Fig. 10.**

7. CONCLUSIONS

Selecting the best protocol among available is found to be a critical task, therefore, this work focuses on evaluating the performance of IPv6 based protocols (RIPng, EIGRPv6 and OSPFv3) in various real time applications like database, video, voice and HTTP. The observations have been done using the same topology with different protocols. Performance has been calculated according to a number of metrics to find the effects of these routing protocols. EIGRPv6 still outperformed OSPFv3 and RIPng in terms of convergence and adjusting to failures, therefore it is the fastest protocol. In DB query response time, this is for the first time that EIGRPv6 performance was the poorest as compared to RIPng and OSPFv3. While in HTTP page response time, EIGRPv6 is better than RIPng and OSPFv3. In video and voice packet delay variation, packet end-to-end delay and voice jitter, EIGRPv6 is the best. As a next research step, work can be done on the security analysis of the presented protocols.

REFERENCES

- Chandel, S. T. and Sharma, S., 2016, *Performance Evaluation of IPv4 and IPv6 Routing Protocols on Wired, Wireless and Hybrid Networks*, International Journal of Computer Networks and Applications (IJCNA), Vol. 3, No. 3, PP. 57-62.
- Hinds, A., Atojoko, A. and Zhu, S. Y., 2013, *Evaluation of OSPF and EIGRP Routing Protocols for IPv6*, International Journal of Future Computer and Communication, Vol. 2, No. 4., PP. 287-291.
- Iqbal, A. and Khan, S. L., 2015, *Performance Evaluation of Real Time Applications for RIP, OSPF and EIGRP for flapping links using OPNET Modeler*, International Journal of Computer Networks and Communications Security, Vol. 3, No. 1, PP. 16-26.
- Kaur, J. and Singh, E., 2014, *Simulation Based Performance Analysis of IPv6 Based IS-IS, OSPFv3 and OSPFv3_IS-IS Protocols*, international journal of software and hardware research in engineering, Vol. 2, No. 8, PP. 25-28.
- Narula, R. and Aggarwal, P., 2014, *Performance Evaluation of RIP and OSPF in IPv6 Using OPNET 14.5 Simulator*, International Journal of Technical Research and Applications, Vol. 2, No. 6, PP. 37-41.
- Odom, W., 2013, *Cisco CCENT/CCNA ICND1 100-101 Official Cert Guide*, book, Cisco Press.
- Odom, W., 2013, *Cisco CCNA Routing and Switching ICND2 200-101 Official Cert Guide*, book, Cisco Press.
- Sankar, D. and Lancaster, D., 2010, *Routing Protocol Convergence Comparison using Simulation and Real Equipment*, Advances in Communications, Computing, Networks and Security, PP. 186-194.
- Sethi, A. S. and Hnatyshin, V. Y., 2013, *The Practical OPNET® User Guide for Computer Network Simulation*, book, CRC Press.
- Sirika, S. and Mahajine, S., 2016, *Performance Evaluation of Dynamic Routing Protocols for Real time application*, International Journal of Engineering Trends and Technology (IJETT), Vol. 32, No. 7, PP. 328-337.

- Whitfield, R. J. and Zhu, S. Y., 2015, *A Comparison of OSPFv3 and EIGRPv6 in a Small IPv6 Enterprise Network*, International Journal of Advanced Computer Science and Applications, Vol. 6, No. 1, PP. 162-167.
- Yehia, M. A., Aziz, M. S. and Elsayed, H. A., 2011, *Analysis of IGP Routing Protocols for Real Time Applications: A Comparative Study*, International Journal of Computer Applications, Vol. 26, No. 3, PP. 11-17.

Table 1. Application Description

Voice	IP Telephony and Silence Suppressed
Video	High resolution Video
Database	High Load
HTTP	Searching

Table 2. Node_11 and Node_9 link failure and recovery

Node_11 to Node_9 Failure and Recovery timing	
Time	Status
150	Failure
250	recovery

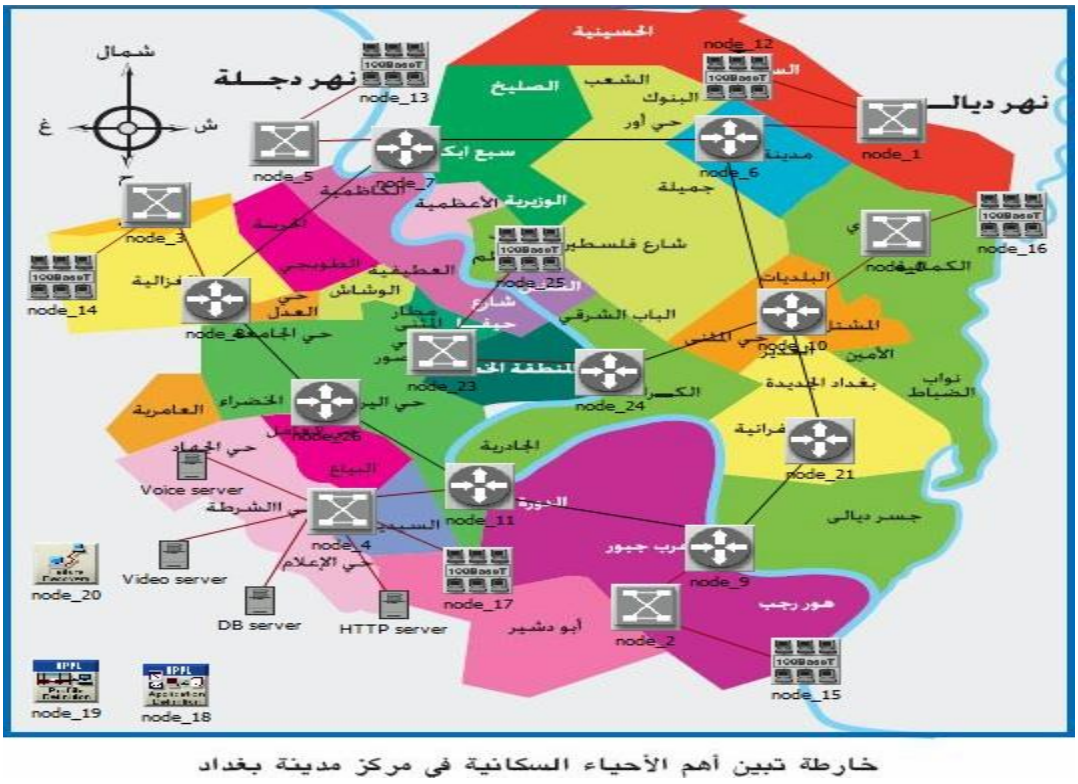

Figure 1. Network model.

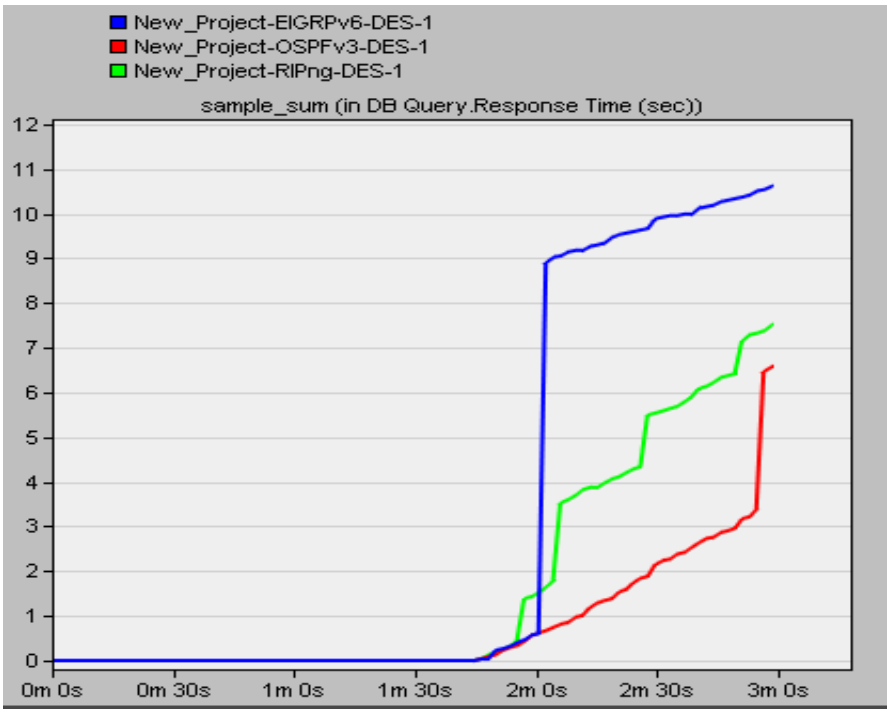

Figure 2. DB query response time.

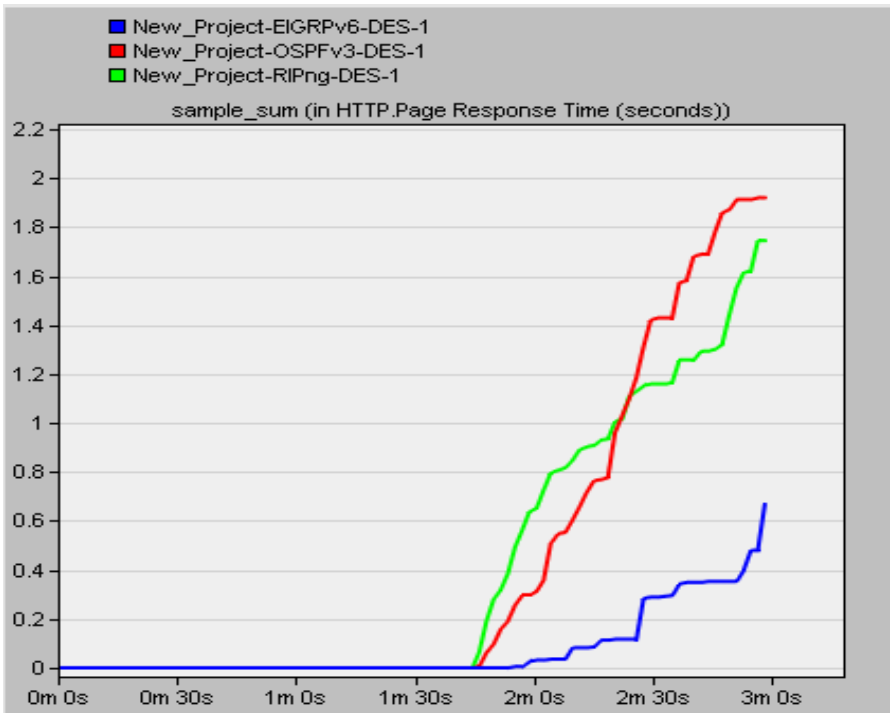

Figure 3. HTTP page response time.

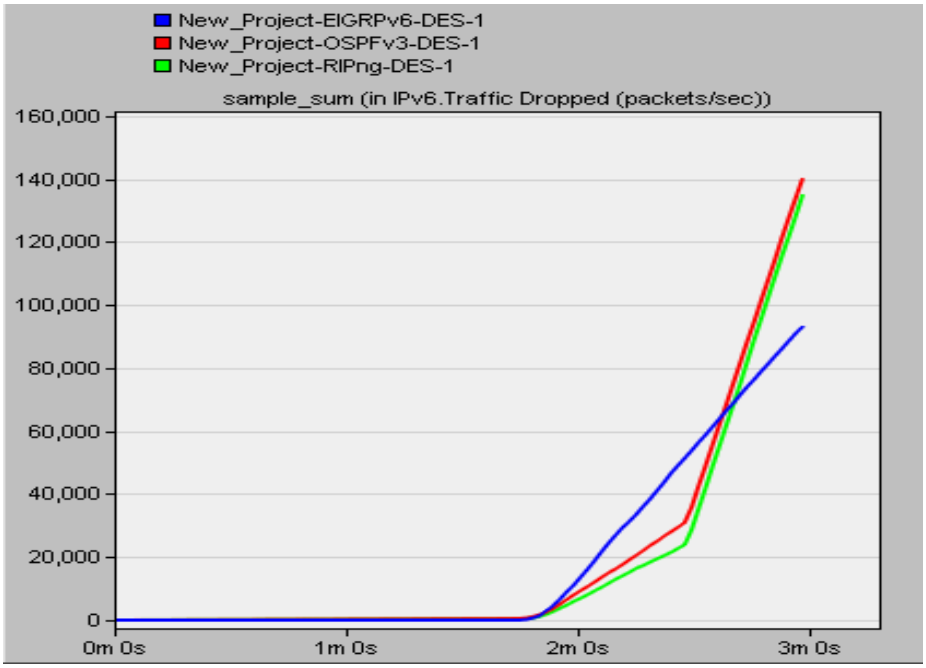

Figure 4. Traffic dropped.

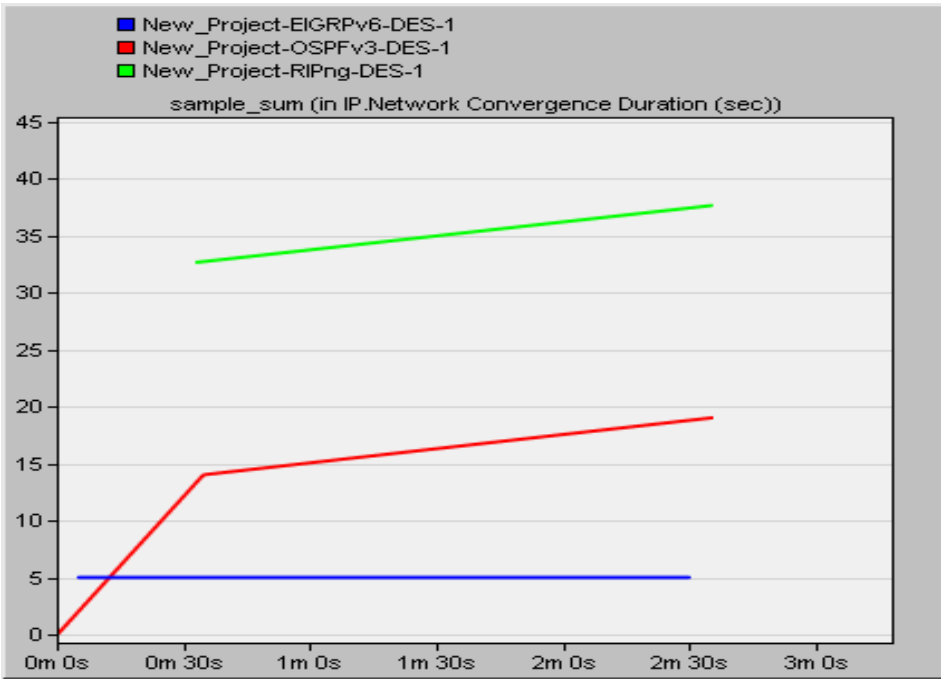

Figure 5. Network convergence duration.

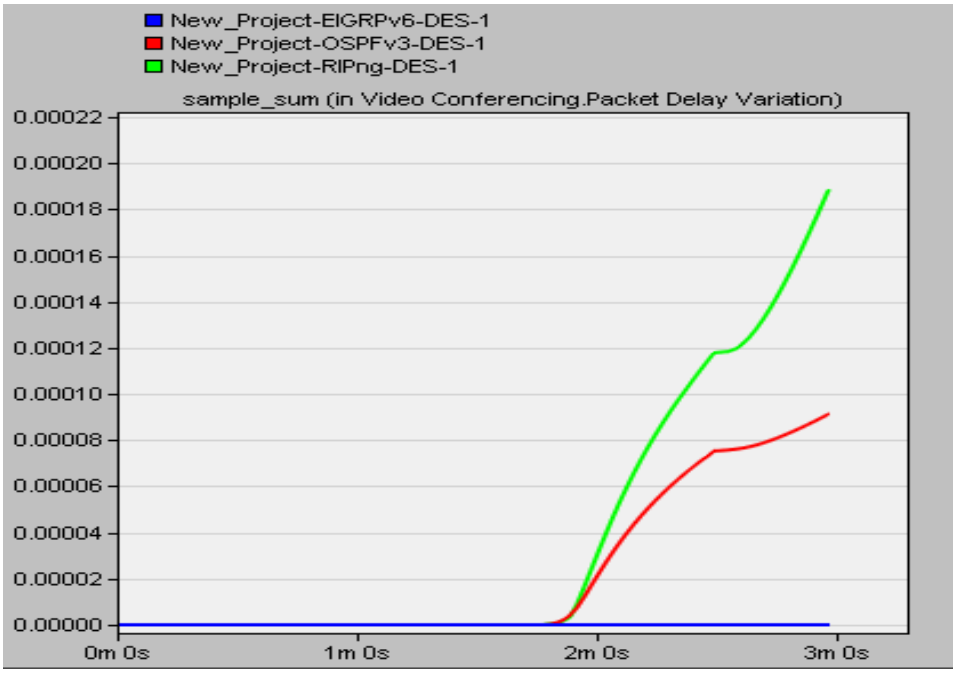

Figure 6. Packet delay variation in video conferencing.

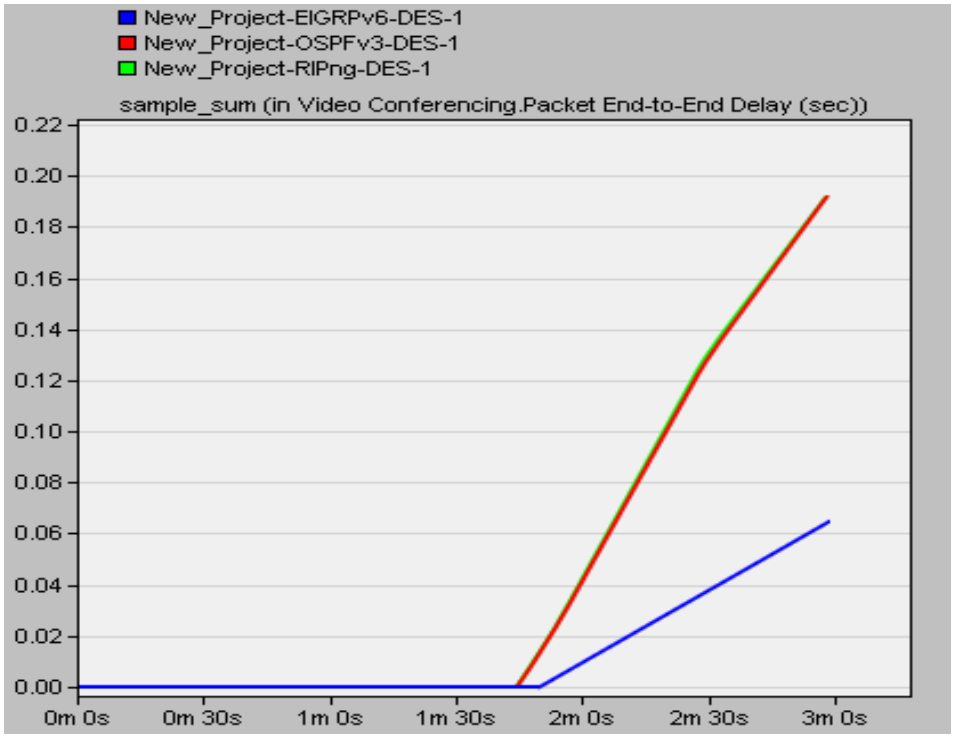

Figure 7. Packet end-to-end delay in video conferencing.

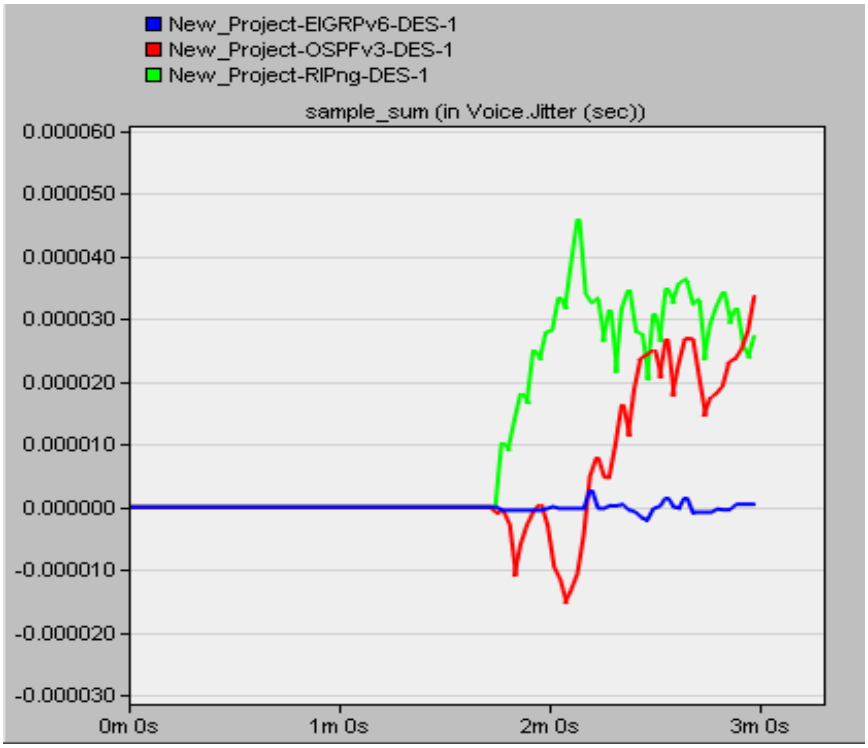

Figure 8. Voice jitter.

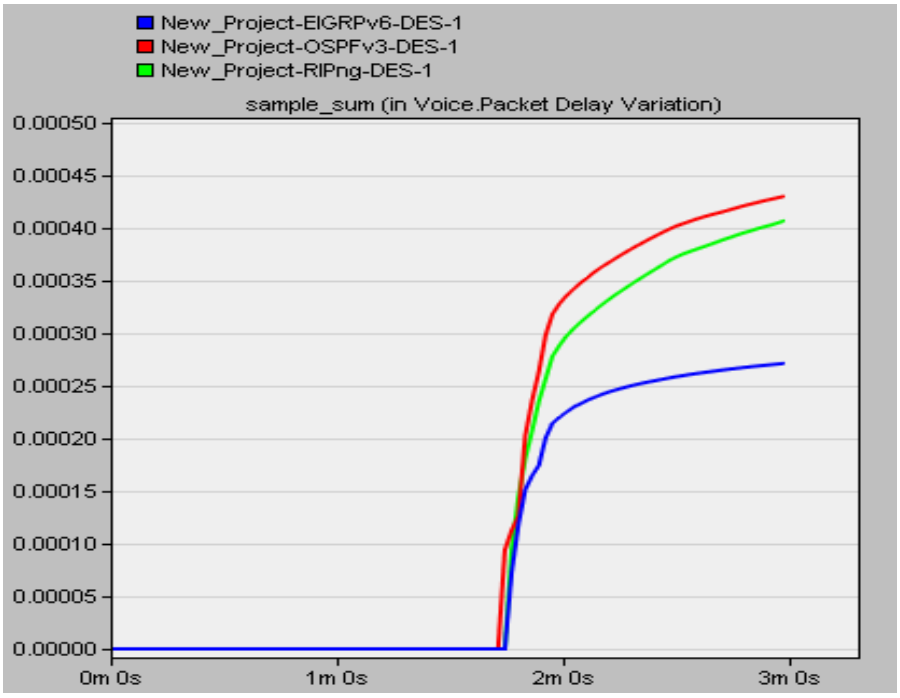

Figure 9. Packet delay variation in voice.

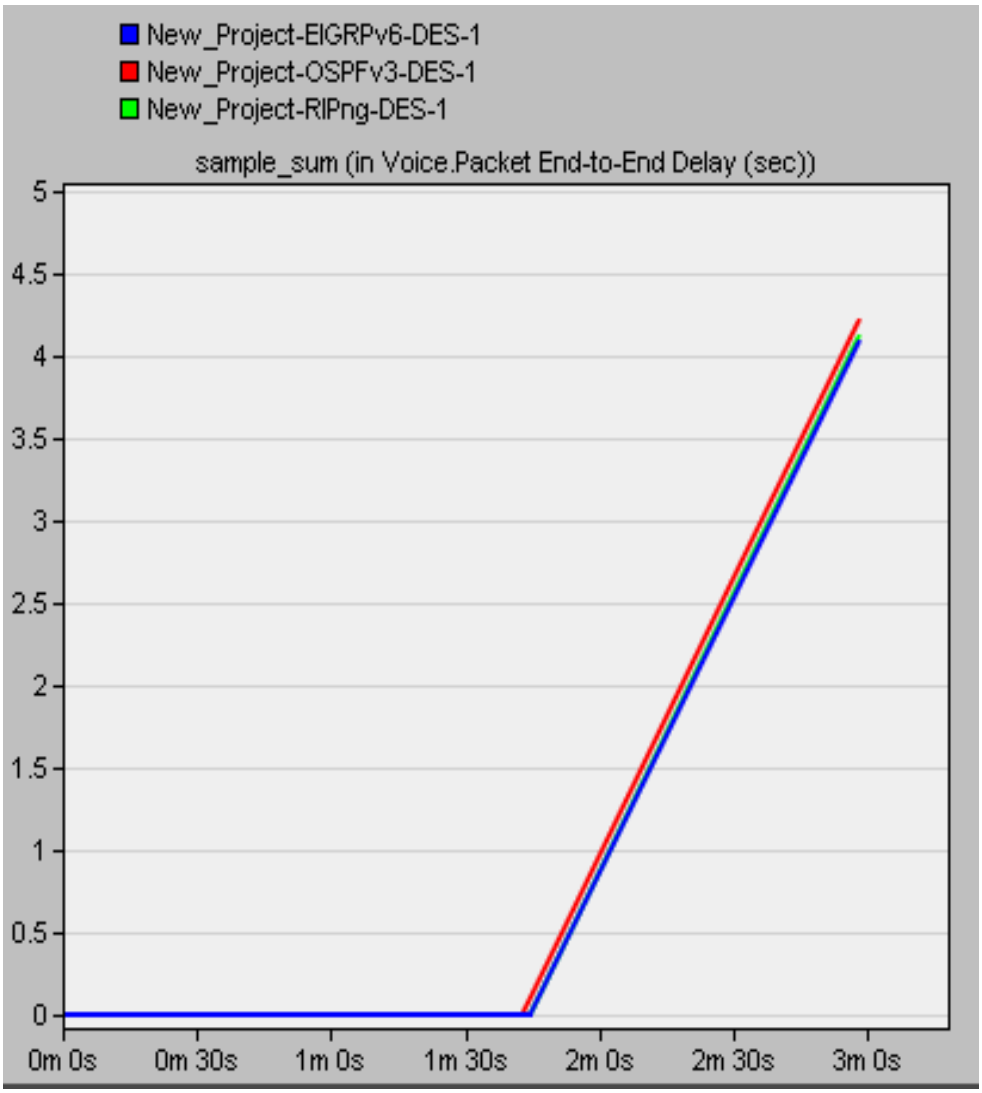

Figure 10. Packet end-to-end delay in voice.

Optimum Design of Power System Stabilizer based on Improved Ant Colony Optimization Algorithm

Ruba AL-MulaHumadi
Assistant Professor
Mechanical Engineering Dept.
College of Engineering,
University of Baghdad, Iraq.
rubamkh@yahoo.com

Dr. Nizar Hadi Abbas
Assistant Professor
Electrical Engineering Dept.
College of Engineering,
University of Baghdad, Iraq.
drnizaralmsaodi@gmail.com

Mohanad Azeez Joodi
Assistant Lecturer
Electrical Engineering Dept.
College of Engineering,
University of Baghdad, Iraq.
eng_muhanad73@yahoo.com

ABSTRACT

This paper presents an improved technique on Ant Colony Optimization (ACO) algorithm. The procedure is applied on Single Machine with Infinite Bus (SMIB) system with power system stabilizer (PSS) at three different loading regimes. The simulations are made by using MATLAB software. The results show that by using Improved Ant Colony Optimization (IACO) the system will give better performance with less number of iterations as it compared with a previous modification on ACO. In addition, the probability of selecting the arc depends on the best ant performance and the evaporation rate.

Keywords: SMIB, PSS, ACO.

التصميم الامثل لـــ مثبت نظام القدرة المبني على خوارزمية مستعمرة النمل المطورة

ربى الملا حمادي
استاذ مساعد
قسم هندسة الميكانيك
كلية الهندسة
جامعة بغداد

د. نزار هادي عباس
استاذ مساعد
قسم هندسة الكهرباء
كلية الهندسة
جامعة بغداد

مهند عزيز جودي
مدرس مساعد
قسم هندسة الكهرباء
كلية الهندسة
جامعة بغداد

الخلاصة

يقدم البحث تقنية محسنة لخوارزمية مستعمرة النمل (ACO).الفكرة مطبقة على نظام SMIB مع مثبت نظام القدرة (PSS) في ثلاثة احمال مختلفة حيث تمت المحاكاة باستخدام برنامج MATLAB .بينت النتائج ان النظام باستخدام تقنية مستعمرة النمل المتطورة يعطي اداء افضل مع اقل عدد من التكرارات بالمقارنة مع تحويرات سابقة اجريت على مستعمرة النمل. كذلك ان احتمالية اختيار او تحديد مسار النمله يعتمد ايضا على افضل اداء للنمل ومعدل التبخر لمادة الفيرومون التي تفرزها النمله.

1. INTRODUCTION

In the last years, much effort has been invested in improving the damping performance of power systems using Power system stabilizers (PSS). PSS provides a supplementary excitations control signal that enhances the damping capabilities of synchronous machines. The choice of parameters for the PSS is important as it affects the overall dynamic performance of the power system, there are various forms of PSS controllers, and the famous types are lead-lag compensator (i.e., classical PSS) and PID.

Kundur, 1993, illustrated the construction, function, and operation of a PSS that uses auxiliary stabilizing signals to control the excitation system so as to improve power system dynamic performance. Commonly used input signals to the power system stabilizer are shaft speed, terminal frequency, and power. PSS will add a component of electrical torque in phase with the rotor speed.

A robust PID stabilizer was proposed by **Otaru, et al., 2004**. The authors used a genetic algorithm to enhance the performance of the considered system which is a synchronous generator connected to an infinite bus, this model is sufficient for low-frequency oscillations studies, the PID stabilizer gains are designed optimally using Genetic Algorithm (GA) to arrive at the optimal setting of the controller. Another PID-PSS was proposed by **Hosseini, et al., 2007,** where the gain setting of PID-PSS is optimized by minimizing an objective function using GA. The dynamic response was compared with other two stabilizers named FUZZY-PSS and LQR-PSS. The authors revealed that their stabilizer gave better performance. They applied the proposed stabilizer on single machine infinite bus (SMIB) system and the simulations were made in MATLAB.

Abdul-Ghaffar, et al., 2013, used hybrid particle swarm bacteria foraging optimization (PSO-BFA) in tuning the PID parameters. This research considers the stabilization of a synchronous machine connected to an infinite bus via a PID. Simulation results were presented with and without the proposed controller then compared with the classical PID. They applied the controller to SMIB system. The results showed that using of hybrid control gave better performance.

Duman and Ozturk, 2010, presented a Real Coded Genetic Algorithm (RCGA) based PID controller to improve power system dynamic stability applied on (SMIB). Different controllers' structures are presented; conventional power system stabilizer (CPSS), optimized PSS and RCGAPID are used to improve the stability. Two performance indexes; integral absolute error (IAE) and integral squared error (ISE) were used as objective functions. Different loading conditions were studied. The results show that the ISE is better than IAE for the optimization problem.

A Harmony Search Algorithm (HSA) approach is presented by **Abdul Hameed, et al., 2014**, for the robust and optimal design of PID controller to PSS for damping low-frequency power oscillation. Also, they applied their technique to infinite bus single machine system, Eigenvalue analysis by using genetic algorithm based PSS (GAPSS) under different operating conditions reveals that under-damped and lightly damped oscillation modes are shifted to a specific stable zone in the S- Plane.

Boroujeni, et al., 2011, demonstrated a different type of stabilizers to generate supplementary damping control signals for the excitation system to damp the low frequency oscillation of the electric power system, they applied a new optimal technique PID type PSS based on (PSO-PSS) to a typical single machine infinite bus power system. The simulation results demonstrated that these design is showing the guarantee of the robust stability and robust performance of the power system to some conditions.

A new technique in designing a power system stabilizer PSS was presented by **Mahmoud and Soliman, 2012**, based on a combination of Particle Swarm Optimization (PSO) and Linear Matrix Inequality (LMI) in order to eliminate the number of variables. They applied their idea on (SMIB) using MATLAB environment. Finally, they concluded that their method was effective and convergence as the system confirms better performance under different loading conditions.
Soliman, et al., 2008, demonstrated another type of PSS that minimizes the maximum overshoot in order to alleviate the generator shaft fatigue. They used PSO algorithm in order to fix the gain of the PSS and lead time compensator. They applied their stabilizer to SMIB system at different loading conditions, the results showed the effectiveness and robustness of the proposed technique.
The rest of this paper is organized as follows: the mathematical model is illustrated in the next section. Ant colony optimization and its' modifications are demonstrated in the third section while the fourth section contains the results and discussion. Finally, a conclusion is demonstrated in the last section.

2. MATHEMATICAL MODEL

In this section, the mathematical model of the system with PSS and finding the transfer function are described.

2.1 SMIB

A synchronous machine with infinite bus system was taken in this research as a test system, as shown in Fig.1. The state space model "A, B, C, and D" are shown in appendix **Abdul-Ghaffar, et al., 2013,** and **Mahmoud** and **Soliman, 2012,** with the machine data in pu are X_d=1.6,$\dot{X}_d$ = 0.32 X_q=1.55, ω_d=2*π*50 rad/sec, $T'_{do} = 6\ sec,$ and M=10, transmission line reactance X_e=0.4, r_e=0. The machine constants k_1 to k_6 are as ref. **Mahmoud and Soliman, 2012,** and their values are depending on the loading conditions.
The transfer functions of the system for three loading conditions are tabulated in Table 1.

2.2 Power System Stabilizer (PSS)

The transfer function of power system stabilizer is

$$pss\ TF = K_i \frac{sT_w}{1+sT_w}\left[\frac{1+sT_1}{1+sT_2}\frac{1+sT_3}{1+sT_4}\right] \quad (1)$$

Where K_i represents the gain of the PSS

$\frac{sT_w}{1+sT_w}$ washout
$\left[\frac{1+sT_1}{1+sT_2}\ \frac{1+sT_3}{1+sT_4}\right]$ lead-lag compensator.

The limits for T_1 to T_4, T_W and K_i as ref. **Mahdiyeh, et al., 2010.**

$0.01 < T_1, T_2, T_3, \& T_4 < 2$ sec.

$1 < K_i < 50$

2.3 System with PSS

After connecting the PSS with the system as shown in **Fig.1**, the signal flow graph of the overall system will be as shown in **Fig.2**.

3. CLASSICAL ANT COLONY OPTIMIZATION (CACO) ALGORITHM

CACO is kind of optimization that is based on the behavior of ants in searching of the food process. The flow chart of CACO is illustrated in **Fig.3**.

3.1 Modified Ant Colony Optimization (MACO) Algorithm

The flowchart of this method is shown in **Fig.4**. A modification was made by **Mathiyalagan, et al., 2010**, that deal with the process of updating the pheromone. This equation is illustrated in the flowchart of **Fig.4**, as one can see there the new pheromone depends on the pheromone evaporation rate (ρ). In addition to this, the initial pheromone is entered in a random way with a dependency on the pheromone evaporation rate.

3.2 Improved Ant Colony Optimization (IACO) Algorithm

The proposed ACO algorithm in this research work is represented by a new improvement through modifying the updating pheromone equation; by adding the pheromone deposited by the best ant ($\zeta * f_{best} / f_{worst}$) multiplied by (k) in case more than one ant take the best path. The flowchart of this process is illustrated in **Fig. 5**.

4. RESULTS AND DISCUSSION

The results of this research are simulated by MATLAB R2013 environment executed on the core (TM) i5, 2.5GHz and 4 RAM system. 8 overall proper transfer functions (SMIB with PSS) were taken for 3 loading regimes (heavy load, nominal load, and light load). 4 design variables were taken; T_1, T_2, T_W, and gain of PSS. Two different methods of optimization were taken; modified ant colony optimization (MACO) introduced by **Mathiyalagan, et al., 2010,** and proposed improved ant colony optimization (IACO), 4 ants were taken for each variable and two evaporation rate (ρ= 0.5 and 0.2). Table 1, shows the results; the system alone, the system with PSS applying MACO and the system with PSS applying IACO at ρ=0.5.

Table 2, shows the results of the system with PSS applying MACO and the system with PSS based on IACO at ρ=0.2.

In spite of getting the same results sometimes, IACO algorithm is better than the MACO algorithm that because of two reasons; the number of iterations in the first method (MACO) is between 10-500 iterations while it is between 1-15 iterations in the second method (IACO). This means the second method is faster.

The second reason deals with the process of updating the pheromone that affects the probability of selecting the arc.

$$\text{MACO } \tau_{1j}^{(2)} = [\{\rho + \left(\frac{1-\rho}{1+\rho}\right)\}\tau_{1j}^{old}] + [\{\rho - \left(\frac{\rho}{1+\rho}\rho\right\} * \Delta\tau_{1j}] \qquad (2)$$

$$\text{IACO } \tau_{1j}^{(2)} = \left[\left\{\rho + \left(\frac{1-\rho}{1+\rho}\right)\right\} * \tau_{1j}^{old}\right] + \left[\left\{\rho - \left(\frac{\rho}{1+\rho}\right)\right\} * k * \frac{\xi f_{best}}{f_{worst}}\right] \qquad (3)$$

It is clear from the 1st equation that the last term ($\Delta\tau_{1j}$) is constant while the last term in the 2nd equation takes the effect of the best ant that makes the probability of selecting the arc closer to the optimal solution then the number of iteration will be less

5. CONCLUSIONS

Many researchers studied the stability problem of power system with the existence of PSS, and many methods were taken in order to analyze the system performance. One of these methods is ACO, an additional improvement to a previous modification of ACO algorithm is proposed in this paper. It is clear from the results that the system gives better performance when using IACO than when using MACO. That because the number of iterations is less and the simulation process will be faster. The process of updating the pheromone depends on the effect of the best ant.

Detailed illustrations about the used programs and the followed execution procedure:

The pare presents 3 flowcharts; Fig.3 shows Conventional ACO, Fig.4 shows Modified ACO, **Fig.5** Improved ACO. Illustrations of MATLAB codes for Modified ACO and Improved ACO are presented. While Conventional ACO was presented in a previous paper by another researcher.

Program 1/ no flowchart presented in this paper.

```
clear
clc
% from paper Soliman, et al, 2008.
% system alone (machine data)
xq=1.55; xd=1.6; xd_dash=0.32;M=10; wo=100*pi;Tdo_dash=6;D=0;
xe=0.4;re=0; Te=0.05; Ke=25; V=1;
%  three load conditions are considered
% ====================================
% heavy load    nominal load    light load
% ----------[]-------------[]-----------
%   P = 1     []   P=0.7      []   P=0.4
%   Q=0.5     []   Q=0.3      []   Q=0.1
% ----------------------------------------
P=input('input active power')
Q=input('input reactive power')
% calculations of c1-c7 and k1-k6 constants
c1=V^2/(xe+xq);
c2=(xd_dash+xe)/(xd+xe);
c3=c1*((xq-xd_dash)/(xe+xd_dash));
c4=V/(xe+xd_dash);
c5=(xd-xd_dash)/(xe+xd_dash);
c6=c1*xq*((xq-xd_dash)/(xe+xq));
c7=xe/(xe+xd_dash);

K1=c3*(P^2/(P^2+(Q+c1)^2))+Q+c1;
K2=c4*(P/(sqrt(P^2+(Q+c1)^2)));
K3=c2;
K4=c5*(P/(sqrt(P^2+(Q+c1)^2)));
K5=c4*xe*(P/(V^2+Q*xe))*(c6*((c1+Q)/(P^2+(c1+Q)^2))-xd_dash);
```

```
K6=c7*((sqrt(P^2+(Q+c1)^2))/(V^2+Q*xe))*(xe+(c1*xq*(c1+Q))/(P^2+(c1+Q)^2));
%%%%%%%%%%%%%%%%%%%%%%%%%%%__________________________%%%%%%%%%%%%%

% x=[delta(delta)  delta(w)  delta(Eq')  delta(Efd)]
A=[  0              wo     0                      0
   -K1/M          -D/M    -K2/M                   0
   -K4/Tdo_dash     0     -1/(K3*Tdo_dash)       1/Tdo_dash
   -K5*Ke/Te        0     -K6*Ke/Te              -1/Te];


B=[0 0 0  Ke/Te]';
C=[0  1 0 0];
D=0  ;
[num,Den]=ss2tf(A,B,C,D);
disp('sys alone')
G=tf(num,Den)% tf of sys alone
eig(G);
s=stepinfo(G)
     tr=s.RiseTime;
     ts=s.SettlingTime;
     Mp=s.Overshoot;
     Ess=abs(1-dcgain(G))
figure(1);
step(G);
title('sys alone');

%  pss
syms s
 % T1 T2 T3 T4 compensators time
 T1= [0.02 0.05 0.11   0.2   0.3  0.4   0.55   0.15 ];
 T3=T1;
 T2 =[0.01 0.03  0.07  0.09  0.12  0.22  0.45  0.065 ];
 T4=T2;
 ks=[1   7   11   17   26   35   40   45];    % pss gain
 Tw=[1   2   6    8    10   12   14   16] ;   % washout time
for i=1:8  % 8 is the number of states of T1 T2 T3 T4

G1=ks(i)*(s*Tw(i)/(1+s*Tw(i)))*((1+s*T1(i))/(1+s*T2(i)))*((1+s*T3(i))/(1+s*T4
(i)));  %pss TF
    [N1,D1]=numden(G1);  % of pss
    n1=sym2poly(N1);
    d1=sym2poly(D1);
    disp('TF of PSS');
    GG1=tf(n1,d1); % TF of PSS
%figure(2)
%step(GG1)
%title('pss alone')
              %%% pss with sys
     [n_sp,d_sp]=feedback(num,Den,n1,d1,+1);
     disp('sys with pss');
     i
     G_sp=tf(n_sp,d_sp);
     figure;
     step(G_sp);
     title('sys with pss');
     S=stepinfo(G_sp)
     tr=S.RiseTime;
```

```
      ts=S.SettlingTime;
      Mp=S.Overshoot;
      Ess=abs(1-dcgain(G_sp))
      % the objective function
      fitt(i)= (0.25*tr) + (0.5*ts) + (0.25*Ess);
      TF(i)=G_sp;
end
fitt;TF;
      %%%%%% this is the end %%%%%%
```

How to execute the programs:
First of all, execute the program 1 by entering active and reactive powers according to the load regimes (heavy, nominal and light) loads. Taking, for example, the first case (heavy load condition; active power is 1 and reactive power is 0.5. The program will continue its execution until getting the transfer function of the system alone as:

$$G = \frac{-8.132\ s}{s^4 + 20.46\ s^3 + 98.45\ s^2 + 922.7\ s + 2363}$$

ts, tr and ESS can be obtained from "`stepinfo`" MATLAB command as:

```
s =
      RiseTime: 0
   SettlingTime: 156.2869
    SettlingMin: -0.0114
    SettlingMax: 0.0084
      Overshoot: Inf
     Undershoot: Inf
           Peak: 0.0114
       PeakTime: 0.4433
Ess =
   1
```

We have 4 variables (T_1, T_2, Ks, and Tw) each one of 8 values as stated in the program. At the end of the program, we will get 8 transfer functions (`TF`) and 8 values of the objective function (`fitt`).

Now go to the second program

Program 2: flowchart of Fig.4 in this paper depending on equation of ref. **Mathiyalagan, et al., 2010.**

```
%% Modified Ant colony optimization Mathiyalagan, et al., 2010.
% applied on SMIB WITH PSS
clear
clc
N= input('the no. of ants') % write N=4; no_of_ants for each variable
p=input('no. of states')% write 8; no_of_states
% for min < T1, T2, ks, Tw < max, from program1
n=input('no. of design') % write 1 for each time u execute the program
% because we have4 design variables are PSS gain, T1 T2 Tw
% x is a matrix of 8 overall TF obtained from program1
syms TF1,syms TF2, syms TF3, syms TF4, syms TF5, syms TF6, syms TF7, syms TF8
```

```
x=[TF1  TF2  TF3  TF4  TF5  TF6  TF7  TF8]

%fx=fitt results from program1
disp('1:heavy load,2:nominal load, 3:light load')
load=input('load')
if load==1
   fx= [55.4714  18.2018  9.3514  2.3952  1.1983  3.3588  52.3429  1.2541] %
heavy load
elseif load==2
   fx=[18.5437   10.7712    6.8578    2.3386    1.2461    2.6462   11.7511
1.3481]% nominal load
elseif load==3
   fx =[11.0834    7.5520    5.4010    2.2261    1.0898    1.9588    5.4122
1.5132] %light load
end

jj=1:8  % the order at the 8 states

roo=input('roo');  % roo=0.2   0.5   0.9
iteration=1

tao=1-roo*rand;    % initial pheromone
for i=1:p
    tao1(i)=tao;
end

p1j=tao/sum(tao1);

x1=[0    p1j   2*p1j  3*p1j  4*p1j  5*p1j   6*p1j   1]

syms ant1, syms ant2, syms ant3, syms ant4
ant=[ ant1    ant2     ant3      ant4]

r=rand(1,N)  %N is the number of ants
for i=1:N
    for j=1:p
        if r(i)> x1(j) & r(i)<x1(j+1)
           xx(i)=x(j);    % to present the TF
           fx1(i)=fx(j);  % to present the fitness
           order(i)=jj(j); % to present the index
        end
    end
end
xx;
fx1, order
fbest=min(fx1)
fworst=max(fx1)
% to print ant number and x
k=0;
for i=1:N
    if fbest==fx1(i)
        best_ant =[xx(i),   ant(i),   order(i)]
        k=k+1;
    elseif fworst==fx1(i)
        worst_ant=[xx(i),   ant(i),   order(i)]
    else
    end
```

```
end
k

t1_j=tao

while k<N
   % step 4
   % ants return home and start again in search of food
   iteration=iteration+1

   % modification
   %t_new=t1_j=(roo+((1-roo)/(1+roo)))*t1_j+(roo-(roo/(1+roo)))*0.2; from
ref. Mathiyalagan, et al., 2010.

   t1_j=(roo+((1-roo)/(1+roo)))*t1_j+(roo-(roo/(1+roo)))*0.2 % new value
   % go to step 2
   for j=1:p
       t(j)=t1_j;
   end
   sum(t);
   p1_j=t/sum(t);
   p1_j


    % to prepare x11:x18 in range 0-1
   x11(1)=0;
   x1=0;
   for i=2:7
       x1=x1+p1_j(i-1);
       x11(i)=x1;
   end
   x11(8)=1;
   x11

   r=rand(1,N)
   for i=1:N
       for j=1:p
           if r(i)> x11(j) & r(i)<x11(j+1)
              xx(i)=x(j);
              fx1(i)=fx(j);
              order(i)=jj(j);
           end
       end
   end
   xx
   fx1, order
   fbest=min(fx1)
   fworst=max(fx1)
   % to print ant number and x
   k=0; % k is the no. of best ants
   for i=1:N
       if fbest==fx1(i)
          best_ant= [xx(i), ant(i), order(i)]
          k=k+1;
       elseif fworst==fx1(i)
          worst_ant=[ xx(i), ant(i), order(i)]
       else
```

```
        end
    end
    k

end
```

To execute program 2 input

```
N=4;
P=8;
n=1;
```

Remove the lines:

```
syms TF1,syms TF2, syms TF3, syms TF4, syms TF5, syms TF6, syms TF7, syms TF8
x=[TF1  TF2  TF3  TF4  TF5  TF6  TF7  TF8]
```

Write `x=TF,` to let x=8 transfer function that described in program 1.
Then input load 1, to execute for heavy load case.
Input `roo=0.2;`
After that, the Ant Colony will be operated with the fitness function according to that presented in **Mathiyalagan, et al., 2010.**
Wait for the final results. All the ants will follow the same direction. And the program will give you the best transfer function also the program will give you the number of iterations.
The results are shown in Table2.
Now repeat for `roo=0.5,` the results are shown in Table 3.

Finally, follow the same procedure as described above but this time on program 3. The difference is the analysis is done according to our fitness equation.

Program 3/ flowchart of Fig.5 in this paper depending on our equation

```
%% Modified Ant colony optimization   "our equations"
% applied on SMIB WITH PSS
clear
clc
N= input('the no. of ants') % write N=4; no_of_ants for each variable
p=input('no. of states')% write 8; no_of_states
% for  min < T1, T2, ks,Tw < max, from program1
n=input('no. of design') % write 1 for each time u execute the program
% because we have4 design variables are PSS gain, T1 T2 Tw
% x is a matrix of 8 overall TF obtained from program1
syms TF1,syms TF2, syms TF3, syms TF4, syms TF5, syms TF6, syms TF7, syms TF8
x=[TF1  TF2  TF3  TF4  TF5  TF6  TF7  TF8]

%fx=fitt results from program1
disp('1:heavy load,2:nominal load, 3:light load')
load=input('load')
if load==1
   fx= [55.4714  18.2018  9.3514  2.3952  1.1983  3.3588  52.3429  1.2541] %
heavy load
elseif load==2
   fx=[18.5437   10.7712    6.8578    2.3386    1.2461    2.6462   11.7511
1.3481]% nominal load
elseif load==3
   fx =[11.0834    7.5520    5.4010    2.2261    1.0898    1.9588    5.4122
1.5132] %light load
end

jj=1:8  % the order at the 8 states
```

```
roo=input('roo');  % roo=0.2   0.5   0.9

iteration=1

tao=1-roo*rand;    % initial pheromone
for i=1:p
    tao1(i)=tao;
end

p1j=tao/sum(tao1);

x1=[0    p1j   2*p1j  3*p1j  4*p1j  5*p1j   6*p1j   1]

syms ant1, syms ant2, syms ant3, syms ant4
ant=[ ant1    ant2     ant3      ant4]

r=rand(1,N)  %N is the number of ants
for i=1:N
    for j=1:p
        if r(i)> x1(j) & r(i)<x1(j+1)
            xx(i)=x(j);    % to present the TF
            fx1(i)=fx(j);  % to present the fitness
            order(i)=jj(j); % to present the index
        end
    end
end
xx;
fx1, order
fbest=min(fx1)
fworst=max(fx1)
% to print ant number and x
k=0;
for i=1:N
    if fbest==fx1(i)
        best_ant =[xx(i),   ant(i),   order(i)]
        k=k+1;
    elseif fworst==fx1(i)
        worst_ant=[xx(i),   ant(i),   order(i)]
    else
    end
end
k

t1_j=tao;
t_2=tao;

while k<N
   % step 4
   % ants return home and start again in search of food
   iteration=iteration+1

   % modification
   %t_new=(p+(1-p)/(1+p))*t_old+(p-p/(1+p))*sum(delta(t)) our equation
   t1_j=(roo+((1-roo)/(1+roo)))*t1_j % old value
   zeta=2; % scaling parameter
```

```
    sum_delta_t=k*zeta*fbest/fworst
    t_2=(roo+((1-roo)/(1+roo)))*t_2+sum_delta_t

    % go to step 2
    for j=1:p
        if j==best_ant(3)  % at j=3 best ant for the first case
           t(j)=t_2;
        else
           t(j)=t1_j;
        end
    end
    sum(t);
    p1_j=t/sum(t);
    p1_j

     % to prepare x11:x18 in range 0-1
    x11(1)=0;
    x1=0;
    for i=2:7
        x1=x1+p1_j(i-1);
        x11(i)=x1;
    end
    x11(8)=1;
    x11

    r=rand(1,N)
    for i=1:N
        for j=1:p
            if r(i)> x11(j) & r(i)<x11(j+1)
               xx(i)=x(j);
               fx1(i)=fx(j);
               order(i)=jj(j);
            end
        end
    end
    xx
    fx1, order
    fbest=min(fx1)
    fworst=max(fx1)
    % to print ant number and x
    k=0; % k is the no. of best ants
    for i=1:N
        if fbest==fx1(i)
           best_ant= [xx(i), ant(i), order(i)]
           k=k+1;
        elseif fworst==fx1(i)
           worst_ant=[ xx(i), ant(i), order(i)]
        else
        end
    end
    k

end
```

The same is done for nominal and light loads. The results are shown in Tables 2 and 3.

REFERENCES:

- Abdul Hameed, K., and Palani, S., 2014, *Robust Design of Power System Stabilizer using Harmony Search Algorithm*, Automatika, Vol. 55, No. 2, PP. 162–169.
- Abdul-Ghaffar, H. I., Ebrahim, E. A., and Azzam, M., 2013, *Design of PID Controller for Power System Stabilization Using Hybrid Particle Swarm-Bacteria Foraging Optimization*, WSEAS Transactions on Power Systems, Issue 1, Vol. 8, PP. 12-23.
- Boroujeni, S. M. S., Hemmati, R., Delafkar, H., and Boroujeni, A. S., 2011, *Optimal PID Power System Stabilizer Tuning based on Particle Swarm Optimization*, Indian Journal of Science and Technology, Vol. 4, No. 4, PP. 379-383.
- Duman, S., and Öztürk, A., 2010, *Robust Design of PID Controller for Power System Stabilization by Using Real Coded Genetic Algorithm*, International Review of Electrical Engineering (I.R.E.E.), Vol.5, No. 5, PP. 2159-2170.
- Hosseini, S. H., Reza, R., and Hamed, K., 2007, *Application of Genetic Algorithm to Design PID Controller for Power System Stabilization*, 5th International Conference on Electrical and Electronics Engineering (ELECO 2007), Bursa, Turkey.
- Kundur., P., 1993, *power system stability and control*, McGraw-Hill, New York.
- Mahdiyeh Eslami, Hussain Shareef, Azah Mohamed and S. P. Ghoshal,2010, *Tuning of power system stabilizers using particle swarm optimization with passive congregation*, International Journal of the Physical Sciences Vol. 5(17), PP. 2574-2589, Available online at http://www.academicjournals.org/IJPS
ISSN 1992 - 1950 ©2010 Academic Journals.
- Mahmoud, M. S., and Soliman, H. M., 2012, *Design of Robust Power System Stabilizer Based on Particle Swarm Optimization*, Circuits and Systems, Vol.3, PP. 82-89.
- Mathiyalagan, P., Dhepthie, U. R., and Sivanandam, S. N., 2010, *Enhanced Hybrid PSO-ACO Algorithm for Grid Scheduling*, ICTACT journal on soft computing, Issue:01, PP. 54-59.
- Otaru, M. U., Al-Musabi, N. A., and Al-Baiyat, S. A., 2004, *Robust PID Stabilizer Design using Genetic Algorithms*, Proceedings of the 2nd IEEE GCC Conference, Bahrain, PP. 33-36 ,
- Rao, S. S., 2009, *Engineering Optimization Theory and Practice*, 4th edition, John Wiley & Sons. INC.
- Soliman, H. M., Bayoumi, E. H. E., and Hassan, M. F., 2008, *PSO–Based Power System Stabilizer for Minimal Overshoot and Control Constraints*, Journal of Electrical Engineering, Vol. 59, No. 3, PP. 153–159.

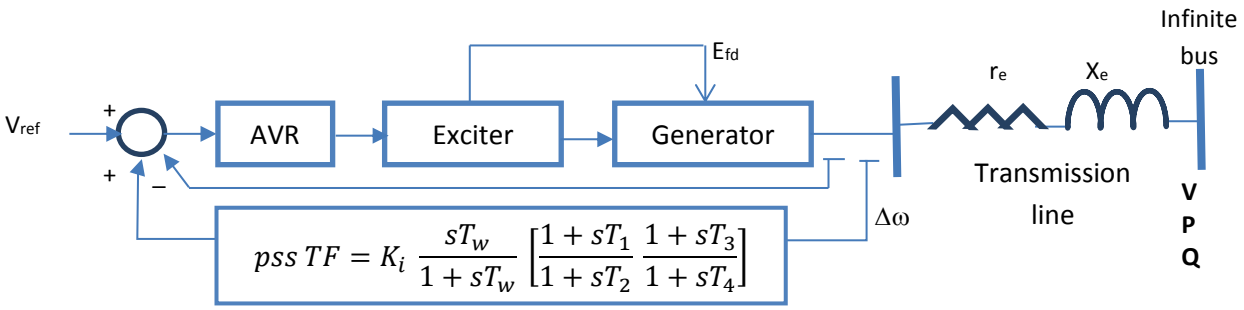

Figure 1. A synchronous machine with the infinite bus.

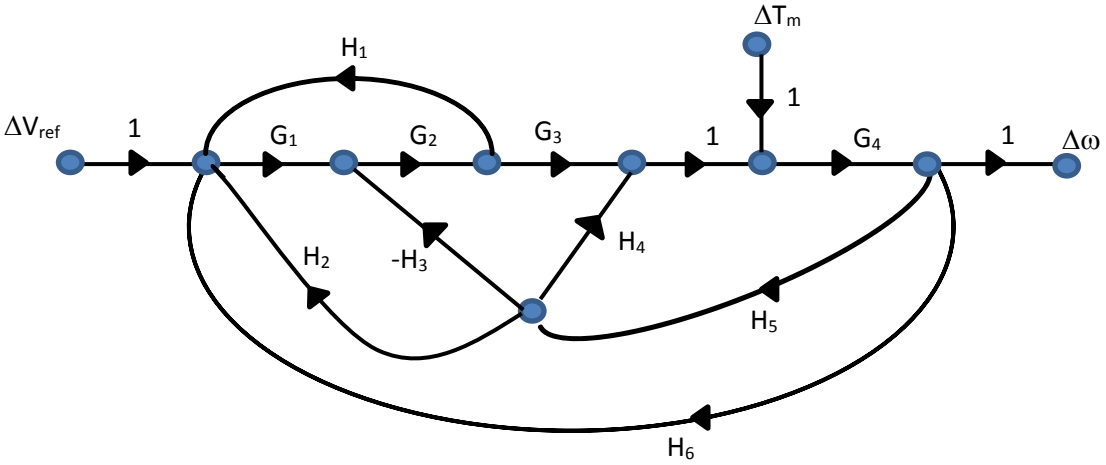

Figure 2. Signal flow graph of the system with PSS.

Where:

$$G_1 = \frac{K_E}{1 + sT_E}, \quad G_2 = \frac{K_3}{1 + sT_3}, \quad G_3 = K_2, \quad G_4 = \frac{1}{M}$$

$$H_1 = K_6, \quad H_2 = K_5, \quad H_3 = K_4, \quad H_4 = K_1, \quad H_5 = \frac{314}{s}, \quad H_6 = P_{ss}$$

♦♦1 the no. of paths or arcs is the permissible discrete values (X_{11}, X_{12}, X_{13}, …, X_{1P}) within a selected range.

♦♦2 the design variables are T_1, T_2, T_W, and G_{PSS}.

♦♦3 the fitness function =0.25*tr+0.5*ts+0.25*Ess

♦♦4 generate 4 random numbers, one for each ant.

♦♦5 K is the number of best ant ζ is the scaling factor assumed to be 2. **Rao, 2009.** $\tau_{1j}^{old}=(1-\rho)*\tau_{1j}^{(1)}$, ρ=0.5 pheromone decay factor **Rao, 2009.**

♦♦6 if the no. of best ants (k)=the no. of ants (N), that means all the ants follow the same path

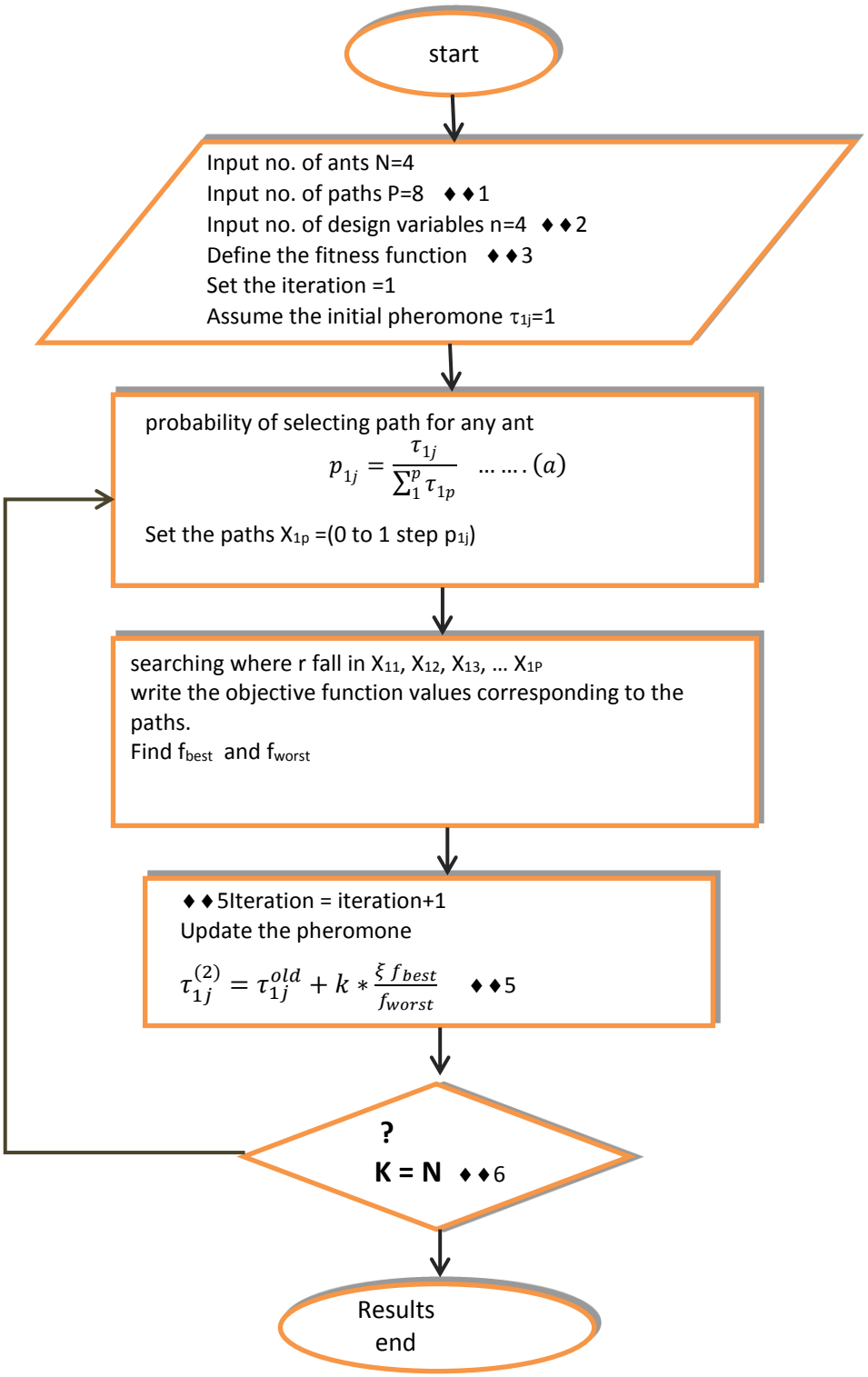

Figure 3. The flowchart of CACO algorithm.

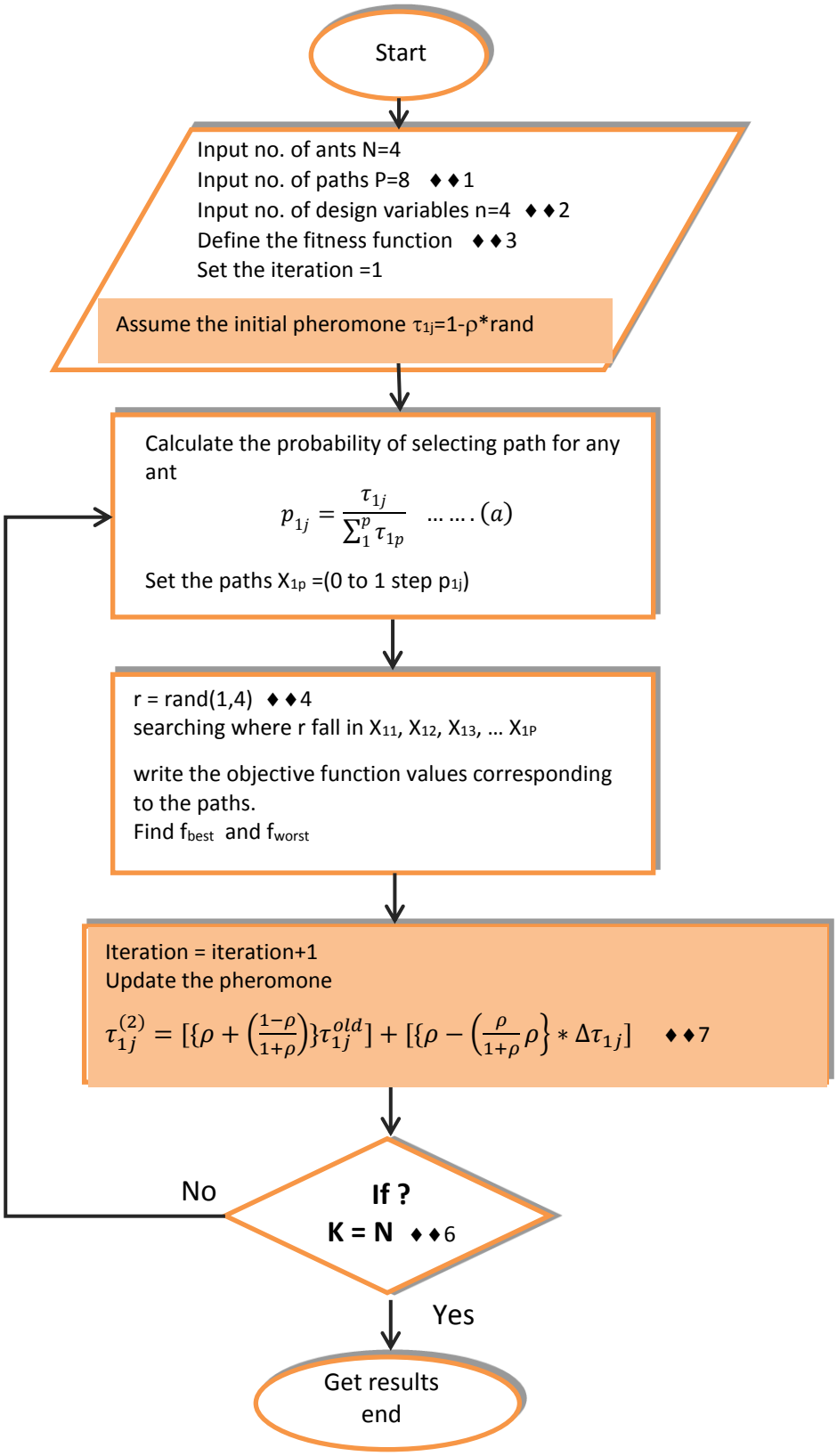

Figure 4. The flowchart of MACO algorithm.

♦♦7 $\Delta\tau_{1j}$=0.2 constant value according to ref. **Mathiyalagan, et al., 2010**.

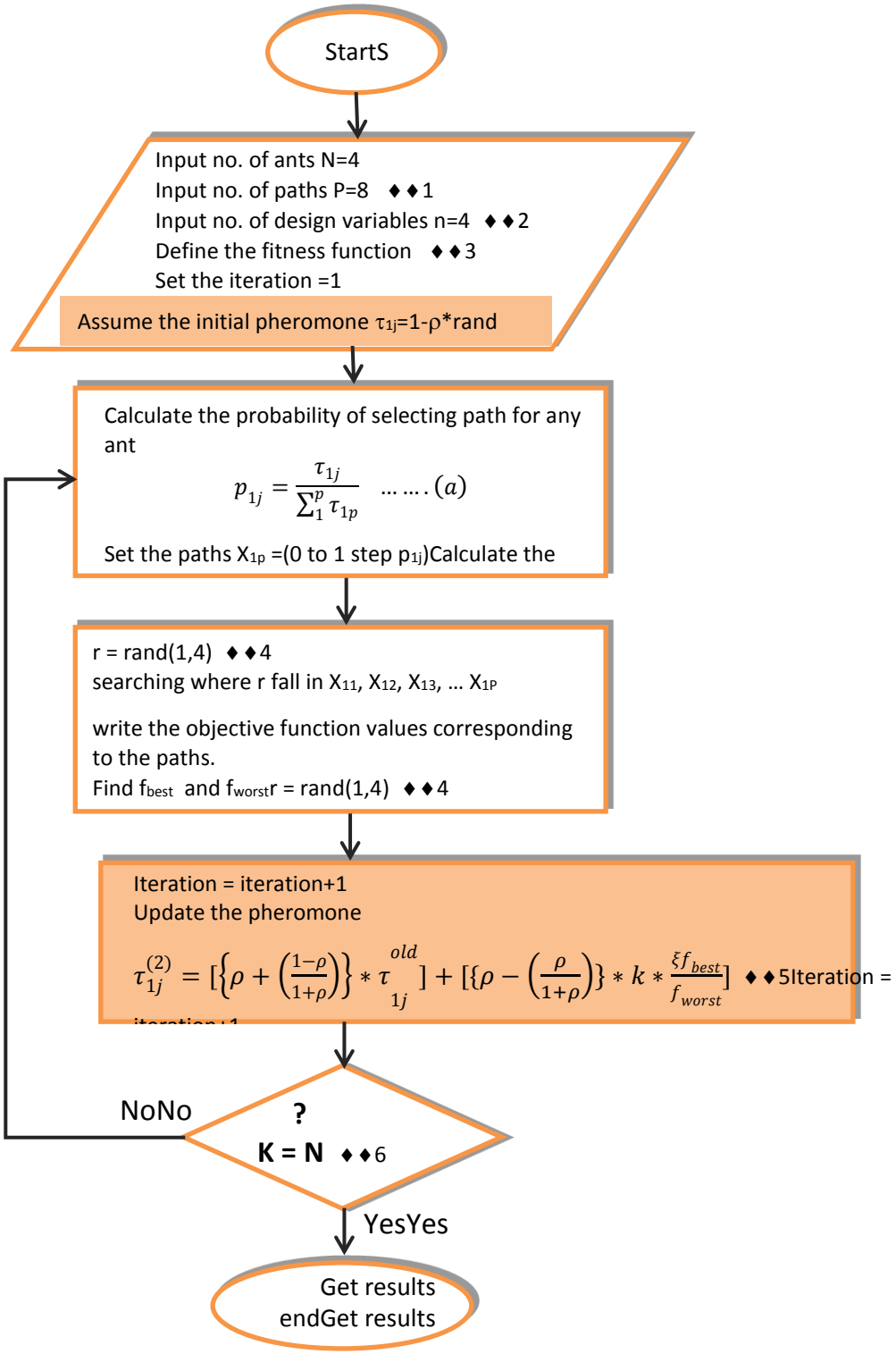

Figure 5. The flowchart of IACO algorithm.

Table 1. Loading conditions and transfer functions

Loading condition	Transfer function
Light load	$\frac{-6.326\ s}{s^4 + 20.46\ s^3 + 79.4\ s^2 + 558.4\ s + 1242}$
Nominal load	$\frac{-7.553\ s}{s^4 + 20.46\ s^3 + 89.15\ s^2 + 756.9\ s + 1795}$
Heavy load	$\frac{-8.132\ s}{s^4 + 20.46\ s^3 + 98.45\ s^2 + 922.7\ s + 2363}$

Table 2. The system time response performance at ρ=0.5

	System alone	MACO ρ=0.5	IACO ρ=0.5
Heavy load P=1 Q=0.5	ts =156.28 sec	ts=1.89	ts=1.89
	tr=0 sec	tr=0	tr=0
	Ess=1	Ess=1	Ess=1
	Fig. 6	**Fig. 7,** TF5	**Fig. 7,** TF5
Nominal load	ts=41.40	ts=1.99	ts=1.99
P=0.7 Q=0.3	tr=0	tr=0	tr=0
	Ess=1	Ess=1	Ess=1
	Fig. 8	**Fig. 9,** TF5	**Fig. 9,** TF5
Light load	ts=23.58	ts=3.41	ts=1.67
P=0.4 Q=0.1	tr=0	tr=0	tr=0
	Ess=1	Ess=1	Ess=1
	Fig. 10	**Fig. 11,** TF6	**Fig. 12,** TF5

Table 3. The system time response performance at ρ=0.2

	MACO ρ=0.2	IACO ρ=0.2
Heavy load P=1 Q=0.5	ts=18.20	ts=1.89
	tr=0	tr=0
	Ess=1	Ess=1
	Fig. 13, TF3	**Fig. 7,** TF5
Nominal load	ts=1.99	ts=1.99
P=0.7 Q=0.3	tr=0	tr=0
	Ess=1	Ess=1
	Fig. 9, TF5	**Fig. 9,** TF5
Light load	ts=1.67	ts=1.67
P=0.4 Q=0.1	tr=0	tr=0
	Ess=1	Ess=1
	Fig. 12, TF5	**Fig. 12,** TF5

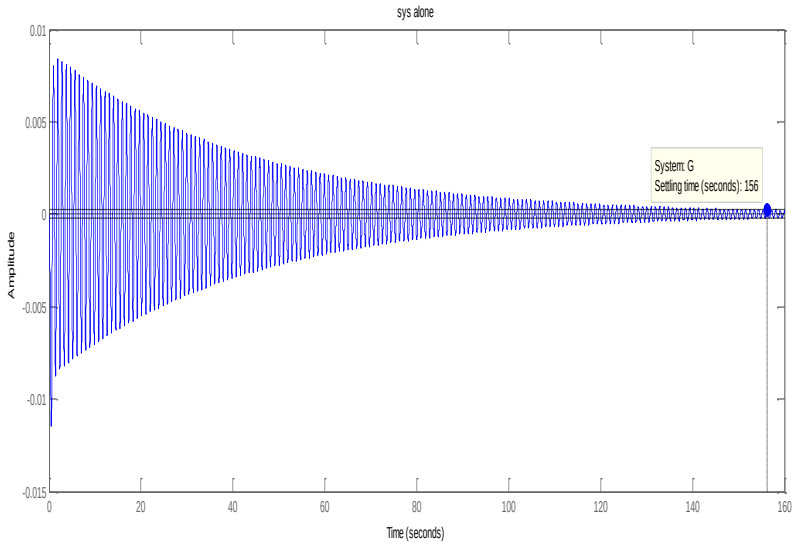

Figure 6. System alone (without PSS) for heavy load regime.

$$TF = \frac{-8.132\ s}{s^4 + 20.46\ s^5 + 98.45\ s^2 + 922.7\ s + 2363}$$

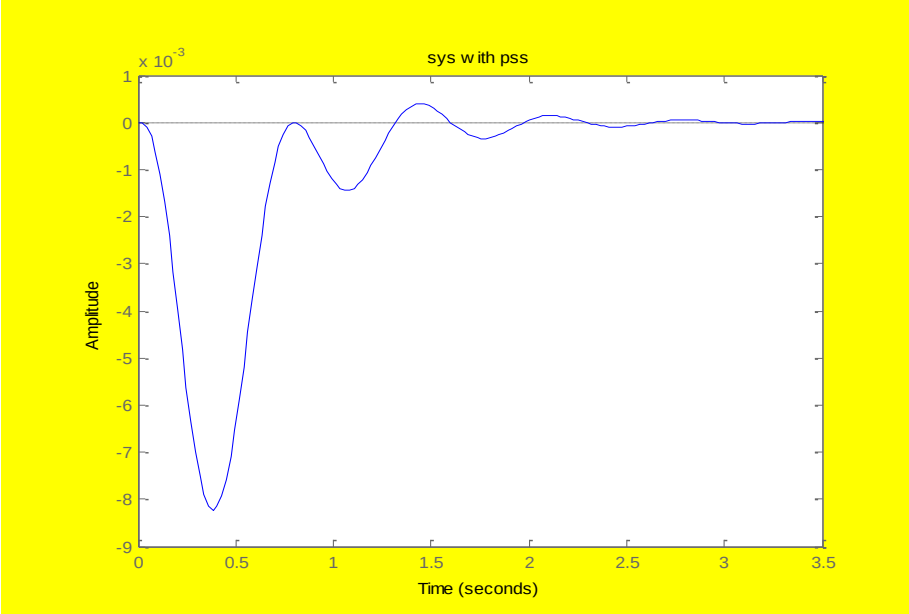

Figure 7. The system with PSS for heavy load regime based on MACO and IACO at ρ=0.5 & 0.2.

$$TF = \frac{-731.9\ s^4 - 1.227*10^4\ s^3 - 5.204*10^4\ s^2 - 5082\ s}{90\ s^7 + 3351\ s^6 + 4.614e04\ s^5 + 4.821*10^5\ s^4 + 3.041*10^6\ s^3 + 1.085*10^7\ s^2 + 1.57*10^7\ s + 1.477*10^6}$$

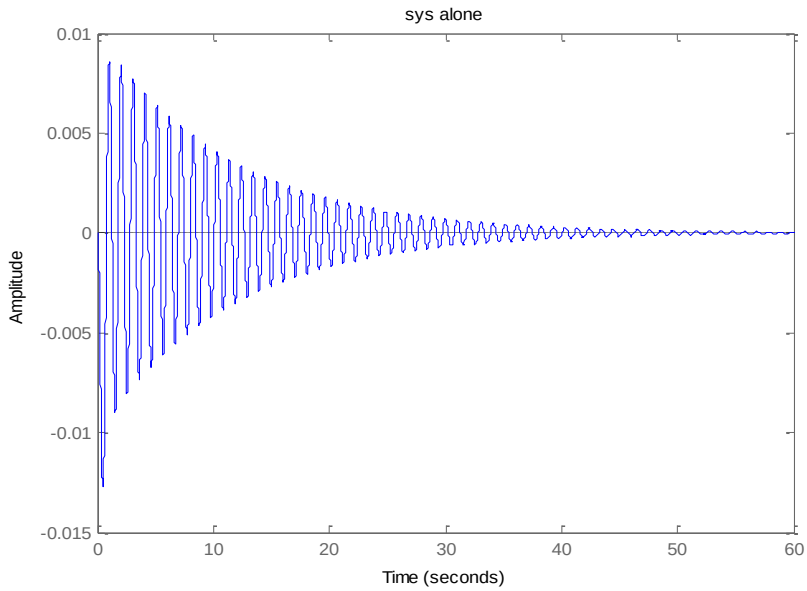

Figure 8. System alone (without PSS) for nominal load regime.

$$TF = \frac{-7.553\ s}{s^4 + 20.46\ s^3 + 89.15\ s^2 + 756.9\ s + 1795}$$

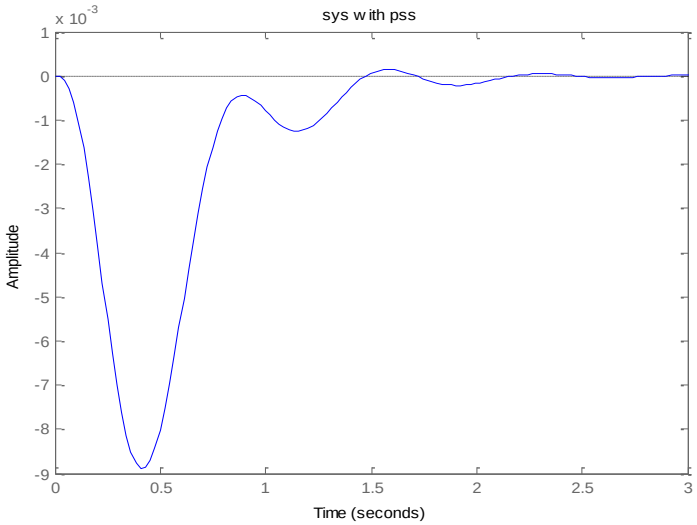

Figure 9. The system with PSS for nominal load regime based on M1CO and IACO at ρ=0.5 & 0.2.

$$TF = \frac{-679.8\ s^4 - 1.14*10^4\ s^3 - 4.834*10^4\ s^2 - 4720\ s}{90\ s^7 + 3351\ s^6 + 4.53*10^4\ s^5 + 4.447*10^5\ s^4 + 2.623*10^6\ s^3 + 8.836*10^6\ s^2 + 1.196*10^7\ s + 1.122*10^6}$$

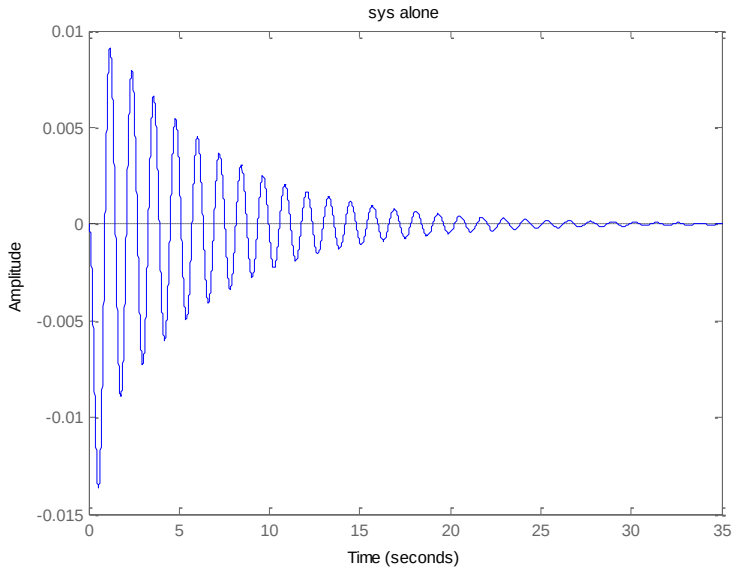

Figure 10. The system alone (without PSS) for light load regime.

$$TF = \frac{-6.326\ s}{s^4 + 20.46\ s^3 + 79.4\ s^2 + 558.4\ s + 1242}$$

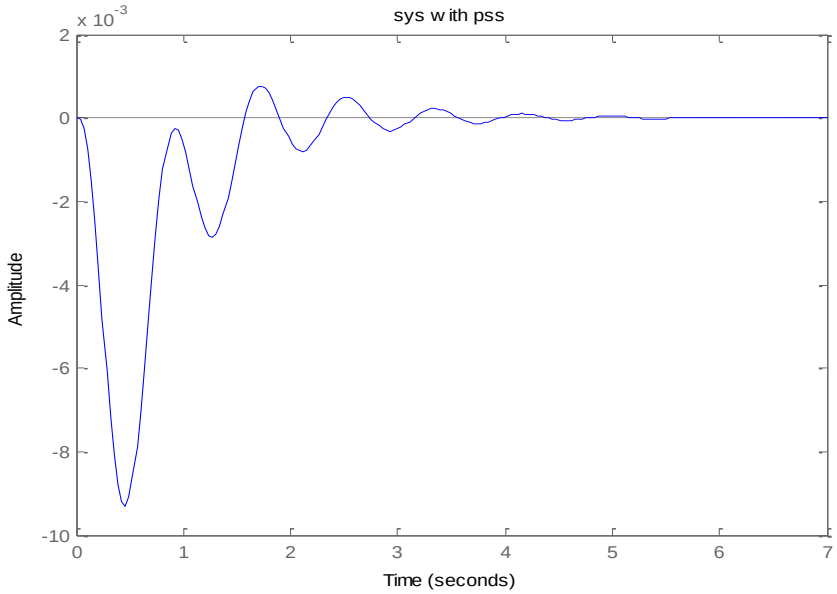

Figure 11. The system with PSS for light load regime based on MACO at ρ=0.5.

$$TF = \frac{-9186\ s^4 - 8.427*10^4\ s^3 - 1.967*10^5\ s^2 - 1.582*10^4\ s}{1452\ s^7 + 4.303*10^4\ s^6 + 4.19*10^5\ s^5 + 3.57*10^6\ s^4 + 1.707*10^7\ s^3 + 4.074*10^7\ s^2 +}$$

$4.001*10^7\ s + 3.104*10^6$

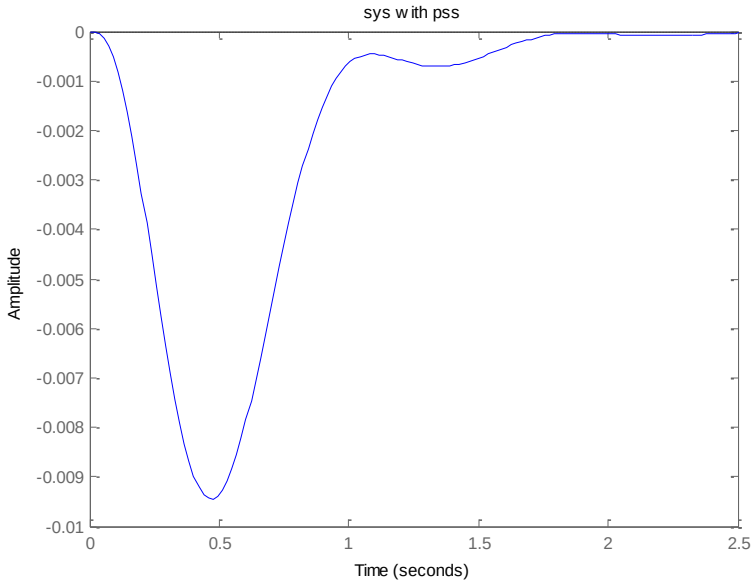

Figure 12. The system with PSS for light load regime based on MACO & IACO at ρ=0.5 & 0.2.

$$TF= \frac{-569.4\ s^4 - 9546\ s^3 - 4.049*10^4\ s^2 - 3954\ s}{90\ s^7 + 3351\ s^6 + 4.442*10^4\ s^5 + 3.942*10^5\ s^4 + 2.092*10^6\ s^3 + 6.525*10^6\ s^2 + 8.295*10^6\ s + 7.76*10^5}$$

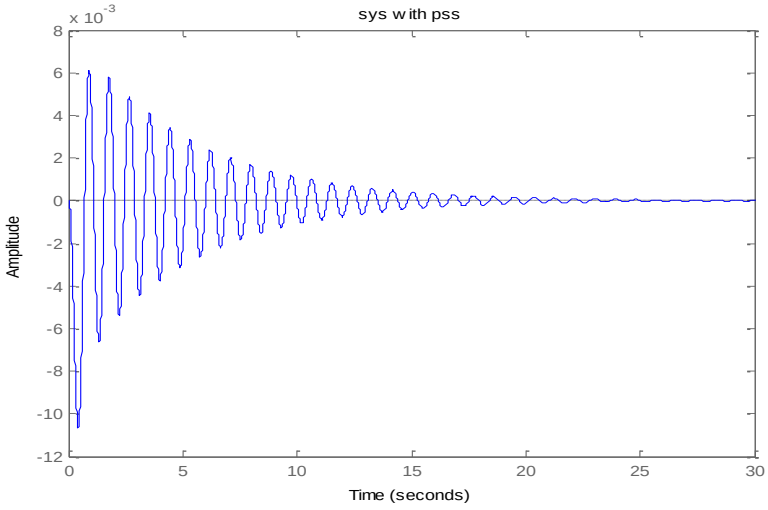

Figure 13. The system with PSS for heavy load regime based on MACO at ρ=0.2.

$$TF= \frac{-2391\ s\text{^}4 - 6.871e04\ s\text{^}3 - 4.993e05\ s^2 - 8.132e04\ s}{294\ s^7 + 1.447*10^4\ s^6 + 2.632*10^5\ s^5 + 2.434*10^6\ s^4 + 1.592*10^7\ s^3 + 8.297*10^7\ s^2 + 1.543*10^8\ s}$$

$+2.363*10^{7}$

Appendix:

The system A, B, C, and D are **Mahmoud, and Soliman, 2012**.

$$A=\begin{bmatrix} 0 & w_o & 0 & 0 \\ -\frac{k_1}{M} & 0 & -\frac{k_2}{M} & 0 \\ -\frac{k_4}{T_{do}^{'}} & 0 & -\frac{1}{T} & -\frac{1}{T_{do}^{'}} \\ -\frac{k_E k_5}{T_E} & 0 & -\frac{k_E k_6}{T_E} & -\frac{1}{T_E} \end{bmatrix}$$

$$x=\begin{bmatrix} \Delta\delta & \Delta w & \Delta E_q^{'} & \Delta E_{fd} \end{bmatrix}$$

$$B=\begin{bmatrix} 0 \\ 0 \\ 0 \\ \frac{k_E}{T_E} \end{bmatrix}$$

C=[0 1 0 0], T=k_3 T'$_{do}$

Optical Character Recognition Using Active Contour Segmentation

Nabeel Oudah. M
Lecturer
Uruk University
nabeeloude@mail.ru

Maher Faik Esmaile
Lecturer
Iraqi Cement State Company
maherfaiq2000@yahoo.com

Estabraq Abdulredaa
Assistant Lecturer
Al-Israa College University
estabraq_ai_1989@yahoo.com

ABSTRACT

Document analysis of images snapped by camera is a growing challenge. These photos are often poor-quality compound images, composed of various objects and text; this makes automatic analysis complicated. OCR is one of the image processing techniques which is used to perform automatic identification of texts. Existing image processing techniques need to manage many parameters in order to clearly recognize the text in such pictures. Segmentation is regarded one of these essential parameters. This paper discusses the accuracy of segmentation process and its effect over the recognition process. According to the proposed method, the images were firstly filtered using the wiener filter then the active contour algorithm could be applied in the segmentation process. The Tesseract OCR Engine was selected in order to evaluate the performance and identification accuracy of the proposed method. The results showed that a more accurate segmentation process shall lead to a more accurate recognition results. The rate of recognition accuracy was 0.95 for the proposed algorithm compared with 0.85 for the Tesseract OCR Engine.

Keywords: OCR, active contour, Segmentation, Automatic Character Recognition, Pattern Recognition, Tesseract OCR Engine.

التعرف الصوئي على الحروف والارقام بااستخدام برنامج الماتلاب

نبيل عوده منيخر
مدرس
جامعة اوروك

ماهرفائق اسماعيل
مدرس
شركة الاسمنت العراقية

استبرق عبد الرضا
مدرس مساعد
كلية الاسراء الجامعة

الخلاصة

تحليل الوثائق من الصور الملتقطة بواسطة الكاميرا هي عملية ذات تحديات متزايدة. حيث ان هذه الصور غالبا ما تكون صور مركبة وذات جودة سيئة، تتألف من مختلف الكائنات والنصوص؛ مما يجعل عملية التحليل التلقائي معقدا. التعرف على الحروف البصرية (OCR)هي واحدة من تقنيات معالجة الصور التي لديها القدرة على اجراء عملية التعرف على الحروف والكلمات بصورة اوتوماتيكية. تقنيات معالجة الصور الحالية تحتاج إلى إدارة العديد من العوامل من اجل اجراء عملية التمييز بصورة صحيحة في مثل هذه الصور. وتعتبر عملية تجزئة الصورة (Segmentation) واحدة من هذه العوامل الأساسية المؤثرة. ناقش هذا البحث تاثير دقة عملية التجزئة (Segmentation) للحرف من صورته وتاثيرها على عملية التعرف الالي. وفقا للطريقة المقترحة، تم تصفية الصورة أولا باستخدام فلتر ويينر (Wiener fitler) ومن ثم يمكن تطبيق خوارزمية active contour لأجراء عملية عملية التجزئة. تم اختيار Tesseract OCR Engine من أجل تقييم الأداء وتحديد دقة الطريقة المقترحة. واظهرت النتائج انه كلما كانت عملية التجزئة دقيقة فان نتائج التعرف ستكون أكثر دقة. وكان معدل دقة التمييز للحروف ٠,٩٥ للخوارزمية المقترحة مقارنة مع ٠,٨٥ لخوارزمية Tesseract OCR Engine.

1. INTRODUCTION

Optical character recognition (OCR) is considered as one of the greatest useful implementations of automatic pattern recognition. Many researches and developments were applied actively for the OCR field since the mid 1950's, **Otu, 1979, Amit Choudhary, 2014**. At present, 100$ is the cost of a rationally good OCR packages. Yet, these OCR packages are still of a limited use for only the recognition of text documents that have high printing quality or carefully written hand printed texts. there are many attempts as well to decrease the replacement error rates and refusal rates even on good quality machine printed text, because the efficient human typist , in spite of the lower printing speed is yet performing much less rates of errors.

The need for the OCR arises when printed information should be legible for man and machine (computer) with the lack of predefined substitution inputs. The individual characteristic of the OCR over the other methods of automatic identification is that there is no need to control the information production process. Typically, an OCR system consists of the following processing steps, **Amit Choudhary, 2014:**

- ✓ Gray level scanning at an appropriate resolution, typically 300{1000 dots per inch,
- ✓ Preprocessing:
  a- Binarization (two-level thresholding), using a global or a locally adaptive method,
  b- Segmentation to isolate individual characters,
  c- (Optional) conversion to another character representation (e.g., skeleton or contour curve)
- ✓ Feature extraction
- ✓ Recognition using one or more classifiers.
- ✓ Contextual verification or post processing.

Many researches were done on the OCR systems. Some of these methods can consider the binarization techniques, **Niblack, 1986, Mori, et al., 1992**, to be as text detection methods. However, when these techniques are used to process a complex scene images their accuracy shall be limited. Luo et al. from Motorola China Research Center have presented camera based mobile OCR systems for camera phones in, **Xi-Ping, et al., 2004, Xi-Ping, et al., 2005**. In, **Xi-Ping, et al., 2004**, the skew angle is assessed from a business card image which is firstly down sampled. After that, this angle is used to correct the skew text regions which are then binarized. The lines and characters within these text regions are segmented and thereafter they are recognized by passing them on an OCR system which is made of a two layer template based classifier. In, **Xi-Ping, et al., 2005**, a presentation of analogous system for Chinese-English mixed script business card images is shown. An outline of a prototype Kanji OCR to recognize Japanese texts which are machine printed and are translated into English has been presented by, **Koga, et al., 2005**. **Laine, Laine, and Olli, 2006,** made a system that just deals with the English capital letters. In the beginning, the input captured mage is skew. This image is repaired by searching for a line with the greatest number of successive white pixels through maximizing the given alignment standard. After that, segmentation is done for the image on the basis of X-Y Tree decomposition then the image is to be recognized via detecting the Manhattan distance based similarity for a set of centroid to boundary features. Yet, this is only applicable for addressing the English capital letters and the acquired precision does not reach the limit of satisfaction to apply this method in reality. The principle of the Region-based and connected component (CC) techniques**, Zhang, and Kasturi, 2008**, is the presumption of the difference between the pixel features of the text and non-text. To obtain correct results from these methods, training sets for classifiers and prior information of text position and scale are required to be

used. The application of the Hybrid methods by **Yi-Feng, et al., 2009**, showed some improvements which are a combination of region-based methods, CCs, and layout analysis methods. Lately, **Li, et al., 2008** and **Du, et al., 2009,** used the Mumford-Shah model, **Mumford, and Shah, 1989**, and Chan-Vese piecewise approximation, **Chan, and Vese, 1999**, respectively to present text line segmentation for handwritten documents.

In, **Wumo, et al., 2001**, one more work is presented to recognize Chinese script of business card images. Furthermore, the developmental researches on the OCR systems for mobile devices extend beyond the limitation of document images recognition. A work on reading LCD/LED displays has been presented by **Shen, at el., 2006,** using a camera phone. In, **Bae, et al., 2005**, a representation for a character recognition system for Chinese scripts has been done.

Based on the above mentioned studies, the OCR systems feasibility is assured besides the fact of the ability of the OCR systems to deal with the handheld devices. However, the approachable computation and accurate segmentation must be the characteristic of these systems' algorithms. They should be computationally efficient, low memory consuming and an efficient segmentation algorithm.

In this paper, we are proposing an automated extraction of characters from images using Weiner filter (as preprocessing) with active contour algorithm to obtain both the character's local and global properties so as to earn a reliable digits' detection. We aim in this research to show the effect of the segmentation process on the OCR recognition accuracy rate from applying an active contour algorithm with Weiner filter and compare the results with the Tesseract OCR Engine, **Smith, 2007, Smith, et al., 2009**, that was the HP Research Prototype and it has been developed and sponsored by Google since 2006. It is considered one of the most accurate open-source OCR engines then available and the Matlab company has built and depended it as a function in its products within the version 2014a and above.

2. METHODOLOGY

In our current work we present an automatic character recognition algorithm that is used to recognize English characters found in image/graphics embedded text documents taken by camera like plate of car's numbers images.

Commonly, color images can be obtained by the modern handheld devices. Color pixels are the component of a color image. These color pixels combines three basic color components i.e. red (r), green (g) and blue (b). The range of values for all these color components is 0-255. Thus, the corresponding gray scale value (x, y) for every single pixel that is also lies between 0-255. Through the scanning process, a digital image of the original document is captured.

The proposed OCR system has the components as can be shown in **Fig. 1**. Firstly, an optical scanner is used to convert the analog document into digits. When the detection of the text containing areas is done, then these symbols can be processed, noise elimination process using Wiener filter is performed in order to make features extraction process in the next step easier. After that, a segmentation process is performed to extract every symbol. Every symbol is then identified through the comparison between the extracted features and the descriptions of the symbol classes gained during a former learning phase. In the end, the words and numbers of the original text are reconstructed by using contextual information.

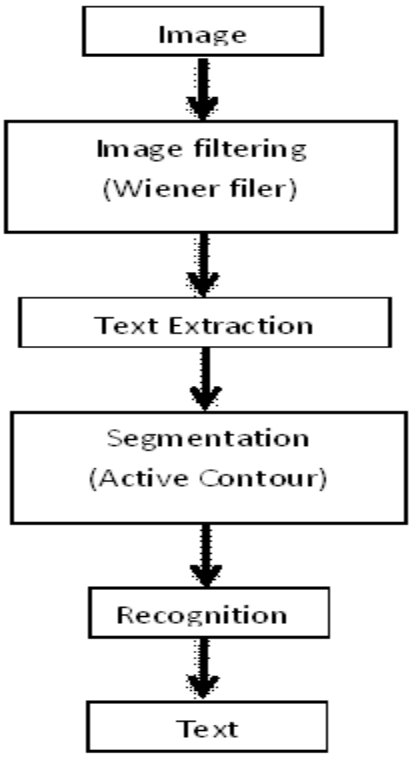

Figure 1. Block diagram of the proposed algorithm.

2.1 Preprocessing

A definite amount of noise can be found in the image that is produced by the scanning process. Smoothing involves both filling and thinning procedures whereas the filling process is done to remove small breaks, gaps and holes in the digitized characters whilst the thinning process will decrease the line width. The Wiener filter would be used in this work to filter out the noise from the corrupted images The Wiener filter is the mean square error optimal stationary linear filter for images degraded by additive noise and blurring. In other words, it minimizes the overall mean square error in the process of inverse filtering and noise smoothing.

2.2 Active Contour

It can be defined as a parametric curve which attempts to move into a place to make its energy decrease and spline guided by external constraint forces and influenced by image forces that pull it toward features such as lines and edges, **Esmaile, et al., 2013, Tiilikainen**. A general edge-detector that can be defined by a positive and decreasing function, depending on the gradient of the image, such that, **Esmaile, et al., 2013, Xu, et al., 1998**:

$$E^*_{snake} = \int_0^1 E_{int}V(s) + E_{img}V(s) + E_{con}V(s)ds \quad (1)$$

From Equation (1) we can find that there are three terms to consist the snake energy. E_{int} is the first term

which is referred to the internal energy of the snake. E_{img} is the second term and is referred to the image forces. Lastly, the term E_{con} is referred to the external constraint forces. Another term is found here. It is the term E_{ext} and it is used to denote the external snake forces which are made up from both the sum of the image force, E_{img} and the external constraint force, E_{con}. The internal energy of the snake is given by, **Esmaile, et al., 2013, Xu, et al., 1998**:

$$E_{int} = \frac{1}{2}\left(\alpha(s)\|V_s(s)\|^2 + \beta(s)\|V_{ss}(s)\|^2 \right), \quad (2)$$

In this equation the measure of the elasticity is given by the first-order term $\| Vs (s)\|^2$ (The first derivatives) and the measure of the curvature is obtained from the second-order term $\| Vss (s)\|^2$ (The second derivatives). The first and second derivatives of the contour represent these energy terms and called "Elastic forces" and "Bending forces", respectively. The total snake energy is controlled by the coefficients $\alpha(s)$ and $\beta(s)$ in such a way that the snake is to be more elastic and less rigid by reduction or rising and vice versa. The parameters α(s) and β(s) in front of each term represents weighting functions. In general, values of these weighting functions are constants for all snaxels. Selecting an appropriate set of these constants creates one of difficulties of the snake. They have large impact in snake's behaviors and totally control the performance of deformation process. Each object in an image requires different set of constants value for snake to perform well. The one way to solve this problem is to make the snake dynamically change these values to suitable values during deformation process. However, it requires a computer to recognize shapes or topologies of an object in an image automatically. Therefore, the solution is left for further improvement of the snake. Currently, these parameters are up for a user to select at the initialization process.

The snake is pulled to the closest image edge via the image forces E_{img}**.** Performance of the image energy can be done depending on the following:

$$E_{img} = w_{int}E_{int} + w_{edge}E_{edge} + w_{term}E_{term} \quad (3)$$

The image forces that are formed by a linear combination of line, edge and termination energy terms will lead to the formation of the energy term. These energy terms are computed from the image in which the Eline and Eedge can be performed as:

$$E_{line} = I(x,y), \quad (4)$$

$$E_{edge} = -\left|\nabla I(x,y)\right|^2, \quad (5)$$

where, I(x,y) represents the image intensity. The term E_{term} can be defined as the curvature of the level contour in Gaussian smoothed image. The adjustment of the weights, w can lead to the creation of a wide range of snake behavior.

The external constraints forces E_{con} are written as, **Esmaile, et al., 2013, Guerrero, et al., 2003**:

$$E_{con} = (x_i - x_{i-1})^2 + (y_i - y_{i-1})^2 \quad (6)$$

Processing of the E_{con} is achieved by allowing the user to introduce a "volcano icon" that aids in pushing the snake faraway. The benefit of this action is to push the snake out of an undesired local minimum. In case when there is discrimination, the representation of the contour is done by N points P1, P2, P3,… PN whereas P1 = (xi, yi) and the first derivative is approximated by a finite difference, **Tang, 1982, Esmail, et al., 2013**.

2.3 Template-matching and correlation techniques

The difference between these methods and the other methods is that there is no actual extraction of features. Instead of that, a direct matching is done for the matrix containing the image of the input character with a set of prototype characters that represents each probable class. A computational process is done for the space between the pattern and each prototype. The best matching class of the prototype is then assigned to the pattern. The hardware implementation of this method is simple and easy. It was applied in many commercial OCR machines. Nevertheless, this method is affected by noise and style variations and it lacks the ability of processing rotated characters.

3. RESULTS AND DISCUSSION

In order to do the OCR performance evaluation there are no standardized test sets exist for character recognition and as the performance of an OCR system is highly dependent on the quality of the input. This makes it difficult to evaluate and compare different systems. Still, recognition rates is usually used to assess the performance of an OCR system, and usually presented as the percentage of characters correctly classified. Accordingly, the following criteria can be applied:

$$Recognition\ rate = CR \times 100 / TT \quad (7)$$

where CR, the number of correctly recognized characters, and TT, the total number of tested characters.

In order to show the effect of the segmentation process over the recognition process accuracy, the proposed need to be compared with another algorithm. Based on that, Tesseract OCR Engine that was built and depended as a function by the Matlab company within the 2014a version was selected for the purpose of that comparison because of its accurate performance with low computational time. The performance and accuracy of the proposed algorithm were measured subjectively and objectively using English sample text and car's plate images (with noised images and different images' resolution and quality).

With Tesseract OCR Engine, **Smith, 2007, Smith, et al., 2009**, the images were filtered, binarized, clipped and resized. Lines of text were then extracted from the images. The font size was identified; segmentation was performed on each line to segment characters taking in consideration the characteristics of English Verdana font's templates. MATLAB (R2014a/64-bit) is used to implement the proposed OCR algorithm. On the other side, the same images have been processed by our proposed methods wherein the first step, the image had been filtered using the wiener filter then had been segmented using active contour algorithm. After that, the recognition process had been applied with the same template that is used in the Tesseract OCR Engine. The hypothesis here is that the accurate

segmentation will lead to the less error rate and high recognition accuracy performance. **Fig. 2** shows the active contour performance to do the segmentation process for the letters. **Fig. 3 and 6** show the results of the proposed algorithm and the Tesseract OCR Engine.

Regarding **Fig. 3**, the proposed algorithm and Tesseract OCR Engine could recognize the connected letters successfully and there is no difference in the both algorithms accuracy's results.

Fig. 4 shows the result of the proposed algorithm and Tesseract OCR Engine for the noised image by the salt and pepper wherein the proposed algorithm could overcome the noise effects while the Tesseract OCR Engine showed approximately 99% error rate with all tested images and it could not overcome the noise effect whereas this test illustrates clearly the effect of the segmentation algorithm on the OCR accuracy and performance. Since the Tesseract OCR Engine wasn't able to overcome the salt and pepper noise type which is considered as a simple type of noise, for this reason there was no need to perform more tests with another type of noise.

As can be seen in **Fig. 5b**, and **5b** the proposed algorithm showed more accuracy than the Tesseract OCR Engine (see 4c, and 5c) wherein some errors can be seen with the results of the Tesseract OCR Engine.g., the symbol (") in the **Fig. 5c** instead of 1, and Z instead of 2 in the **Fig. 6c**). On the same context, an error occurred with the proposed algorithm as can be seen in **Fig. 6b** wherein the letter (I) was not recognized correctly. Table 1 shows the recognition rate and rejection rate for the proposed algorithm and the Tesseract OCR Engine with noised images and with different images' resolution and quality. According to the calculations in Table 1, we can estimate that the error rate was 0.05 and 0.15 for the proposed algorithm and the Tesseract OCR Engine respectively.

4. CONCLUSION

Nowadays, optical character recognition is most effective for constrained matter that is documents generate under various control. This paper has discussed the effect of segmentation accuracy on OCR wherein the active contour with Weiner filter are proposed to be applied in the segmentation process and compared the obtained results with the Tesseract OCR Engine . The results have been shown that more segmentation accuracy results more recognition accuracy. Based on the simulation results, the proposed algorithm has achieved high recognition rate and consequently low error rate results.

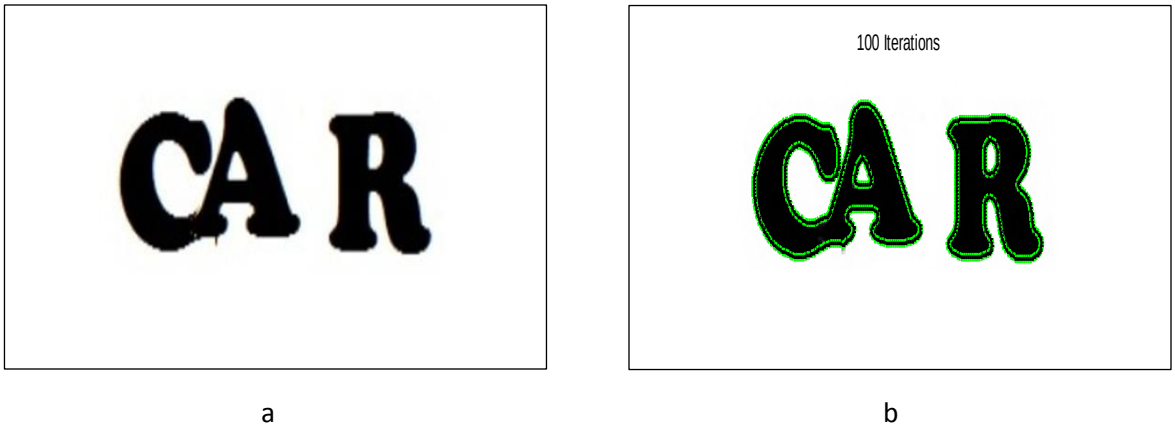

Figure 2. Active contour segmentation, a- original image, b- segmented image.

a

b

c

Figure 3. the comparison result between the proposed algorithm the Tesseract OCR Engine, a. the original image, b. the proposed algorithm, c. the Tesseract OCR Engine.

a

b

c

Figure 4. the comparison results between the proposed algorithm the Tesseract OCR Engine, a. the original image, b. the proposed algorithm, c. the Tesseract OCR Engine.

Table 1. The result of Recognition Rate and Error Rate for the proposed Algorithm and Tesseract OCR Engine

	Connected Letters		Noised Images		Different images quality	
	Proposed	**Matlab**	**Proposed**	**Matlab**	**Proposed**	**Matlab**
Character Recognition Rate	**98%**	**98%**	**98%**	**1%**	**95%**	**90%**
Error rate	**2%**	**2%**	**2%**	**99%**	**5%**	**10%**

a

b

c

Figure 5. the comparison result between the proposed algorithm the Tesseract OCR Engine, a. the original image, b. the proposed algorithm, c. the Tesseract OCR Engine.

a

b

c

Figure 6. the comparison result between the proposed algorithm the Tesseract OCR Engine, a. the original image, b. the proposed algorithm, c. the Tesseract OCR Engine.

REFERENCES

- Amit C., "A Review of Various Character Segmentation Techniques for Cursive Handwritten Words Recognition", International Journal of Information & Computation Technology, ISSN 0974-2239 Volume 4, Number 6, pp. 559-564, 2014.
- Bae. S., Kim K. K., Chung Y. G. and Yu W. P., "Character Recognition System for Cellular Phone with Camera", Proceedings of the 29th Annual International Computer Software and Applications Conference, vol. 1, pp. 539-544, 2005.
- Chan T. and Vese., "An active contour model without edges", in Proceeding of the Second International Conference on Scale-Space Theories in Computer Vision (Scale-Space '99), Corfu, Greece, September pp. 26–27, 1999.
- Du X., Pan W., and Bui T. D., "Text Line Segmentation in Handwritten Documents Using Mumford-Shah Model, Pattern Recognition", vol. 42, pp. 3136-3145, 2009.
- Esmaile M.F., Marhaban M.H., Mahmud R., Saripan, M.I., "Cross -sectional area calculation for arbotary shape in the image using star algorithm with Green's theorem". IEEJ Transactions on Electrical and Electronic Engineering 8(5):497-504(IF:0.343), 2013.
- Guerrero J., Salcudean S. E., McEwen J. A., Masri B. A., Nicolaou S., "Deep Venous Thrombosis Screening System Using Numerical Measures," in Proc. 25th Annual International Conference of the IEEE Engineering in Medicine and Biology Society, Cancun, pp. 894-897, 2003.
- Koga M., Ryuji M., Tatsuya K., Toshikazu T., Masahiro Y. and Teruyuki Y., "Camera-based Kanji OCR for Mobile-phones: Practical Issues", Proceedings of the Eighth International Conference on Document Analysis and Recognition, pp. 635-639, 2005.
- Laine M. and Olli S. N., "A standalone OCR system for mobile camera-phones", Personal, Indoor and Mobile Radio Communications, 2006 IEEE 17th International Symposium, pp.1-5, Sept. 2006
- Li Y., Zheng Y., Doermann D., and Jaeger S., "Script-Independent Text Line Segmentation in Freestyle Handwritten Documents", IEEE Trans. Pattern Anal. Machine Intell., vol. 30, no. 8, pp. 1313 – 1329, 2008.
- Mori S., Suen C. Y., and Yamamoto K., "Historical review of OCR research and developement," Proceedings of the IEEE, vol. 80, pp. 1029-1058, July 1992. 3.
- Mumford D. and Shah., "Optimal approximation by piecewise smooth functions and associated variational problems", Comm. Pure Appl. Math., 42, 577-685, 1989.
- Niblack W., "An Introduction to Image Processing", Prentice-Hall, Englewood Cliffs, NJ, pp. 115-116, 1986.
- Otsu N., "A threshold selection method from grey level histogram", IEEE Trans SMC, 9, pp. 62-66, 1979.
- Shen, H. and Coughlan, J., "Reading LCD/LED Displays with a C amera Cell Phone", Proceedings of the 2006 Conference on Computer Vision and Pattern Recognition Workshop, 2006.

- Smith R., An Overview of the Tesseract OCR Engine, Proceedings of the Ninth International Conference on Document Analysis and Recognition (ICDAR 2007) Vol 2, pp. 629-633, 2007.
- Smith, R., D. Antonova, and D. Lee. Adapting the Tesseract Open Source OCR Engine for Multilingual OCR. Proceedings of the International Workshop on Multilingual OCR, (2009).
- Tang G. Y., "A Discrete version of Green's theorem," IEEE Trans. Pattern Anal Mach Intell, vol. 4, pp. 242-249, 1982.
- Tiilikainen. P., "Comparative Study of Active Contour Snakes," unpublished.
- Wumo P., Jianming J., Guangshun S., Wang Q. R., "A System for Automatic Chinese Business Card Recognition", ICDAR, pp. 577-581, 2001.
- Xi-Ping L., Jun L. and Li-Xin Z., "Design and implementation of a card reader based on build-in camera", International Conference on Pattern Recognition, pp. 417-420, 2004.
- Xi-Ping L., Li-Xin Z., Gang P., Jun L. and Bai-Hua X., "Camera based mixed-lingual card reader for mobile device", International Conference on Document Analysis and Recognition, pp. 665-669, 2005.
- Xu C., Prince J. L., "Snakes, Shapes, and Gradient Vector Flow," IEEE Trans. Image Process, vol. 7, pp. 359-369, 1998.
- Yi-Feng P., Xinwen H., Cheng-Lin L., "Text Localization in Natural Scene Images based on Conditional Random Field", 10th International Conference on Document Analysis and Recognition, Barcelona, Spain, 2009.
- Zhang J. and Kasturi R., "Extraction of text objects in video documents", Recent progress, in Proceeding of the Eighth IAPR Workshop on Document Analysis Systems (DAS'08), pages 1–13, Nara, Japan, 2008.

Second Order Sliding Mode Controller Design for Pneumatic Artificial Muscle

Ammar Al-Jodah
Assistant Lecturer
Control and Systems Eng. Dep.
University of Technology, Baghdad- Iraq
ammar.aljodah@gmail.com

Laith Khames
Assistant Lecturer
Control and Systems Eng. Dep.
University of Technology, Baghdad- Iraq
laithkhames@yahoo.com

ABSTRACT

In this paper, first and second order sliding mode controllers are designed for a single link robotic arm actuated by two Pneumatic Artificial Muscles (PAMs). A new mathematical model for the arm has been developed based on the model of large scale pneumatic muscle actuator model. Uncertainty in parameters has been presented and tested for the two controllers. The simulation results of the second-order sliding mode controller proves to have a low tracking error and chattering effect as compared to the first order one. The verification has been done by using MATLAB and Simulink software.

Keywords: PAM, Sliding Mode Controller.

تصميم متحكم منزلق النمط من الدرجة الثانية لعضله اصطناعية هوائية

عمار الجوده
مدرس مساعد
قسم هندسة السيطرة و النظم
الجامعة التكنولوجية، بغداد-العراق

ليث خميس
مدرس مساعد
قسم هندسة السيطرة و النظم
الجامعة التكنولوجية، بغداد-العراق

الخلاصة

في هذه الورقة تم تصميم مسيطرين منزلقين النمط ذوي الرتبه الاولى و الثانيه للسيطرة على ذراع روبوتيه تدار بواسطة اثنين من العضلات الاصطناعية الهوائية. وقد تم تطوير نموذج رياضي جديد للذراع على أساس نموذج العضله الهوائية الضخمه. تم اختبار المسيطرين بعد الاخذ بعين الاعتبار عدم اليقين في المعاملات. المحاكاة اثبتت ان المسيطر المنزلق ذو الرتبه الثانيه يمتلك نسبة خطأ تتبع منخفضة و كذلك نسبة تأثير الثرثرة منخفضه بالمقارنة مع المسيطر المنزلق ذو الرتبه الاولى. تم التحقق باستخدام برنامج ماتلاب و سيمولينك.

الكلمات الرئيسية: عضلة اصطناعية هوائية ، متحكم الانزلاق.

1. INTRODUCTION

In the past few years, Pneumatic Artificial Muscles (PAMs) has received great attention in the robotics industry for its compact size and high power. Robots are basically exoskeletons with actuators that provide the motion through torque and forces on the joints. Actuators are normally DC or AC motors, hydraulic or pneumatic cylinders. Despite the many advantages of these actuators, there is still a need for an actuator which is compact, flexible and has the ability to deliver higher power. Higher power applications required electric or hydraulic power to move, but pneumatics still have the potential to deliver high power with a compact design. For many years, the Pneumatic actuators were limited in the simple, repetitive tasks with a low level of automation. Pneumatic actuators were not adapted to be used in robotic systems very easily, the mean two obstacles were: 1- Pneumatic systems required complex controllers to achieve a high accuracy. 2- compliance (not robust to load variations). Air compressibility is the prime reason for those obstacles, **Caldwell, et al., 1995.**

PAMs overtake the main obstacles mentioned earlier since these PAMs has all the advantages of pneumatic actuators such as the low cost and compactness, and it does not have the disadvantages of low power and lack of compliance. Such light weight actuators have a great benefit in robotic systems since it will not greatly affect the payload. **Tondu, and Lopez, 2000**

A PAM is simply a cylinder made of a flexible rubber which fits inside a helical braided plastic sheath, **Ching-Ping Chou, and Hannaford, 1996**. This structure makes the PAM widened and shortened when its cylinder inflated. When PAM shorten it deliver high axel force as compared to its weight. The way PAM construction make it very similar to its human counterpart in the extent of its size and force.

Controlling PAM is a very challenging task since PAMs are continuously changing in shape, size, internal pressure, temperature, and axel force. With all these changes it is hard to find an accurate model for the PAM. The nonlinear and robust control technique is highly favorable in controlling PAMs where no accurate model is presented. Several works has been done using those techniques which includes: backstepping control, **Carbonell, et al., 2001** , adaptive control, **Lilly, 2003** and the sliding mode control **Utkin, 1978** , **Carbonell, et al., 2001** , **Lilly, and Liang Yang, 2005** , **Van Damme, et al., 2007** , and **Boudoua, et al., 2015** .

Sliding mode controllers are in the leads of robust controllers that are able to overtake the model uncertainties and external disturbances. I this paper a new model of one link robotic arm actuated by two large scale PAMs is presented. The model of PAMs is augmented with the model of one link robotic arm to have the overall model. Sliding mode controller will be used to control the arm to follow the desired trajectory. Second order sliding mode controller is used to overcome the chattering effect.

This paper is arranged as follows. Section 2 contains the derivation of the mathematical model of one link arm actuated by PAMs in the bicep/tricep configuration. Section 3 presents the derivation of a sliding mode controller for the robotic arm. Section 4 presents simulation results of the control system with the first order and second order sliding mode controllers. Section 5 contains the conclusions.

2. THE MATHEMATICAL MODEL

In general, before any controller design, it is important to obtain a mathematical model for the system to be controlled which is the closest approximation of its true behavior. The system can then be analyzed, and the controller can be designed to meet the required performance. The single link robotic arm is shown in Fig. **1**. The equation of motion of the single link robotic arm is given by

$$(ml^2 + I)\ddot{q} + mgl\cos q = \tau \quad (1)$$

Where $q, \ddot{q}$ are the arm rotation angle and angular acceleration respectively, m is the mass at the end of the arm, l is the arm length, I is the arm moment of inertia, g is the gravitational acceleration, and τ is the torque required to rotate the arm. The torque is generated by the bicep and tricep PAMs and is given by the equation , **Lilly, and Liang Yang, 2005**:

$$\tau = (F_t(.) - F_b(.))r \quad (2)$$

Where $F_t(.)$ and $F_b(.)$ are the forces generated from the tricep and bicep PAMs respectively, r is the pully radius. The PAM model given by **Repperger, et al., 1998,** is used to find $F_t(.)$ and $F_b(.)$ as follows

$$F_t(.) = -K_t(x_t)x_t - B_t(\dot{x_t})\dot{x_t} + P_t \quad (3)$$

$$F_b(.) = -K_b(x_b)x_b - B_b(\dot{x_b})\dot{x_b} + P_b \quad (4)$$

Where $K_t(x_t), K_b(x_b)$ is the tricp and bicep PAM spring coeffecients respectively. These coeffecients are nonlinear function of PAM postion. $B_t(\dot{x_t}), B_b(\dot{x_b})$ is the tricp and bicep PAM damper coeffecients respectively. These coeffecients are nonlinear function of PAM velocity. x_t, x_b are the amount of PAM contraction for tricep and bicep respectively. $\dot{x_t}, \dot{x_b}$ are the velocity of PAM contraction for tricep and bicep respectively. P_t, P_b are the pressure of tricep and bicep PAMs respectively. The $K_i(x_i), B_i(\dot{x_i})$, where $i = (b, t)$ is given by **Repperger, et al., 1998**:

$$K_i(x_i) = k_{1i}x_i^2 + k_{2i}x_i + k_{3i} \qquad i = (b, t) \quad (5)$$

$$B_i(\dot{x_\iota}) = b_{1i}\dot{x_\iota}^2 + b_{2i}\dot{x_\iota} + b_{3i} \qquad i = (b, t) \quad (6)$$

Where $k_{1i}, k_{2i}, k_{3i}, b_{1i}, b_{2i},$ and b_{3i} are constants given in **Table 1, Repperger, et al., 1998**. These constants takes two states, one when the PAM inflated and the other one when it is deflated. The bicep and tricep PAM state is given by

$$\dot{q} < 0 \Rightarrow \begin{cases} bicep\ inflated \\ tricep\ deflated \end{cases}$$
$$\dot{q} > 0 \Rightarrow \begin{cases} bicep\ deflated \\ tricep\ inflated \end{cases} \quad (7)$$

The pressure of tricep and tricep PAM is given by

$$P_t = P_{0t} + \Delta P \quad (8)$$

$$P_b = P_{0b} + \Delta P \quad (9)$$

Where P_{0t}, P_{0b} are the initial pressure of the tricep and bicep respectively, ΔP is the pressure difference between the tricep and bicep respectively. ΔP is the control input to the system. The amount of muscle contraction x_t, x_b is given by **Lilly, and Liang Yang, 2005**:

$$x_t = \left(\frac{\pi}{2} + q\right)r, \dot{x}_t = r\dot{q} \quad (10)$$

$$x_b = \left(\frac{\pi}{2} - q\right)r, \dot{x}_b = -r\dot{q} \quad (11)$$

Where the angle $\frac{\pi}{2}$ is considered as the zero position at which both x_t and x_b is zero.

By substituting Eq. (8) and Eq. (9) in Eq. (3) and Eq. (4), after that substituting in Eq. (2) gives

$$\tau = (-K_t(x_t)x_t - B_t(\dot{x}_t)\dot{x}_t + P_{0t} + \Delta P + K_b(x_b)x_b + B_b(\dot{x}_b)\dot{x}_b - P_{0b} + \Delta P\ )r \quad (12)$$

By substitute Eq. (5) and Eq. (6) in Eq. (12)

$$\begin{aligned}\tau = \big(&-(k_{1t}x_t^2 + k_{2t}x_t + k_{3t})x_t - (b_{1t}\dot{x_t}^2 + b_{2t}\dot{x}_t + b_{3t})\dot{x}_t + P_{0t} + \Delta P \\ &+ (k_{1b}x_b^2 + k_{2b}x_b + k_{3b})x_b + \big(b_{1b}\dot{x_b}^2 + b_{2b}\dot{x}_b + b_{3b}\big)\dot{x}_b - P_{0b} \\ &+ \Delta P\ \big)r\end{aligned} \quad (13)$$

By substituting Eq. (10) and Eq. (11) in Eq. (13) and the result in Eq. (1) gives

$$\left.\begin{gathered}\ddot{q} = \delta_1 q^3 + \delta_2 q^2 + \delta_3 q + \delta_4 \dot{q}^3 + \delta_5 \dot{q}^2 + \delta_6 \dot{q} + \delta_7 \cos q + \delta_8 + bu \\ u = \Delta P \\ \delta_1 = \frac{-r^3(k_{1b} + k_{1t})}{ml^2 + I} \\ \delta_2 = \frac{\frac{3\pi r^4}{2}(k_{1b} - k_{1t}) + r^3(k_{2b} - k_{2t})}{ml^2 + I} \\ \delta_3 = -\frac{(3\pi r^4/2)(k_{1b} - k_{1t}) + \pi r^3(k_{2b} + k_{2t}) + r^2(k_{3b} + k_{3t})}{ml^2 + I} \\ \delta_4 = \frac{-r^4(b_{1b} + b_{1t})}{ml^2 + I} \\ \delta_5 = \frac{r^3(b_{2b} - b_{2t})}{ml^2 + I} \\ \delta_6 = \frac{-r^2(b_{3b} - b_{3t})}{ml^2 + I} \\ \delta_7 = -\frac{glm}{ml^2 + I} \\ \delta_8 = -\frac{r(P_{0b} - P_{0t}) + \frac{\pi r^4}{8}(k_{1t} - k_{1b}) + \frac{\pi r^3}{4}(k_{2t} - k_{2b}) + \frac{\pi r^2}{2}(k_{3t} - k_{3b})}{ml^2 + I} \\ b = \frac{2r}{ml^2 + I}\end{gathered}\right\} \quad (14)$$

The robotic arm parameters are assumed as in **Table 2**.
To consider the uncertainty, the system is represented as following

$$\left.\begin{gathered}\ddot{q} = f_0 + \Delta f + bu \\ f_0 = \delta_1 q^3 + \delta_2 q^2 + \delta_3 q + \delta_4 \dot{q}^3 + \delta_5 \dot{q}^2 + \delta_6 \dot{q} + \delta_7 \cos q + \delta_8 \\ \Delta f = \Delta\delta_1 q^3 + \Delta\delta_2 q^2 + \Delta\delta_3 q + \Delta\delta_4 \dot{q}^3 + \Delta\delta_5 \dot{q}^2 + \Delta\delta_6 \dot{q} + \Delta\delta_7 \cos q + \Delta\delta_8\end{gathered}\right\} \quad (15)$$

Where the nominal values $\delta_i, i = 1,2, \dots ,8$ are given in **Table 3** which obtained by substituting the parameters of **Table 1** and **Table 2** in Eq. (14).
The uncertainty parameters $\Delta\delta_i, i = 1,2, \dots ,8$ is a percentage of the nominal values.

3. SLIDING MODE CONTROLLER DESIGN

The task in sliding mode controller design is to find a function of states called sliding function and a state-feedback control law $u\big(x(t)\big) = u_{eq} + u_{sw}$. The control law will drive the state towards the sliding surface (reaching phase), and then makes it slide on it to origin $x = [0 \quad 0 \quad ... \quad 0 \ ]^T$ (sliding phase). If the states were the error and its derivatives, then a tracking behavior can be ensured if the states return to origin, **Utkin, et al., 2009** . The reaching condition is given by $s\dot{s} < 0$, which is satisfied by the switching part of the control action u_{sw}. The sliding condition is to maintain $s = 0$, which is satisfied by the equivalent part of the control action u_{eq}. The error equation is given by

$$e = q - q_d \tag{16}$$

Where q_d is the desired angle. Diffrentiate Eq. (16) gives

$$\dot{e} = \dot{q} - \dot{q}_d \tag{17}$$

The second derivative of Eq. (17) gives

$$\ddot{e} = \ddot{q} - \ddot{q}_d \tag{18}$$

Define the surface function as following

$$s = \dot{e} + \lambda e \tag{19}$$

The derivative of the surface function is given by

$$\dot{s} = \ddot{e} + \lambda \dot{e} \tag{20}$$

By substituting Eq. (18) in Eq. (20) gives

$$\dot{s} = \ddot{q} - \ddot{q}_d + \lambda \dot{e} \tag{21}$$

By substituting Eq. (15) in Eq. (21) gives

$$\dot{s} = f_0 - \ddot{q}_d + \lambda \dot{e} + \Delta f + bu \tag{22}$$

The proposed control law is given by

$$u = \frac{1}{b}\left(u_{eq} + u_{sw}\right) \tag{23}$$

Where the proposed u_{eq} is

$$u_{eq} = -f_0 + \ddot{q}_d - \lambda \dot{e} \tag{24}$$

Substituting Eq. (24) in Eq. (23) then the result in Eq. (22) gives

$$\dot{s} = \Delta f + u_{sw} \tag{25}$$

Let $u_{sw} = -k \ sign(s)$, Eq. (25) becomes

$$\dot{s} = \Delta f - k \ sign(s) \tag{26}$$

The reaching condition $s\dot{s} \leq 0$ must be satisified as following

$$\begin{aligned} s\dot{s} &= s\Delta f - ks \ sign(s) \\ &= s\Delta f - k|s| \\ &\leq |s||\Delta f| - k|s| \\ &\leq -|s|(k - |\Delta f|) \end{aligned} \tag{27}$$

the above equation is true if the following condition hold

$$k > |\Delta f| \tag{28}$$

In this paper,it has been noted from simulation that selecting k as $k = 1$, will be enough to cancel out the uncertainties in the system. Choosing a value more than one will cause more chattering in the control action.

It is well known that the classical sliding mode controller has a high chattering in the control action. The chattering effect makes things difficult in the implementation because of the high frequency of on and off states which are never practical for the PAM system. To solve this problem, chattering reduction methods is used. One of the methods to reduce the chattering is to consider the second order sliding mode. In the second order sliding mode, the derivative of control action appears in the second derivative of the surface function which represents the virtual control as following, **Bartolini, et al., 2009**:

$$\ddot{s} = \varphi(t,x) + \gamma(t,x)\dot{u}$$

and the following conditions are assumed

$$|u| \le U_M$$
$$0 < \Gamma_m < \gamma(t,x) < \Gamma_M$$
$$|\varphi(t,x)| < \Phi$$

Where U_M, Γ_m, Γ_M, and Φ are positive constants. One of the efficient second order sliding mode algorithms is the super twisting algorithm. The super twisting controller is widely implemented in real-time applications for its high robustness and easy to implement properties. It can be seen as a nonlinear version of the classical PI controller. Super twisting is an algorithm developed specifically to control systems of relative degree one with the main advantage of chattering reduction. The trajectories of the 2-sliding exhibit a twisting motion around the origin, hence the name, see **Fig. 2**. The continuous control $u(t)$ has two terms. The first one is a continuous function of the sliding variable. The second one is an integration of a discontinuous first order differential equation. The control algorithm is defined by the following control law, **Bartolini, et al., 2009:**

$$\mathrm{u} = -\lambda|\mathrm{s}|^{\rho}\mathrm{sign}(s) + \int -\mathrm{W}\ \mathrm{sign}(s)dt \tag{29}$$

the convergence to the sliding manifold will be in finite time if the following sufficient conditions satisfied, **Bartolini, et al., 2009**:

$$W > \frac{\Phi}{\Gamma_m}$$
$$\lambda^2 \ge \frac{4\Phi}{\Gamma_{\mathrm{m}}^2}\frac{\Gamma_M(W+\Phi)}{\Gamma_m(W-\Phi)} \tag{30}$$
$$0 < \rho \le 0.5$$

From Eq. (25), differentiate $\dot{s}$ again to get

$$\ddot{\mathrm{s}} = \Delta\dot{f} + \dot{u}_{sw} \tag{31}$$

From Eq. (31), $\gamma(t,x) = 1$, $\varphi(t,x) = \Delta\dot{f}$, both are bounded. These conditions $0 < \Gamma_m < \gamma(t,x) < \Gamma_M$ and $|\varphi(t,x)| < \Phi$ are satisfied since both $\gamma(t,x)$ and $\varphi(t,x)$ are bounded, however, finding an exact value for $\Gamma_m, \Gamma_M, and\ \Phi$ is difficult. But however, The following values can be used for Γ_m and Γ_M: $\Gamma_m = 0.9$, $\Gamma_M = 1.1$. A conservative value of $\Phi = 0.5$ will be assumed since it is difficult to find an exact estimation. Parameters have to satisfy the following conditions: first condition $W > \left(\frac{\Phi}{\Gamma_m} = 0.5556\right)$ a value of $W = 1$ is chosen, second condition

$\lambda^2 \geq \left(\frac{4\Phi}{\Gamma_m^2}\frac{\Gamma_M(W+\Phi)}{\Gamma_m(W-\Phi)} = 3.6885\right) \Rightarrow \lambda \geq 1.9205$ a value of $\lambda = 2$ is chosen. And finally ρ chosen as $\rho = 0.5$.

4. SIMULATION RESULTS

The Classical Sliding Mode Control (CSMC) system is shown in **Fig. 3**. A smooth desired angle trajectory is used to test the proposed controllers given by **Lilly, and Liang Yang, 2005:**

$$q_d = \pi/2 + 0.5(\sin(2\pi \times 0.02t) + \sin(2\pi \times 0.05t) + \sin(2\pi \times 0.09t)) \quad (32)$$

The initial angle is $57.2958°$. The uncertainty in the parameters is taken as 5 percent. The sampling time has been chosen as 0.001 second. **Fig. 4** shows the desired and actual trajectory of the robot arm angle, it can be noted that the two trajectories are matched after few seconds of the initial position. **Fig. 5** shows the angular velocity of the Arm. It can be noted that the arm suffers from oscillation in the velocity which is comes from the chattering phenomena in the control action. **Fig. 6** shows the control action which has a high amount of chattering this is also apparent in torque in **Fig. 7**, in practice this control action cannot be implemented since there is no way to supply such pressure in this high frequency.

The Second Order Sliding Mode Control (SOSMC) system is shown in **Fig. 8**. The desired angle trajectory is given by Eq. 32. The initial angle is $57.2958°$. The uncertainty in the parameters is also taken as 5 percent. **Fig. 9** shows the angle response of the arm under SOSMC which is faster than the case of CMC. In **Fig. 10** the angular velocity does not suffer from any chattering, that can also be noted in the control action in **Fig. 11** and torque in **Fig. 12**.

In order to measure the effectiveness of the two controllers and make a clear performance comparison, a more aggressive reference command is used. A sudden change reference command is used to test the command following and chattering phenomena. The reference command is consisting of two steps, the first one is a step of $50°$ for the first twenty seconds, the second step is $150°$ and it start from the second 20 to the second 60 as in **Fig. 13**.

Fig. 13 shows that CSMC can follow the step command but with high overshoot, and that's perfectly fine because of the aggressive change in the reference command which induce high error in the controller making it produce high control action. The velocity of CSM is shown in **Fig. 14** where a chattering can be seen. The control action and torque in **Fig. 15** and **Fig.16** respectively shows a high amount of chattering. **Fig. 17** shows the phase plane of the closed loop system, the system starts at the initial condition where $e = 1$ and $\dot{e} = 0$, then it start the reaching phase as can be seen as a half circle below the surface line (the blue line) then it hits the surface line and slide along it to the zero. When the second step happen the system state jumps from zero and enter the reaching phase again as can be seen as the upper half circle then it hits the surface line and slide along it to the zero. It can be noticed the chattering happening in the sliding phase when the states move along $s = 0$. In **Fig. 18** it can be noticed the surface function has a sudden jump at the start of each step and it reach zero after around three seconds.

In SOSMC the angle response is shown in **Fig. 19** where the angle follows the desired command with high overshoot similar to the case of CSMC. In **Fig. 20** the velocity does not suffer from any chattering. The control action and torque are shown in **Fig. 21** and **Fig. 22** respectively, both does not have chattering and the curves appear like a filtered version of the case of CSMC, that's because the Signum function is appeared under the integration operator. The phase plane in **Fig. 23** does not show any chattering and the states slide smoothly in the sliding phase. The surface function curve is shown in **Fig. 24**, the surface function requires

around four seconds to reach zero from the sudden jump, which is a one second more in case of CSMC, this increase in time comes with chattering free unlike the case of CSMC.

5. CONCLUSIONS

In this work, a single link robotic arm actuated by a large scale pneumatic muscle actuator has been studied and explained. A new mathematical model has been developed for this system which has not been developed in pervious researches. This robotic arm suffers from uncertainties in the parameters, these uncertainties comes from the compressibility of the air. In order to have an accurate position tracking, a robust control algorithm is needed. A classical sliding mode controller has been desired as a first step to control the system. It has been noted that this type of controller has a high chattering in the control action which make it impractical to implement in a real system. To mitigate this problem. A second order sliding mode controller is designed. In this controller the term responsible of the chattering phenomena is integrated. The integration operation reduces the chattering greatly and that has been showed in the results.

REFERENCES

- Bartolini, G., Pisano, A. and Usai, E., 2009. *On The Second-Order Sliding Mode Control of Nonlinear Systems With Uncertain Control Direction*. Automatica, Vol. 45, No. 12, pp.2982–2985.

- Boudoua, S., Hamerlain, M. and Hamerlain, F., 2015. *Intelligent Twisting Sliding Mode Controller Using Neural Network for Pneumatic Artificial Muscles Robot Arm*. In 2015 International Workshop on Recent Advances in Sliding Modes (RASM). IEEE, pp. 1–6.

- Caldwell, D.G., Medrano-Cerda, G.A. and Goodwin, M., 1995. *Control of Pneumatic Muscle Actuators*. IEEE Control Systems, Vol. 15, No. 1, pp.40–48

- Carbonell, P., Jiang, Z.P. and Repperger, D.W., 2001. *Nonlinear Control of A Pneumatic Muscle Actuator: Backstepping Vs. Sliding-Mode*. In Proceedings of the 2001 IEEE International Conference on Control Applications (CCA'01) , pp. 167–172.

- Ching-Ping Chou and Hannaford, B., 1996. *Measurement and Modeling of Mckibben Pneumatic Artificial Muscles*. IEEE Transactions on Robotics and Automation, Vol. 12 No. 1, pp.90–102.

- Van Damme, M. et al., 2007. *Proxy-Based Sliding Mode Control of a Manipulator Actuated by Pleated Pneumatic Artificial Muscles*. In Proceedings 2007 IEEE International Conference on Robotics and Automation, pp. 4355–4360.

- Lilly, J.H., 2003. *Adaptive Tracking for Pneumatic Muscle Actuators in Bicep and Tricep Configurations*. IEEE Transactions on Neural Systems and Rehabilitation Engineering, Vol. 11 No. 3, pp.333–339.

- Lilly, J.H. and Liang Yang, 2005. *Sliding Mode Tracking for Pneumatic Muscle Actuators in Opposing Pair Configuration*. IEEE Transactions on Control Systems Technology, Vol. 13 No. 4, pp.550–558.

- Repperger, D.W., Johnson, K.R. and Phillips, C.A., 1998. *A VSC Position Tracking System Involving a Large Scale Pneumatic Muscle Actuator*. In Proceedings of the 37th IEEE Conference on Decision and Control, pp. 4302–4307.

- Tondu, B. and Lopez, P., 2000. *Modeling and Control of Mckibben Artificial Muscle Robot Actuators*. *IEEE Control Systems Magazine*, Vol. 20, No 2, pp.15–38.

- Utkin, V., Guldner, J. and Shi, J., 2009. *Sliding Mode Control in Electro-Mechanical Systems*, 1st edition, Florida, United States, CRC Press.

- Utkin, V.I., 1978. *Sliding Modes and their Application in Variable Structure Systems*. 1st edition, Moscow, Russia, MIR Publishers.

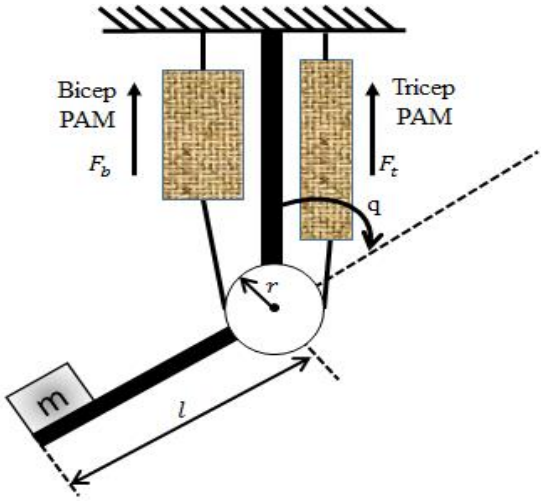

Figure 1. Single link robotic arm actuated by PAMs.

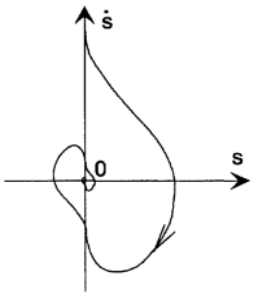

Figure 2. Super-twisting algorithm phase trajectory.

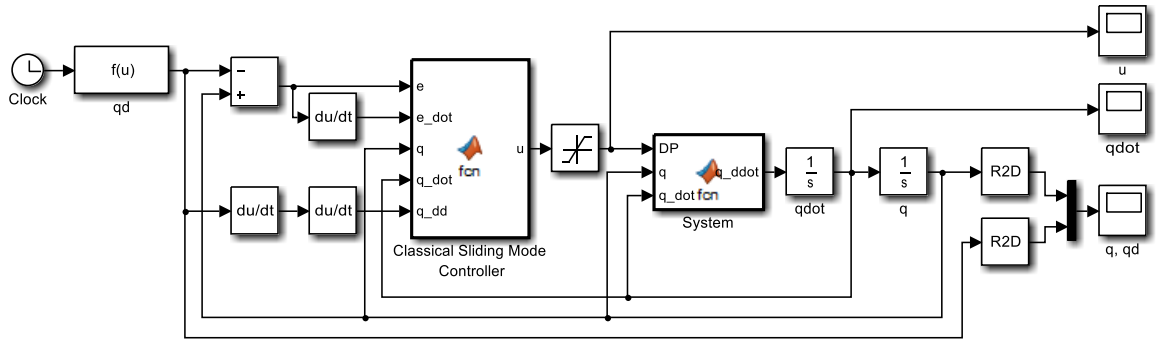

Figure 3. Classical sliding mode control system Simulink.

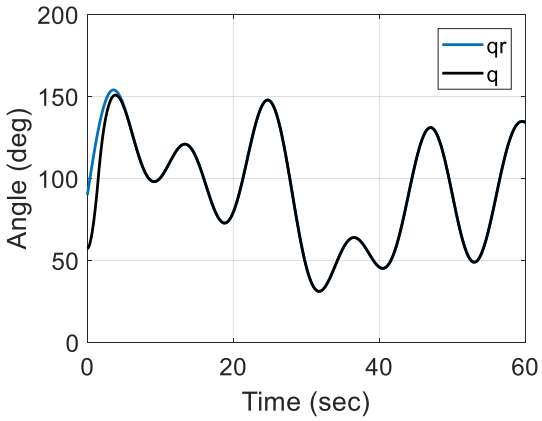

Figure 4. Angle response of CSMC.

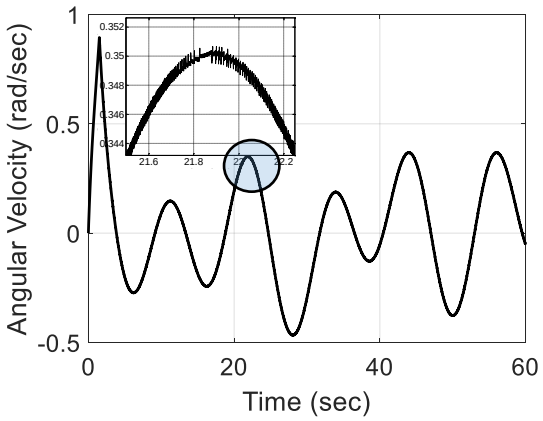

Figure 5. Angular velocity response of CSMC.

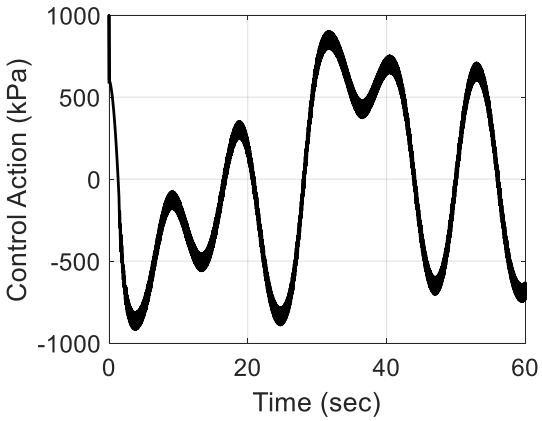

Figure 6. Control action of CSMC.

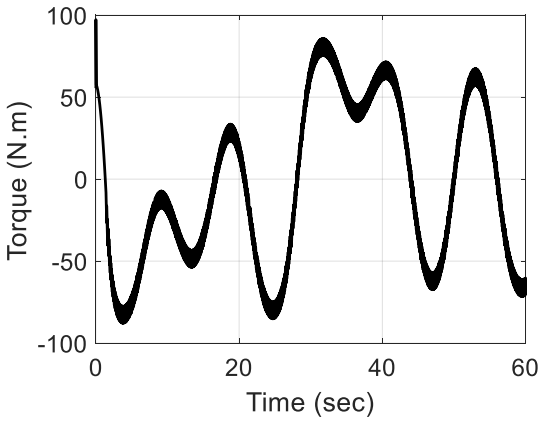

Figure 7. Torque of CSMC.

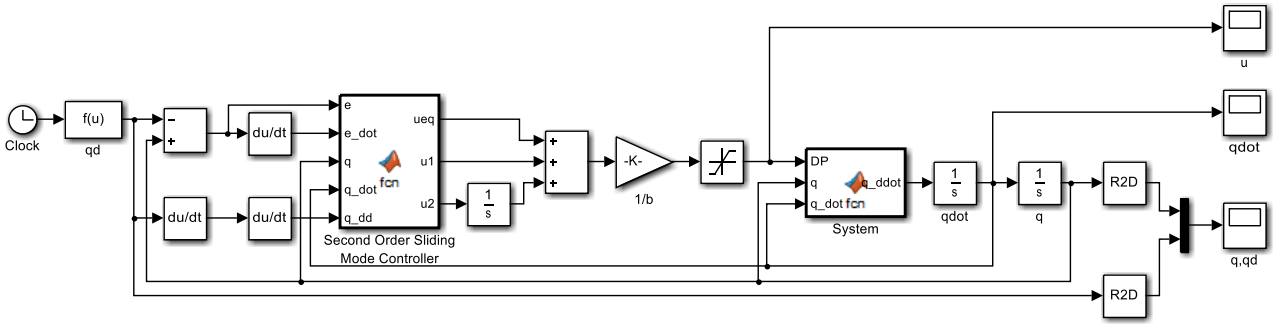

Figure 8. Second order sliding mode control system Simulink.

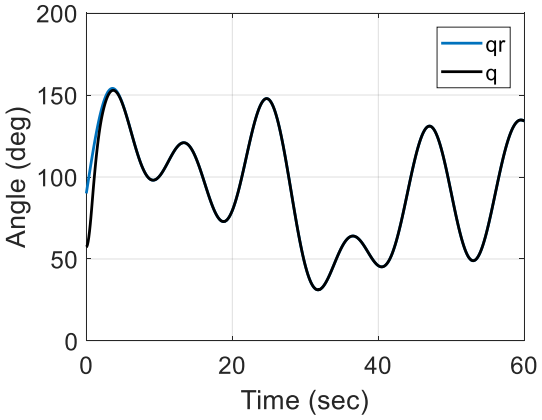

Figure 9. Angle response of SOSMC.

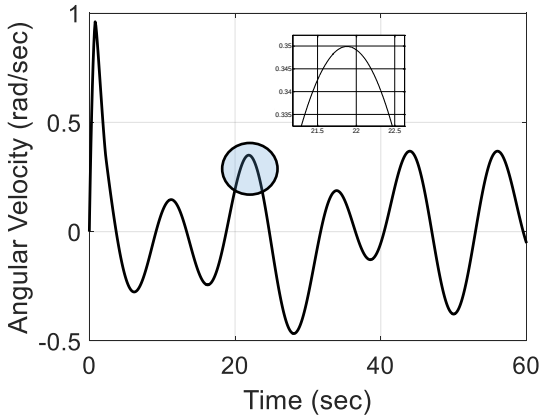

Figure 10. Angular velocity response of SOSMC.

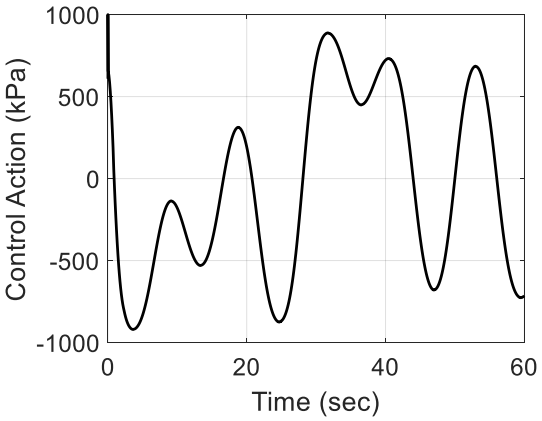

Figure 11. Control action of SOSMC.

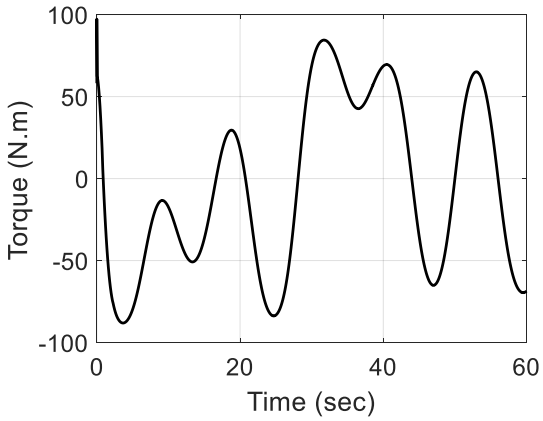

Figure 12. Torque of SOSMC.

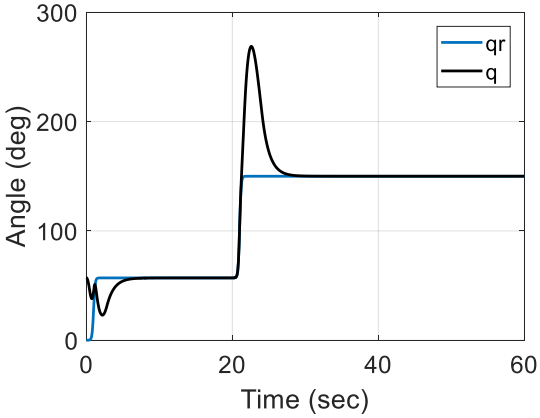

Figure 13. Angle response of CSMC for step command.

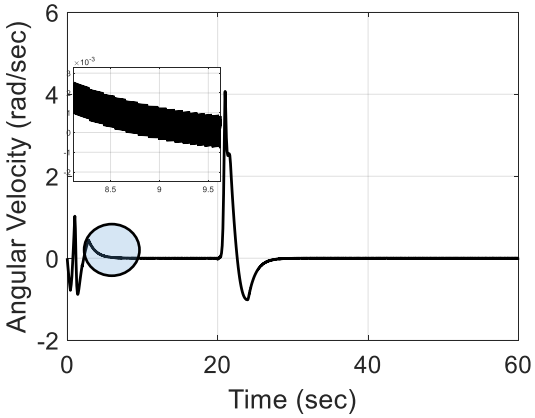

Figure 14. Angular velocity response of CSMC for step command.

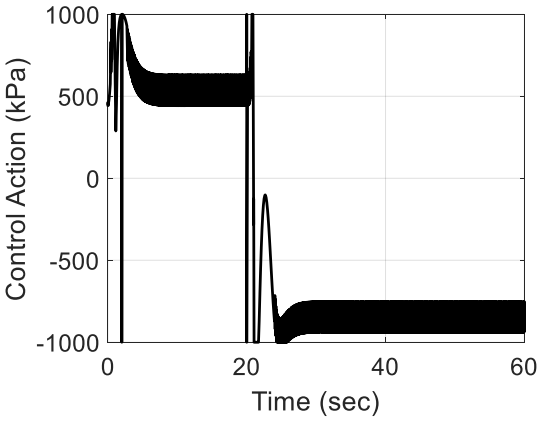

Figure 15. Control action of CSMC for step command.

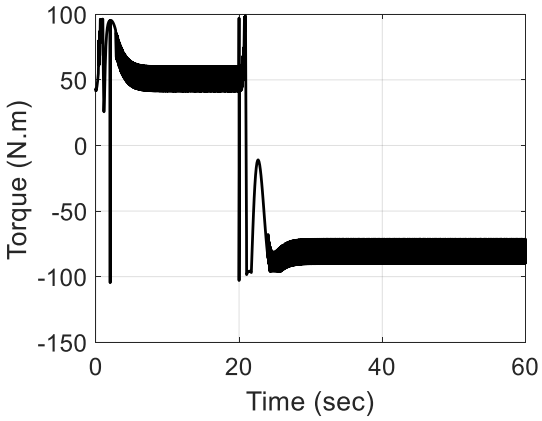

Figure 16. Torque of CSMC for step command.

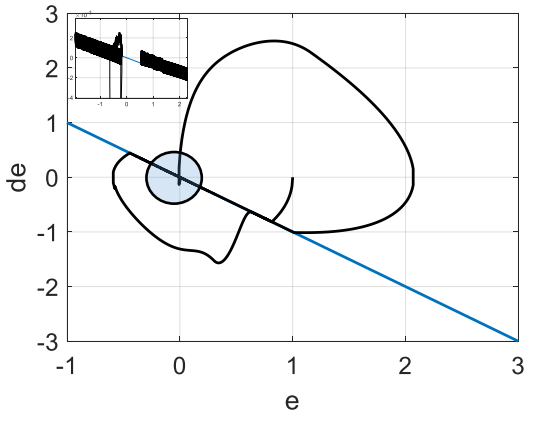

Figure 17. Phase plane of CSMC for step command.

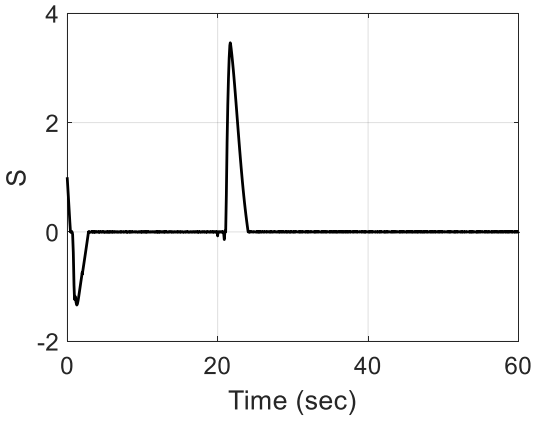

Figure 18. Surface curve of CSMC for step command.

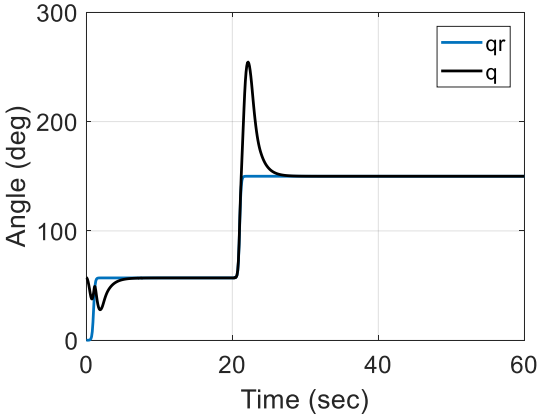

Figure 19. Angle response of SOSMC for step command.

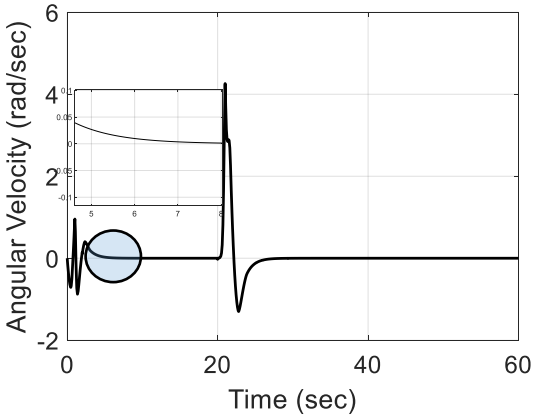

Figure 20. Angular velocity response of SOSMC for step command.

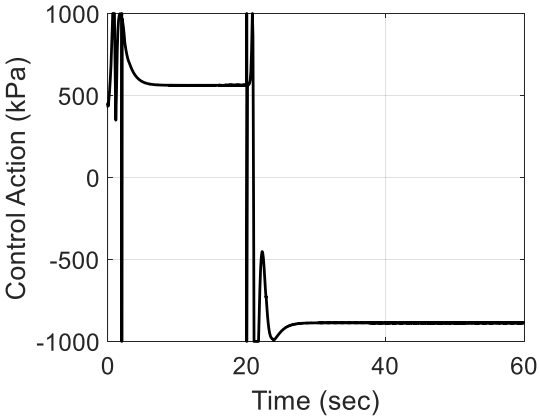

Figure 21. Control action of SOSMC for step command.

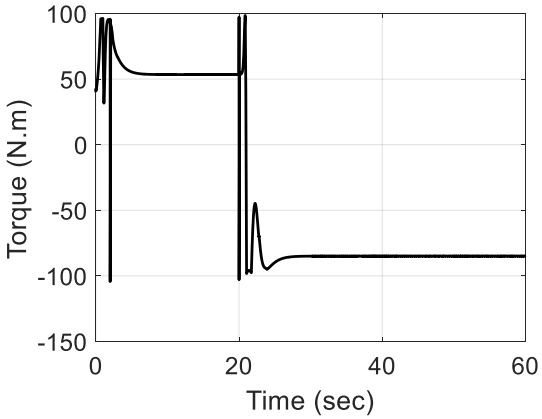

Figure 22. Torque of SOSMC for step command.

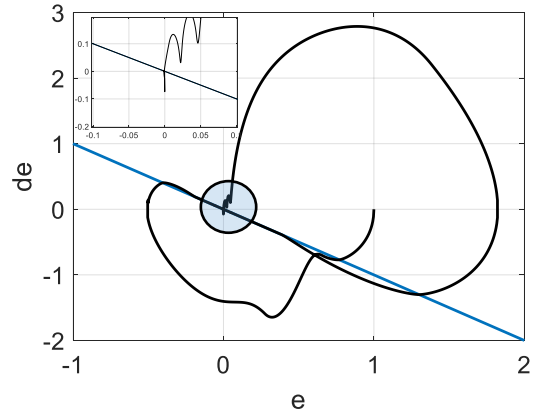

Figure 23. Phase plane of SOSMC for step command.

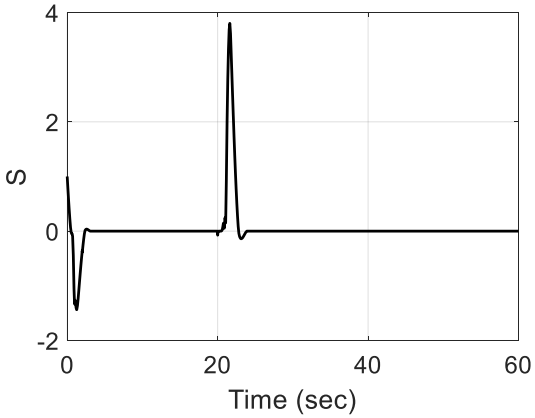

Figure 24. Surface curve of SOSMC for step command.

Table 1. Bicep and tricep PAM parameters, **Repperger, et al., 1998.**

Parameter	Inflated	Deflated
k_{1i}	1.6	3.6
k_{2i}	-10.9	-20.7
k_{3i}	27.1	47.23
b_{1i}	0.04	0.12
b_{2i}	-1.3	-2.49
b_{3i}	12.6	14.48

Table 2. The robotic arm parameters (assumed).

Parameter	value	unit
m	20	Kg
l	0.5	m
I	1.667	$Kg.m^2$
g	9.81	m/s^2
r	0.05	m
P_{0b}	400	kPa
P_{0t}	400	kPa

Table 3. The total system parameters (calculated from Eq. 14)

Parameter	$\dot{q} > 0$	$\dot{q} < 0$
δ_1	-0.00012581	-0.00012581
δ_2	-0.0002257	0.0002257
δ_3	-0.033579	-0.033579
δ_4	-1.9355e-07	-1.9355e-07
δ_5	-2.879e-05	2.879e-05
δ_6	-0.013103	-0.013103
δ_7	-18.9871	-18.9871
δ_8	0.015115	-0.015115
b	0.019355	0.019355

A Nonlinear MIMO-PID Neural Controller Design for Vehicle Lateral Dynamics model based on Modified Elman Neural Network

M.Sc. Khulood E. Dagher
Al-Khwarizmi Collage of Engineering, University of Baghdad
Baghdad - Iraq
dagherkhulood@kecbu.uobagdad.edu.iq

ABSTRACT

This paper presents a new design of a nonlinear multi-input multi-output PID neural controller of the active brake steering force and the active front steering angle for a 2-DOF vehicle model based on modified Elman recurrent neural. The goal of this work is to achieve the stability and to improve the vehicle dynamic's performance through achieving the desired yaw rate and reducing the lateral velocity of the vehicle in a minimum time period for preventing the vehicle from slipping out the road curvature by using two active control actions: the front steering angle and the brake steering force. Bacterial forging optimization algorithm is used to adjust the parameters weights of the proposed controller. Simulation results based Maltab package show the control methodology has effectiveness performance in terms of the excellent dynamic behavior of the vehicle model by minimizing the tracking error and smoothness control signals without saturation state obtained, especially when adding a bounded external disturbances to the vehicle model.
Keywords: Modified Elman Neural Network; PID Controller; 2-DOF Vehicle Model; Bacterial Optimization Algorithm.

تصميم مسيطر عصبي تناسبي-تكاملي- تفاضلي لا خطي متعدد الإدخال والإخراج لنموذج المركبة الجانبي الحركي مبني على أساس الشبكة العصبية ايلمن المعدلة

م. خلود اسكندر داغر
كلية هندسة الخوارزمي – جامعة بغداد
dagherkhulood@kecbu.uobagdad.edu.iq

الخلاصة

إن هذا البحث يقدم تصميم جديد لمسيطر عصبي تناسبي تكاملي تفاضلي متعدد الإدخال والإخراج لقوة توجيه الفرامل الفعال ولتوجيه العجلات الأمامية الفعالة لنموذج المركبة (2-DOF) مبني عل أساس الشبكة العصبية ايلمن المعدلة. إن الهدف الأساسي من هذا العمل هو تحقيق الاستقرارية ة تحسين أداء الحركي للمركبة من خلال تحقق معدل الدوران المطلوب وتقليل السرعة الجانبية في اقصر وقت ممكن لمنع انزلاق المركبة خارج المنعطف باستخدام قوة توجيه الكبح وتوجيه العجلات الأمامية. لقد تم استخدام الخوارزمية الامثلية البكتريا ليجاد و تعديل أوزان العناصر للمسيطر المقترح.من خلال نتائج المحاكاة باستخدام الحقيبة البرمجة ماتلاب تبين إن لهذا المسيطر أداء متين من حيث تصرف حركي ممتاز لنموذج المركبة بتقليل الخطأ ألتتابعي ونعومة إشارات السيطرة بدون الحصول على حالة الإشباع وبصورة خاصة عندما تم إضافة ضوضاء خارجية إلى نموذج المركبة.
الكلمات الرئيسية: الشبكة العصبية ايلمن المعدلة، المسيطر التناسبي التكاملي التفاضلي، نموذج المركبة (2-DOF)، الخوارزمية الامثلية البكتريا.

1. INTRODUCTION

Recently, intelligent vehicles give precious serve for both driver and passengers; they have played a very serious role in traveling safety, comfortably as well as they have reduced the risk of traffic problems. Since the vehicles confront unexpected parameter such as rain, side air force, vehicle wear, road condition, tire pressure loss and external disturbance, different automatic control systems have been developed in a modern car to prevent the spinning, drifting and rolling problems in order to help the driver to keep control on vehicle and to effectively reduce accident by using the modem automotive system technology such as Vehicle Dynamics Control (VDC), Anti-lock Brake System (ABS), Acceleration Slip Regulation (ASR) System, Electronic Stabilization Program (ESP) and Automatic Guidance Control (AGC), **Youngjin, et al., 2017 and Aalizadeh, et al., 2016**.

Thus, many researchers address different ways to control the steering and yaw rate some of these researches are: in, **Chen-Sheng, et al., 2012,** a robust control algorithm which consists of fuzzy neural network for automatic steering vehicle was introduced. In **Mumin, et al., 2014,** a robust PID controller for automated path following steering control driving was presented. In addition to that, **Hongliang, et al., 2010,** designed a sliding mode and back stepping yaw stability controller to make the vehicle yaw rate follow its reference based on model of vehicle yaw rate and wheel dynamics. Also in, **Haiping, et al. 2010**, a robust yaw moment controller for improving both handling and stability was proposed. In, **Ming, et al., 2012 and Bruin, et al., 2000,** the integral robust multi-tier model based back steeping vehicle steering control was explained. In, **Aalizadeh, et al., 2016,** a bee's algorithm and neural network were used as an efficient controller for front steering vehicle was proposed. In, **Gilles, et al., 2013,** a high order sliding mode control for autonomous vehicles was introduced. **Pan, et al., 2012,** designed an adaptive PID for autonomous vehicles control. **Hajjaji, et al., 2006 and Xianjian, et al., 2017**, showed a robust fuzzy controller for vehicle lateral dynamics. **Shijing, et al., 2008**, designed a genetic fuzzy neural network controller for four wheel steering. In **Guo, et al., 2014**, neural network slide mode controller for intelligent vehicle trajectory tracking was presented.

The motivation for this work is taken from **Haiping, et al., 2010, Youngjin, et al., 2017 and Aalizadeh, et al., 2016:** to investigate the stability of the vehicle dynamics by achieving the desired yaw rate and minimizing the lateral velocity to zero value in a short period of time for preventing the vehicle from sliding out the road curvature through designing a two active control actions: the front steering angle and the brake steering force.

The contribution of this research paper is a swift control action which is generated using MATLAB simulation based on the proposed design of the nonlinear MIMO-PID-MENN control law and Bacterial forging optimization algorithm that leads to achieve the yaw rate of the vehicle with minimum lateral velocity. In addition to that, it is distinguished by performance robustness for bounded disturbance effects.

The remainder of this paper is organized as follows: Section 2 described the mathematical model of 2-DOF vehicle. Section 3 presented the proposed of nonlinear PID-MENN controller with Bacterial forging tuning algorithm. Section 4, the performance of the numerical simulation results of the proposed control algorithm is illustrated. The conclusions are drawn in section 5.

2. MODEL OF VEHICLE LATERAL DYNAMICS

In general, the vehicle lateral dynamics motion is affected by many variables such as vehicle speed, vehicle mass and tires state on road, **Mark, et al., 2014**. In order to describe the mathematical vehicle later dynamics model and to achieve the stability of the system, the independent control of lateral and yaw motion requires at least one additional control input, the first one is the front steering angle and the second control signal is as one from three possible solutions as follows: rear wheel steering angle; braking forces; and torque driving wheel, **Martin, et al., 2017**.

This paper focuses on the vehicle yaw rate and lateral velocity as the desired outputs and there are two control actions the front steering angle and the differential braking as inputs to the vehicle model.

Fig. 1 shows the two DOF vehicle model and it is widely used for lateral control design and has been shown to provide accurate response characteristics compared to more complex models for conditions up to 0.3g lateral acceleration, **Haiping, et al., 2010** and **Hajjaji, et al., 2006.**

To describe the mathematical model of vehicle lateral motion with interaction dynamic behavior in multi-input multi-output system can be taken, **Mark, et al., 2014 and Martin, et al., 2017,** as follows:

$$\begin{bmatrix} \dot{L}v \\ \dot{Y}r \end{bmatrix} = \begin{bmatrix} -\frac{C_f + C_r}{MU} & -\frac{C_f a - C_r b}{MU} - MU \\ -\frac{C_f a - C_r b}{IU} & -\frac{C_f a^2 + C_r b^2}{IU} \end{bmatrix} \begin{bmatrix} Lv \\ Yr \end{bmatrix} + \begin{bmatrix} \frac{C_f}{M} & 0 \\ \frac{aC_f}{I} & \frac{T}{2I} \end{bmatrix} \begin{bmatrix} \delta_f \\ F_{BS} \end{bmatrix} \quad (1)$$

$$\begin{bmatrix} y_1 \\ y_2 \end{bmatrix} = \begin{bmatrix} 1 & 0 \\ 0 & 1 \end{bmatrix} \begin{bmatrix} Lv \\ Yr \end{bmatrix} + \begin{bmatrix} d_{\delta_f} \\ 0 \end{bmatrix} \quad (2)$$

Where:

Lv and y_1: represent the lateral velocity; Yr and y_2: represent yaw rate; a : is (1 m) the distance from the center of mass to front axle. b: is (1.5 m) the distance from the center of mass to rear axle; T: is (1.5 m) the vehicle track; C_f : is (55000 N/rad) the front tire cornering stiffness; C_r : is (45000 N/rad) the rear tire cornering stiffness; g: is (9.81 m/sec^2) the acceleration of gravity; I: is (1500 kg m^2) the vehicle moment of inertia; M: is (1000 kg) the vehicle mass; δ_f : is the front steering angle; F_{Bs} : is brake steer force; d_{δ_f} : is the dynamics disturbances.

The brake steer force F_{Bs} in equation (1) can be described as in equations (3 and 4) as follows **Martin, et al., 2017**:

$$M_{BS} = \frac{T}{2}(F_{XR} - F_{XL}) \quad (3)$$

$$F_{BS} = F_{XR} - F_{XL} \quad (4)$$

where:

M_{BS} : is brake steer moment. F_{XR} and F_{XL} : are front and rear longitudinal tire forces respectively.

3. NONLINEAR MIMO-PID-MENN CONTROL DESIGN

In general, the traditional PID controller cannot be used as efficient organizers to achieve the desired outputs for multi-input multi-output system with dynamic behavior interaction. In fact, the proposed controller must work properly and instantly for different roads curvature to prevent the vehicle from sliding out the road in real time. Therefore, the general nonlinear MIMO-PID-MENN controller structure will be designed as shown in **Fig. 2**, where the outputs of the nonlinear MIMO-PID-MENN controller automatically control the vehicle lateral motion by using the brake steering force and the front wheel steering angle during the vehicle rotation on the curvatures.

It consists of three parts:

The first part is the simple structure of the PID controller that has many abilities such as an applicability, high robustness performance and widespread use with three control gains parameters that can be optimized and adjusted during the on-line control process. The PID control equation is given by Eq. (6), **Al-Araji, 2014**.

$$u(t) = k_p e(t) + k_i \int_0^t e(t)d(t) + k_d \frac{de(t)}{dt} \quad (6)$$

where: the proportional gain (k_p); the integral gain (k_i); the derivative gain (k_d); the control action ($u(t)$) and the error signal ($e(t)$).

The second part is modified Elman recurrent neural network which constructed from four layers and each has its own operation as explained below, **Al-Araji, et al., 2011**:

- Input Layer: It works as a buffer i.e. passes the data with scaling modification.
- Hidden layer: It contains the non-linear activation functions.
- Context layer: It works as a memory for the previous layer i.e. non-linear activation functions.
- Output layer: It represents a linear collector unit which adds the all fed signals with scaling modification.

The structure of nonlinear MIMO-PID-MENN controller is shown in **Fig.3**. The parameters weights of the proposed controller are: $kp_{1,2}$,$ki_{1,2}$ and $kd_{1,2}$ hidden layers weights while the parameters weights in the context layers are $Vc_{1,2}$; *Li* **:** Linear node activation function; *H* **:** Sigmoid nonlinear activation function. $h^o_{c\,1,2}(k)$: are context unit outputs; $h_{1,2}(k)$:are hidden unit outputs; α **:** is the self-connections feedback gain it is represented randomly between (0 to 1); β: is the connection weight from the hidden layer to the context layer it is represented randomly between (0 and 1); $e_{Yr}(k)$ *and* $e_{Lv}(k)$*:*are input error signals; $F_{BS}(k)$: is the differential braking system control action signal; $\delta_f(k)$: is the front wheel steering angle control action signal. The proposed control law equation for both the brake steering force control signal and the front wheel steering angle control signal of the MIMO-PID-MENN controller for the vehicle lateral dynamics motion are as follows:

$$\delta_f(k) = h_1(-) - h_2(-) \tag{7}$$

$$F_{BS}(k) = h_2(-) - h_1(-) \tag{8}$$

The outputs $h_{1,2}(-)$ of the modified Elman neural network as in equations (9 and 10) depend on the sigmoid activation function, **Al-Araji, 2015**:

$$h_1(-) = \frac{2}{1+e^{-net_1(-)}} - 1 \tag{9}$$

$$h_2(-) = \frac{2}{1+e^{-net_2(-)}} - 1 \tag{10}$$

$net_{1,2}(-)$ are calculated from these equations (11 and 12), respectively:

$$net_1(-) = (kp_1 \times (e_{Yr}(k) + ki_1 \times (e_{Yr}(k) - e_{Yr}(k-1) + kd_1 \times (e_{Yr}(k) - e_{Yr}(k-1)) + (Vc_1 \times h^o_{c\,1}(k)) \tag{11}$$

$$net_2(-) = (kp_2 \times (e_{Lv}(k) + ki_2 \times (e_{Lv}(k) - e_{Lv}(k-1) + kd_2 \times (e_{Lv}(k) - e_{Lv}(k-1)) + (Vc_2 \times h^o_{c\,2}(k)) \tag{12}$$

Where:

$$h^o_{c\,1}(k) = \alpha h^o_{c\,1}(k-1) + \beta\delta_f(k-1) \tag{13}$$

$$h^o_{c\,2}(k) = \alpha h^o_{c\,2}(k-1) + \beta F_{BS}(k-1) \tag{14}$$

So, the feedback nonlinear MIMO-PID-MENN controller is very necessary to track and stabilize the tracking error in each of the lateral velocity and the yaw rate for the vehicle model outputs by using two control signals front steering angle and braking force.

Therefore, the new proposed nonlinear MIMO-PID-MENN has considerable properties which can be summarized by :

- Fast learning, high adaptation performance, high order control performance and this is due to the context units in MENN which memorize the previous activations of the hidden units.
- Good dynamic characteristic, no output oscillation and strong robustness performance and it is due to the self-connections in the context units which increase the order of the controller model.

In this work, a scaling factor S_F is needed to be added in the output layer for the MIMO-PID-MENN controller to convert the scaled values to actual values and it is equal to 5000 because the maximum value of the differential braking system control action for this model is equal to 5000 N.
The parameters weights of the MIMO-PID-MENN controller $kp_{1,2}$, $ki_{1,2}$, $kd_{1,2}$, *and* $Vc_{1,2}$ will be on-line adjusted by using Bacterial forging optimization algorithm.
The third part is Bacterial forging optimization algorithm which is proposed by **Passino, 2002**, it was considered a successful foraging strategy because of the notion of the natural selection which tended to eliminate the animals as well as it can be defined as a swarm intelligence technique because it had an individual and group foraging policies of the (E. Coli) bacteria in human intestine, **Das, et al., 2009**, as shown in **Fig. 4**.
The E. Coli bacteria is one of bacterial types, so it is always trying to find the best place by using two kinds of motion (swim or tumble) in order to get a high nutrient level and to avoid noxious places as shown in **Fig. 5**, **Das, et al., 2009**. The first motion is forward swimming or running when E. Coli bacteria are moving at a very fast rate in the direction of higher nutrient level and it is called "chemo-taxis". The second motion is tumbling in uncertain direction with a very small displacement movement when the bacteria are arrived in a place with a lower nutrient level, **Munoz, et al., 2010.**
In general, Bacterial foraging optimization theory is explained by moving in the direction of nutrient value, where every bacterium releases chemical substances of attractant when heading to a nutritious place and repellent when they are near a noxious place and the following steps: Chemo-taxis, Swarming, Reproduction and Elimination and dispersal, **Das, et al., 2009 and Munoz, et al., 2010.**

Chemo-taxis Step: the equation that described the E. coli cell movement through swimming or tumbling via flagella as in Eq. (15):

$$P(i,(j+1),k,l) = P(i,j,k,l) + C(i)\emptyset(i) \quad (15)$$

Where:
$P(i,j,k,l)$: is the i^{th} bacterium position [kp_1, ki_1, kd_1, kp_2, ki_2, kd_2, Vc_1 and Vc_2] at the j^{th} chemo-taxis at k^{th} reproduction and l^{th} elimination and dispersal step.
$C(i)$: is the step size of the tumble direction.
$\emptyset(i)$: is the random of the length direction.

Swarming Step: this step gives the bacteria meet into groups to search the perfect path of food and reach the desired place quickly where every bacterium must be tried to attract other bacteria to make a high bacterial density by using Eq. (16):

$$J_{cc}(P(j,k,l),N(j,k,l)) = \sum_{i=1}^{S} J_{cc}^{i}\,(P(-),N(-)) \quad (16)$$

Where:
$J_{cc}(P(-),N(-))$: is the cost function value.
S : is the total number of bacteria.
p : is the number of parameters to be optimized as $P = \left[P_1, P_2, \ldots, \theta_p\right]^T$.

Reproduction Step: The healthier bacteria will generate two bacteria in the same location while the lower healthy bacteria ultimately die therefore, the swarm size is kept a constant.

Elimination and Dispersal step: in this step, the process of elimination and dispersal is very important to guarantee the diversity of new individuals and to find a place that may be near from a good food sources and in this algorithm the probability value to make the bacteria eliminated and dispersed is (0 to 1) where the elimination and dispersal probability value is denoted as (P_{ed}).
The flowchart of the nonlinear MIMO-PID-MENN tuning control algorithm is shown in **Fig. 6.**

4. SIMULATION RESULTS

The proposed MIMO-PID-MENN controller with tuning control algorithm based on Bacterial forging optimization is carried out by Laptop computer simulation using Matlab package (2012) as m file program codes. In this paper, seven regions of operation have been taken depending on the variable speed of the vehicle as "15, 25, 35, 40, 30, 20 and 10" m/sec therefore, we have seven transfer functions for the dynamic model of the vehicle that was described in section two. So The desired lateral velocity for the dynamic model of the vehicle should be zero value in order to overcome the vehicle which may rotate around itself at high vehicle velocity while the desired yaw rate should be defined as in Eq. (17):

$$Yr_{des}(k) = \frac{U(k)}{R} \tag{17}$$

Where: R is curvature radius and it is equal to 100 m.

It is very important to add scaling function at output of the proposed controller in order to overcome a numerical problem that is involved within real values by converting the scaled values to actual values where the differential braking range is $\pm$ 5000 N while the front steering angle is ± 0.1rad.

To apply the proposed control scheme to the 2-DOF vehicle model, the proposed tuning control algorithm of BFO defined the parameters as follows: S is the total bacteria number and it equals to twenty; I the iteration number and it is equal to twenty; N_c is the number of chemo-tactic steps and it equals to ten; N_s is the swimming length and it equals to five; N_{re} is the number of reproduction steps and it equals to four; N_{ed} is the number of elimination-dispersal events and it equals to three; p_{ed} is the number of elimination-dispersal probability and it equals to 0.25 as proposed value and p is the cell number in BFO tuning algorithm and it equals to eight because of only eight parameters weights of MIMO-PID MENN controller to be adjusted.

To show the performance of the proposed MIMO-PID-MENN controller, there are seven steps change in the desired of yaw rate with sampling time is equal to 0.01 sec for minimum time constant from these seven transfer functions based on Shannon theorem while the desired lateral velocity is equal to zero.

Fig. 7-a observes the actual yaw rate output of the vehicle mode is fast tracking the desired yaw rate without overshoot state while the **Fig. 7-b** shows the actual lateral velocity of the vehicle that started from -2 $\times 10^{-7}$ m/sec at very short transit state to zero value at steady state. The yaw rate error and lateral velocity error can be shown in **Figs. 8-a,** and **b**, respectively. **Figs. 9-a,** and **b** show the response of the two feedback control actions brake steer force "differential braking" and front steering angle respectively in order to achieve the desired yaw rate and to make the lateral velocity is equal to zero. The parameters weights of the nonlinear MIMO-PID-MENN controller have been adjusted and tuned in each state of the seven steps change in the desired yaw rate for the vehicle model, as shown in **Table 1**.

To confirm that the nonlinear MIMO-PID-MENN has a capability of the adaptation and robustness performance, a disturbance term $\delta_{dis} = 2\times10^{-3}\sin(100t)$, **Haiping, et al., 2010** has been added to the vehicle model that represents the dynamics disturbances. **Fig. 10-a** shows the response of the yaw rate of the vehicle which did not drift from the desired as well as it has very small overshoot while **Fig. 10-b** shows the lateral velocity of the vehicle that the response has a very small oscillation magnitude equals to ±0.008 m/sec. The yaw rate error signal and lateral velocity error can be shown in the **Figs. 11- a,** and **b**, respectively for disturbance effects. The differential braking control signal and the front steering angle control signal of the nonlinear MIMI-PID-MENN for vehicle model with disturbance effect can be shown in **Figs. 12-a,** and **b**, respectively .

5. CONCLUSIONS

The nonlinear MIMO-PID-MENN controller with Bacterial forging optimization algorithm for MIMO dynamic vehicle motion model has been presented in this paper. The yaw rate and lateral velocity are the state outputs of the 2-DOF vehicle model and they are excellent tracked the desired inputs because the proposed controller with BFO algorithm generated two control actions front steer angle and differential brake through finding and tuning the best and high stable parameters weights of the controller with minimum time and no oscillation in the output. Simulation results of lateral motion show that the effectiveness of proposed nonlinear MIMO-PID-MENN controller; this is demonstrated by the minimized tracking error of the lateral velocity and yaw rate to reach zero value in a short time period as well as the smooth control signal which has been obtained at different velocities of the vehicle model, especially when adding the external front steering angle disturbances problem.

6. REFERENCES

- Aalizadeh, B. and Asnafi, A., 2016, "*Integrated Bees Algorithm and Artificial Neural Network to Propose an Efficient Controller for Active Front Steering Control of Vehicles*". International Journal of Automotive and Mechanical Engineering (IJAME). Vol. 13, No. 2, pp. 3476 - 3491.
- Al-Araji, A. , 2014, "*Applying Cognitive Methodology in Designing On-Line Auto-Tuning Robust PID Controller for the Real Heating System*. Journal of Engineering. Vol. 20, No. 9, pp. 43-61.
- Al-Araji, A., 2015, "*A Cognitive PID Neural Controller Design for Mobile Robot Based on Slice Genetic Algorithm*". Engineering & Technology Journal. Vol. 33, No. 1, pp. 208-222.
- Al-Araji, A., Abbod, M., Raweshidy, H., 2011, "*Design of a Neural Predictive Controller for Nonholonomic Mobile Robot Based on Posture Identifier*". Proceedings of the IASTED International Conference Intelligent Systems and Control (ISC 2011), Cambridge, United Kingdom, pp.198-207.
- Bruin, D., Damen, A., Pogromsky, A. and Boscli, J., 2000, "*Backstepping Control for Lateral Guidance of All-wheel Steered Multiple Articulated Vehicles*". IEEE Intelligent Transportation Systems Conference Proceedings Dearborn (MI), USA, pp. 95-100.
- Chen-Sheng, T., Yong-Nong, C., 2012, " *A Robust Fuzzy Neural Control Approach for Vehicle Lateral*". Dynamics. Procedia Engineering, Vol. 29, pp. 479 – 483.
- Das, S., Biswas, A., Dasgupta, S. and Abraham, A., 2009 "*Bacterial Foraging Optimization Algorithm: Theoretical Foundations, Analysis, and Applications*". Foundations of Computational Intelligence, Vol. 203 of the series Studies in Computational Intelligence, pp. 23-55.
- Gilles, T., Reine, T. and Ali, C. ,2013, "*Higher-Order Sliding Mode Control for Lateral Dynamics of Autonomous Vehicles with Experimental Validation*". IEEE Intelligent Vehicles Symposium, Gold Coast, Australia, pp.678-683.
- Guo, L., Ping-shu, G., Yang, X. and LI, B., 2014,"*Intelligent Vehicle Trajectory Tracking Based on Neural Networks Sliding Mode Control*". International Conference on Informative and Cybernetics for Computational Social Systems (ICCSS), pp. 57-62.
- Haiping, D., Nong, Z. and Guangming, D.,2010,"*Stabilizing Vehicle Lateral Dynamics With Considerations of Parameter Uncertainties and Control Saturation Through Robust Yaw Control*". IEEE Transactions on Vehicular Technology, Vol. 59, No. 5, pp. 2593-2597.
- Hajjaji, A., Chadli, M., Oudghiri, M. and Pagès, O., 2006," *Observer-based Robust Fuzzy Control for Vehicle Lateral Dynamics*". Proceedings of the 2006 American Control Conference Minneapolis, Minnesota, USA, pp. 4664-4669.
- Hongliang, Z. and Zhiyuan, L., 2010, "*Vehicle Yaw Stability-Control System Design Based on Sliding Mode and Backstepping Control Approach*". IEEE Transactions on Vehicular Technology, Vol. 59, No. 7, pp. 3674-3678.
- Mark, W., Matthias, D. and Tobias. O, 2014,"*State Estimation of Vehicle's Lateral Dynamics using Unscented Kalman Filter*". The 53rd IEEE Conference on Decision and Control. Los Angeles, California, USA, pp. 5015-5020.
- Martin, M. and Martin H., 2017," *Linear Analysis of Lateral Vehicle Dynamics*". The 21st International Conference on Process Control (PC), Strbske Pleso, Slovakia. , pp. 240-246.
- Ming, X. and Mark, M., 2012, "*Backstepping Vehicle Steering Controller Using Integral and Robust Control Based on Dynamic State Estimation*". IEEE/RSJ International Conference on Intelligent Robots and Systems, pp. 3132-3137.

- Mumin, E., Esmail, C., Bilin, G. and Levent, G., 2014," *Robust PID Steering Control in Parameter Space for Highly Automated Driving*". Hindawi Publishing Corporation International Journal of Vehicular Technology, Vol. 2014, pp. 1-8.
- Munoz, M., Halgamuge, S., Alfonso, W. and Caicedo, E., 2010, "*Simplifying the Bacteria Foraging Optimization Algorithm*". The IEEE World Congress on Computational Intelligence, Barcelona, Spain, pp. 4095-4101.
- Pan, Z., Jiajia, C., Yan, S., Xiang, T., Tiejuan X. and Tao, M., 2012," *Design of a Control System for an Autonomous Vehicle Based on Adaptive-PID*". International Journal of Advanced Robotic Systems. Vol. 9, No. 44, pp. 1-11.
- Passino, K., 2002, "*Biomimicry of Bacterial Foraging for Distributed Optimization and Control*". The IEEE Control Systems and Managements. pp. 52–67.
- Shijing, W., Enyong, Z., Ming, Q., Hui, R. and Zhipeng, L., 2008, "*Control of Four-Wheel-Steering Vehicle Using GA Fuzzy Neural Network*". International Conference on Intelligent Computation Technology and Automation, pp. 869-873.
- Xianjian, J., Guodong, Y. and Junmin, W.,2017," *Robust Fuzzy Control for Vehicle Lateral Dynamic Stability via Takagi-Sugeno Fuzzy Approach*". American Control Conference Sheraton Seattle Hotel, Seattle, USA, pp. 5574-5579.
- Youngjin, J., Minyoung, L., In-Soo, S. and Kwanghee, N., 2017,"*Lateral Handling Improvement with Dynamic Curvature Control for an Independent Rear wheel Drive EV*". International Journal of Automotive Technology, Vol. 18, No. 3, pp. 505−510.

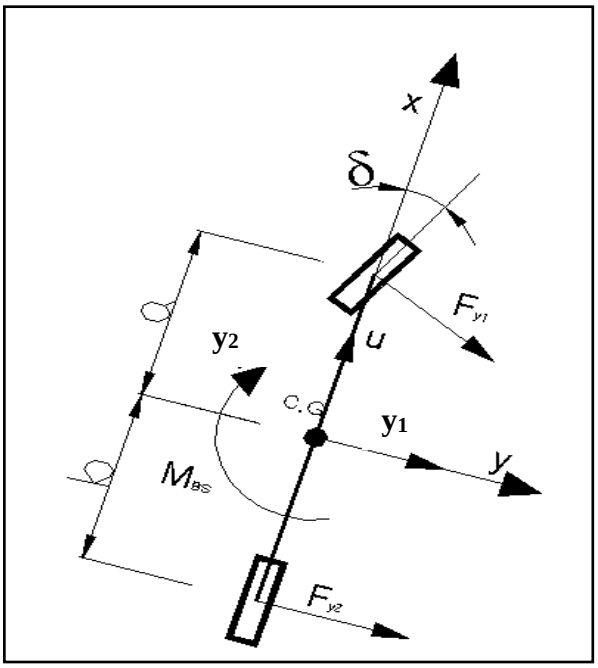

Figure 1. The Schematic diagram of two DOF Vehicle Models.

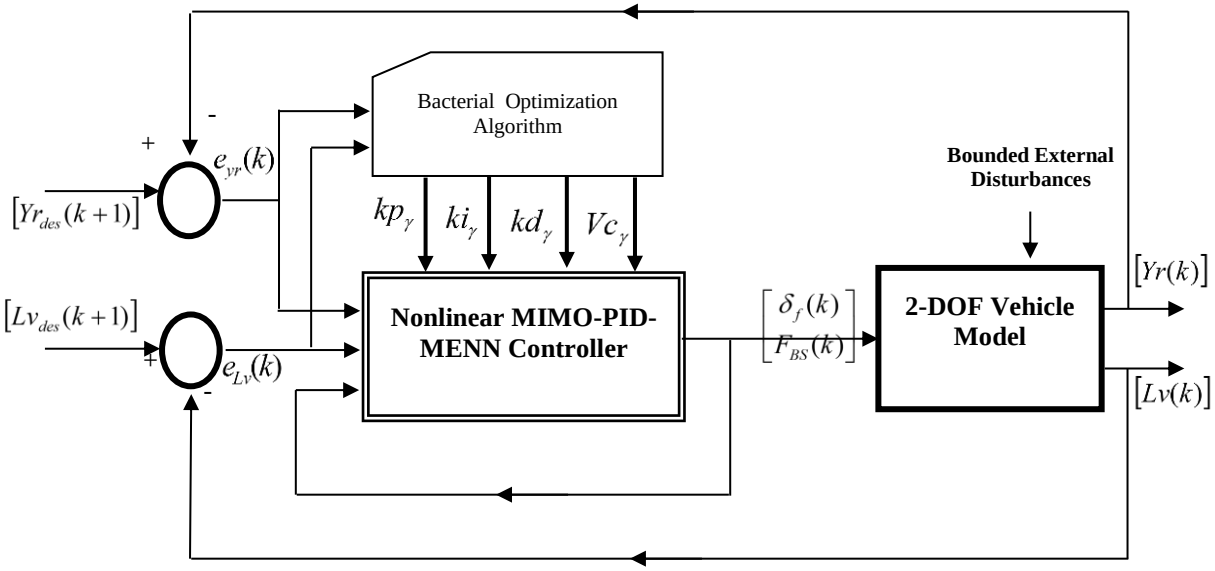

Figure 2. The structure of the proposed controller for 2DOF vehicle models.

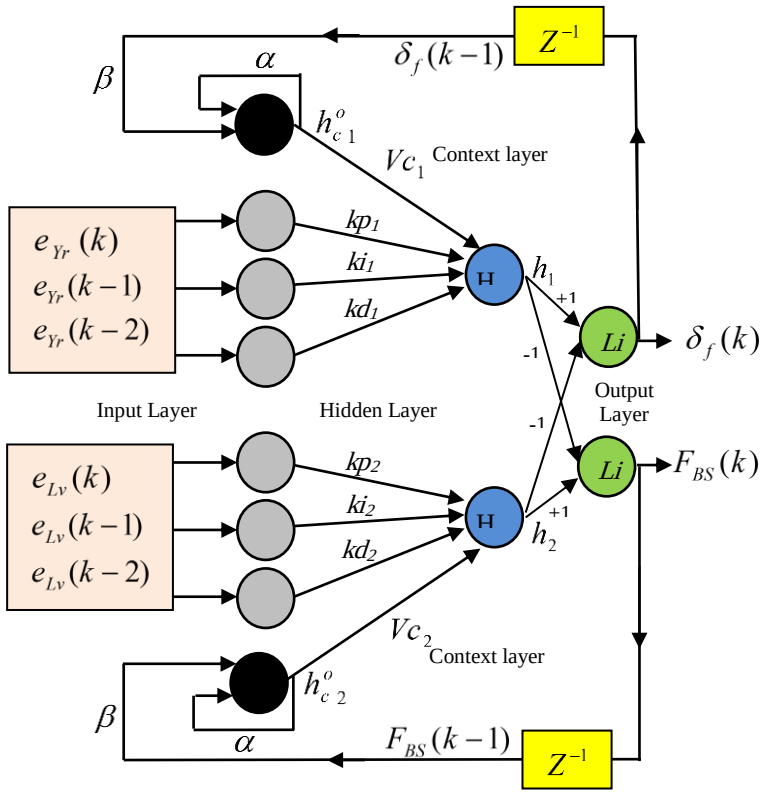

Figure 3. The proposed nonlinear MIMO-PID-MENN controller structure.

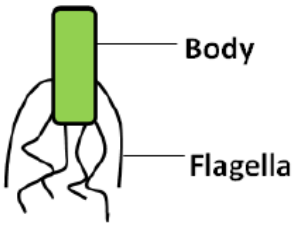

Figure 4. the structure of the bacterium.

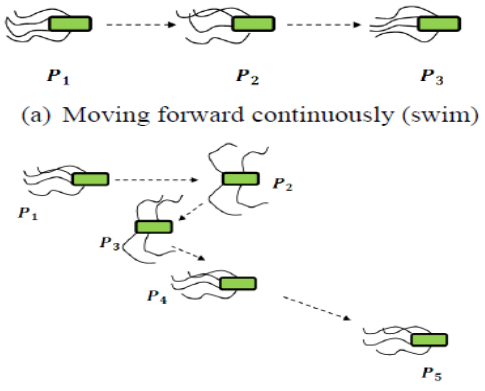

Figure 5. kinds of E. Coli bacterium motion.

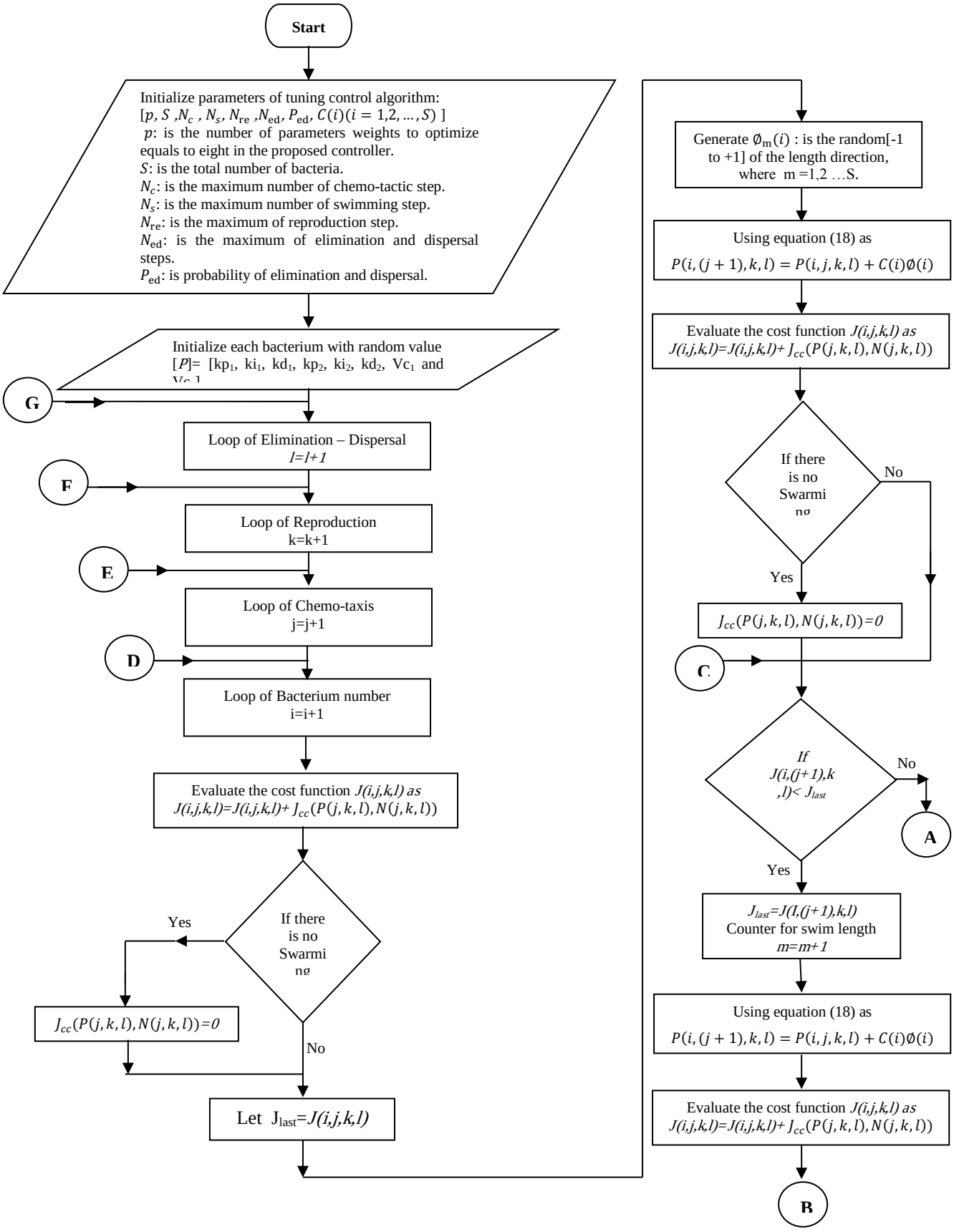
Start
Initialize parameters of tuning control algorithm: [$p, S, N_c, N_s, N_{re}, N_{ed}, P_{ed}, C(i)(i = 1,2, \dots, S)$]
p: is the number of parameters weights to optimize equals to eight in the proposed controller.
S: is the total number of bacteria.
N_c: is the maximum number of chemo-tactic step.
N_s: is the maximum number of swimming step.
N_{re}: is the maximum of reproduction step.
N_{ed}: is the maximum of elimination and dispersal steps.
P_{ed}: is probability of elimination and dispersal.
Initialize each bacterium with random value [P]= [kp1, ki1, kd1, kp2, ki2, kd2, Vc1 and
G
Loop of Elimination – Dispersal
l=l+1
F
Loop of Reproduction
k=k+1
E
Loop of Chemo-taxis
j=j+1
D
Loop of Bacterium number
i=i+1
Evaluate the cost function J(i,j,k,l) as
J(i,j,k,l)=J(i,j,k,l)+ $J_{cc}(P(j,k,l),N(j,k,l))$
If there is no Swarming
Yes
$J_{cc}(P(j,k,l),N(j,k,l))=0$
No
Let J_{last}=J(i,j,k,l)
Generate $\emptyset_m(i)$: is the random[-1 to +1] of the length direction, where m =1,2 …S.
Using equation (18) as
$P(i,(j+1),k,l) = P(i,j,k,l) + C(i)\emptyset(i)$
Evaluate the cost function J(i,j,k,l) as
J(i,j,k,l)=J(i,j,k,l)+ $J_{cc}(P(j,k,l),N(j,k,l))$
If there is no Swarming
No
Yes
$J_{cc}(P(j,k,l),N(j,k,l))=0$
C
If J(i,(j+1),k,l)< J_{last}
No
A
Yes
J_{last}=J(I,(j+1),k,l)
Counter for swim length
m=m+1
Using equation (18) as
$P(i,(j+1),k,l) = P(i,j,k,l) + C(i)\emptyset(i)$
Evaluate the cost function J(i,j,k,l) as
J(i,j,k,l)=J(i,j,k,l)+ $J_{cc}(P(j,k,l),N(j,k,l))$
B

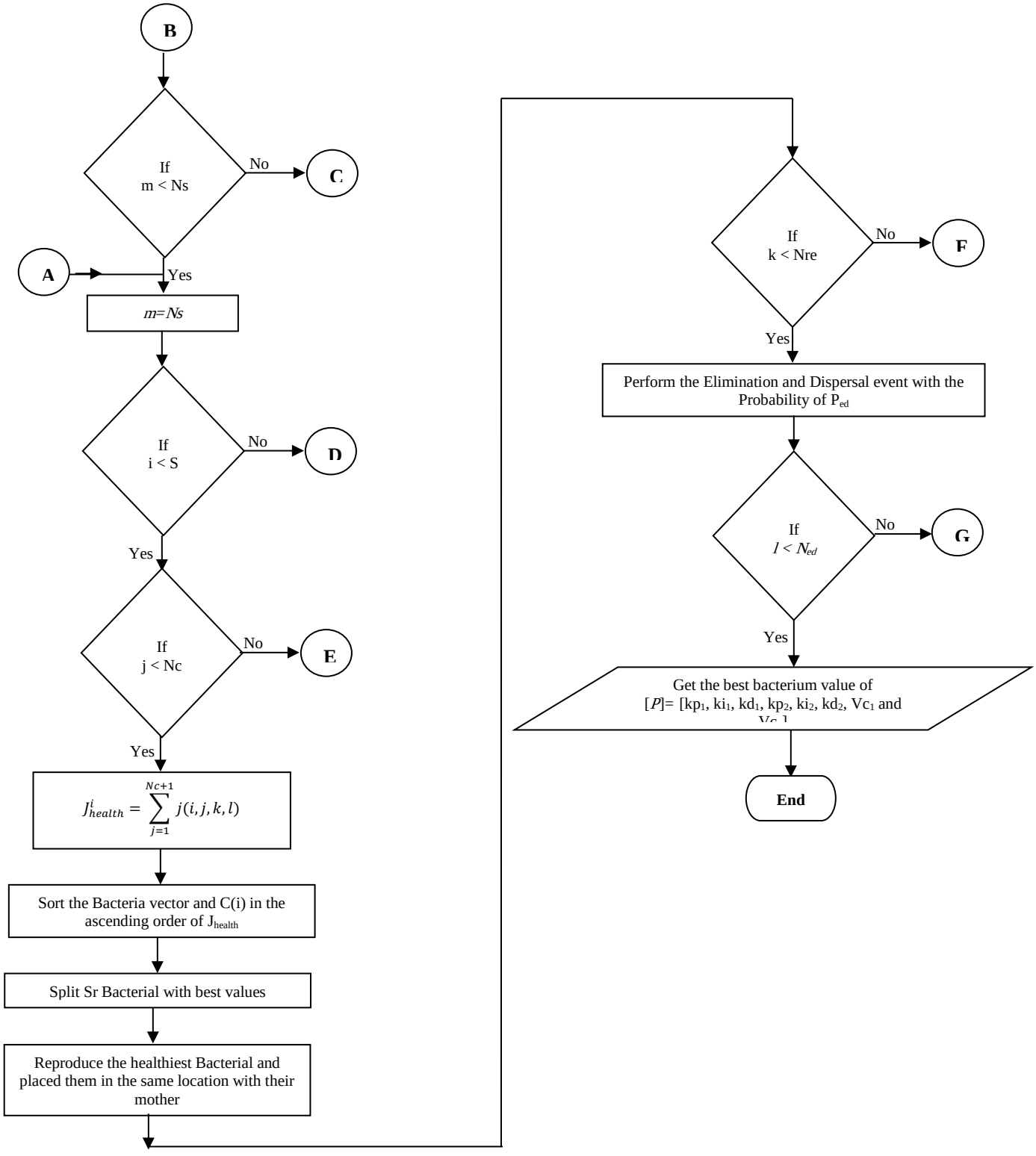

Figure 6. The flow chart of Bacterial forging tuning control parameters algorithm.

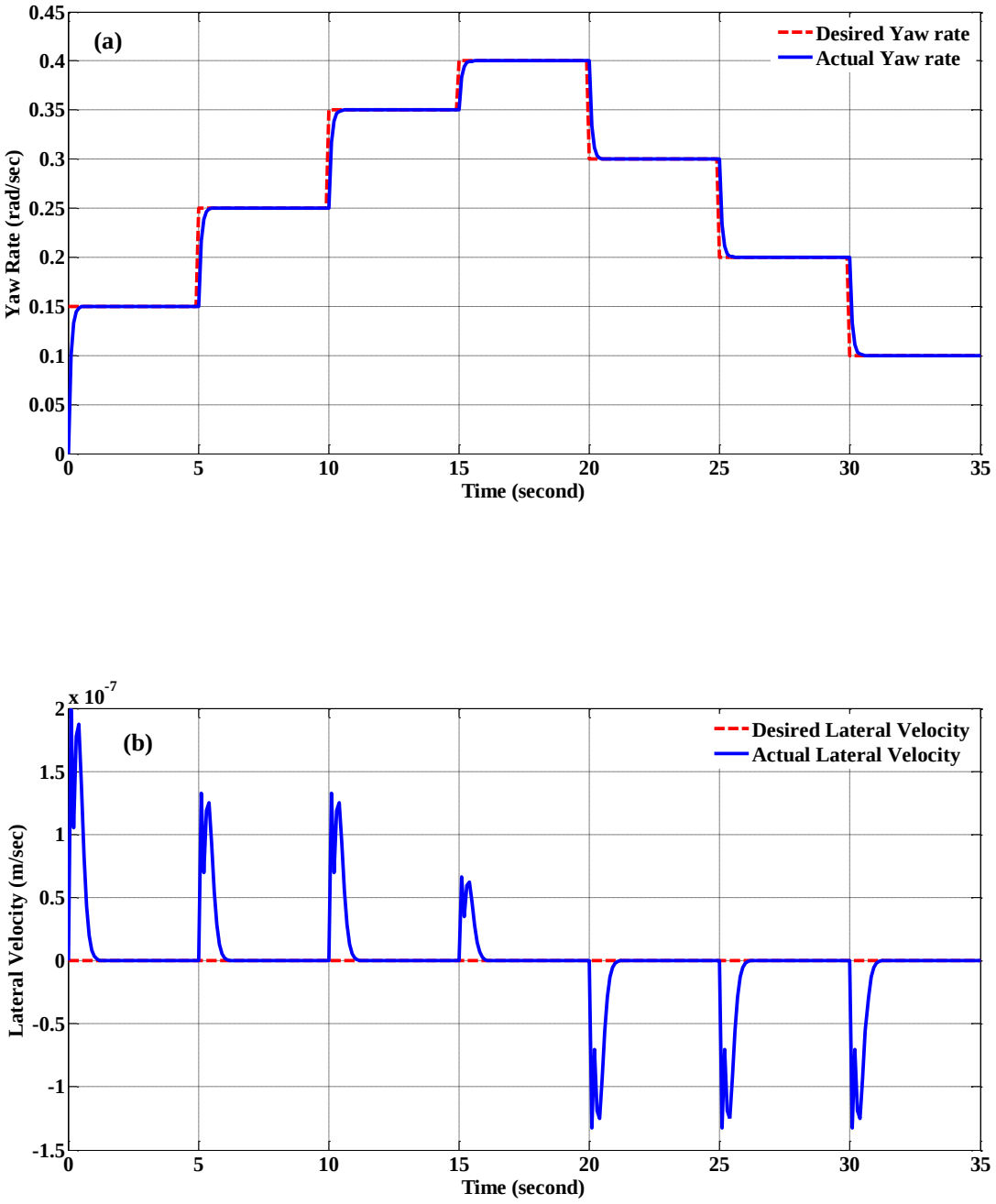

Figure 7. a) The response of the Yaw Rate (rad/sec); b) The response of the Lateral Velocity (m/sec)

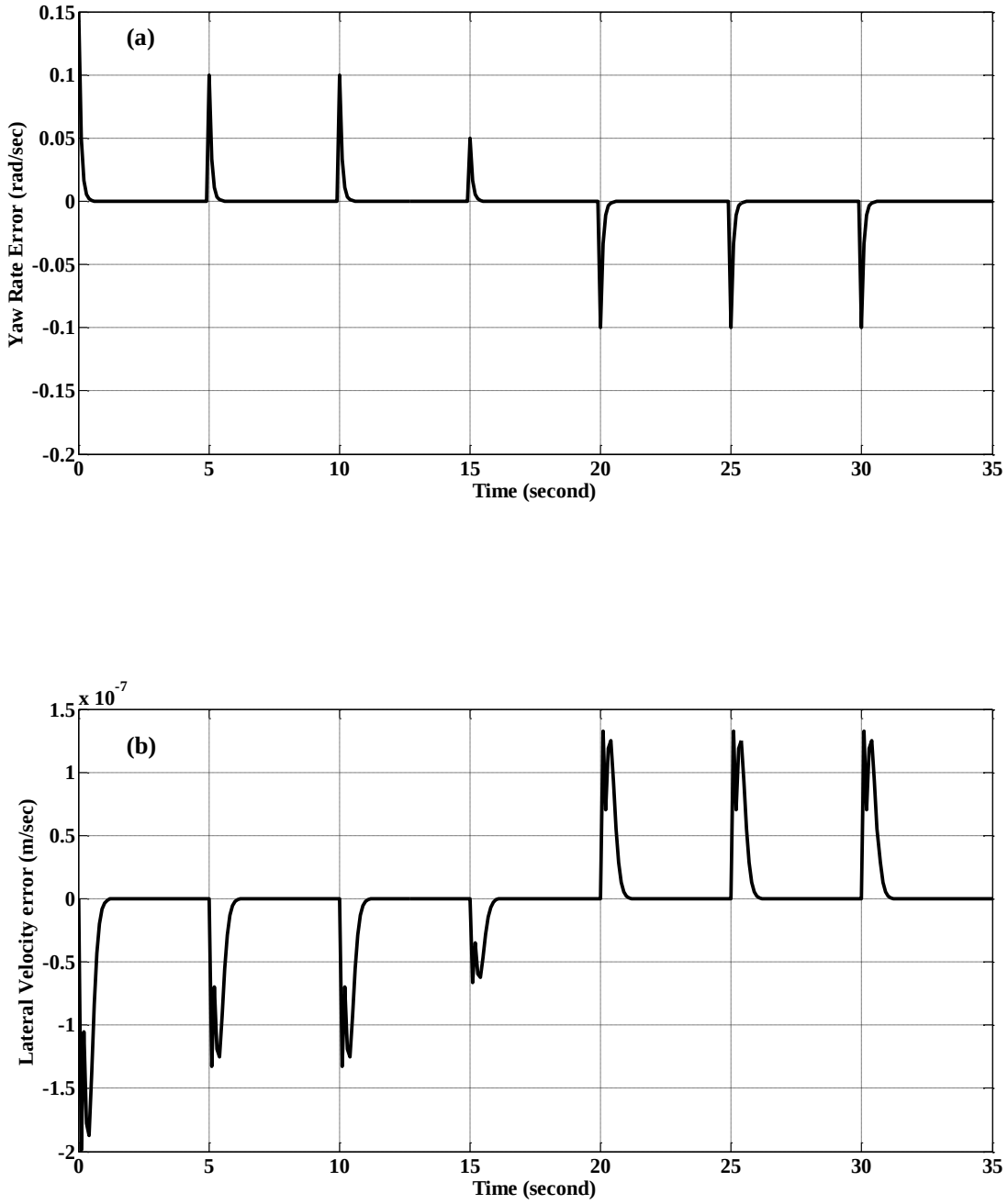

Figure 8. The error signal between the desired and actual output of the vehicle model: a) yaw rate error signal; b) lateral velocity error signal

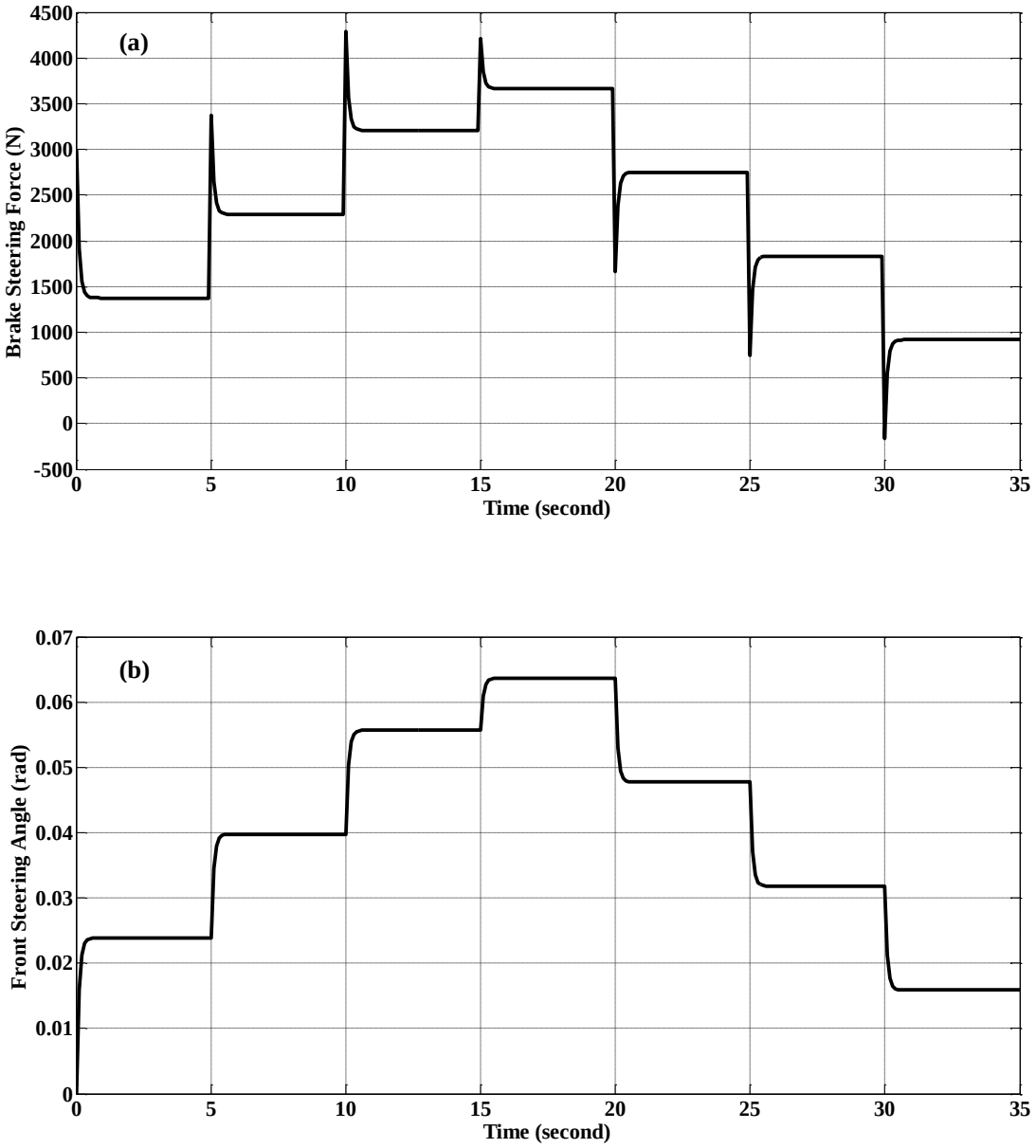

Figure 9. The actual output of the proposed controller a) the differential braking action; b) the front steering angle action.

Table 1. The parameters weights of the nonlinear MIMO-PID-MENN controller.

Vehicle Velocity	kp_1	ki_1	kd_1	Vc_1	kp_2	ki_2	kd_2	Vc2
15	0.237	0.471	0.101	1.322	0.381	0.113	0.219	1.071
25	0.466	0.311	0.111	0.949	0.428	0.299	0.331	1.033
35	0.722	0.236	0.399	0.467	0.751	0.957	0.831	0.993
40	0.731	0.697	0.674	0.513	0.399	0.966	0.877	1.405
30	0.651	0.993	0.841	0.911	0.364	0.387	0.592	0.862
20	0.923	0.716	0.839	0.923	0.199	0.644	0.553	0.997
10	0.771	0.763	0.159	0.532	0.147	0.723	0.801	1.079

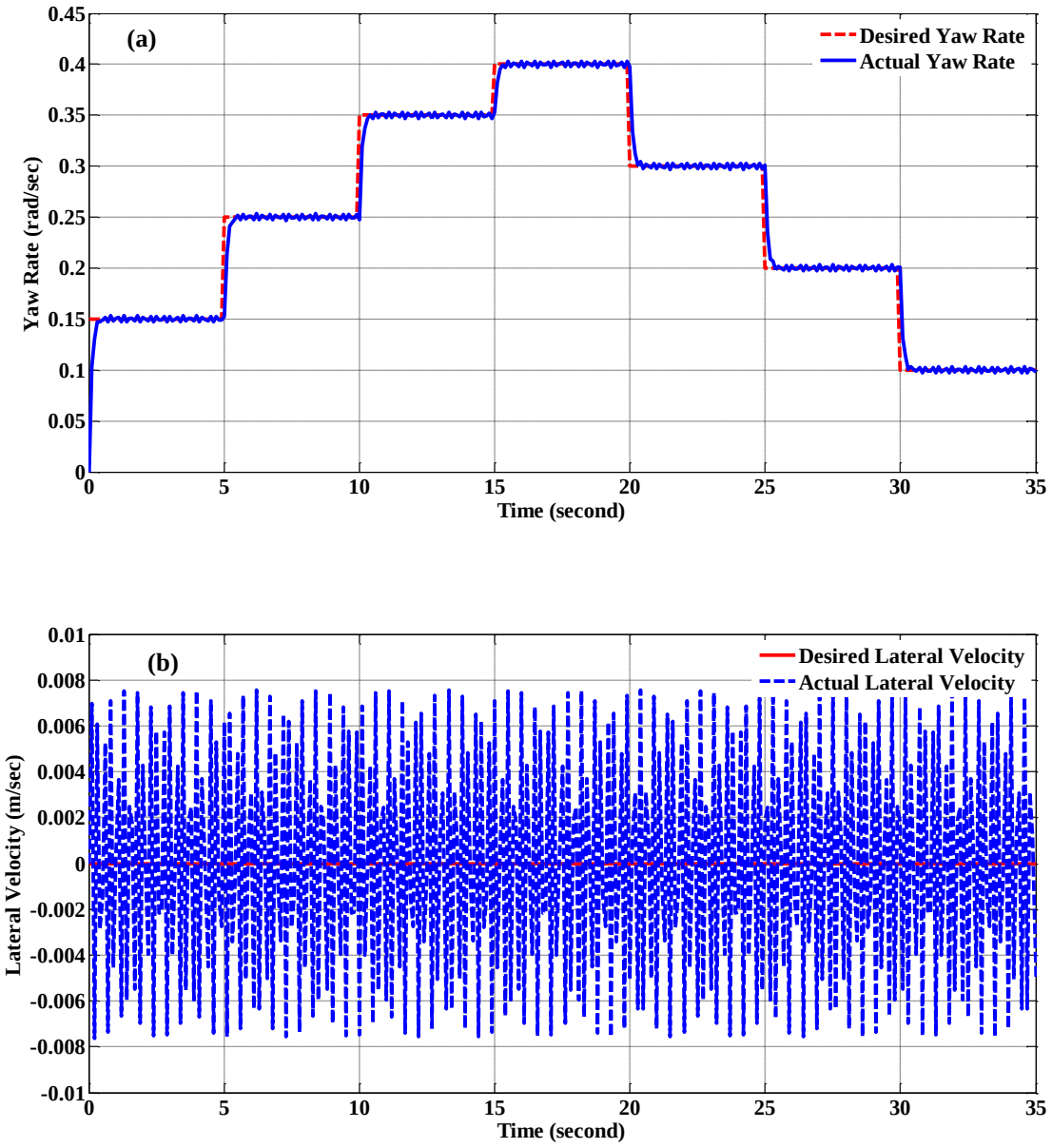

Figure 10. a) The response of the Yaw Rate (rad/sec) with disturbance effect; b) The response of the Lateral Velocity (m/sec) with disturbance effect.

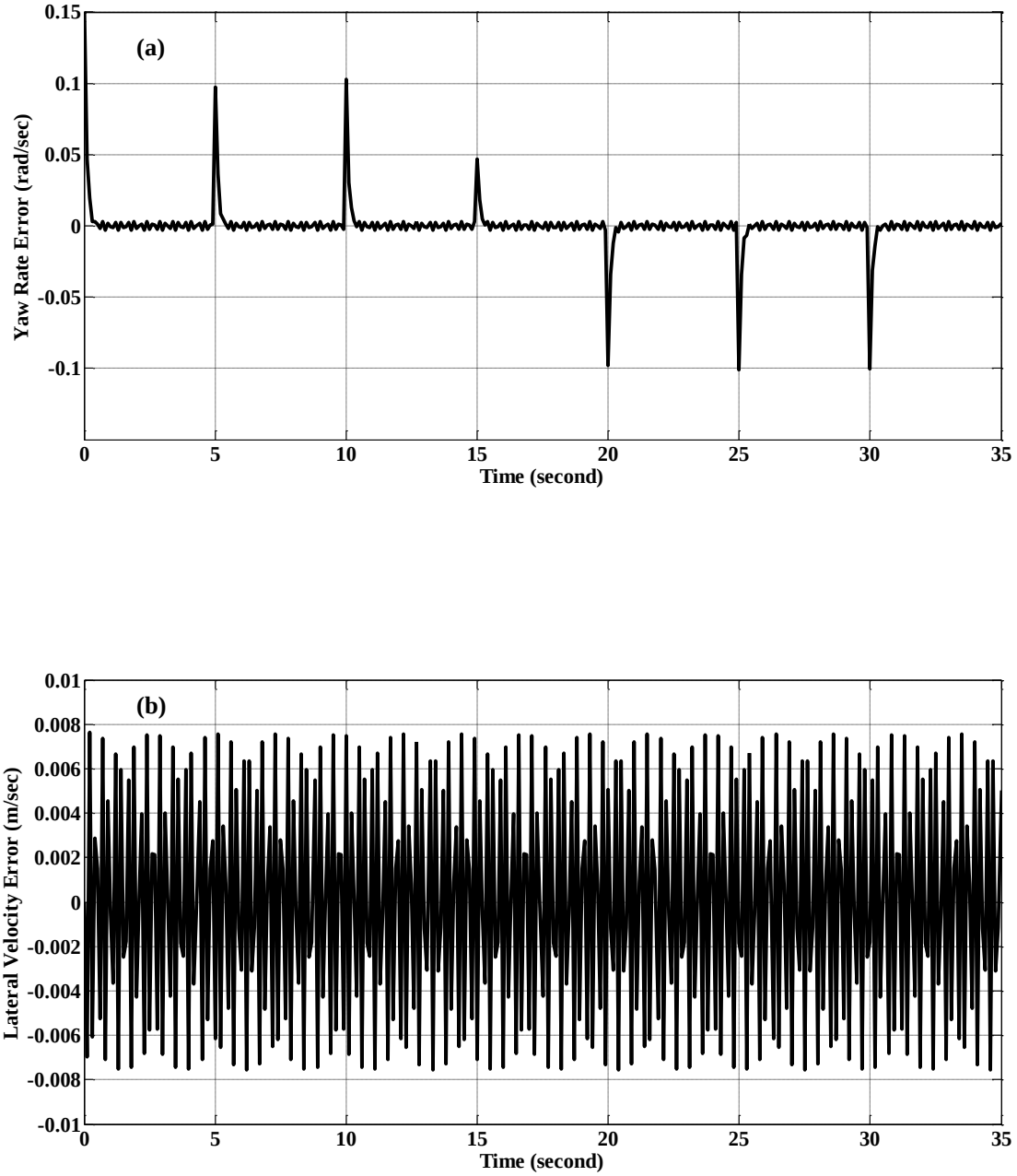

Figure 11. The error signal between the desired and actual output of the vehicle model with disturbance effects: a) yaw rate error signal; b) lateral velocity error signal

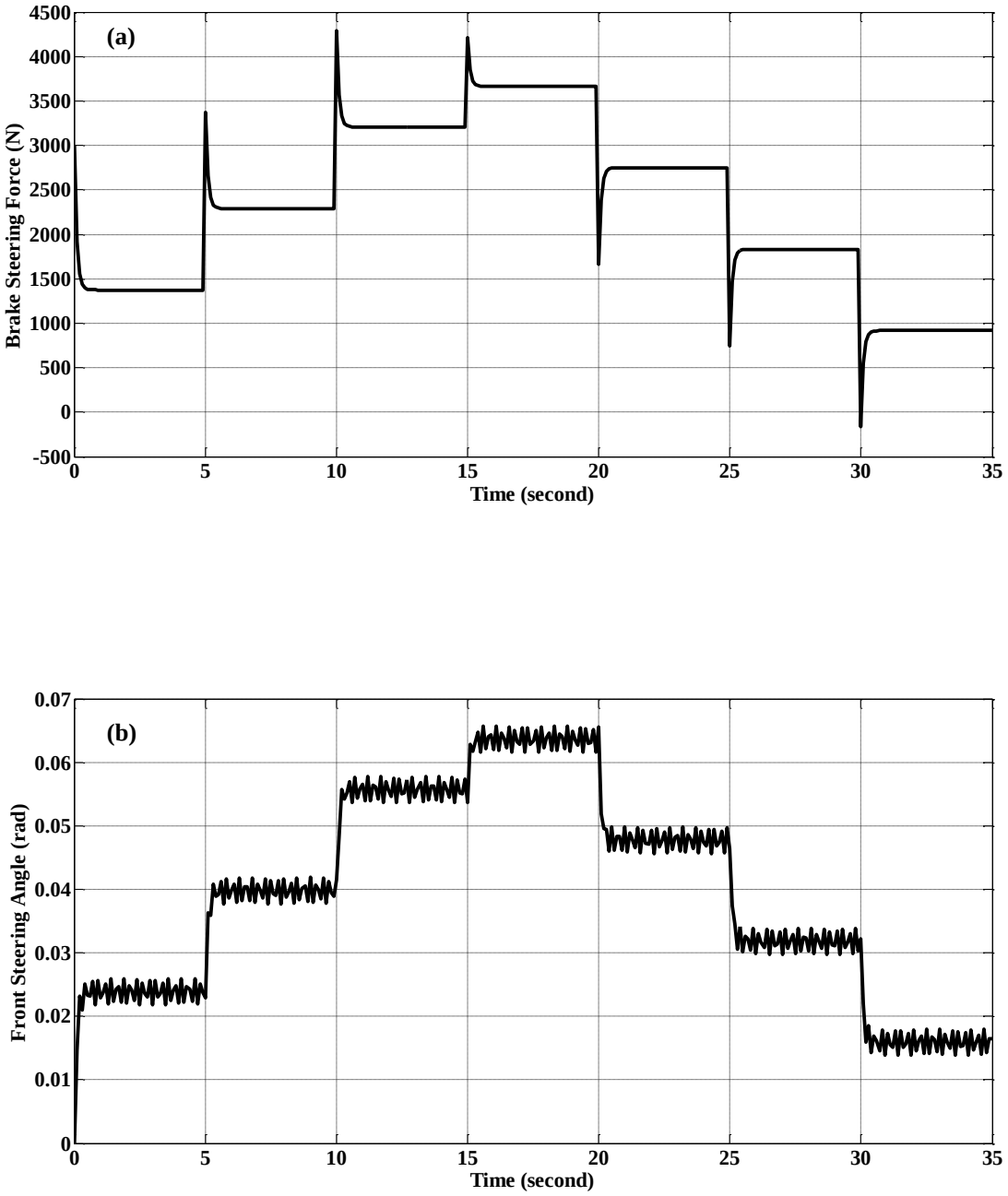

Figure 12. The actual output of the proposed controller with disturbance effects a) the differential braking action; b) the front steering angle action.

Regression Modeling of EDM Process for AISI D2 Tool Steel with RSM

Dr.Shakir M.Mousa
Lecture
, Al-Furat Al-Awsat Technical University/ Technical Institute of Al- Mussaib
shakir.aljabiri_89@yahoo.com

ABSTRACT

In this paper, Response Surface Method (RSM) is utilized to carry out an investigation of the impact of input parameters: electrode type (E.T.) [Gr, Cu and CuW], pulse duration of current (I_p), pulse duration on time (T_{on}), and pulse duration off time (T_{off}) on the surface finish in EDM operation. To approximate and concentrate the suggested second- order regression model is generally accepted for Surface Roughness Ra, a Central Composite Design (CCD) is utilized for evaluating the model constant coefficients of the input parameters on Surface Roughness (Ra). Examinations were performed on AISI D2 tool steel. The important coefficients are gotten by achieving successfully an Analysis of Variance (ANOVA) at the 5 % confidence interval. The outcomes discover that Surface Roughness (Ra) is much more impacted by E.T., T_{on}, T_{off}, I_p and little of their interactions action or influence. To predict the average Surface Roughness (Ra), a mathematical regression model was developed. Furthermore, for saving in time, the created model could be utilized for the choice of the high levels in the EDM procedure. The model adequacy was extremely agreeable as the constant Coefficient of Determination (R2) is observed to be 99.72% and adjusted R^2-measurement (R^2_{adj}) 99.60%.
Keywords: Response Surface Methodology, Electrical Discharge Machining, Central Composite Design, Analysis of Variance, Surface Roughness.

تحليل ونمذ جة معلمات التشغيل على خشونة السطح في عملية القطع بالشرارة الكهربائية للفولاذ العدةD_2 AISI بأستخدام منهجية أستجابة السطح

الدكتور المهندس :شاكر محمود موسى
جامعة الفرات الاوسط التقنية/ المعهد التقني المسيب

الخلاصة

في هذا البحث، استخدمت طريقة استجابة السطح للتحقق من تاثير متغيرات التشغيل: نوع الالكترود (كرافيت، نحاس وتنكستن النحاس)، التيار النبضي، زمن تفريغ الشحنة وزمن توقف الشحنة على خشونة السطح في عملية التشغيل بالشرارة الكهربائية. لدراسة النموذج المقترح لخشونة السطح من الدرجة الثانية، استخدمنا التصميم المركب المركزي لتخمين معاملات النموذج للمتغيرات الاربعة سالفة الذكر على خشونة السطح. التجارب نفذت على فولاذ العدد D2 تم الحصول على المعاملات المؤثرة بتنفيذ تحليل التباين (ANOVA) عند مستوى من الاهمية مقداره 5% . النتائج بينت ان خشونة السطح تتأثر بمتغيرات التشغيل الاربعة وبعض تفاعلاتهم. النموذج الرياضي طور لتنبأ متوسط خشونة السطح في عملية التشغيل بالشرارة الكهربائية. كذلك يمكن استخدام النموذج الرياضي في اختيار مستويات في عملية الشرارة الكهربائية لتوفير وقت التشغيل. كفاءة النموذج الرياضي مقنعة جدا لان معامل التحديد 99.72 % والمعامل الاحصائي 99.60 %.
الكلمات الرئيسية: منهجية استجابة السطح، التشغيل بالشرارة الكهربنئية،التصميم المركب الوسطي،تحليل االتباين، خشونة السطح.

1. INTRODUCTION AND LITERATURE REVIEW:

Electrical discharge machining (EDM) process newly developed thermal non-conventional cutting techniques for difficult metals to machine such as ceramics, heat-resistant steels, tool steel, super alloy, composites, carbides, etc. These materials used either non-conventional materials with special features and properties or newly formed developed materials with high-achievement ability. Now today's especially manufacturing industry is confrontation from these modern and advanced "difficult-to-cut" materials, capital requirements wanted, (three dimensional (3D) complex shapes), high or great precision and high surface finish) and machining high cost. Developed materials engage and play a gradually important pivotal role in advanced industries. The properties of the material greatly improved (such as mechanical properties, heat resistance, corrosion resistance, and wear resistance) the economic interest to the especially manufacturing industries through get better product design and output product achievement. Non-conventional machining methods are unable to achieve machine product materials economically because traditional machining methods depend on removing materials rate by using cutting tools harder than the workpiece. But one of advanced processes using the material features and properties, such as melting, temperature, electrochemical equivalent, electrical conductivity, and thermal etc. **Puertas, et al., 2004**, anatomized the impact of (EDM) input parameters on material removal rate (MRR), electrode wear and surface quality inspection in tungsten carbide workpiece material. A quadratic mathematical model was amelioration for each one of the output parameter responses and it was noted that for material removal rate (MRR) and current intensity, the parameter was the most effective, followed by τ, the interaction, and Ton influence of the first just the two. The amount value of material removal rate (MRR) also increased, when intensity and τ were increased and decreased amount value with Ton.Therefore for the prediction of multi-regression mathematical models and surface roughness finish, empirical equation models are applied and utilized**. Patel, et al., 2007**, verify the machining general characteristics, such as the mechanism of material removal rate (MRR) and surface integrity of AL_2O_3-SiC-Tic material with (EDM). The final result refers to the white layer (recast layer) and surface roughness (Ra) increase with a pulse on time and current. Material removal rate (MRR) for the reasons of the evaporation, decomposition, some extent oxidization, and dissolution or separation melting at lower current and thermal spelling at higher current, **Kuppan, et al., 2007.** In this study, strong mathematical model for average surface roughness (Ra) and material removal rate (MRR) of deep hole drilling form of Inconel 718 was obtained. The set of experiments were planned and designed using central composite design (CCD) and response surface methodology (RSM) was used to the same model. It appears that material removal rate (MRR) is very affected by peak current, duty factor and the input operating parameters were making the best (optimized) for maximum material removal rate (MRR) with the required surface roughness Ra. **Chiang, 2008,** had explained the influences of Ip, Ton, τ and voltage on the responses; MRR, electrodes wear ratio and Ra. The experiments were planned according to a CCD and the influence of parameters and their interactions were investigated using ANOVA. A mathematical model was developed and claimed to fit and predict MRR accurately with a 95% confidence. Results show that the main two significant factors affecting the response are the Ip and the τ.). **Biswas, and Pradhan,**

2008, displayed Adaptive Neuro-Fuzzy Interence Systems (ANFISs) model to predict and forecast material removal rate (MRR) of workpiece AISI D2 tool steel with Ip, duty cycle (τ) and Ton as operating parameters. All experimental results were found to be in agreement and very good approval with the mathematical model predictions. **Kanagarajan, et al., 2008,** selection, Ton, Ip, electrode rotation flushing and pressure as design input operating parameters to research the (EDM) process accomplished such as material removal rate (MRR) and surface roughness (Ra) on Tungsten carbide. The most effective input operating parameters for decreasing the surface roughness (Ra) have been specified using the response surface methodology (RSM) and experimentally make sure by conducting affirmation experiments. **Pradhan, et al., 2009,** also suggested just the two artificial neural networks (ANNs) mathematical models for the prediction of surface roughness (Ra) with the similar workpiece material and operating parameter and then estimate the experimental results. It is supposed that the mathematical models could predict surface roughness (Ra) they successfully accomplished. In **Rao, et al., 2010**, a central composite design (CCD) is applied and utilized to conduct the output response surface final approach and set of experiments are utilized for the improvement of analysis of surface roughness (Ra) with E.T., I_p, and T_{off} , T_{on} as input operating factors and a second-order polynomial model. **Medfai, et al., 2011,** studied the influence of the cutting conditions on machining operation by EDM of steel materials 42CD4-42 CrM04 on surface layer quality by the development of a regression model. The results show that the surface layer quality and the volume of the removal influence considerably with nature of the electrode used and the different materials machined by EDM. In, **Khalid Hussain Syed, et al., 2013,** paper, tool electrode materials used are electrolytic copper and W300 die steel respectively, concentration powder, pulse on- time and pulse peak current are taken as input operating parameters. The output response parameter is white layer (WLT) or thickness recast material. Mathematical or empirical model is developed for output white layer by utilizing response surface methodology(RSM) to research the influence of process operating parameters. In this research study, a central composite design is applied research to conduct the response surface approach and a experiment is utilized for the software development of a second-order polynomial model and analysis of surface roughness SR with input parameters as (Ip, E.T, Toff and Ton).

2. EXPERIMENTATION

The set of experiments have been achieved to study the influence of different characteristics machining input operating parameters on Ra of tool steel. This work has been pledged to realize the influence of process operating parameters.T. E, I_p, T_{off} and T_{on} on surface roughness (Ra)**.** The number of experiments was carried out on a die sinking type EDM computer numerical control (CNC) machine model (CHMER EDM). The kind of workpiece material utilized in this work was AISI D2 tool steel, with dimensions (35×35×3) mm and surface roughness Ra (2 μm) to be formed or machined. The chemical composition of the workpiece material is shown in **Table 1.** In this study, the electrolytic copper cylindrical shaft is selected as the tool electrode with dimensions (100 mm long and 30 mm diameter) were mounted axially at positive polarity. The working gap between the workpiece and electrode the is (0.20 mm). The grade oil was used as dielectric fluid with pressure (0.3) Kg/cm^2 for cleaning and flushing. Description of each workpiece surface layer condition was achieved traceable of the surface roughness (Ra) profile measurement on a wide variety of surface. A portable

surface roughness tester (type Pocket Surf III/ PMD 90101) was used to measure the Ra of AISI D2 tool steel. At the beginning of measuring surface roughness (Ra), any specimen was washed and cleaned in liquid type(acetone) and then dried with hot air blower. To obtain validity period and accuracy, five observed value times of surface roughness was measured along five different directions. Then finding the mean value for each treatment combination, the cutoff length was 0.8 mm **Fig.1** shows a picture of the measuring .and **Fig.2** shows a picture of the EDM machine type (.CM 323C+50N).

.

3. RESPONSE SURFACE METHODOLOGY (RSM)

The method response surface methodology (RSM) is a collection of mathematical model and statistical techniques method, it can be used for, improvement, development, and optimisation of processes in order to solve the problems of engineering, **Boopathi and Sivakumar, 2014.** Design of Experiments (DOE) as a scientific method utilized to exact convergent value and without the knowledge of function for which only a few quantity of values are calculated. These relationships are the product by utilizing many designs such as least square error or a mistake fitting of the response surface. The very popular one is the Central Composite Design (CCD) is utilizing because it gives a relatively more accurate forecast or prediction of all response parameter median with reference to amounts measured during this period of experimentation**, Mason, et al., 2003**. A Central Composite Design (CCD) displays the feature that a certain amount of modification is suitable and be able to utilize in the two-step chronological age response surface methodology. In these type of scientific methods, there's a probability that the set of experiments may be finished or stop with any runs and be decided that the prediction regression model is acceptable. In Central Composite Design CCD, the end boundary or limits of the set of experimental range to learn are understood and are well made as great to the full extent able to be done to get an evident output response from the empirical model. Operating parameters (E.T., Ip, Ton, and Toff) are carefully chosen as being the more significant for this general investigation. The various levels were taken for this research show or represent in **Table 2**. The result of arranging in the behavior of the experiments utilize a Central Composite Design CCD with input operating parameters, the important points utilized are sixteen points formed a cube, six center points position and eight axial points, in the overall of 30 work s in three blocks**.** The average rate of change value in surface roughness (Ra) is shown in **Table 3**. The second-order response surface model is usually utilized when the response cumulative distribution function is non-linear. In this study, a second-order response surface model has been used to explains the behavior of the system and relation between the input operating parameters and output parameters response. The second-order response surface model in Eq.(1), **2003**.

$$\mathbf{Y} = \beta_o \sum_{i=1}^{k} \beta_i X_i + \sum_{i=1}^{k} \beta_{ii} X_i^2 + \sum_{i<j=2}^{k} \beta_{ij} X_i X_j \pm \varepsilon \qquad (\mathbf{1})$$

where Y is the congruent output expected for the response, X_i is the input operating parameters, X_iX_j andX^2_{ii} are the interaction terms and squares, of these operating parameters. The unbeknown regression coefficients to be estimated are β_o, β_i, β_{ij} and β_{ii} and the error or noise observed in the response surface model is indicated that ε.

The unbeknown coefficients are found and be specified from the set of experimental data as given in **Table 4**. The used or accepted as normal or average mistakes in the evaluation of the correlation coefficients are arranged (data) in tabular form in the column، constant SE coif. The F-value is a test to determine main influences are significant and interaction, are studied at the level 95% of confidence and the operating parameters having p-value the probability of

obtaining more than 0.05 are insignificant or unimportant (shown with * in p-column). For the suitable fitting of surface roughness Ra, by the backward elimination operation, the non-significant terms are eliminated. The regression model is evaluated again or differently by determining or limit the not known coefficients, which are arranged (data) in tabular form in **Table 5**. The new mathematical model made to clarify surface roughness Ra describe that electrode type E.T., Pulse duration of current (I_p), Pulse duration on time (T_{on}), Pulse duration off time (T_{off}), Electrode type E.T..2, E. T. × Pulse duration on time(T_{on}), Electrode type E.T. × Pulse duration off time (T_{off}), Pulse duration of current (I_p) × Pulse duration off time (T_{off}) and Pulse duration on time(T_{on}) × Pulse duration off time (T_{off}) are the greatest extent influences operating parameters in order to do this of statistical significance. The last empirical model for surface roughness Ra is specified in Eq. (2).

$$\mathbf{Ra = 4.46833 - 0.70333\ E.T. + 0.14111\ Ip - 0.53389\ Toff + 0.45556\ Ton - 0.07375E.T - 0.16167\ E.T.2.\times Ton + 0.08625E.T.\times Toff - 0.1025Ip\times Toff - 0.055Ton\times Toff} \quad \mathbf{(2)}$$

Since electrical discharge machining EDM method is non-linear behavior in the state of nature, a linear polynomial will not be capable prophesy the output parameter carefully, and for this reason, the second-order response surface model or quadratic mathematical model have set up to be strong enough modeling the EDM method. The analysis of variance (ANOVA) display in table for the reduced or shorten quadratic mathematical model **Table 6** describe an estimation of the present value of the constant coefficient of determination, (R2) as far as 99.75%, which is an indication of how much a change or difference in the output parameter is clarified or explained by the mathematical model. The higher level constant coefficient of determination (R2), denotes the suitable or get the better fitting of the empirical mathematical model with the technical information.

The empirical mathematical model sufficiency examination contains the placement test for the importance of the empirical mathematical model, lack of fit and model coefficients, which is achieved when utilizing analysis of variance (ANOVA) on the shorten empirical mathematical model **Table 6**. The overall mistake or error of regression models collect the total of mistakes or errors in interaction terms, and linear square (18.49148 + 0.43095 +0.191964=19.114394). The residual value mistake is the collect of lack-of-fit and pure mistakes. The fit abstract recommends that the quadratic mathematical model statistically results in information important influence for data analysis of surface roughness (Ra). In the table, p-value for the lack-of-fit about 0.094, which is tenuous influence, so the mathematical model is surely enough. On the other hand, the mean square mistake of refined error is even less than that of lack-of-fit. The final report for empirical mathematical model measures to check tested for (ANOVA) (F-test) refers that the being sufficiency of the test report is decided. The calculated set of values of output parameters, model charts and graphs are created for the more content analysis in another part. A total residual value analysis has been achieved for improving the charts and graphs output and response are shown below in **Fig.3**. When the normal conditional probability plot of residuals expose that set of experimental information and data are propagation approximately condition along the direct straight line, corroborative a useful connection between a set of experimental and predicted values level for the output parameter is shown below in **Fig. (3 - a)**. In the scheme of residuals against a completely fitted set of values

are shown below in **Fig. (3 - b)**, only too small amount difference can be visually seen. The generating histogram of residuals is shown below in **Fig. (3 - c)** as well display a Gaussian probability distribution in which is favored, and at last, in residuals versus the required order of a set of experimentations are shown below in **Fig. (3- d)** both of them positive and negative residues are clearly visible, indicating that nothing special direction which is deserved across from a statistical information analysis from this point of view. As a total, all the models do not really show any weakness.

.4. RESULTS AND DISCUSSION

Fig. 4 displays the greater influence and make plans to carry out of the four input operating parameters which under control on surface roughness Ra. It is comprehensible that all input parameters have great effect and strong impacts on surface roughness Ra which is confirming by a consequence, are shown below in **Table 6**. Specifically designed, change the electrode type (E. T) alone or only one for a Gr to Cu then CuW, while conservation the other operating parameters constant at their middle amount levels, can be reduced in surface roughness (Ra) by percentage 28% about (4.93μm - 3.55 μm), which is a great variance interval or space than those produced by another input operating factors. This is because the least removal of debris reached for that material, which means a result is brought that minimum and of little depth or shallower craters were made in the workpiece surfaces with CuW. In addition to this, the surface roughness (Ra) increased change by percentage 5 % about (4.41 μm - 4.61 μm), with pulse current (Ip) become greater or make increases about (24 Amp - 36 Amp). In other words the greater or increase in pulse current (Ip) for various reasons happened elevated level of surface roughness (Ra) accordingly the pulse current (Ip) is greater or increases, electrostatic discharge make a sudden stoppage on the superficial layers of the workpiece very strong, intensely and creates a sensation an effective force on the liquefied by heat metal in a large or small crater, due to exceedingly molten metal to be pushed outside of the large or small crater, and the surface roughness (Ra) of machine leading to superficial layers increases, **Shabgard, et al., 2011.** At the same surface roughness (Ra) change increased by percentage 23 % (4.02 μm - 4.92 μm) such as the pulse on time (Ton) increased change from low to high of different level at constant middle amount of set of values of other input operating factors Long pulse on time(Ton) lead to the high performance in heat transfer inside the dielectric fluid and workpiece, the is capable to remove the molten or liquid metal, such as make flushing of dielectric pressure in constant certain amount. In another statement, during the time that the pulse on time (Ton) is increased change, the melting isothermals permeate moreover into the interior design of the reference material, and the liquid material or molten effect region extends most or extra into the material and this produces a greater extent recast or white thick layer. Consequently, such as the pulse on time(Ton) increases change the surface roughness (Ra) increases that can be corroborated by **Hascalık and Caydas, 2007.** At the end, the direction of pulse off time (Toff) is similar to electrode type (E.T.) where applicable reduction in surface roughness (Ra) by percentage 23 % (5.04 μm - 3.89 μm) when pulse off time (Toff) increases (25 μsec - 75 μsec), reduce levels out of (Toff) form the higher up than frequency range that output yields less than (Ra). Moreover, for a long time period of (Toff) output yields lowered metal removal (MR) for this reason get least or smaller and little depth of craters are obtain. The longtime period of (Toff) supplies best refrigeration

influence and required time to straight flush out away or subtract the molten material molten material which liquefied by heat and fragments and debris from the working spark gap or distance between the workpiece and electrode. Thus, a longer period of (Toff) attends low (Ra) **Jahan, et.al, 2011. Fig. 5** displays the synchronous influence of electrode type(E.T.) and pulse on time (Ton) on the surface roughness (Ra), (a) and (b) in three-dimensional (3D) surface and two-dimensional (2D) contour interval format. It is clearly able to be seen that smaller surface roughness (Ra) be able to get selected a great level of electrode type (E.T.) less pulse on time (Ton). That is referred to carrying capacity of debris away far by CuW electrode as well as possible with the reduction in pulse on time (Ton), the extremely weak spark become a shorter period, which makes small craters, temperature and hence good surface finish. The group influence of pulse off time (Toff) and electrode type (E.T.) at a constant level (middle amount of value) of a pulse on time (Ton) and pulse current (Ip) there has been a performance display in Fig.5 in two and three-dimensional surface with the contour format shape. It is able to be complimented that the decrease surface roughness (Ra) is accomplishable at the upper part right zone of the contour plot region where the pulse off time (Toff) and electrode type (E.T.) are their highest amount levels. This unnatural phenomenon happens and is able to refer to a feature of carrying capacity debris away far by CuW electrode as well as possible the refrigeration influence on workpiece and electrode with long pulse off time (Toff) hence decreasing the surface roughness (Ra). **Fig. 6** clarifies the together influence of pulse off time (Toff) and pulse current (Ip) over surface roughness (Ra). It is clearly visible that more smoothly achieved without bitterness surfaces can be marks obtained specifying when high value pulse off time (Toff) and low pulse current (Ip) which is accomplishable at the uppercase level left zone of the contour plot region. This is due to the discharge sparking hits the surface layer of the specimen less value of intensely with lower pulse current (Ip) and, as mentioned over, the refrigeration influence on workpiece and electrode with long period pulse off time (Toff) and as a consequence reducing the surface roughness (Ra). **Fig. 7** describes the contour plot and surface of surface roughness (Ra) with regard to pulse off time (Toff) and pulse on time (Ton). From this, it is strongly recommended to stratify get low pulse on time with a considerable pulse off time (the upper class left portion of **Fig. 7 (b)**) to create much more smooth or polished or refined work surfaces. This is because a medium as the dielectric fluid influenced which is qualified for pure or clear away the molten or liquefied material with low level pulse on time (Ton) and the refrigeration influence above-mentioned with long pulse off time. From the (ANOVA) analysis of variance (Table 6), the interaction of pulse current and pulse off time is the very considerable (significant) influence on surface roughness (Ra), followed by electrode type (E.T.) × pulse off time (Toff), electrode type (E.T.) × pulse on time(Ton) and then pulse on time(Ton) × pulse off time (Toff).

5. CONCLUSION

The main conclusions achieved can be summarized as follows:

1. The operating parameters have more significant effect on Ra surface roughness were the. Electrode type E.T., Pulse duration off time (T_{off}) and Pulse duration on time (T_{on}), E. T.^{2}, Electrode type E.T.. × Pulse duration on time(T_{on}), Electrode type E.T. × Pulse duration off time (T_{off}), Pulse duration of current (I_p) × T_{off} and Pulse duration on time(T_{on}) × Pulse duration off time (T_{off}) with the estimate the worth of a parameter a confidence specified range (level) of 95%.
2. The final test result refers that with a view to getting a low amount of value of surface roughness Ra during the work period of this research, Pulse duration of current (I_p) and Pulse duration on time (T_{on}) must be stable as less as much as possible to be done, whereas the T. E. and T_{off} should be stable as high as possible to be done.
3. The improved mathematical regression model for the surface roughness Ra is able and influential used for the optimal or best option of the (EDM) drilling work in process operating factors to accomplish high surface finish of AISI D2 tool steel material of workpieces.
4. Although the (EDM) drilling work in process input operating factors on AISI D2 tool steel workpieces are extremely interconnected system stochastic nature and due their inherently complex, however, the practical approach of response surface methodology coupled can usefully help recognizing process good behavior and determine suitable (EDM) operating conditions meeting all accomplishment search criteria in accept compromise in such a manner.
5. This study assists researchers and industries in developing productivity a strong, trustworthy knowing range and prediction based on evidence of surface roughness (Ra) without a doubt achieve more experiments with an (EDM) drilling work in process for AISI D2 tool steel workpieces.

6. REFERENCES

- Puertas, C. J. Luis, and L. Alvarez, (2004) "Analysis of the influence of edm parameters on surface quality, mrr and ew of wc-co," Journal of Materials Processing Technology, vol. 153-154, no. 1-3, pp. 1026–1032.
- Patel K.M, Pandey, P.M, Rao P,V (2007) "Surface integrityand and material removal mechanism with the EDM of AL_2O_3 ceramic composite " Int, Journal of Refractory metals and hard l and materials 27 issue 5,892-899
- P. Kuppan, A. Rajadurai, and S. Narayanan, (2007) "Influence of EDM process parameters in deep hole drilling of inconel 718," International Journal of Advance Manufacturing Technology, vol. 38, pp. 74–84.
- K. Chiang, (2008**)** "Modeling and analysis of the effects of machining parameters on the performance characteristics in the edm process of Al2O3+TiC mixed ceramic," International Journal of Advanced Manufacturing Technology, vol. 37, no. 5-6, pp. 523–533,
- M. K. Pradhan and C. K. Biswas, (2008) "Neuro-fuzzy model on material removal rate in electrical discharge machining in AISI D2 steel," Proceedings of the 2nd

International and 23rd All India Manufacturing Technology, Design, and Research Conference, vol. 1, pp. 469–474.

- D. Kanagarajan, R. Karthikeyan, K. Palanikumar, and P. Sivaraj, (2008) "Influence of process parameters on electric discharge machining of WC/30%Co composites," Proceedings of the Institution of Mechanical Engineers, Part B: Journal of Engineering Manufacture, vol. 222, no. 7, pp. 807–815.
- M. K. Pradhan, R. Das, and C. K. Biswas, (2009) "Comparisons of neural network models on surface roughness in electrical discharge machining," Proceedings of the Institution of Mechanical Engineers, Part B: Journal of Engineering Manufacture, vol. 223, p. (In Press).
- P. S. Rao, J. S. Kumar, K. V. K. Reddy and B. S. Reddy, (2010), Parametric study of electrical discharge machining of AISI 304 stainless steel International Journal of Engineering Science and Technology, 2 (8), pp 3535-3550.
- Medfai A.Boujelbene M, Bayraktar E,2011, A mathematical model to choose effective cutting parameters in electroerosion, EDM, Journal of Achievements in Materials and Manufacturing Engineering, Vol,47,
- Khalid Hussain Syed et al 2013, Studies on Recast-Layer in EDM using Aluminum Powder Mixed Distilled Water Dielectric Fluid, School of Mechanical &Building Sciences, VIT University, Vellore Tamil Nadu ,India.
- S. Boopathi and K. Sivakumar, (2014), Study of water assisted dry wire-cut electrical discharge machining, Indian Journal of Engineering and Materials Science, Vol. 21, pp 75-82.
- R. Mason, R. Gunst, Dallas, Texas and J. Hess, (2003) Statistical Design and Analysis of Experiments With Applications to Engineering and Science (Second Edition), A John Wiley & sons publication.
- Minitab User Manual Release 16 MINITAB Inc,(2003) State College, PA, USA.
- M. Shabgard, N. Oliaei, M. Seyedzavvar and A. Najadebrahimi, (2011), Experimental investigation and 3D finite element prediction of the white layer thickness, heat affected zone, and surface roughness in EDM process, Journal of Mechanical Science and Technology, Vol.25, pp 3173-3183.
- Hascalık and U. Caydas, (2007), Electrical discharge machining of titanium alloy (Ti–6Al–4V), Applied Surface Science, Vol. 253, pp 9007–9016.
- M. P. Jahan, M. Rahman, Y. S. Wong, (2011), A review on the conventional and micro-electro discharge machining of tungsten carbide, Int. J. Mach. Tools and Manufact., Vol 51, pp 837-858.

Table 1. Chemical composition of the AISI D2 tool steel workpiece [wt. %].

Material	C	Si	Mn	Mo	Cr	Ni	V	Co	Fe
Wt.%	1.5	0.3	0.3	1.0	12.0	0.3	0.8	1.0	Balance

Figure 1. Set up for surface roughness measurement.

Figure 2. shows a picture of the EDM machine.

Table 2. Different variables used in the experiment and their levels.

Variable	**Unit**	**Coded/Actual level**		
		-1	**0**	**1**
Electrode type E.T.	-	Gr	Cu	CuW
Pulse duration of current (I_p)	Amp.	24	30	36
Pulse duration on time(T_{on})	µsec.	50	100	150
Pulse duration off time (T_{off})	µsec.	25	50	75

Table 3. Design layout with experimental results and predictions for AISI D2 tool steel work piece.

Exp. No.	Pt Type	Blocks	E. Sh.	Ip (Amp.)	Ton(µsec.)	Toff(µsec.)	Ra(µm)	Ra(Fit) Calculated (Regression)	Residual
1	1	1	-1	-1	1	-1	6.501	6.542	-0.041
2	1	1	-1	-1	-1	1	4.257	4.239	0.018
3	1	1	-1	1	1	1	5.39	5.419	-0.029
4	0	1	0	0	0	0	4.884	4.915	-0.031
5	1	1	1	-1	-1	-1	3.784	3.734	0.050
6	1	1	1	-1	1	1	3.828	3.814	0.014
7	1	1	1	1	-1	1	3.168	3.128	0.040
8	1	1	1	1	1	-1	5.181	5.178	0.003
9	1	1	-1	1	-1	-1	5.83	5.845	-0.015
10	0	1	0	0	0	0	4.906	4.915	-0.009
11	1	2	-1	1	-1	1	4.411	4.376	0.035
12	1	2	-1	1	1	-1	7.205	7.130	0.075
13	0	2	0	0	0	0	4.928	4.915	0.013
14	1	2	1	1	1	1	3.883	3.847	0.036
15	1	2	-1	-1	1	1	5.324	5.282	0.042
16	1	2	1	1	-1	-1	4.191	4.217	-0.026
17	1	2	1	-1	-1	1	3.058	3.095	-0.037
18	1	2	-1	-1	-1	-1	5.258	5.256	0.002
19	0	2	0	0	0	0	4.95	4.915	0.035
20	1	2	1	-1	1	-1	4.675	4.695	-0.020
21	-1	3	0	1	0	0	5.071	5.070	0.001
22	-1	3	0	0	0	1	4.279	4.328	-0.049
23	-1	3	0	0	1	0	5.412	5.416	-0.004
24	-1	3	0	0	-1	0	4.422	4.414	0.008
25	-1	3	-1	0	0	0	5.423	5.511	-0.088
26	0	3	0	0	0	0	4.895	4.915	-0.020
27	-1	3	0	-1	0	0	4.851	4.760	0.091
28	-1	3	0	0	0	-1	5.544	5.502	0.042
29	0	3	0	0	0	0	4.84	4.915	-0.075
30	-1	3	1	0	0	0	3.905	3.964	-0.059

Table 4. Estimated Regression Coefficients for Ra (Before elimination).

Term	Coef.	SE Coef.	T-value	P-value
Constant	4.506408	0.017109	266.0088	0.000
Block 1	-0.0022	0.012726	-0.17473	0.865
Block 2	0.011938	0.012726	0.012726	0.365
E. T.	-0.71036	0.010686	-67.1387	0.000
I_p (Amp.)	0.142521	0.010686	13.47037	0.000
T_{on} (µsec.)	0.460116	0.010686	43.48656	0.000
T_{off} (µsec.)	-0.53923	0.010686	-50.9646	0.000

E. T.×E. T.	-0.22113	0.028452	-7.84871	0.000
I_p (Amp.)×I_p (Amp.)	0.051571	0.028452	1.83012	0.093**
T_{on} (µsec.)×T_{on} (µsec.)	0.011171	0.028452	0.39693	0.701**
T_{off} (µsec.)×T_{off} (µsec.)	0.006121	0.028452	0.21715	0.833**
E. T.×I_p (Amp.)	-0.02399	0.011332	-2.13716	0.054**
E. T.×T_{on} (µsec.)	-0.07449	0.011332	-6.63772	0.000
E. T.×T_{off} (µsec.)	0.087113	0.011332	7.76286	0.000
I_p (Amp.)×T_{on} (µsec.)	0.00505	0.011332	0.45046	0.663**
I_p (Amp.) ×T_{off} (µsec.)	-0.10353	0.011332	-9.22534	0.000
T_{on} (µsec.) ×T_{off} (µsec.)	-0.05555	0.011332	-4.95001	0.000
	R^2 = 99.86% $R^2_{(adj.)}$ = 99.69%			

Table 5. Estimated Regression Coefficients for Ra (After backward elimination).

Term	Coef.	SE Coef	T-value	P-value
Constant	4.47883	0.01674	267.507	0.000
E. T.	-0.70333	0.01199	-58.661	0.000
Ip (Amp.)	0.14111	0.01199	11.769	0.000
T_{on} (µsec.)	0.45556	0.01199	37.995	0.000
T_{off} (µsec.)	-0.53389	0.01199	-44.529	0.000
E. T. ×E. T.	-0.17917	0.02322	-7.717	0.000
E. T. ×T_{on} (µsec.)	-0.07375	0.01272	-5.799	0.000
E. T. ×T_{off} (µsec.)	0.08625	0.01272	6.782	0.000
Ip (Amp.) ×T_{off} (µsec.)	-0.10250	0.01272	-8.060	0.000
T_{on} (µsec.) ×T_{off} (µsec.)	-0.05500	0.01272	-4.325	0.000
	R^2= 99.72% $R^2_{(adj.)}$ = 99.60%			

Table 6. Analysis of Variance for Ra (µm).

Source	DF	Seq SS	Adj SS	Adj MS	F	P
Regression	9	19.11439	19.11439	2.123824	817.377	0.000
Linear	4	18.49148	18.49148	4.622854	1779.166	0.000
E.T.	1	9.082284	9.082284	9.082284	3495.428	0.000
I_p	1	0.365568	0.365568	0.365588	140.6988	0.000
T_{on}	1	3.810312	3.810312	3.810271	1466.423	0.000
T_{off}	1	5.233314	5.233314	5.233283	2014.092	0.000
Square	1	0.191964	0.191964	0.191944	73.8684	0.000
E.T. × E.T.	1	0.191964	0.191964	0.191944	73.8684	0.000
Interaction	4	0.43095	0.43095	0.107753	41.4732	0.000
E.T. × T_{on}	1	0.08874	0.08874	0.08876	34.1598	0.000
E.T. × T_{off}	1	0.12138	0.12138	0.1214	46.7262	0.000
I_p × T_{off}	1	0.171462	0.171462	0.171462	65.994	0.000
T_{on} × T_{off}	1	0.049368	0.049368	0.049368	19.0026	0.000
Residual	20	0.05304	0.05304	0.002652		

Error						
Lack-of-Fit	15	0.04692	0.04692	0.003131	2.6316	0.151
Pure Error	5	0.006018	0.006018	0.001214		
Total	29	19.114394				

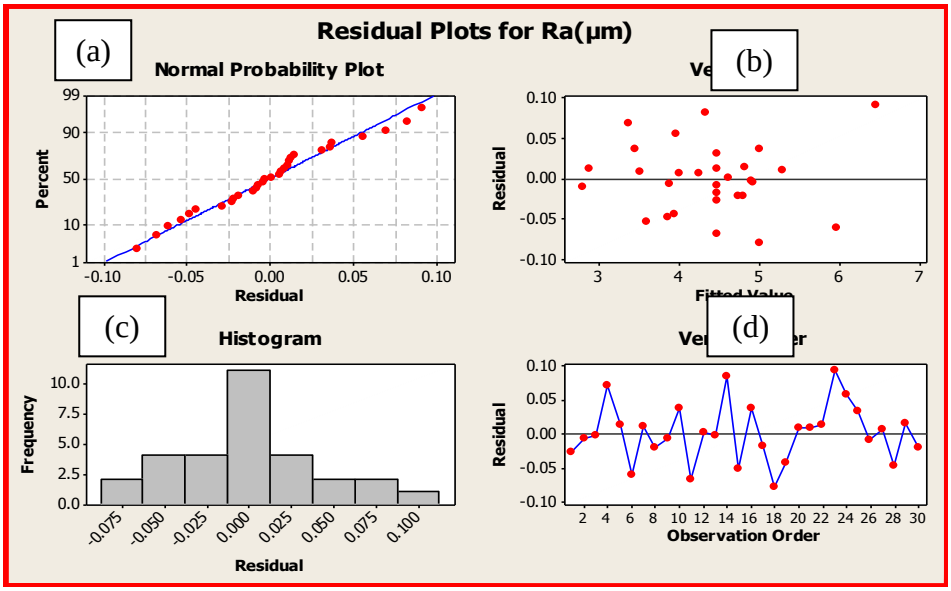

Figure 3. Residual Plot for Ra (µm).

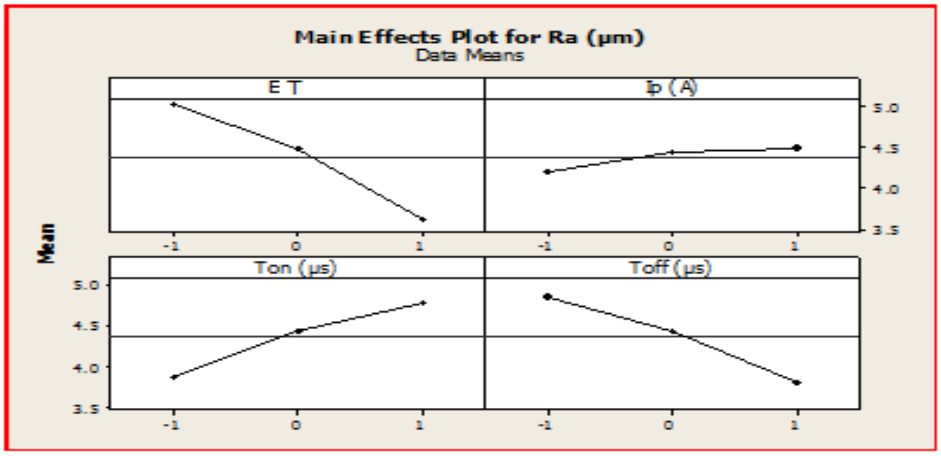

Figure 4. Main effect plots for Ra (µm).

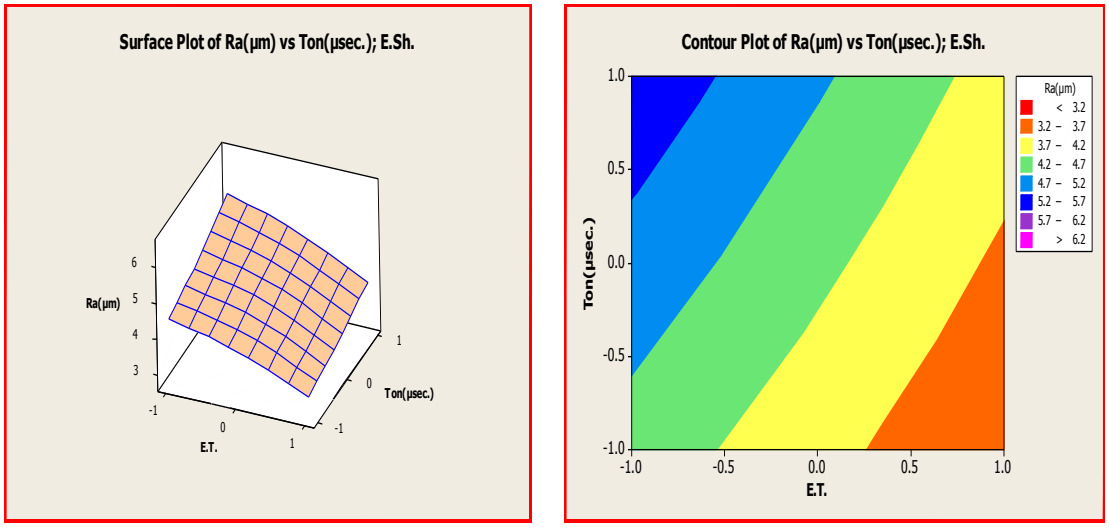

(a) (b)

Figure 5. Response surface plot (a) and contour plot (b) of Ra versus electrode shape (E.T.) and pulse on time (T_{on}).

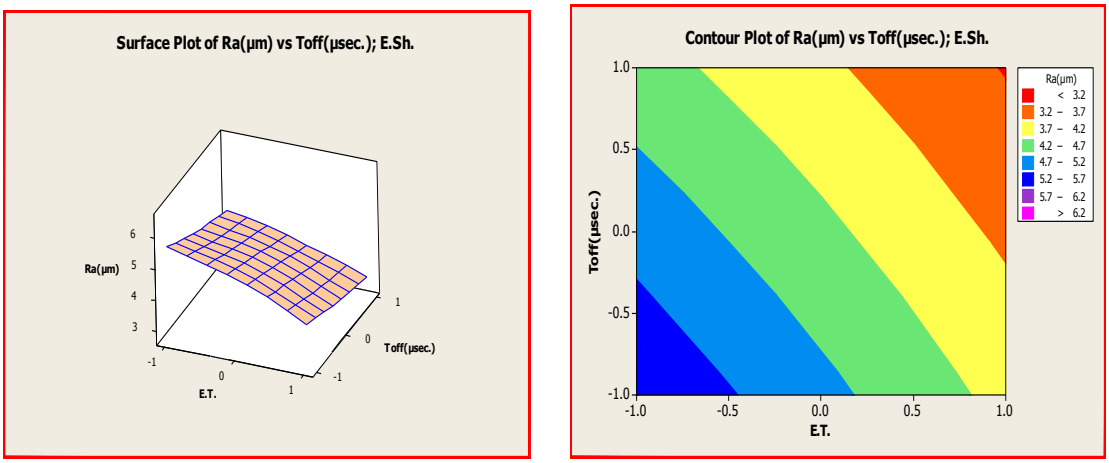

(a) (b)

Figure 5. Response surface plot (a) and contour plot (b) of Ra versus electrode shape E.T. and pulse off time(T_{off}).

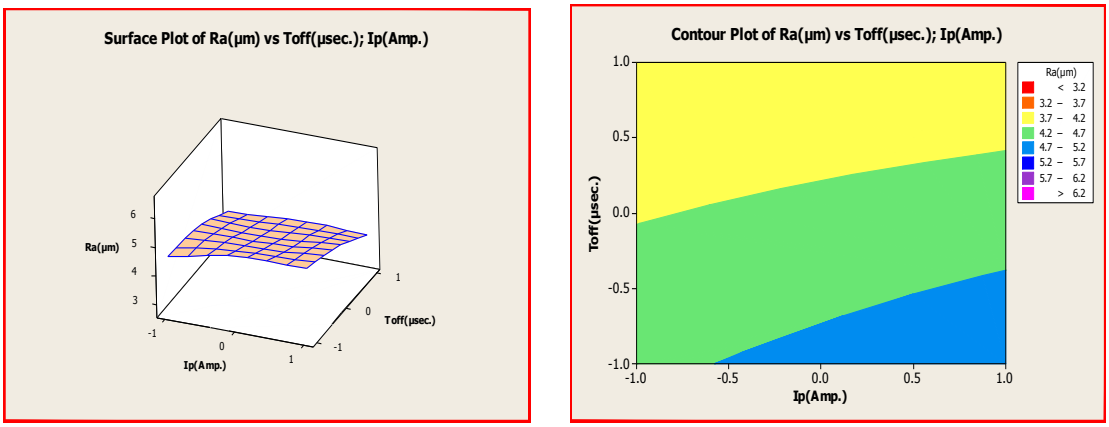

(a) (b)

Figure 6. Response surface plot (a) and contour plot (b) of Ra versus pulse current (I_p) and pulse off time(T_{off}).

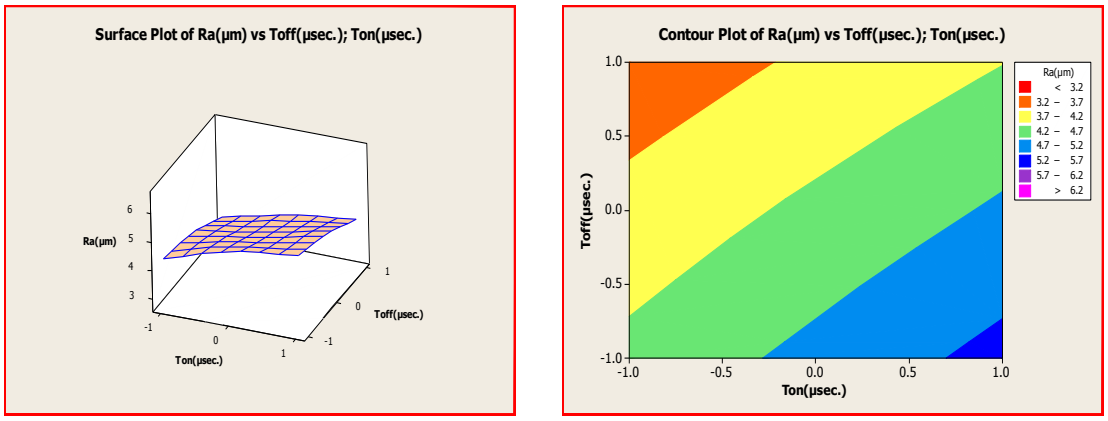

(a) (b)

Figure 7. Response surface plot (a) and contour plot (b) of Ra versus pulse on time(T_{on}) and pulse off time(T_{off}).

The effect of Laser Shock Peening on Fatigue Life Using Pure Water and Hydrofluoric Acid As a Confining Layer of Al – Alloy 7075-T6

Dr. Shaker Sakran Hassan
Professor
Mechanical Engineering Dept.
University of Technology
shaker_sakran1952_1@yahoo.com

Asst. Prof. Dr. Mohsin Nori Hamzah
Assistant Professor
Mechanical Engineering Dept.
University of Technology
20066@uotechnology.edu.iq

Raad Mohammed Abed
Lecturer
Ministry of Higher Education
and Scientific Research
raad1232002@yahoo.com

ABSTRACT

Laser shock peening (LSP) is deemed as a deep-rooted technology for stimulating compressive residual stresses below the surface of metallic elements. As a result, fatigue lifespan is improved, and the substance properties become further resistant to wear and corrosion. The LSP provides more unfailing surface treatment and a potential decrease in microstructural damage. Laser shock peening is a well-organized method measured up to the mechanical shoot peening. This kind of surface handling can be fulfilled via an intense laser pulse focused on a substantial surface in extremely shorter intervals. In this work, Hydrofluoric Acid (HF) and pure water as a coating layer were utilized as a new technique to improve the properties and to harden the treated surface of the Al - alloy 7075-T6. Fatigue life by means of laser peened workpieces was improved to 154.3%, 9.78%, respectively, for Hydrofluoric (HF) and pure water compared to un-peened specimens. And the outcomes of Vickers hardness test for laser shock peening with acid and pure water as well as un-peened specimens were 165.2HV30, 143.95HV30 and 134.7HV30, respectively showed a significant improvement in the hardness property.

Keywords: laser shock peening, aluminum alloy 7075-T6, pure water, HF acid, fatigue life.

تأثير السفع بالليزر على عمر الكلال باستخدام ماء نقي وحامض الهيدروفلوريك كطبقة حاجزة لسبيكة الالمنيوم 7075 -T6

الاستاذ الدكتور شاكر سكران حسن
قسم الهندسة الميكانيكية.
الجامعة التكنولوجية

الاستاذ المساعد نوري محسن حمزة
قسم الهندسة الميكانيكية
الجامعة التكنولوجية

رعد محمد عبد
وزارة التعليم العالي والبحث العلمي

الخلاصة

تعتبر عملية السفع بالليزرعملية تكنولوجية كفوءة نتيجتها نشوء اجهاد انضغاطي متبقي اسفل السطوح المعدنية ولذلك هذه العملية مهمة لتحسين عمرالكلال وخصائص المواد مثل مقاومة البلي والتآكل وهي ذات موثوقية عالية وتقلل من تدهور البناء الجزيئي. وهذا النوع من التعامل الميكانيكي بدون اتصال مباشر مع سطح المعدن. وتجري هذه العملية من خلال تسليط نبضات مكثفة من الليزر على سطوح المعادن وبأوقات قليلة جدا. وفي هذا البحث أستخدم حامض الهيدروفلوريك كتقنية جديدة وماء نقي كطبقة فوق سطح السبيكة الالمينوم 7075 لتحسين خواص السبيكة وتصليد سطح السبيكة. وقد تحسن عمر الكلال باستخدام الليزر الى 154.3% ، 9.78% على التوالي عند استعمال حامض الهيدروفلوريك والماء النقي مقارنة مع السطوح غير المعالجة. والنتائج المستحصلة من فحص فيكرز للصلادة عند استخدام حامض الهيدروفلوريك والماء النقي والقطع غير المعالجة كانت كالتالي (165.2HV30، 143.95HV30، 134.7 HV30) على التوالي وأظهرت تحسن مهم في خاصية الصلادة.

1. INTRODUCTION

The utilization of laser-generated power pulses to enhance the fatigue lifespan through stimulating compressive residual stress close to the surfaces of material components has been in expansion for further than 30 years **Clauer**, **et al., 1983.** Laser shock peening (LSP) is a cold working method, capable to initiate compressive residual stress and thus augment the resistance of the element to process fatigue. The important results obtained from this method were improved in hardness, tensile strength and fatigue life, which is attributed to LSP. The enhance in fatigue life is a result of significant residual surface stresses formed due to shock process, and to expand under the metal surface **Hu,** and **Yao, 2006**. Research by **Gomez, et al., 2005,** concluded that the Al- alloy 6061-T6 by using low energy Nd: YAG laser with a coating, laser peening can expansively obtain better surface compressive stress and micro-hardness with a little enhance in surface roughness. This compressive stress leads to an increase in fatigue life and wear resistance of the metal. This process permits, peening of complex geometries (e.g., aero-engine blades, fastener holes, etc.). It was experimentally found out that the LSP usually generates compressive areas, more than 4 mm deep, in comparison to about 0.25 mm generated by the conventional shoot peening, **Ding**, and **Ye**, **2006**.

Some corporation, **Mannava**, **et al**., **1996 – Casarcia**, **et al., 1996,** used either small output energy (around 1 J/pulse) or elevated energies (20 - 40 J/pulse) lasers on aluminum alloys. **Sano**, **et al., 2000 – Azer**, **et al.**, **2004**. They have revealed the practicability of using LSP in an industrial situation, with a big range of design (flanked by 5 mm and 10 mm diameters of impacts), materials and applications. The advantages of the treatments against other impact treatments (ultrasonic peening, shoot-peening, deep rolling) are quite well known; a good protection of surface roughness, and big affected depths (superior to 3 mm).

Surface treatment by LSP for the most parts includes applying an ablative or thin aluminum tape to the surface of a segment. This tape is vaporized by a laser beat, delivering a quickly extending plasma. The plasma is bounded by stagnant water sprayed on the surface. And the impact is to create a high-amplitude, short interval shock wave in the workpiece, **Achintha**, and **Nowell**, **2011**. As the stress wave engenders, more restricted plastic distortion happens and, once the shock has been applied, nonconformity between the plastically deformed material and encompassing elastic locally creates a residual stress, **Achintha**, and **Nowell**, **2013**. **Privy**, **2000,** illustrated the application of laser shock peening to lessen fatigue, to make improvement in hardness of the surface of the materials and to enhance the microstructural characteristics of metallic materials. Such upgrades were assumed to expand their benefit life for particular appliances. Additional research by **Prevey**, and **Jayaraman**, **2005**, demonstrated that powerful laser accomplishes better surface completely, style, minimize the organization time and additionally initiate profound shock waves into the material surface. This operates the laser shock peening an unrivaled method and more valuable towards a mechanical function. **Qureshi, et al., 2001**, likewise gave a case of the aviation producing area where the laser shock peening is gradually surpassing the other traditional technique of surface treatment utilizing shoot peening. **Hackel, 2005**, publicized that a beat of 25 J used for 25 ns was created by Nd: Yttrium Lithium Fluoride (YLF) laser.
The shocks were concentrated onto the specimen, and the region to be peened was sheltered with a material (black shaded glue tape) that is actives as an ablative in addition to thermal securing coating. Water was set up to stagnate over the specimens to absorb the laser pulse vitality and

thermal shock. Ionization and vaporization amid water supported peening are commonly produced because of the photon penetration in the liquid, which creates a plasma in the supported liquid. A get-together of plasma inside the water creates stunning waves that instantly enter into the treated surface of the specimen, adjacent plastically compressing the surface. The plastic strain after that fortifies compressive residual stress in the specimen at an around the depth of 1- 8 mm, relying upon the laser pulses factors and other technical considerations. In this work, it was determined, to analyze the state where an ablative layer exists as hydrofluoric acid (HF) as a new technique and pure water as a coating layer and to describe the fatigue lifespan associated with different levels of stress levels. The aim of this research is to evaluate the impact of HF acid and pure water, as a covering surface layer of the laser on the fatigue properties utilizing Al-alloy 7075.

2. EXPERIMENTAL WORK

The substance of the test is an aluminum alloy of 7075-T6, which is normally utilized for airplane structural auxiliary parts and other exceedingly focused on basic applications where high quality and enormous improvement to corrosion are required. The profile and measurements of the workpiece according to (DIN 50133) standard assurance are shown up in **Fig.1**.

The examinations were performed at the SIER-Baghdad (State Company for Inspection and Engineering Rehabilitation). Table (1) and (2), this examination gave the chemical compositions and static properties of Al- alloy 7075-T6.

The fundamental objective of the investigation tests is to produce the S-N curve for all cases that mentioned in the test arrange. A reverse cyclic bending loading test was performed by utilizing AVERY fatigue testing, mechanical machinery at various rates of cycles, as shown in **Fig.2**. The applied load is computed from the bending moment and the deflection angle applied to specimens. A revolution mechanical counter is associated specifically with the engine to record the number of cycles.

2.1 Laser Peening Process

There are diverse manners to build the absorption of the power of the laser, which is a high-energy laser pulse beat on the surface, and the black tape on the surface of the workpiece is a precise approach to improve this power with water as a repression layer.

The procedure essentially focuses the laser pulses alone to present an intensity of plasticity or plastic deformation, which empowers the surface of the material to pick up quality through stimulation of compressive residual stress. The procedure is complex as it includes water-assisted, laser preparing and the utilization of an absorptive layer, which both give an additional impact. First, a coating of black absorptive tape is set on the substrate to be dealt with, which is made from polyvinyl chloride (PVC) as the backing materials coated with rubber adhesive which could resist high voltage, high temperature and high ability of absorption of energy of the laser. The absorptive coatings in whichever case assist the material’s size to absorb the occurrence laser pulses.

Second, the stagnant or stream of pure water is prepared to pour above the treated surface of the material to be peened. Third, the exceptional beat of the laser is guided at the material to be peened.

These pulses of laser act similar to a shoot (bead) like in the mechanical shoot peening. In this work, hydrofluoric acid (HF) was utilized as another technique to upgrade the force of the laser that affects on the Al- alloy 7075-T6.

The treated surface of this layer is vaporized, keeping on to absorb energy, creating a plasma. The extension of the plasma is guarded by the water, resulting in an extremely rapid augment in pressure, which generates a shock wave within the material, plastically distorting closest to surface section. And to evade the reaction between the acid and the alloy, an exceptionally slight 100 µm layer of nylon covers the surface of the workpiece, then pouring the HF acid with 1-2 mm in depth over the workpiece, precisely on the contracted zone of the workpiece, as shown in **Fig. 3**, which demonstrates the workpiece with black tape and slight covering of acid. Prior to the laser treatment, the workpiece surface was smoothened with 200 emery paper to give Ra (average roughness) about 0.6 µm.

There are evident points of interest that empower the laser shock peening to subsist a much predominant method, in contrast with the other mechanical shoot peening methods. They are given as follows:

- Infiltration profundity of compressive remaining residual stress within the treated material is recognized to be much more prominent than that prompted by the shot peening surface treatment. This implies that the failure rate of treated surface with LSP is much lesser than that of the treated surface by means of the mechanical shoot peening method.
- Laser shock peening additionally makes available enhancements in surface roughness dissimilar to the mechanical shoot peening method that produces rough generated surface.
- Mechanical shoot peening needs instrument alters, though no device alter is necessitated for laser shock peening. This wipes out the needless set-up of working time and thus raises the fabrication throughput.
- No recollection of the impacted shoot is necessitated as the laser shock peening is a contact-less process with abnormal state of stability and repeatability permitting the surface treatment with negligible support and high-quality standards.
- All laser construction currently operate with better movement system and flexibility of progress that guides the programming of complex profile and geometries, that permits a simple programming from a two-dimensional (2D) to three-dimensional (3D) PC supported outline (CAD) design (tool way or beam way) and this characteristically permits development in six axes of movement, which is just an offer by the new and costly shoot peening arrangement with six-pivot mechanical movement systems.
- Furthermore, laser shock peening additionally offers an exact quality control where the consideration of the laser is capable of being observed continuously, upon which fault can be promptly repaired.

2.2 Laser Peening Treatment Device

To create a hardened surface lying on metals, Nd: YAG laser has been used. A laser appliance was used in this study (Q-switched neodymium YAG laser) as shown in **Fig. 4**, for laser peening which includes the following properties: Laser wavelength is about 1.065 μm, Pulse duration was 7 nanoseconds, Pulse energy was 300 mJ, and the laser spot is typically 5 mm in diameter.

2.3 Vickers Hardness Test

The Vickers hardness test approach includes of indenting the treated material by a diamond indenter, as a correct pyramid with a quadrangle bottom with an edge of 136 degrees between opposite confronts applied to a load of 30 kgf. The applied load is usually connected for 10 to 15 seconds. The dual diagonals of the breach left in the treated surface succeeding to the expulsion of the load are determined using a microscope and their normal computed. The region of the inclining surface of the space is determined. The Vickers hardness is the remainder obtained by separating the kgf load. And the results come from the Vickers hardness test type LAYREE as shown in **Fig. 5** for laser shock peening, with acid and water in addition to un-peened specimens, was 165.2HV30, 143.95HV30 and 134.6HV30, respectively.

3. RESULTS AND DISCUSSION

After finishing all experimental tests for laser shock peening, AVERY fatigue testing, and the Vickers hardness test, the following issues can be remarked.

3.1 Compressive Residual Stresses Induction

During laser shock peening the treated surface is turned out to be greatly harder and wear safe in the state of substances with existing plasticity. The surface compressive residual stress represses the early failure and prolongs the fatigue life and wear. This is a particular material to parts under frictional and shear stresses. The useful existence of the designing parts is anticipated by either. Fracture mechanics techniques or by measurable fatigue test information determined by stress life (S/N) or strain life (e/N) technique.

3.2 S-N Schemes

Fatigue life against the average recognized nominal stress range data used for the treated specimens and un-peened specimens are plotted to determine S-N curves which are appeared in **Fig.6**.These curves comprise of five levels of stress with three recordings for each level. The test results demonstrate that every point of interest treated at high cycle fatigue region by LSP with HF acid and pure water accomplished significant improvement in life and strength arrive at 154.3%, 9.78% respectively compared to un-peened specimens. Three S-N curves for three cases were drawn in S-N curves for the shock laser with pure water, HF acid, and un-peend alloy can be formulated by the equations, $\sigma f = 863.18*N f^{-0.157}$, $\sigma_f = 890*N_f^{-0.162}$ and $\sigma f = 870*N_f^{-0.159}$, respectively.

Increment in load capacity and bending strength amid bending as appeared in **Fig.7**, tension exists in the lower sector of the structure and compression happens on the high sector.

The forces performing on the minor surface are tense, the connotation that the structure in bending has the probable to fracture if the tensile stress reaches the ultimate tensile strength of the structure. The higher segment of the structure is in compression. This compression over the structure area makes a state of balance at the middle plane. Laser shock peening could incite extra compressive stress on the minor layer where the tensile stress is affecting. This would turn around the positive tensile stress into negative compressive stress and hinder the structure from cracking.

It would likewise improve the resistance of materials to break (crack start and grow from surface imperfections) thus upgrading and enhancing bending load capability. While the peened treated surface is in compression, necessitated force to instigate yielding at the base surface (layer) will likewise increase. Because of the utilization of surface treatment handle, for example, shot peening or laser shock peening, the stimulated compressive stress performing on the minor surface will imply that the performing created for the duration of the bending moment have to beat the peening-initiated compression. This demonstrates the bending strength of the material is upgraded by commencing a surface layer of compressive stress, permitting the treated material to include under higher bending strengths in association with the untreated material under similar bending situations.

The fundamental rule behind laser peening with the test in pure water and HF acid confinement can be clarified as follows. Pure water and HF acid are not utilized to cool the surface rather than serving the key capacity of keeping the plasma produced due to the high amount electrons content, compared to pure water which is ineffective enough to pass on all energy of the laser.The laser pulses interact with the opaque overlay surface and is utilized as a medium to infiltrate the laser pulses through the HF acid and pure water in view of the capacity of the acid to pass on the laser influence, which comprises of two combined waves, electrical wave, and magnetic waves, so the acid can pass on the waves in an efficient way through it. Hence it is depicted that the HF acid - laser fatigue lives extend the lifetime compared to pure water-laser fatigue lives and un-peened lives. This extension represents the factor of safety in comparison with the base metal behavior.

4. CONCLUSIONS

The high cycle fatigue life increment resulting from HF acid laser as a powerful technique influencing on the cyclic fatigue relies on upon the affected stress. At lower stresses, the fatigue life is more noteworthy than that of un-peened. However, at high stress, the stresses in general in large increments because of the high stress, which is the main factor in controlling the crack growth, i.e. quickens the propagation of the crack and the crack growth rate turns out to be faster than those of lower stresses. It can give a picture of that the compressive residual stress avoids the initiation and propagation of the cracks. And this lead to, that hydrofluoric acid - laser peening is an impact surface treatment technique better than water - laser peening and shows signs of improvement high cycle fatigue properties and hardening the surface of aluminum alloy 7075-T6 as the Vickers hardness test point out this conclusion. This improvement articulates to the consideration of safety measures correlation with the base metal finish.

REFERENCES

- Achintha, M., and Nowell, D., 2011, *Residual Stress in Complex Geometric Features Subjected to Laser Shock Peening*, J Strain Anal Eng, Journal of Materials Processing Technology 211 (6):1091-1101.
- Achintha, M. Nowell, D., Shapiro, K., and Withers, P.J., 2013, *Eigenstrain Modelling of Residual Stress Generated By Arrays of Laser Shock Peeing Shots and Determination of The Complete Stress Field Using Limited Strain Measurements*, Surface Coat Technol,216 pp. 68–77.
- Prevey, P., 2000, *The Effect of Cold Work on The Thermal Stability of Residual Compression in Surface Enhancement In718*. In: Proceedings of the 20th ASM Material Solutions Conference & Exposition, St Louis, MO, 10–12 October.
- Prevey, P. and Jayaraman, N., 2005, *Overview 0f Plastic Burnishing For Mitigation of Fatigue Damage and Mechanism*, In Proceedings of the 9th international conference of Shoot Peening on Fatigue and Fracture of steels, Paris, 6–9 September, pp.267–272.
- Qureshi M., Malik M., and Dubey, R., 2001, *Use of lasers for shoot peening*, In: International Conference on Shoot Peening and Blast Cleaning, p. 171.
- Ding, K., and Ye, L., 2006, *Simulation of Multiple Laser Shock Peening of A 35cd4 Steel Alloy*", J. of Materials Processing Technology, 178, pp. 162-169.
- Mannava, S. McDaniel, A. E., and Cowie, W. D., 1996, *General Electric Company* (Cincinnati, OH), US Patent, 5, 492, 447.
- Casarcia, D. A., Cowie, W. D., and Mannava, S. 1996, *General Electric Company* (Cincinnati, OH). US Patent, 5,584,586.
- Sano, Y., Kimura, M., Sato. K., Obata, M., and Sudo, A., 2000, *Development and Application of Laser Peening System to Prevent Stress Corrosion Cracking of Reactor Core Shroud Proceedings*", of the 8th international conference on nuclear engineering (ICONE-8) (Baltimore, USA).
- Azer. M, and Scheidt, D. 2004, *On The Applications of Lasers and Electro Optics*, Proceedings of Icaleo, 2004 (San Francisco, USA).
- Achintha, M., and Nowell, D., 2011, *Eigenstrain Modelling of Residual Stresses Generated By Laser Shock Peening*, J Mater Process Technol, 211pp.1091–101.
- Clauer, A. H., Walters, C. T., and Ford, S. C., 1983, *The Effects of Laser Shock Processing on The Fatigue Properties of 2024-T3 Aluminum*, Lasers in materials processing. Metals Park (Ohio): ASM International.
- G, Gomez-Rosas., C. Rubio- Gonzalez., and JL. Ocana, 2005, *High Level Compressive Residual Stresses Produced in Aluminum Alloys by Laser Shock Processing*, Applied Surface Science, Vol. 252, pp. 883-887.
- Hackel L, 2005, *Shaping the future-laser peening technology has come of age*, The Shoot Peener, 19 (3): 3.
- Hu, Y., and Yao, Z., Hu, J., 2006, *3D FEM simulation of Laser Shock Processing. In: Surface & Coating Technology* 201, p. 1426-1435.

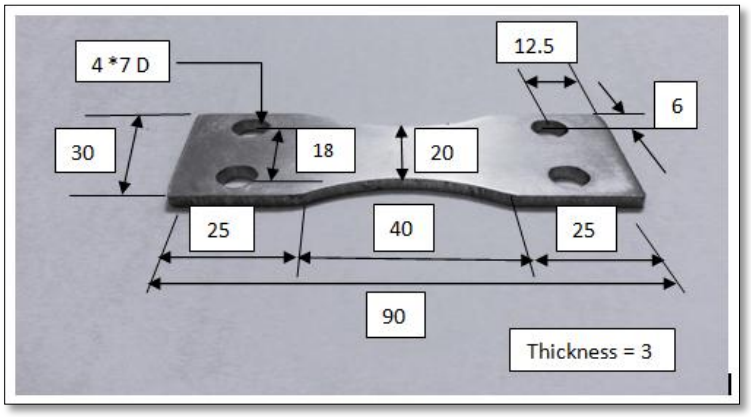

Figure 1. Fatigue specimen geometry, dimensions in millimeter agreement to (DIN 50133) standard requirement.

Table 1. Chemical compositions of the experimental and standard AL- alloy 7075, wt%, [ASTM].

	Zinc	**Titanium**	**Silicon**	**Manganese**
Stand.	6.1 Max.	0.2 Max	0.4 Max.	0.3 Max.
EXP.	5.52	0.028	0.26	0.11
	Iron	Copper	Chromium	Magnesium
Stand.	0.5 Max.	1.2-2	0.28 Max.	2.1-2.9
EXP.	0.24	1.82	0.183	2.15

Table 2. The average mechanical properties of three specimens of Al- alloy 7075-T6.

Property	**Experimental**	**Standard**
Ultimate stress	530 MPa	502MPa
Yield stress	496 MPa	406 MPa
Fatigue strength	206 MPa	156 MPa
Modulus of elasticity	75.6 GPa	74 GPa
Poisson's ratio	0.32	0.33
Elongations %	14.6	16

Figure 2. Fatigue bending machine.

.

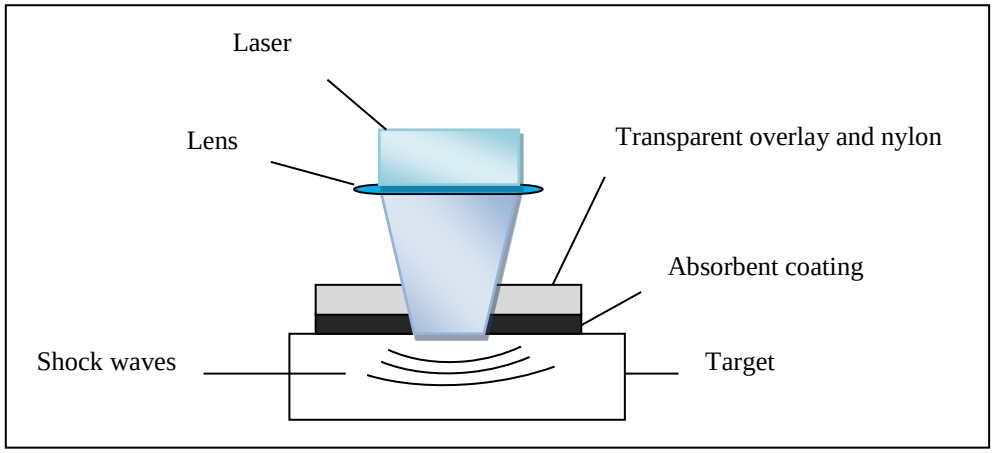

Figure 3. The basic principle of laser shock peening.

Figure 4. Specimen applied under laser power.

Figure 5. Vickers hardness test.

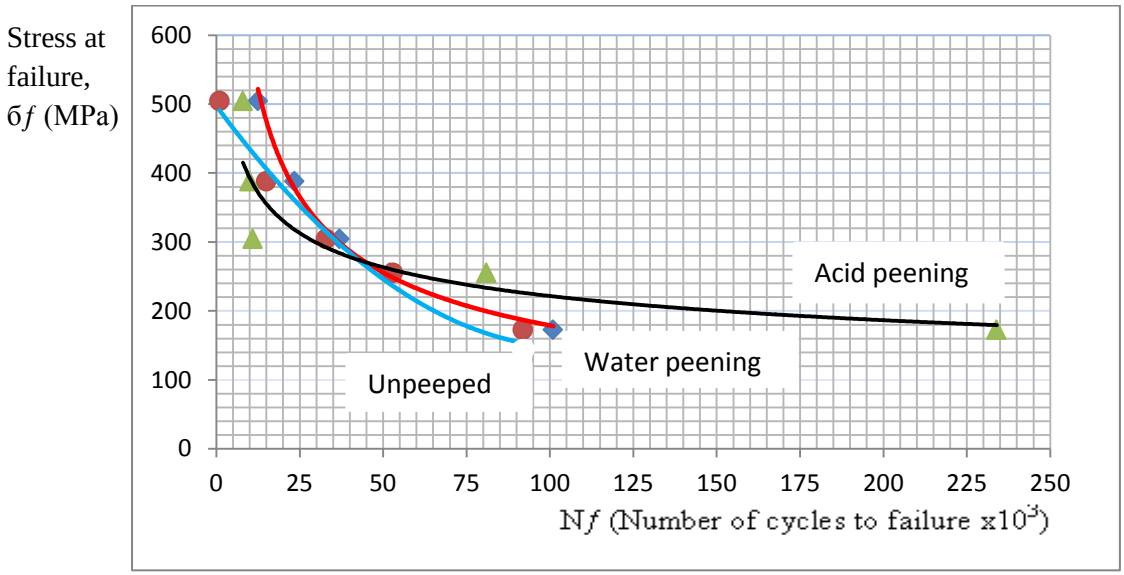

Figure 6. S-N curves at a constant load for un-peened, and laser shock peening with pure water and HF acid.

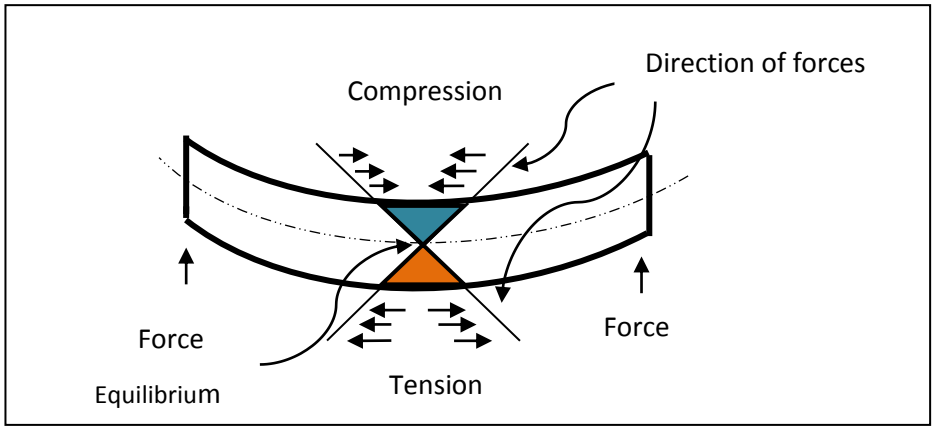

Figure 7. Graphic diagram viewing the allocation of stress across the material in bending.

Determination Optimum Inventory Level for Material Using Genetic Algorithm

Watheq Hayawi Laith
Lecturer
College of Administration and Economics -University Of Sumer
wahe36 @ yahoo.com

Sawsan Sabeeh Al-Zubaidy
Assistant Professor
Department of Production Engineering and Metallurgy-University Of Technology
Sawsan2006@yahoo.com

Mahmoud Abbas Mahmoud
Assistant Professor
Department of Production Engineering and Metallurgy-University Of Technology
dr.mahmoudalnaimi@yahoo.com

ABSTRACT

The integration of decision-making will lead to the robust of its decisions, and then determination optimum inventory level to the required materials to produce and reduce the total cost by the cooperation of purchasing department with inventory department and also with other company's departments. Two models are suggested to determine Optimum Inventory Level (OIL), the first model (OIL-model 1) assumed that the inventory level for materials quantities equal to the required materials, while the second model (OIL-model 2) assumed that the inventory level for materials quantities more than the required materials for the next period. This study was applied in Wasit Company for Textile Manufacturing in the Textile Factory, where it produces five products, which are printed striped, plain, poplin, dyed poplin and Naba weave. The products are made from cotton and they are passing through several stages to transfer to the final product. A genetic algorithm is used to determine the optimum quantity of the purchase a cotton and colors for each month and with minimum cost. Where the purchasing and transportation costs were either constant or variable with respect to purchased quantities while holding cost is kept constant. The results showed that the total cost of the first model is minimum than the second model because the holding cost for this model is less from the second model, while the purchasing and transportation costs from two models are equals. The percentage of purchasing cost for cotton is the biggest value, more 99% of purchasing cost for two models.

Keyword: Inventory Level, Genetic Algorithm, Decision-making.

تحديد مستوى الخزين الامثل للمواد باستخدام الخوارزمية الجينية

م. واثق حياوي لابذ
كلية الادارة والاقتصاد
جامعة سومر

أ.م.د. سوسن صبيح الزبيدي
قسم هندسة الانتاج والمعادن
الجامعة التكنولوجية

أ.م.د. محمود عباس محمود
قسم هندسة الانتاج والمعادن
الجامعة التكنولوجية

الخلاصة

تكامل أتخاذ القرارات سيؤدي الى ترصين هذه القرارات ومن ثم تحديد مستوى الخزين الامثل للمواد المطلوبة والتي تكفي لعملية الإنتاج وأن تقليل الكلفة الكلية من خلال التنسيق بين قسم المشتريات وقسم الخزين وكذلك مع بقية أقسام الشركة الأخرى.

تم اقتراح نموذجيين لتحديد مستوى الخزين الأمثل للمواد المطلوبة، في النموذج الأول تم افتراض أن مستوى الخزين يساوي المواد المطلوبة بينما في النموذج الثاني تم افتراض أن مستوى الخزين أكثر من المواد المطلوبة للفترة اللاحقة.

هذه الدراسة طبقت في شركة واسط لصناعة المنسوجات في معمل النسيج، حيث ينتج خمس منتجات وهي البازة والسادة والبوبلين والبوبلين المطبوع ونسيج النبأ. المنتجات تصنع من القطن ويمر بعدة مراحل ليصبح منتج نهائي وقد استخدمت الدالة الجينية لتحديد أمثل كمية مشتراه من القطن والالوان لكل شهر وباقل كلفة حيث كانت كلف الشراء والنقل أما ثابته أو متغيرة مع الكمية المشتراة، بينما كانت كلف الاحتفاظ ثابتة. بينت النتائج ان الكلفة الكلية للنموذج الأول كانت أقل من النموذج الثاني لكون كلفة الاحتفاظ لهذا النموذج أقل بينما كلف النقل والشراء متساوية في النموذجين.

نسبة كلفة الشراء لمادة القطن تجاوزت 99% من كلفة الشراء وللنموذجين.

1.INTRODUCTION

The companies select a single or multiple suppliers to fulfill the demands, and replenishment order quantity is split into different portions for each supplier at the same time. From the previous study, basically, there are two types of supplier selection problem. In the first type of supplier selection, a single supplier can fulfill the entire buyer's demand. In the other type of supplier selection, there exists no single supplier who can satisfy the entire buyer's needs. In this situation, the buyer has to split order quantities among suppliers for having a stable environment of competitiveness, **Demirtas, and Üstün, 2008**. There are several studies that deal with optimum inventory level, Park et. al. developed a mathematical model in which the retailer placed orders based on the EOQ policy and allocated them to the multiple manufacturers. In their model, production allocation ratios and the shipment frequencies at the manufacturers, as well as the purchasing cycle length at the retailer, were formulated to minimize the average total cost at the manufacturers and retailer, **Park, et al., 2006**.

Sarker et. al. consider EOQ-like batch sizing models that account for the possibility of rework being done during cycles, as well as after a certain number of cycles. Especially the latter deals with quite some far going issues and hence provides some useful insights. Nonetheless, the paper stresses the need for flawless production, since rework will always be more expensive than the first-time-right production**, Sarker, et al., 2008**.

Wadhwa and Ravindran introduced multiple objective multiple supplier selection models for low risk and cost products. The first objective was to minimize the total purchasing cost, which concluded total variable cost, fixed cost, inventory holding cost, and the bundling discounts. The second objective was to minimize the reject units under supplier capacity constraint. The shortage was not allowed and the multi-objective model was solved by preemptive goal programming, **Wadhwa, and Ravindran, 2010**.

Araújo and Alencar put forward a model for selecting suppliers and evaluating the performance of those already working with a company. A simulation was conducted in a food industry. This sector has a high significance in the economy of Brazil. The model enables the phases of selecting and evaluating suppliers to be integrated. This is important so that a company can have partnerships with suppliers who are able to meet their needs. Additionally, a group method is used to enable managers who will be affected by this decision to take part in the selection stage, **Araújo and Alencar, 2015**.

2. INVENTORY LEVEL

Effective forecasting is essential to achieve service levels, to plan allocation of total inventory investment, to identify needs for additional production capacity, and to choose between alternative operating strategies, where the accurate forecast is important to increase service levels, decrease inventory levels, and operating costs, **Russell and Taylor, 2009**.

The Just in time (JIT) methodology is far more geared toward towards the stabilization of the inventory levels throughout the supply chain than the traditionally fixed order quantity methodology, also known as the economic order (EOQ) model. Manufacturers need a strategy to decrease total costs for items and to increase customer satisfaction. The purchasing department receives the items from suppliers at the same time of the demand is one of the keys of decreasing the risk for the manufacturers. Just-In-Time (JIT) model is one of the ways for achieving this goal, but it may not be the optimal solution. The first reason is, in the JIT model the manufacturers order the items whenever they need to meet the demand thus, it covers just pull systems and short planning horizon. The second reason is, by increasing order quantities, the price and shipping cost per item will be decreased, although, in a JIT model, the price breaks for purchasing and transportation costs may not happen at all time points, **Eiliat, 2013**.

3. OPERATING COSTS

Operating costs consist of the following:

3.1 Ordering Costs

The ordering costs is a fixed cost of tracking trucks from a supplier to inventory, labor costs of processing orders, inspection and returning of poor quality products, **Onawumi, et al., 2009**. Conversely to the costs fixed per unit, the inventory costs fixed per order comprises only a portion of the acquisition cost of inventory. This is the cost incurred each time a stock replenishment order is placed and includes costs such as import duties, telephone calls, stock consolidator's fee, etc., **Bredenkamp, 2005**.

3.2 Holding Costs

Holding cost is defined as the cost associated with having one unit in inventory for a period of time. According to them, holding cost consists of four components, **Holstein and Olofsson, 2009**:

1. Capital cost.
2. Inventory service cost.
3. Storage space cost.
4. Inventory risk cost.

Capital cost considers as the major contributor to holding cost. The other components such as inventory service cost, storage space cost, and inventory risk cost are sometimes called out-of-pocket holding costs.

3.3 Purchasing Costs

It is the primary concern of any manufacturing organization to get an item at the right price. But right price need not be the lowest price. It is very difficult to determine the right price; general guidance can be had from the cost structure of the product, **Eiliat, 2013**.

3.4 Transportation Costs

Transportation costs will at first decline as the number of facilities increase, but will eventually increase the number of facilities increase as a result of inbound and outbound transportation costs.

The total cost of transporting products must be measured and not only the cost of moving the products to the warehouse. With fewer locations saving can be obtained by making use of bulk distribution from the manufacturer or supplier. There will, however, be a certain point where there are too many warehouses and fewer inventory of the various item lines will have to be shipped to the warehouse to ensure that there are no items that are overstocked. This will lead to higher costs charged by the transporter due to smaller loads, **Burger, 2003**.

4. GENETIC ALGORITHM (GA)

The genetic algorithm is a stochastic search method for solving both constrained and unconstrained optimization problems that are based on the natural selection process that mimics biological evaluation. It explores the solution space by using concepts taken from natural genetics and evolution theory, **Baz, 2004**. GA starts with an initial set of solutions which is known as a population. The individuals of the population are called chromosomes which are evaluated according to a predefined fitness function, in our case the total cost. Each chromosome includes several genes. The gene represents an order quantity of item I at time point j. For example, if there are 12 items and 12- time points, we will have 144 genes (order quantity) in one chromosome as in **Fig.1**. The chromosomes evolve through successive iterations called generations, **Li, et al, 2010.**

A new generation is created by changing chromosomes in the existing population through

crossover and mutation, **Baz, 2004**, as shown in **Fig.2**.

5. APPLICATION OF PROPOSED METHODOLOGY

This paper was applied in Wasit company for Textile Industries as a case study to determine optimum inventory level for material. Textile Factory produces five products (N=5) which are (printed striped, poplin, Nuba, and dyed poplin weaves), their representation with symbols is (A, B, C, D, and E) respectively, that will make on the same production line inside factory and need setup time to change arrangements this production line when altering the production to another product. The materials required for manufacturing of products (meter) are cotton (ton) and colors (gram) by used bill of materials as shown in **Fig.3**.

Determination of the materials required depend on quantities forecasted in the marketing department, where requested quantities from cotton to the year 2016 is shown in Table.1, making an approximation to near integer number more than requested quantities and also for color as shown in Table 2.

The purchasing department will make the plan to purchase the materials required for the entire year with minimum total cost (holding, purchasing, and transportation costs) depend on forecasting.

6. PROPOSED ALGORITHM TO DETERMINE OPTIMUM INVENTORY LEVEL

Purchasing department study purchasing of materials and determine the best order quantity depending on purchasing, transportation, and holding costs for materials, that can be illustrated in Tables 3, 4 and 5 respectively according to plans of this company for the year 2016.

The assumptions that are used in this algorithm are:

1. Items are always available for shipment.
2. Each item has constant holding and ordering costs.
3. The purchase and transportation costs vary with order quantity or constant.
4. The demands are known and non-constant.
5. The period between time points of planning horizon could be measured in hours, days, months, etc.

The selection of the best order quantity in the textile factory can be classified into two models depending on inventory amounts. **The first model** will attempt reducing the inventory level, therefore will lead to reducing holding cost.

This model will be explained in the section (6.1), that assumed the inventory amounts will equal the demand for next month and will be symbolled as (OIL-Model 1). **The second model** will assume the inventory amounts will exceed the demand for next month to reduce purchasing and transportation costs. This model will be explained in the section (6.2), and the symbol to this model is (OIL-Model 2).

6.1 OIL-Model 1

In this paper used through a hybrid algorithm that compared advantages JIT and EOQ to reduce all costs together to determine the optimum inventory level and it solve by GA where calculate from equation (1) and (2).

$$V_i^j = V_i^{j-1} + Q_i^j - D_i^{j-1}, \ \forall j \in J \setminus \{0\} \quad (1)$$

$$Q_i^j \geq 0 \, , and \ Q_i^0 = 0, \ \forall i \in I \quad (2)$$

Where:

V_i^j = Inventory level for material *i* at time *j*.

Q_i^j = Quantity order for material *i* at time *j*.

D_i^j = Demand for material *i* at time *j*.

The company warehouse has a limited stock capacity for each material $i \in I$ depend on lower and an upper number of units for all materials. The inventory level of material *i* should be greater than or equal to the demand of production department at each time point j when there is no shortage of materials, thus:

$$V_i^j \geq D_i^j \,, \forall i \in I \,, \forall j \in J \quad (3)$$

The price of each material decreases when the number of material increases. The purchasing cost of order quantity is:

$$if Lower \leq D_i^j < Upper \; then \; P_i^j = p_i^k Q_i^j \quad ; \quad \forall i,j \quad (4)$$

Where:

P_i^j = Purchasing cost for material *i* in time *j*.

p_i^k = The set of price breaks of material *i*, where k={1,2,3,….}

The transportation cost for shipping the materials decrease when the number of materials increases, therefore transportation cost of order quantity is:

$$If\left(Lower \leq D_i^j < Upper\right) then \; T_i^j = r_i^m Q_i^j \; ; \forall i,j \quad (5)$$

Where:

T_i^j = Transportation cost for material *i* in time *j*.

r_i^m = The set of price breaks of transport material *i*, ether m={ 1,2,3,….}.

Material *i* has a unit holding cost h_i per time period. The total holding cost for storing order quantities of material *i* between time points j and j+1 is:

$$H\left(Q_i^j\right) = h_i V_i^j \; ; \forall i,j \quad (6)$$

Let $C\left(Q_i^j\right)$ be the total cost, that is the summation of purchasing, holding and transportation costs. Form equations (4), (5) and (6) we have:

$$\text{Minimize Z= } C\left(q_i^j\right) = \sum_{i \in I} \sum_{j \in J} \left(P\left(Q_i^j\right) + H\left(Q_i^j\right) + R\left(Q_i^j\right)\right) \quad (7)$$

The solutions are given after 500 runs in MATLAB program. Each run gives various total cost with a various set of order quantities, then compares them to give best order quantities with minimal total cost, that equal to1563661500 dinars at run number 178 as shown in **Fig.4**, the order quantities for this factory can be shown in Table.6 and Tables 7 shows inventory levels (V_i^j). Tables 8, 9, and 10 show the holding, purchasing, and transportation costs for all items in a year 2016. Figure (5) gives a summarized the percentage of the holding, purchasing and transportation costs.

6.2 OIL-Model2

This model uses the same equations as the first model except that the equation number (1) has changed to become:

$$V_i^j \geq V_i^{j-1} + Q_i^j - D_i^{j-1} \,, \qquad \forall j \in J \setminus \{0\} \quad (1)$$

The order quantities for this factory can be shown in Table .11.The solutions are given after 500 runs in MATLAB program. Each run gives various total cost with a various set of order quantities, then compares them to give best order quantities with minimal total cost, that equal to 1592049000

dinars at run number 151 as shown in **Fig. 6.** Tables 12 shows inventory levels.
Tables 13, 14, and 15 show the holding, purchasing, and transportation costs respectively for all items in the year 2016.
Fig.7 gives a summarized the percentage of the holding, purchasing and transportation costs. The percentage of purchasing cost is the biggest value, 87% and the percentage of purchasing cost for cotton is the biggest value, more 99% of purchasing cost.
Decision maker in production department will make the plan to execute accepted demands with minimum setup time for the entire year and determine the best sequence of products and to all demands by coordination with another department to integrate decision making inside the factory.

7. CONCLUSIONS

The best order quantity in the textile factory depends on reducing each holding, purchasing, and transportation costs together by using GA, can be classified to two models depend on inventory amounts.
The main conclusions of this paper are:
1. The total cost of (OIL-Model 1) less than (OIL -Model 2), where total cost for (OIL -Model 1) equals to1563661500 and for (OIL-Model 2) equal to 1592049000 dinars.
2. The holding cost of (OIL -Model 1) less than (OIL -Model 2), where holding cost for (OIL -Model 1) equals to12188000 and for (OIL -Model 2) equals to 40575500 dinars.
3. The percentage of purchasing cost 89% , Transportation cost 10% and holding cost 1% from the total cost of (OIL -Model 1).
4. The percentage of purchasing cost 87% , Transportation cost 10% and holding cost 3% from the total cost of (OIL -Model 2).
5. The percentage of purchasing cost of cotton is the biggest value, more 99% of purchasing cost for two models.
6. The proposed methodology can be applied to another industrial company, especially organizations which work in a dynamic environment more than Wasit company.

8. REFERENCE

- Araújo M. and Alencar D., 2015, *Integrated Model for Supplier Selection and Performance Evaluation,* South African Journal of Industrial Engineering August Vol.26.
- Baz, M.A., 2004, *A Genetic Algorithm for Facility Layout Problems of Different Manufacturing Environments*, Computer and industrial engineering , vol.47, No.23, pp. 233-246.
- Bredenkamp F., 2005, *The Development of a Genetic Just-In-Time Supply Chain Optimization Software Tool*, Master thesis, Unversity of Stellenbosch, Industrial Engineering.
- Burger F., 2003, *The Impact of Warehousing and Transportation on Supply Chain Effectiveness*, Msc.Thesis, Rand Afrikaans University.
- Demirtas, E., and Üstün Ö., 2008, *An Integrated Multiobjective Decision Making Process for Supplier Selection and Order Allocation*." Omega Vol.36.
- Eiliat, H., 2013, *Optimization of Operational Cost for a Single Supplier–Manufacturer Supply Chain*, Msc. Thesis, University of Windsor Industrial and manufacturing systems engineering.

- Holstein, J. and Olofsson, A. 2009, *Inventory Control - At Maintenance Unit Tetra Pak in Lund.* Msc. Thesis. Lund University, Lund University – Production Management, http://www.pm.lth.se/fileadmin/pm/Exjobb/Exjobb.
- Li, M. J., Chen D.S., Cheng, F., Wang, Y., Zhon, L.Y. and Lang J.L.,2010, *Optimizing Emission Inventory for Chemical Transport Models by Using Genetic Algorithm*, Atmospheric Environment, Vol.44, No. 32, pp. 3926-3934.
- Onawumi A., Oluleye A., and Adebiyi K.,2009, *An Economic Lot Size Model with Shortages and Inflation*, International Business Management, Vol (3), No.(4).
- Park S.S., Kim T., Hong Y., 2006, *Production Allocation and Shipment Policies in a Multiple-Manufacturer–Single-Retailer Supply Chain*. International Journal of Systems Science , Vol. 37.
- Russell and Taylor, 2009, *Operations Management Along the Supply Chain*, 7th ed. Chichester: John Wiley & Sons, Ltd.
- Sarker B., Jamal A., Mondal S., 2008, *Optimal Batch Sizing in a Multi-stage Production System with Rework Consideration*, European Journal of Operational Research Vol.184.
- Wadhwa, V. and Ravindran A., 2010, *Multi-objective Supplier Selection Models*. Proceedings of the Industrial Engineering Research Conference.

List of Abbreviations

Abbreviations	Meaning
OIL	Optimum Inventory Level
OIL -Model 1	Optimum Inventory Level with inventory
OIL –Model2	Optimum Inventory Level without inventory
JIT	Just In Time
EOQ	Economic Order Quantity
GA	Genetic Algorithm

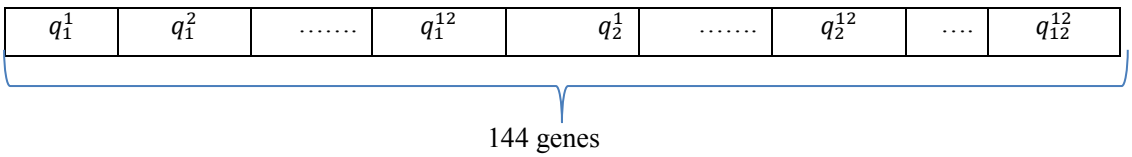

Figure 1. Chromosome with 144 genes.

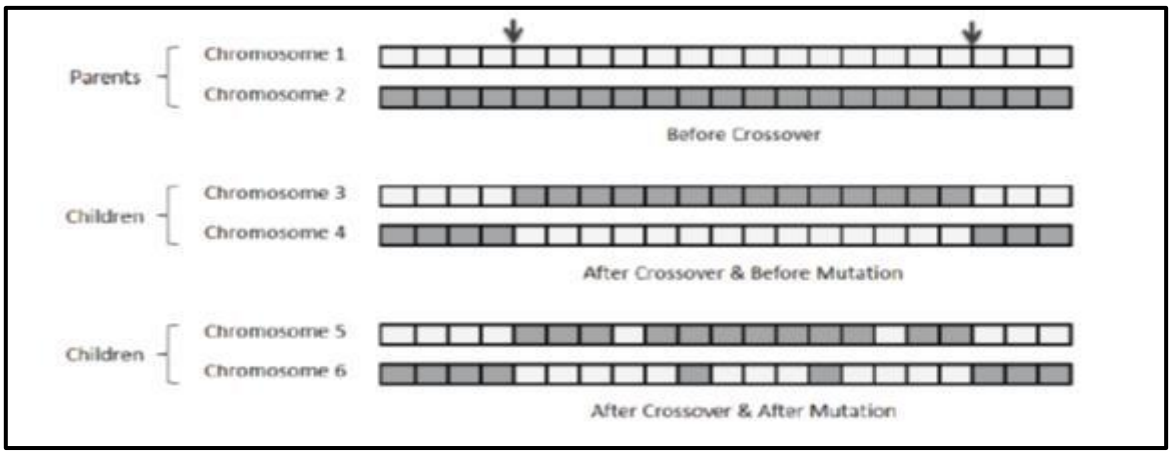

Figure 2. Crossover and mutation.

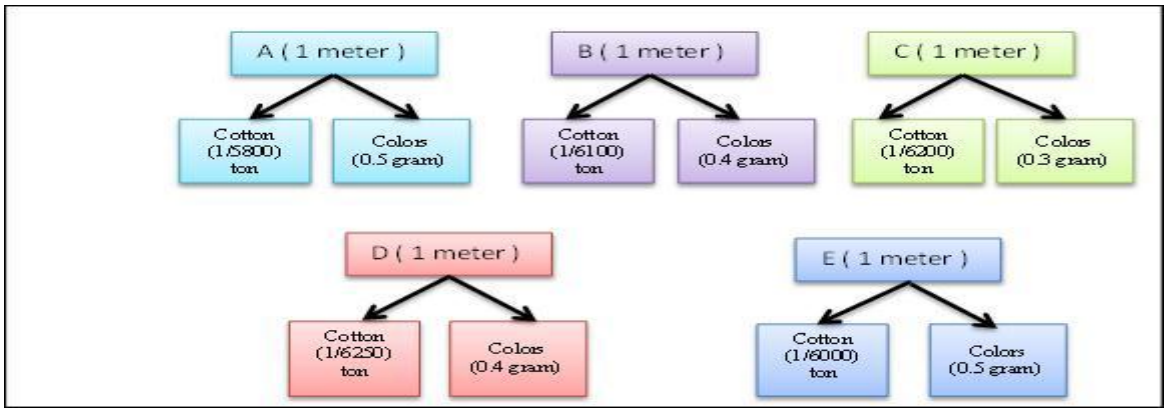

Figure 3. Bill of materials for products of textile factory.

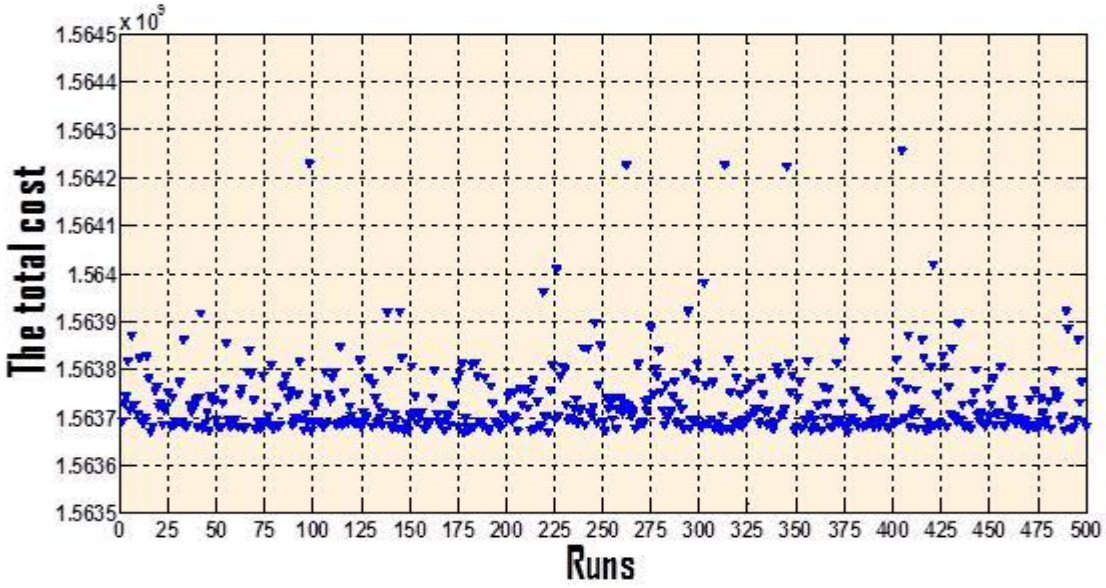

Figure 4. Comparing runs in the MATLAB programming for the first model.

Figure 5. Dividing total cost for the first model.

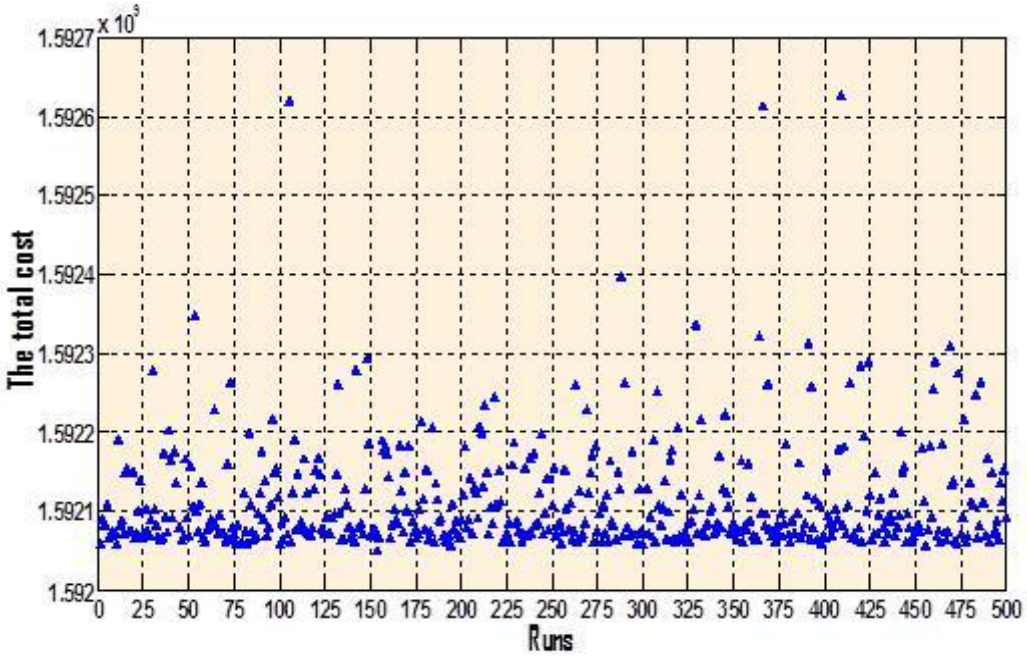

Figure 6. Comparing runs in the MATLAB programming for the second model.

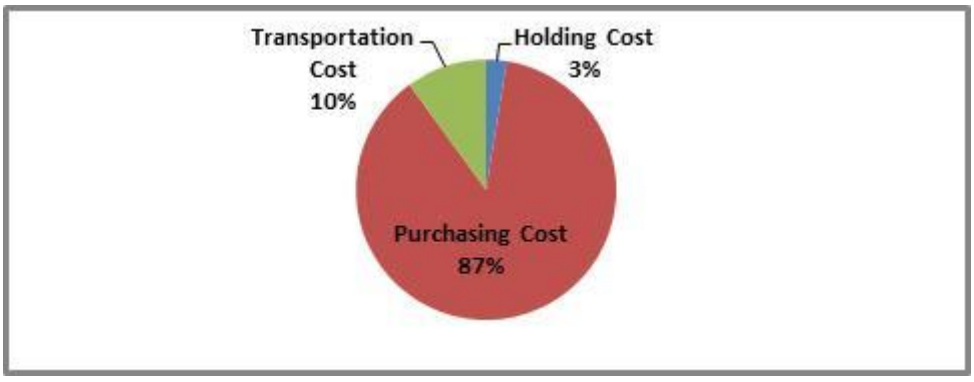

Figure 7. Dividing total cost for the second model.

Table 1. Materials required from cotton (ton) to the year 2016.

Products / months	A	B	C	D	E	Total
January	15.607	6.477	34.187	2.070	0.112	59
February	12.116	3.822	55.784	1.014	0.000	73
March	7.110	5.022	54.635	0.000	0.000	67
April	16.012	7.955	17.921	0.000	0.820	43
May	11.334	15.557	39.329	6.332	0.067	73
June	9.229	13.767	36.073	2.868	0.452	63
July	5.259	8.628	16.140	0.000	0.000	31
August	10.595	11.394	36.216	0.000	0.000	59
September	10.024	9.433	16.769	0.000	0.000	37
October	15.105	15.550	28.510	1.765	0.048	61
November	14.271	6.044	26.385	2.564	0.000	50
December	8.414	5.313	25.258	0.000	0.000	39

Table 2. Materials required from colors (kg) to the year 2016.

products / months	A	B	C	D	E	Total
January	45.26	15.8036	63.588	5.1752	0.002588	130
February	35.135	9.3256	103.758	2.5356	0.001268	151
March	20.62	12.2532	101.622	0	0	135
April	46.435	19.4108	33.333	0	0	100
May	32.87	37.9596	73.152	15.8296	0.007915	160
June	26.765	33.5904	67.095	7.1692	0.003585	135
July	15.25	21.0512	30.021	0	0	67
August	30.725	27.8016	67.362	0	0	126
September	29.07	23.016	31.191	0	0	84
October	43.805	37.942	53.028	4.4136	0.002207	140
November	41.385	14.7476	49.077	6.4096	0.003205	112
December	24.4	12.964	46.98	0	0	85

Table 3. The relation between price costs (thousand dinars) per unit and material order quantity.

Material $i \in I$	Price Costs			
	1	2	3	4
Cotton	1- ∞			
	2500000			
Colors	1-250	250-500	500-1000	1000-∞
	3500	3250	3000	2750

Table 4. Transportation costs (thousand dinars) per unit.

Material $i \in I$	r_i^m- r_i^{m-1}		
	0-100	100-250	250-5000
Cotton	300000	275000	250000
Colors	350	350	300

Table .5 Initial inventory level (V_i^0) *and* holding costs per unit.

Material	h_i (Dinar)	V_i^0
Cotton	50000	100 (ton)
Colors	500	150 (KG)

Table 6. Best order quantities for first model.

		$j \in J$											
		Q_i^1	Q_i^2	Q_i^3	Q_i^4	Q_i^5	Q_i^6	Q_i^7	Q_i^8	Q_i^9	Q_i^{10}	Q_i^{11}	Q_i^{12}
$i \in I$	1	0	32	100	10	100	36	31	59	37	100	11	39
	2	0	131	135	100	225	40	67	126	84	251	1	85

Table 7. Inventory levels for the first model.

		$j \in J$											
		V_i^0	V_i^1	V_i^2	V_i^3	V_i^4	V_i^5	V_i^6	V_i^7	V_i^8	V_i^9	V_i^{10}	V_i^{11}	V_i^{12}
$i \in I$	1	100	41	0	33	0	27	0	0	0	0	39	0	0
	2	150	20	0	0	0	95	0	0	0	0	111	0	0

Table 8. Holding costs (thousand dinars) for the first model.

		$j \in J$												Holding Costs
		0	1	2	3	4	5	6	7	8	9	10	11	12	
$i \in I$	1	5000	2050	0	1650	0	1350	0	0	0	0	1950	0	0	12000
	2	75	10	0	0	0	47.5	0	0	0	0	55.5	0	0	188
Total holding costs															12188

Table 9. Purchasing costs (thousand dinars) for the first model.

		$j \in J$												Purchasing Costs
		1	2	3	4	5	6	7	8	9	10	11	12	
$i \in$	1	0	80000	250000	25000	250000	90000	77500	147500	92500	250000	27500	97500	1387500
	2	0	458.5	472.5	350	828.75	140	234.5	441	294	815.75	3.5	297.5	4336
Total purchasing costs (dinars)														1391836

Table 10. Transportation costs (thousand dinars) for the first model.

		$j \in J$												Transportation Costs
		1	**2**	**3**	**4**	**5**	**6**	**7**	**8**	**9**	**10**	**11**	**12**	
$i \in I$	**1**	0	9600	27500	3000	27500	10800	9300	17700	11100	27500	3300	11700	159000
	2	0	65.5	67.5	50	127.5	20	33.5	63	42	125.5	0.5	42.5	637.5
Total transportation costs														159637.5

Table 11. Best order quantities for second model.

		$j \in J$											
		Q_i^1	Q_i^2	Q_i^3	Q_i^4	Q_i^5	Q_i^6	Q_i^7	Q_i^8	Q_i^9	Q_i^{10}	Q_i^{11}	Q_i^{12}
$i \in I$	1	32	100	0	100	36	31	59	37	100	11	39	0
	2	131	135	100	256	39	67	126	84	250	2	85	0

Table 12. Inventory levels for the second model.

		$j \in J$												
		V_i^0	V_i^1	V_i^2	V_i^3	V_i^4	V_i^5	V_i^6	V_i^7	V_i^8	V_i^9	V_i^{10}	V_i^{11}	V_i^{12}
$i \in I$	1	100	73	100	43	100	63	31	59	37	100	50	39	0
	2	150	151	135	100	256	135	67	126	84	250	112	85	0

Table 13. Holding cost (thousand dinars) for the second model.

		$j \in J$												Holding Costs
		0	1	2	3	4	5	6	7	8	9	10	11	12	
$i \in I$	1	5000	3650	5000	2150	5000	3150	1550	2950	1850	5000	2500	1950	0	39750
	2	75	75.5	67.5	50	128	67.5	33.5	63	42	125	56	42.5	0	825.5
Total holding costs															40575.5

Table 14. Purchasing costs (thousand dinars) for the second model.

		$j \in J$												Purchasing Costs
		1	2	3	4	5	6	7	8	9	10	11	12	
$i \in I$	1	80000	250000	25000	250000	90000	77500	147500	92500	250000	27500	97500	0	1387500
	2	458.5	472.5	350	832	136.5	234.5	441	294	812.5	7	297.5	0	4336
Total purchasing costs														1391836

Table 15. Transportation costs (thousand dinars) for the second model.

		$j \in J$												Transportation Costs
		1	2	3	4	5	6	7	8	9	10	11	12	
$i \in I$	1	9600	27500	3000	27500	10800	9300	17700	11100	27500	3300	11700	0	159000
	2	65.5	67.5	50	128	19.5	33.5	63	42	125	1	42.5	0	637.5
Total transportation costs														159637.5

Comparison Between ESP and Gas Lift in Buzurgan Oil field/Iraq

Abdul Aali Al Dabaj

University of Technology/Petroleum Technology Department
E-mail: resaldabaj@yahoo.com

Samaher AbdilRassol Lazim
Lecturer

University of Technology/Petroleum Technology Department
E-mail: samaher.rasul@yahoo.com

Omar Ayad Al-Sallami
Master Student
University of Technology/Petroleum Technology Department
E-mail: o_ayad@ymail.com

ABSTRACT

Buzurgan oil Field which is located in south of Iraq has been producing oil for five decades that caused production to drop in many oil wells. This paper provides a technical and economical comparison between the ESP and gas lift in one oil well (Bu-16) to help enhancing production and maximize revenue. Prosper software was used to build, match and design the artificial lift method for the selected well, also to predict the well behavior at different water cut values and its effect on artificial lift method efficiency. The validity of software model was confirmed by matching, where the error difference value between actual and calculated data was (-1.77%).
The ESP results showed the durability of ESP regarding the increment of water cut value, on the other hand Gas lift design was restricted to surface injection pressure and injected gas volume which in return causes a restriction to production rate specially when water cut value increases. Economically the results showed ESP is cheaper and more applicable than gas lift.
Key words: ESP, gas lift, bazurgan oil field, prosper.

مقارنة بين المضخة الغاطسة والرفع بالغاز في حقل بزركان\العراق

د.عبد العالي الدباج
خبير نفطي
الجامعة التكنولوجية\قسم تكنولوجيا النفط

د.سماهر عبد الرسول
مدرس دكتور
الجامعة التكنولوجية\قسم تكنولوجيا النفط

عمر اياد السلامي
طالب ماجستير
الجامعة التكنولوجية\قسم تكنولوجيا النفط

الخلاصة

علئ مدئ الخمس عقود المنصرمة شهد حقل بزركان الواقع في جنوب العراق انخفاض ملحوض في الانتاج الئ الوقت الحالي مما تطلب ايجاد حلول لانعاش الانتاج في الحقل المذكور. ستوفر هذه الورقة البحثية دراسة لمقارنة الانتاج بين طريقة الرفع بالمضخات الكهربائية الغاطسة والرفع باستخدام الغاز وايضا دراسة اقتصادية مصغرة لايضاح امكانية تطبيق الطريقتين.تم استخدام برنامج بروسبير لبناء ومطابقة نموذج البئر المصمم حاسوبيا وايضا لدراسة تاثير ارتفاع القاطع المائي علئ انتاج الطريقتين.تم الحصول علئ تطابق بين البيانات الحقلية والمحسوبة بفارق (-١,١٧%) .اظهرت النتائج تفوق المضخة الكهربائية الغاطسة علئ الرفع باستخدام الغاز من الناحيتين العملية والاقتصادية ،حيث استطاعت المضخة الغاطسة زيادة

الانتاج اكثر من ضعف وامكانية استمرار الانتاج بهذا المعدل حتئ مع ارتفاع القاطع المائي ومن الناحية الاقتصادية كانت المضخة الغاطسة اقتصادية اكثر.
الكلمات الرئيسية: المضخة الغاطسة، الرفع الصناعي بالغاز، حقل بزركان النفطي، بروسبير

1. INTRODUCTION

Many oil production improvement methods are involved today in the oil industry but, so far ESP and gas lift are the most common methods that are widely used in many oil fields. A study in 2006 proved that gas lift method occupies 50% of artificial lift method and ESP is sharing 30% of the total artificial lift method in the world, **Ehsan, 2011**.

Maximum potential of any field can be achieved from enhancing the production with less expenditures and this can be done by choosing the most economical artificial lift method. The methods selection is vastly variable from a particular field to another. The history of previously used artificial lift method in the selected field or nearby field can provide a great help in choosing the proper method and never forget to mention that the method selection includes operator experience; the available method of installation in different fields; determining what methods will lift at the desired rates and from the required depths; determine the lists of advantages and disadvantages; evaluation of operating costs, initial costs, production capabilities, etc. Computerized method can simplify the selection process and provide a great deal of accuracy and time saving.

Buzurgan oil field is located in the South–Eastern part of the Republic of, the oil field was discovered in 1970, and in November 1976 its development was started. The field consisting of two domes, southern and northern, the main production layer is Mishrif formation at a depth of (4000 m) where 52 wells have been drilled till 2016 in this field, **al Ansary, 2000**.

2. BUILDING AND MATCHING THE WELL MODEL IN PROSPER

Well BU-16 with current production of 946 STB/day showed the serious need for the artificial lift method due to rapid decline in production comparing with year 2000 where the production was 1680 STB/Day. Building the well model in Prosper consists of modeling the physical part, PVT matching and IPR/VLP quality check.

2.1 Physical part: this part includes analyzing the final well reports starting from the casing setting depths to tubing string compositions and depth for each equipment with internal and external diameter for each section then entering the arranged well completion data and perforation intervals, where the final well depth is 4050.25m, tubing depth 3775.5m and Perforation Intervals are 3806-3814.5 m.

2.2 PVT matching: A black oil model has been used to determine the PVT properties that describe the fluid behavior under different flow conditions. The objective of matching is to eliminate uncertainties based on measured data, operating conditions and create a model that follows field measurement by choosing the best correlation that will be used for the future calculations in PROSPER software. **Table 1** shows the used PVT data for matching.

Sorting, analyzing and entering the differential liberation PVT data for well (Bu-16) is the major step after that the software will run a regression process and propose correlations that can match the actual PVT data from the laboratory. The correlations that match the PVT properties in (Bu-16) were Lasater for Bubble point, Gas Oil Ratio and Oil formation volume factor, and Beal et al correlation for Oil Viscosity, **Fig.1** shows the match point of GOR with the selected correlation. The correlation selection criteria are based on the value of parameters 1&2 that are shown in

Table 2, where Parameter1 is a multiplier whereas Parameter 2 is a shift. Therefore, the best correlation is the one with a parameter 1 close to unity and parameter 2 close to zero.

2.3 Pressure Gradient Matching: This step is essential for choosing the correct correlation that matches the well condition for modeling the multiphase flow that occurs during production. Such match is done when a test point known that includes a (flow rate, well head pressure, reservoir pressure, gauge depth that have been used in test and the gauge reading pressure at the test depth). as the software uses a non-linear regression to best fit a gradient survey. Comparison of the fit parameters will identify which correlation required the least adjustment to match the measured data. This process used to calculate the pressure distribution along the production tubing which is important to determine the multiphase flow type in each section on the production pipe.

Three pressure test points as shown in **Table 3** were used for well (Bu-16) to achieve selecting the best pressure gradient correlation. In This Step pressure gradient plots will be generated with different correlations to be compared with measured gradient survey data. The matched correlation (Beggs and Brill) was selected depending on the test points matching with the correlation graphs **Fig.2** and the matching parameters (Standard deviation:0.000976, Parameter1=1.0296, Parameter 2 = 1) where Parameter 1 is the multiplier for the gravity term in the pressure drop correlation and Parameter 2 is the multiplier for the friction term. If all the data are consistent, these two parameters should be within a ±10% tolerance from the unity.

2.4 VLP/IPR Quality check: This is the final step of the matching process it uses the same test points entered in the pressure gradient step to make sure that the vertical lift performance and inflow performance relation match with the selected correlation in the pressure gradient match step, the software usually draw a graph between VLP and IPR to check that the actual field production test point match the calculated in software depending on the selected correlation as shown in **Table 4.**

3. ARTIFICIAL LIFT DESIGN

PROSPER software is built to let the user design an artificial lift method for a well based on the entered data that the user will provide, normally the artificial lift design in PROSPER is achieved after designing and matching a naturally flow single well model. In case of naturally flow wells, where matching the well parameter in its natural flow condition is the corner stone to build an accurate artificial lift design by eliminating the uncertainty when a correct matching is achieved. After matching is achieved and the required correlation is selected, it is time now to design the artificial lift method which includes designing an ESP (Electric submersible pump) and artificial Gas lift for each well.

3.1 ESP Design

Design of Electrical Submersible Pump in PROSPER allows the User to design an ESP installation. The design is performed in two steps:

1. Determine the required pump head to achieve a specified production rate
2.Select a suitable combination of pump, motor and cable for application.

The ESP design starts with selecting the ESP setting depth in this well the selected depth was set to (3800 m) where it should be above the perforation intervals, **Larry, 2007** (3806-3814.5 m).

3.1.1 Operation Frequency**:** ESP can work at different frequencies after selecting many frequencies it turns out the optimum frequency for the current well condition is 60Hz that gave the best operating efficiency; this is an adjustable option than can be set later for different production rate in the future.

3.1.2 Maximum outside diameter: this option is to set the maximum OD for the ESP pump and motor. The selection criteria were based on API recommendation for ESP selection as in **Fig.3**, **Larry, 2007**, the production casing size for well (Bu-16) at the setting depth above perforation was (6 5/8 in) so the selected ESP O.D. for this option is (5.13 in).

3.1.3 Cable length: The total cable length should be about 100 ft. (30 m) longer than the measured pump setting depth to make surface connections at a safe distance from the wellhead, **Larry, 2007**, so an extra 30m were added to the cable length from surface to setting depth.

3.1.4 Design rate**:** The design rate is specified by the casing size for the well where the min rate should be 750 STB/Day and max 12000 STB/Day for (6 5/8 in) and pump size (5.13 in) as shown in **Fig.3**, the design rate is usually set by the desired rate of production according to pump size any rate from 750 STB/Day to 12000STB/day will make the design valid and efficient, so the selected rate was 3500 STB/Day.
The next step is to calculate the head required to be supplied by the pump to achieve a specified production rate. PROSPER uses the IPR from System Inflow Performance and the specified VLP correlation to calculate the flowing pressure at the sand face finds and the pump intake pressure for the design production rate.
The calculated results showed that the head required to achieve the desired production is 1306.5m with pump intake pressure and discharge pressure of (3211 psig) and (5262 psig) respectively.
According to the calculated head, production casing size and the pump efficiency for the condition of selected well the ESP design results are as follow in **Table 5**. **Fig.4** can show the designed ESP assembly efficiency for the selected production rate at 60 Hz operation frequency.

3.2 Gas Lift Design

Using the same matched well model for designing gas lift method, the design production rate was calculated from the possible maximum production rate, other entered parameters were as follow:
Gas lift gas gravity: assuming the same produced gas to be reinjected with specific gravity is 0.76.
3.2.1 Maximum depth of injection: The maximum depth of injection must be shallower than the production packer, the injection depth to be entered in PROSPER was 3700 m.
3.2.2 Operating injection pressure and kick-off injection pressure: Injected pressure is usually ranging from 100 psi to 300 psi per 1000 t (304.8 m) of depth, **Larry, 2007**, so the design injected pressure was 2450 psia where the calculated injection pressure was 2350 psia. injection pressure is important to keep the injection point as deep as possible to the designed injection depth and also to enable inject the gas volume to selected depth.
Gas lift design performance are summarized in **Table 6** where three valves (type Camco R-20 Valve) at depths (1689.6m, 2355m, 2453m) selected according to **Fig.5** that shows the equilibrium curves for Gas lift design. This design is good enough to support lifting the crude oil to the surface with optimum gas injection volume of 2.6 MMSCF/Day with maximum possible production rate. **Fig.6** shows the Gas lift performance curve for well Bu-16.

4. RESULTS

Running Nodal analysis with sensitivity case of water cut increasing on Bu-16 natural flow condition, shows that the well stop production when water cut value reaches to 30%. **Fig.7** shows the IPR/VLP curve behavior at different water cut values for natural flow condition. This analysis shows the importance of an artificial lift method for supporting the production when water cut value increase in the future.

Results showed that ESP will increase the production to (3615 STB/Day) at water cut 0% and the well would continue producing oil when water cut value reaches to 50% **Table 7** summaries the results for ESP design at different water cut values with reservoir pressure 5050 psi while **Fig.8** shows the VLP/IPR with PIP (pump Intake Pressure) after ESP instillation.

Gas lift design shows that the production would increase to maximum value of 3010 STB/Day at reservoir pressure of 5050 Pisa. **Table 8** shows the summary production results for gas lift design in well (Bu-16). **Fig.9** shows the IPR/VLP for gas lift at pressure 5050 psia with different water cut.

5. ECONOMIC EVALUATION

To make this comparison more realistic an economic evaluation conducted. Most of the special economic data for Buzurgan oil field are not available therefor the ESP economic data were obtained from Ahdeb oil field where there are 192 ESP units, while a modern study in West Qurna field, **SOC, PRDC, UOB, 2012** was used for the gas lift equipment prices. The loss of production during the artificial lift method installation and workover also needed to be considered in economic evaluation where the well is shut during installation. The assumed oil price was 50$ per barrel. Field experience in Ahdeb oil field shows that ESP units working life ranging from 430 days to 1000 days. ESP installation take from 3 to 8 days depending on the operations needed to be done. ESP renting cost ranges 260-300$ per day including the maintenance.

Gas lift equipment life time is usually 10-15 years. The relatively high expenses of full field gas lift project are caused by a new compressor having to be purchased. Gas lift high cost comes from the complex surface facilities required to achieve a gas lift design and work over time by minimum 10 days. It's assumed that the gas lift system needs maintenance every 2 years so it would be 7 times during the 15 years for each well. The data listed in **Table 9** show the gas lift estimations.

Its assumed that the ESP need maintenance every 560 days (1.5 year) so it would be 10 times during the 15 years. The assumed workover time for maintenance is 6 days that would shut a well with average production of (1500 bbl/day). The assumed ESP rent cost is 300$ per day and the workover well cost is 1.5 MM USD$. **Table 10** shows the detailed ESP cost estimation.

6. CONCLUSIONS

1-The ESP lift method can increase the production to 3615 STB/Day while Gas lift increases the production to only 3157 STB/Day

2- The results for ESP Design show that the selected pump efficiency was 72.74%.

3- The Gas Lift Design showed that the optimum Gas Injected Volume is 2.6 MMSCF/Day

4- The ESP Design has increased the production by 14.51% more than Gas lift method.

5- ESP was more durable and efficient than gas lift when water cut increased and reservoir pressure decreased in the future.

6- Economic evaluation showed that the ESP lift method was cheaper than gas lift method.

REFERENCES

Ehsan Fatahi, 2011, Selection of the best artificial lift method in one of the Iranian oil field by employment of ELECTRE Model, British Journal of Applied Science and Technology. 172-180.

Larry W. Lake, 2007, petroleum engineering handbook, Society of Petroleum Engineers

Rafeeq al Ansary, 2000, Modern Field Geological Study in Buzurgan Field, Reservoir and Development Study Department, Ministry of Oil, Iraq.

SOC, PRDC, UOB, 2012, Feasibility of Gas Lift Vs ESP to Increase Oil Production Rate in West Qurna Field.

ABBREVIATIONS

BHP: bottom hole pressure, psi
ESP: electric submersible pump
GOR: gas oil ratio, scf/stb
IPR: inflow performance relation
PIP: pump intake pressure
VLP: vertical lift performance

Table 1. PVT data for well (Bu-16).

Property	**Value**
GOR SCF/STB	695.542
Specific gravity of Gas	0.76 (air = 1.0)
Water Salinity (PPM)	80000
Reservoir pressure, Psi	5020
Bubble point pressure , psi	2901.44
API	23.5
Temp. ^{o}C	112

Table 2. Match statistics for well (Bu-16).

Property	Standard deviation	Parameter 1	Parameter 2
Bubble point		0.88772	-42.456
Gas Oil Ratio	20.9841	1.44251	3.4416
Oil FVF	0.019343	1.0544	-0.04633
Oil viscosity	0.080142	0.35178	0.42254

Table 3. Data entry for pressure gradient match.

Well name	Well head pressure (psi)	Test rate (STB/Day)	Gage depth (m)	pressure (psi)
Bu-16	327	946	3370	3976
			3540	4234
			3779	4537

Table 4. Calculated and measured production rate, well (Bu-16), well head pressure:330 psi.

Correlation	Test Rate	Calculated Rate	Error %
Beggs and Brill	946	929.2	-1.77

Table 5. ESP design and specifications.

Parameter	Well Bu-16
Pump Name	CENTRILIFT-E127
Motor Name	Boret- EDB125117B5
Motor Name Plate Power (hp)	168.00
Motor Name Plate Volts (volts)	2100.00
Motor Name Plate Amps (amps)	49.00
Number Of Stages	123
Power Required(hp)	156.743
Pump Efficiency(%)	72.743
Current Used (amps)	16.50
Motor Efficiency(%)	83.419
Motor Speed (rpm)	3464.67
Voltage Drop Along Cable(volts)	67.41
Voltage Required @ Surface(Volts)	2587.41
Cable Name	#1 Aluminium 0.33(volts/1000ft) 95 amps max

Table 6. Bu-16 Gas lift design results, Camco R-20 Valve.

Set num.	Valve Type	Measured depth (m)	Tubing pressure (psia)	Casing Pressure (psia)	Temp.@ Valve (^{o}C)	Port Size (64^{th} in)	R Value	Valve opening pressure (psia)	Valve closing pressure (psia)
1	Valve	1689.6	2070.9	2994.5	107.3	12	0.038	2994.5	2959
2	Valve	2355	2693.8	3103.33	109.6	12	0.038	3103.3	3087
3	Valve	2453	2777.89	3027.89	109.86	12	0.038	3027.89	3018

Table 7. Summary results for ESP, well (Bu-16), Res. Pressure 5050 psi,well head pressure 450 psi.

Water cut %	Liquid Rate (STB/Day)	Oil Rate (STB/Day)	BHP (psia)
0	3615	3615	3915
10	3598	3238	3976
20	3577	2861	3982
30	3551	2485	3990
40	3519	2111	4000
50	3481	1740	4011

Table 8. Gas lift results for well Bu-16, reservoir pressure 5050 psia, gas vol. 2.6 MMSCF/Day, well head pressure 450 psia.

Water cut %	Liquid Rate (STB/Day)	Oil Rate (STB/Day)	BHP (psia)
0	3157	3157	4108
10	3026	2724	4147
20	2896	2317	3185
30	2754	1928	4228
40	2592	1555	4276
50	2485	1242	4308

Table 9. Gas lift cost estimation for one well.

Item	Unit cost MMUSD$
Manifold	3.5
Gas compressor	40
*Shut down cost for work over	5.25
Work over cost for 7 times	10.5
1 Km of (4 in) flow line	0.25
1 km of (14 in) flow line	0.5
Gas storage tank 50 MMSCF	15
Sum	75

*shutdown cost for work over = (10 days work over) × (1500 bbl/day) ×(50$ per bbl.) × (7 times needed for work over during 15 years

Table 10. ESP cost estimation.

Item	Cost for 15 years per well MM USD$
Pump rent	1.642
Shut down cost for work over*	4.5
Work over cost	15
Sum	21.142

*shutdown cost= (6 days work over) × (1500 bbl/Day) × (50$ price for 1 bbl) × (10 times needed for work over in 15 years)

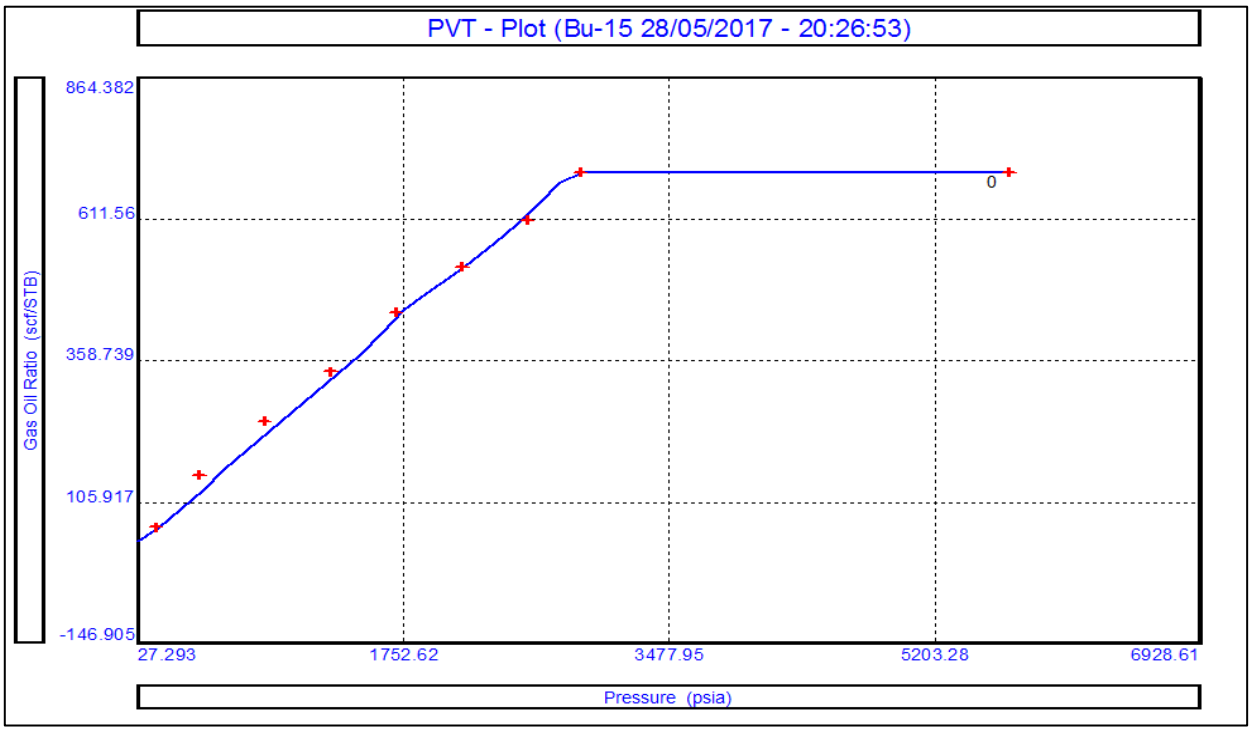

Figure 1. Gas oil ratio matching with Lasater correlation in PVT properties match of avaerage PVT data.

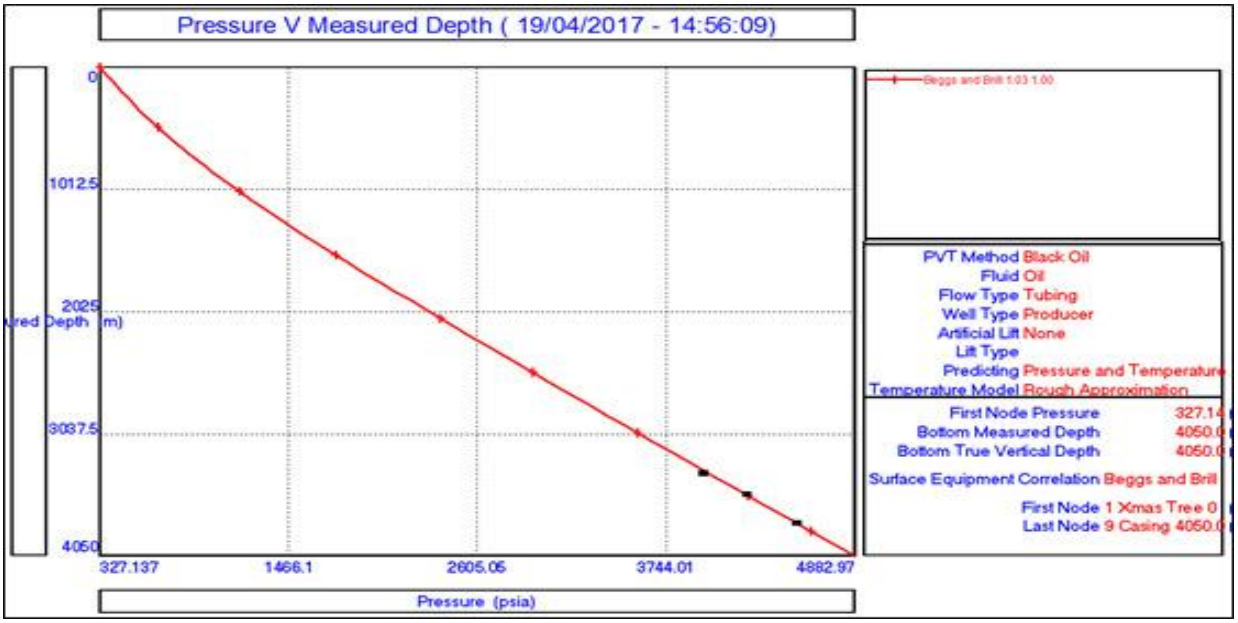

Figure 2. Pressure Gradient match with Beegs and Brill correlation.

Casing Size, in. (mm)	Pump Diameter, in. (cm)*	Flow Rate—Minimum, B/D (m^3/d)**	Flow Rate—Maximum, B/D (m^3/d)**
4 ½ (114.3)	3.38 (8.57)	550	3,100
5 ½ (139.7)	4.00 (10.16)	150	6,800
6 ⅝ (168.3)	5.13 (13.02)	750	12,000
7 (177.8)	5.38 (13.65)	900	18,400
7 ⅝ (193.7)	5.62 (14.29)	9,500	24,000
8 ⅝ (219.1)	6.75 (17.15)	5,000	46,000
10 ¾ (273.0)	8.75 (22.23)	10,300	32,200
13 ⅜ (339.8)	10.25 (26.04)	19,200	58,900

Figure 3. Typical Pump Diameter and Flow Rate for ESP according to API configuration.

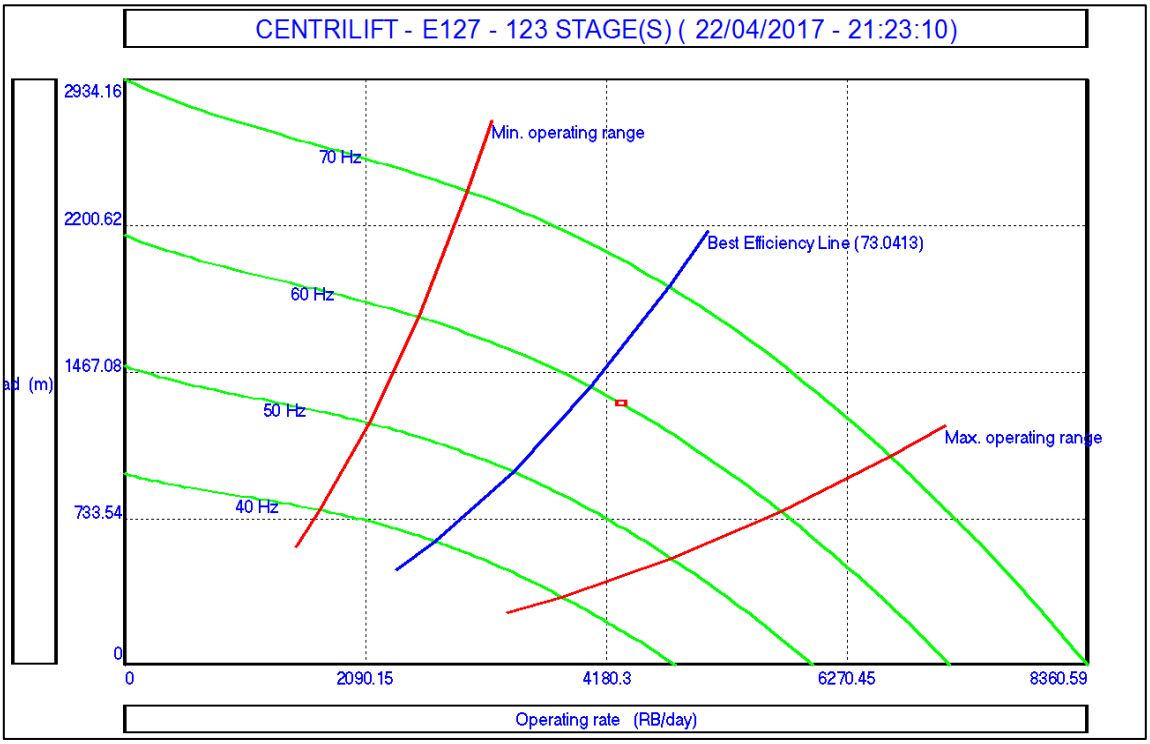

Figure 4. pump efficiency curves at 60 Hz (Bu-16).

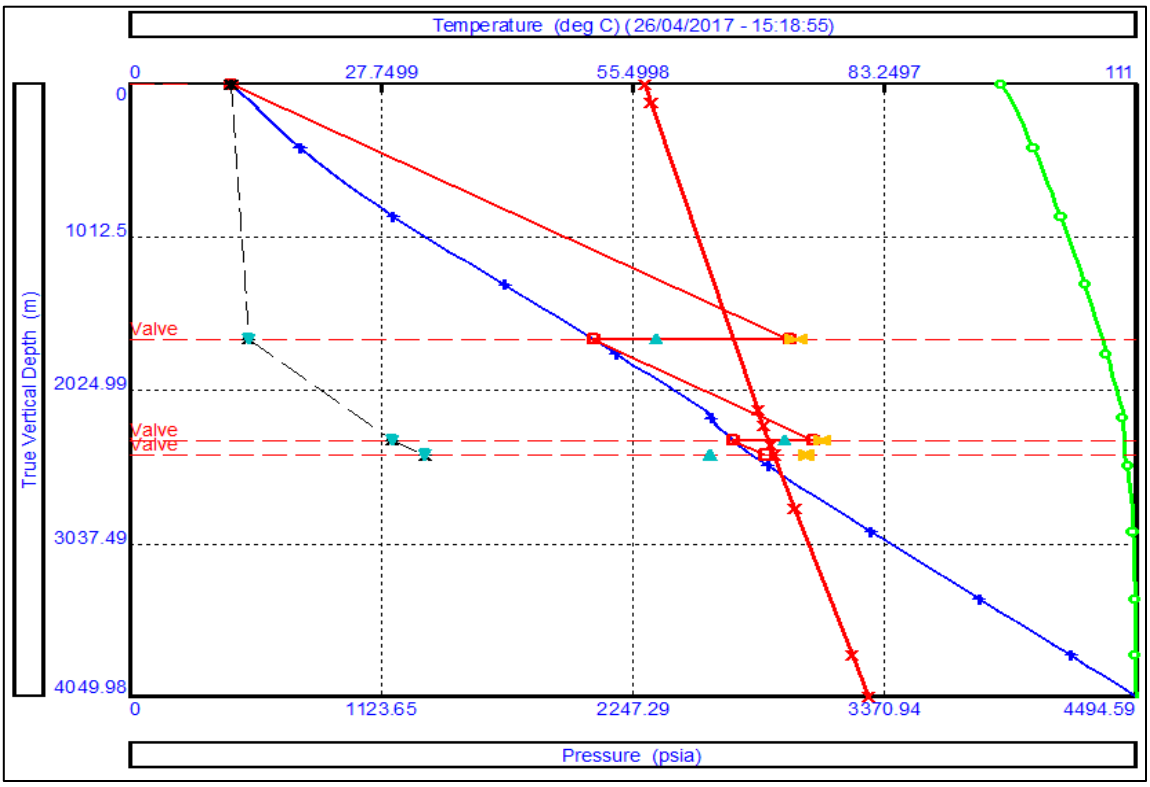

Figure 5. Equilibrium curve for well Bu-16 (Gas Lift).

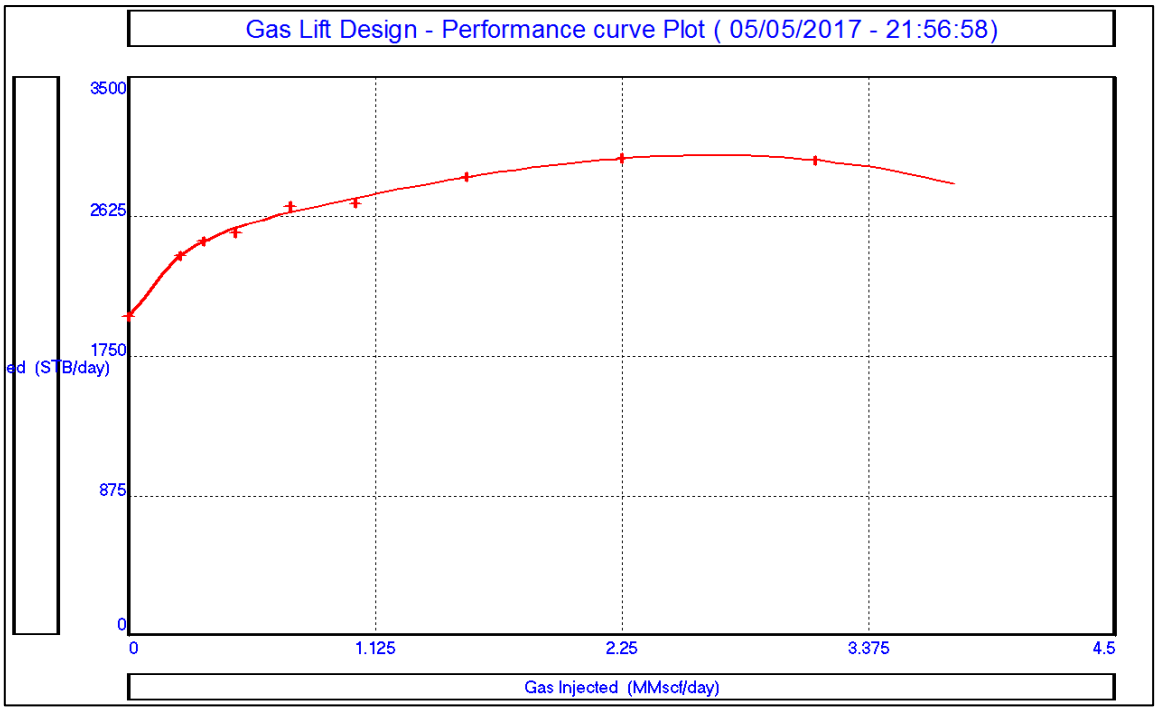

Figure 6. Gas lift performance curve for well Bu-16.

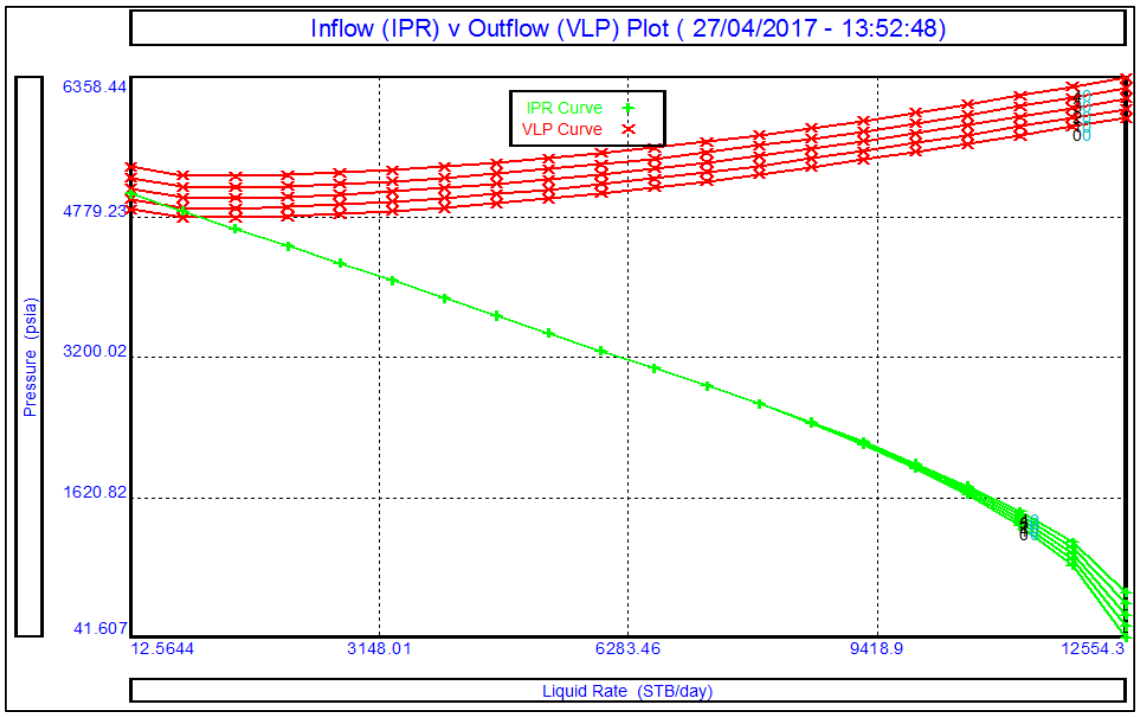

Figure 7. VLP/IPR curve for well (Bu-16), res. Pressure 5050 psia, water cut (0-50 %).

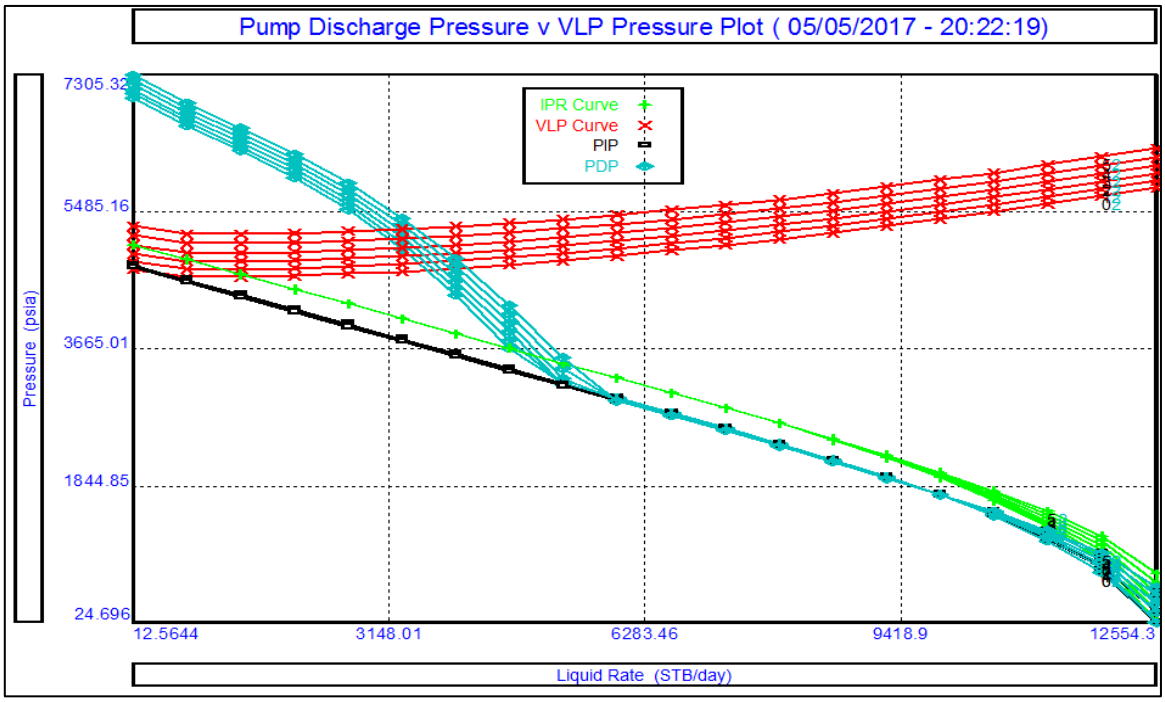

Figure 8. VLP/IPR curve for well (Bu-16) with ESP,

Reservoir. Pressure 5050 psia, water cut (0-50 %).

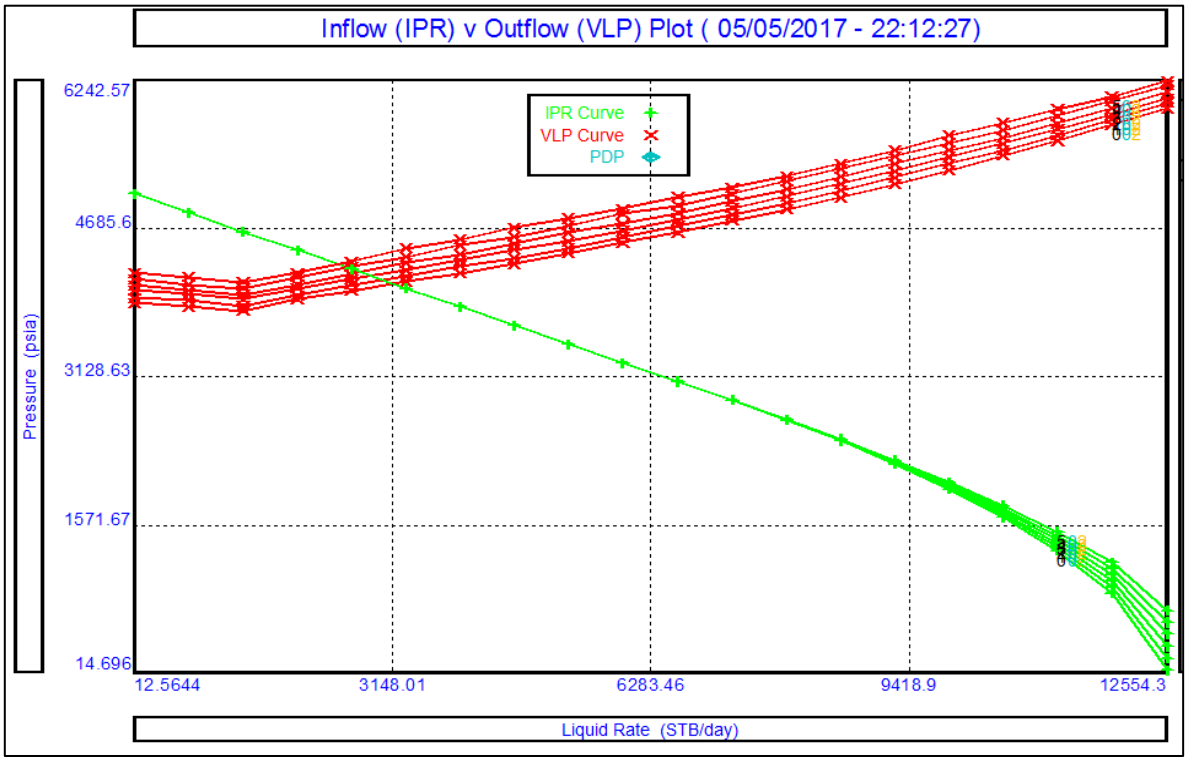

Figure 9. Gas lift VLP/IPR curve for well Bu-16
reservoir pressure 5050 psia, water cut(0-50%).

Producing Coordinate Time Series for Iraq's CORS Site for Detection Geophysical Phenomena

Dr. Oday Yaseen Mohamed Zeki Alhamadani
College Of Engineering, University of Baghdad
E-mail:oday_alhamadani@hotmail.com

Mays Qusay Saeed
College Of Engineering, University of Baghdad
E-mail:alazawemays@yahoo.com

ABSTRACT

Global Navigation Satellite Systems (GNSS) have become an integral part of wide range of applications. One of these applications of GNSS is implementation of the cellular phone to locate the position of users and this technology has been employed in social media applications. Moreover, GNSS have been effectively employed in transportation, GIS, mobile satellite communications, and etc. On the other hand, the geomatics sciences use the GNSS for many practical and scientific applications such as surveying and mapping and monitoring, etc.
In this study, the GNSS raw data of ISER CORS, which is located in the North of Iraq, are processed and analyzed to build up coordinate time series for the purpose of detection the Arabian tectonic plate motion over seven years and a half. Such coordinates time series have been produced very efficiently using GNSS Precise Point Positioning (PPP). The daily PPP results were processed, analyzed, and presented as coordinate time series using GPS Interactive Time Series Analysis. Furthermore, MATLAB (V.2013a) is used in this study to computerize GITSA with Graphic User Interface (GUI).

The objective of this study was to investigate both of the homogeneity and consistency of the Iraq CORSs GNSS raw data for detection any geophysical changes over long period of time. Additionally, this study aims to employ free online PPP services, such as CSRS_PPP software, for processing GNSS raw data for generation GNSS coordinate time series.
The coordinate time series of ISER station showed a +20.9 mm per year, +27.2 mm per year, and -11.3 mm per year in the East, North, and up-down components, respectively. These findings showed a remarkable similarity with those obtained by long-term monitoring of Earth's crust deformation and movement based on global studies and this highlights the importance of using GNSS for monitoring the movement of tectonic plate motion based on CORS and online GNSS data processing services over long period of time.
Key words: tectonic plates motion, CTS, PPP, GITSA, CORS, CSRS.

أنتاج المتسلسلات الزمنية للموقع الأرضي لمحطة ال CORS في العراق للكشف عن الظواهر الجيوفيزيائية

د. عدي ياسين محمد زكي الحمداني
جامعة بغداد-كلية الهندسة

ميس قصي سعيد

الخلاصة

اصبحت انظمة الملاحة جزء لايتجزء من العديد من التطبيقات الجيودسية الواسعة والمختلفة، وأحد هذه التطبيقات استخدام الهاتف المحمول لتحديد موقع المستخدم لتوظيف المعلومات الموقعيه في الكثير من الاستخدامات كوسائل التواصل الاجتماعية و كذلك تحديد مواقع وسائل النقلال المختلفة مثل السيارات والطائرات والسفن. ومن ناحية اخرى يستخدم علم هندسة الجيوماتكس الانظمة الملاحية في العديد من التطبيقات العملية والعلمية كأنتاج الخرائط. في هذا البحث تمت معالجة الارصادات المأخوذة من محطة (ISER) الواقعة في شمال العراق والتي تعتبر من محطات ال(CORS) باستخدام اسلوب تعيين الموقع النقطي الدقيق وعلى مدى ست سنوات ونصف لبناء متسلسلات زمنية لحساب مقدار الحركة في الصفيحة التكتونية العربية، وقد انتجت هذه المتسلسلات الزمنية بكفاءة عالية باستخدام برنامج تحليل المتسلسلات الزمنية التفاعلي (GITSA)، ايضا تم

استخدام برنامج (MATLAB V.2013a) من اجل حوسبة برنامج (GITSA) مع واجهة المستخدم الرسومية (GUI). اظهرت المتسلسلات الزمنية لمحطة (ISER) حركة مقدارها (20.9+ ملم/سنة) باتجاه الشرق، (27.2+ ملم/سنة) باتجاه الشمال، و (11.3- ملم/سنة) باتجاه المركبة الرئسية. حيث اظهرت هذه النتائج تشابهاً كبيراً مع نتائج الدراسات الجيولوجية وهذا يوضح اهمية استخدام الانظمة الملاحية لمراقبة حركة الصفائح التكتونية على مدار فترات زمنية.

الكلمات الرئيسية: حركة الصفائح التكتونية، المتسلسلات الزمنية للمواقع، تعيين الموقع النقطي، المحطات المرجعية المستمرة.

1. INTRODUCTION

Over the past three decades, different navigation positioning systems have been developed by scientific communities due to the urgent needs for precise positioning systems which could work under a wide range of conditions. Thus, the GNSS, which in turn is an abbreviation for Global Navigation Satellite System, has been established and developed. The GNSS has developed noticeably and its applications have been employed in several fields in our daily activities, such as positioning, transportation, and telecommunication. What is more, GNSS has an effective role in different professional fields in geodesy, environmental monitoring, meteorology, mapping **Gleason and Gebre-Egziabher, 2009**.

In General, GNSS employs different navigation satellites to provide independent geospatial positions and enables everybody on this world to have the capacity to acquire information on their locations with near-perfect accuracy and pass on this information to others. Until recently, the GNSS consists of three global operational navigation satellite systems, these are United States NAVSTAR Global Positioning System (GPS), the Russian GLONASS, and the European Union's Galileo. More recently, GNSS has become an integral part of different applications. One of these applications of the navigation systems is the use of the mobile phone to locate the position of mobile owner for many applications of social media. Moreover, the navigation systems can be employed in transportation systems such as, cars, planes and, ships. On the other hand, there is wide range of applications which are specialized in geomatics science such as, mapping, networking, monitoring, etc..., **Noll, et al., 2008**.

The uninterrupted deviations in the geometry of geodetic control networks due to the Earth's deformation, is a major area of interest within the field of physical geodesy. Accordingly, research on the Earth's deformation have been carried out based on employing different space geodetic systems for measuring annual and semi-annual velocity estimates over particular periods. Such of these space navigation systems are Satellite Laser Ranging (SLR), Very Long Baseline Interferometry (VLBI), Global Positioning system (GPS), and Doppler Orbitography and Radiopostioning Integrated by Satellite (DORIS). Over the past three decades, different studies have approved the capability of using GNSS for supporting multidisciplinary applications, particularly the scientific applications which necessitates high level of positional accuracy over long period of time. Such of these applications are the long term monitoring of huge structure and tectonic plate motion, **Larson, et al., 1997**.

Bock, et al., 1993, processed around seventy days of Permanent GPS Geodetic Array (PGGA) data to prove the possibility of employing GPS data for investigation the seismic deformation before and after the seismic activities. **Bock, et al., 1993** results pointed to that there was no pre-seismic movements, robustly constant co-seismic movements at most PGGA positions. What is more, further studies were carried out for measuring the vertical crustal displacements based on estimation vertical velocities of control GPS (CGPS) stations. For example, **Wahr, et al., 2001,** analyzed the carrier-phase observations from two CGPS (Kellyville and Kulusuk) to estimate the up-down crustal signal of the Greenland ice sheet. The **Wahr, et al., 2001,** has received considerable critical attention owning to two reasons. Firstly, they implemented GIPSY OASIS

II V.5.0 for Precise Point Positioning processing technique with precise orbital information and satellite clock corrections produced by Jet Propulsion Laboratory (JPL). Furthermore, the most interesting finding of **Wahr, et al., 2001**, study was that the up-down velocity estimates which were generated based on CGPS observations, were compared with those estimates from absolute gravity measurements. **Deitrich, et al., 2005**, used Bernese GPS Software V5.0 with double-difference positioning technique to analyze GPS raw observation data for ten CGPS over the period from 1995 to 2002, which are distributed in the west part of Greenland, to investigate the crustal deformation in the up-down direction. Their finding should the importance of using homogenous and consistent satellite orbital information, satellite clock corrections, and Earth Orientation Parameters (EOP) for producing precise coordinate times series. **Wahr, et al., 2001**, study were expanded by **Khan, et al., 2008**, where they included additionally 3 CGPSs and analyzed further 7 years of CGPS observations at Kellyville and Kulusuk.
Rudenko, et al., 2013, analyzed GPS data for 403 CGPS which are distributed globally over the period from 1998 to 2007 to produce precise weekly solution. 266 CGPS of 403 CGPS were employed for producing height time series to calculate vertical velocity estimates which were compared later with corresponding estimates from tide gauge stations and additional GPS solutions. **Rudenko, et al., 2013**, study points to the noticeable agreement of about 1 millimeter per year between their solution and other solutions which were produced by Universit´e de La Rochelle. Finally, **Rudenko, et al., 2013,** emphasized on successful application of estimation the vertical displacement for tide gauges sites using GPS coordinate time series to enhance the vertical crust motion in tide gauge measurements of sea level variations.
For more details about the contribution of the coordinate time series generated by GNSS solutions for estimation vertical and horizontal of land movements, the reader is referred to **Alhamadani, 2014** research which addresses the main global and regional studies of the earth's deformation as one of the main and essential applications in geodesy. What is more, **Alhamadani, 2014** highlighted and discussed the role of continuous GNSS measurements for modeling plate motions in both of global and regional scales and modeling Glacial Isostatic Adjustment. The successful application of the GNSS for detection any displacement in stations positions is to process consistent and homogeneous GNSS raw data which consist of carrier-phase and code range observations and produced by Continuously Operating Reference Station (CORS). The CORSs have been significantly utilized in support of three dimensional positioning, meteorology, and geophysical applications around the world.

This research aims to figure out the Arabian tectonic plate motion using one of the CORSs which are located in Iraq. Furthermore, the processing of the raw GNSS data will be carried out using Precise Point Positioning (PPP) technique for producing coordinate time series over particular period of time. The PPP processing technique is carried out in this research using Canadian Spatial Reference System (CSRS) - PPP tool that provide a service for generation of positions of raw GNSS data with higher level of accuracy. Finally, the time series of station coordinates based on CSRS-PPP will be produced in this research using GPS Interactive Time Series Analysis (GITSA) **Goudarzi, M.A, et al., 2013** and **Goudarzi, 2015**.

Consequently, this research assesses the continuity, homogeneity, and precision of the GNSS observations of one CORS in Iraq and this will remarkably show any jump, shift, and any discontinuity in the raw data over the period of time. Based on what has been reviewed above, there are two questions that need to be answered:

1. Are the coordinate time series of CORS which are generated using PPP based in International GNSS Service (IGS) precise orbital information, Earth orientation

parameters, and satellite clock corrections, accurate, consistent, and homogenous over the complete period of time?

2. Are the precision, consistency, and homogeneity of the coordinate time series of Iraqi CORS, generated based on PPP sufficient to provide accurate and reasonable clarification for detecting different geophysical phenomena in Iraq over a period of time?

2. CASE STUDY AREA

Currently, the CORSs represent the main source of continuous raw GNSS observation data. At this time, there are two thousand and six hundred and sixty one CORSs which are distributed globally around the world, six of the CORSs are located in Iraq and distributed from the north to the south of the country. For more information, the reader is referred to https://www.ngs.noaa.gov/. These six CORSs were officially established by the National Geodetic Survey (NGS) and then independently owned and operated. These six CORSs are ISER, ISSD, ISBA, ISKU, ISNA, ISBS as shown in **Fig. 1**. The first two letters (IS) stand for Iraq Surveying while the last two letters stand for the province name, i.e. ER is Erbil, SD is Salah Adin, BA is Baghdad, KU is Kut, NA is Najaf, and finally BS is Basra.

To achieve the goals of this research, the carrier-phase observations from CORS-ISER were processed using Natural Resources Canada (NRCan), Canadian Spatial Reference System - Precise Point Positioning (CSRS-PPP). In this study, the ISER is selected due to the reason that ISER has approximately continuous GNSS raw data in comparison with other five stations over the period from the mid of 2009 to the end of 2016. **Fig. 2** shows the data availability for these six Iraqi CORSs, the horizontal axis presents the time for eight years from 2008 to 2016, where the vertical axis presents the six CORS stations, for example ISER station is being operated from 7th of July 2009 till the present time.

3. SINGLE POINT POSITIONING TECHNIQUE

One of the essential requirements for successful application of GNSS for distinguishing geohazards and anomalies is the availability of precise geodetic positions which have high absolute positional accuracy. These geodetic positions have been produced efficiently through PPP via synchronously computing the receiver clock correction estimates. Generally, PPP represents the practical application of the zero-difference processing technique. However, the successful implementation necessitates precise satellite orbital information which is compatible with precise clock correction estimates and Earth Orientation Parameters (EOP) **Zumberge, et al., 1997**.

As far as the Double-Difference (DD) relative positioning technique is concerned, it has been widely used by the GNSS users due to the reason that in the DD, simultaneous GNSS observations made at a couple of geodetic receivers to a couple of satellites are differenced to abolish some major biases such as the satellite clock and receiver clock biases and possibly diminish part of the atmospheric biases. The efficiency of DD depends on the baseline length between the receivers, GNSS data processing, and the length of period of observation. Nonetheless, these major biases can be modeled and corrected for short baselines of less than 20 km, **Blewitt, 1997**. Consequently, the positional accuracy of unknown stations depends on the accuracy of reference station, and thus, this accuracy is known as a relative accuracy, whereas the positional accuracy of the PPP depends entirely on the accuracy of the satellite position and the satellite clock corrections, **Linette, 2004**.

It is worth to mention here that most of studies of investigation the Earth's deformations based on GNSS positioning have been carried out using DD processing technique to obtain a high level of precision for three dimensional velocity estimates. However, other investigations have shown that absolute three dimensional velocity estimates of stations can be efficiently produced using PPP processing technique. Accordingly, in this research the PPP processing technique is used instead of DD, and this will yield the coordinates of the unknown station in the Earth-fixed Earth-center reference frame.

4. RESEARCH METHODOLOGY

This research was carried out by dealing with three main themes. Firstly, selection the optimum CORS in Iraq based on the data availability. Secondly, using GNSS processing software based on online service. Thirdly, presentation the changes in the three dimensional coordinate using coordinate time series analysis. Thus, the methodology of this research h is summarized as follow:

1. Download the raw GNSS observation data for a CORS-ISER via National Geodetic Survey (NGS) (https://www.ngs.noaa.gov/, (accessed October 11, 2017).
2. Post-processing the GNSS observation data using Natural Resources Canada (NRCan), Canadian Spatial Reference System - Precise Point Positioning (CSRS-PPP) for GNSS raw data post-processing.
3. Using the GPS Interactive Time Series Analysis (GITSA) by computerize it with Graphic User Interface (GUI) in MATLAB (V.2013a) to create coordinate time series.
4. Finding the velocities of the tectonic plate motions by numerical and statistical computations. **Fig. 3** shows the structure of the research methodology.

5. COORDINATE TIME SERIES ANALYSIS – GPS INTERACTIVE TIME SERIES ANALYSIS

Time series analysis is an important part of Geodesy and Geodynamics studies, particularly when continuous GNSS observations are utilized to explore very low rate of deformations. GITSA is precise and robust tools for processing and analyzing coordinate time series, **Goudarzi, et al., 2013**. GITSA software has been developed at the Center for Research in Geomatics (CRG), Laval University. Additionally, GITSA can be employed for investigating different time series in the field of Earth sciences, when the purpose of analysis is to distinguish the temporal behavior of individual of several time dependent variables within the time series. For example, The study of long-term record of mountain uplift, sea level fluctuations, millennium-scale variations in the atmosphere-ocean system and so on.

GITSA performs number of functions which range from time series data file import and transformation to wavelet spectral analysis. Additionally, GITSA comes with some utilities such as a GPS date converter that enables users to convert different date formats which are used in GNSS applications. In summary, all the coordinate time series analysis programing software can be utilized for:

1- Visual interpretation, for instance recurrence plots, spectrogram, and wavelet power spectrum.
2- Operations of time series processing, such as filtering and frequency responses of filters.
3- Statistical analysis, i.e. cross-spectral and auto-spectral analysis, evolutionary power spectrum, and wavelet power spectrum**, Goudarzi, 2015.**

Furthermore, GITSA includes ten math and statistical calculation approaches to make sure the highest level of accuracy and confidentiality in coordinate time series, these approaches are:

1. Jump detection and removal.
2. Outlier detection and removal.
3. Data interpolation.
4. Trend analysis.
5. Residual analysis.
6. Regression analysis.
7. Evolutionary power spectrum.
8. Amplitude spectral analysis.
9. Auto-spectral analysis.
10. Spectral analysis.

6. THE RESULTS AND DISCUSSION

The present study was designed to discuss a number of significant themes in the field of using space positioning techniques for geophysical applications. The first theme in this study focuses on employing one of the CORSs in Iraq for the purpose of detection the tectonic plate motion over the period from June 2009 till to December 2016. This theme necessitates investigating the GNSS data availability of 6 CORSs, which are distributed in Iraq, over the whole period of time which is mentioned before. The ISER CORS has the highest data availability and consequently its GNSS raw data, which was generated and archived in via NOAA's National Geodetic Survey over the whole period, was downloaded for further data processing. The second theme in this research deals with the ability of producing coordinate time series for CORSs in Iraq based on precise point positioning technique. The successful achievement of this theme depends entirely on:

1. using sophisticated software for processing the GNSS raw observation data on daily basis, and
2. using software for analyzing the output coordinates of selected CORS over the whole period of time and presenting the changes in the position components as a time series.

Without a doubt the process of producing precise, continuous and homogenous coordinate time series for ISER represents the most significant achievement and challenge in this research due to different reasons: the positional accuracy of PPP is massively affected by the quality of precise orbital information, satellite clock correction, and the EOP which are used for carrying out PPP processing. What is more and important, the compatibility between these precise products plays an enormous role in output PPP results. Thus, using CSRS online service for processing ISER data over six years and a half leads to a lack in the precision of PPP results as a result of inconsistency in used precise products. Consequently, any discontinuity, contradictory, and unexpected change in the coordinate time series are possibly due to:

1. changing in the used precise product sources, i.e IGS final products, IGS rapid products, or any analysis center own products,
2. changing in the used reference frame that is used for generation the IGS precise products,
3. changing in the station hardware, geodetic antenna and/or receiver, and finally
4. changing in the receiver firmware update.

In general, the findings in this research are presented as a numerical results based on statistical calculations and graphical results which are showed as coordinate time series based on GPS Interactive Time Series Analysis (GITSA) software. The difference in the coordinates are

calculated annually between last day and first day of the year in East, North and Up components over the period from the mid of 2009 to the end of 2015. These annual differences are illustrated in **Table 1** and **Fig. 4**. As it is shown in **Table 1** and **Fig. 4** that the maximum changes in East and Up components is appeared in 2012, while the maximum change in the North component happens in 2011. Overall, **Table 1** and **Fig. 4** show a clear displacement in station position in the direction North East and subsidence in the vertical position. **Table 2** shows the ISER movement in the horizontal direction for every year and the total mean of the horizontal direction for the whole period. **Table 3** demonstrations the annual velocity in millimeters per year from July 2009 to 2015 and the total mean velocity for E, N, and U components. In general, **Table 3** indicates to:

1- 2009/2 has the largest velocity in the Up/Down component, and minimum velocity in the East component.
2- 2010 has the smallest velocity in the Down component.
3- 2011 has the smallest velocity in the North component.
4- 2012 has the largest velocity in the East component.
5- 2013 has the largest velocity in the North component.

The graphical results which are the coordinate time series visualized in three figures, **Fig. 5** is to visualize the difference in the North direction, **Fig. 6** is to visualize the difference in the East direction, while **Fig. 7** is to visualize the difference in the Up direction.

For every figures there is two rectangular axis, the horizontal axis represents the time in years while the vertical axis represents the coordinate. The dots represent the station coordinate while the line on the does represents the stander deviation of the observation. The gabs between the dots caused by a zero value of the stander deviation at particular day.

The coordinate time series and the numerical and statistical analysis of ISER station showed a velocity (+20.9 mm/year) in the East component, (+27.2 mm/year) in North direction, and (-11.3 mm/year) in Up component. These findings showed a remarkable similarity with those obtained from the geological studies and this highlights the importance of using GNSS for monitoring the movement of tectonic plate motion over a particular period of time.

6. CONCLUSIONS

The purpose of the current study was to investigate the effectiveness of employing CORS in Iraq for detection the Arabian tectonic plate motion and any geohazard. Additionally, this study examined the GNSS data availability of six Iraqi CORSs and it has showed that the ISER CORS has the highest GNSS observation data in comparison with other five CORSs over 7.5 years. What is more, free online GPS post-processing services CSRS-PPP is used in this study for processing daily GNSS raw observation data over long period. This processing strategy was carried manually in this study and this represents a vast challenge as it necessities a massive effort for processing huge observation data on daily bases. The analysis of observation data undertaken here has extended our knowledge of the degree of consistency, and precision of satellite orbital information, satellite clock correction, and EOP products which were considered by CSRS-PPP for producing smooth, homogenous, continuous, and reliable position time series. However, the coordinate time series for the East offset of ISER station indicates to a recognizable outlier in the mid of 2011 which is a most likely cause of unpredictable random bias in the carrier phase observables that affects only the East component. On the other hand, the coordinate time series for the ISER station point to identifiable jumps in 2015 in the North, East, up-down components. The most probable reason for these jumps is inconsistency in the products that affect the horizontal and vertical positions, **Goudarzi, 2015**. Generally, the position time

series of ISER CORS showed similar trend, fluctuations and periodic signal over the whole period of processing.

7. REFERENCES

- Alhamadany, O., 2014, *Global NAVIGATION Satellite System Contribution for Observing the Tectonic Plate Movements*: Status and Perspectives. Baghdad University, College of Engineering, Journal of Engineering.
- Blewitt G., 1997, *Basics of the GPS Technique*: Observation Equations. *In: Geodetic Applications for GPS*, Swedish Land Survey.
- Bock, Y., Agnew, D. C., Fang, P., Genrich, J. F., Hager, B. H., Herring, T. A., Hudnut, K. W., King, R. W., Larsen, S., Minster, J. B., Stark, K., Wdowinski, S. & Wyatt, F. K 1993. *Detection of crustal deformation from the Landers earthquake sequence using continuous geodetic measurements.* Nature, 361, 337-340.
- Dietrich, R., Rülke, A. & Scheinert, M. 2005. *Present-day vertical crustal deformations in West Greenland from repeated GPS observations*. Geophysical Journal International, 163, 865-874.
- Gleason, S. & Gebre-Egziabher, D. 2009. *GNSS applications and Methods / Scott Gleason*, Demoz Gebre-Egziabher, editors, Artech House.
- Goudarzi, M.A., Cocard, M., Santerre, R. et al. 2013, *GPS Interactive Time Series Analysis Software. GPS Solution*, 17: 595. DOI 10.1007/s10291-012-0296-2.
- Goudarzi, M. A., 2015, N*oise Behavior in CGPS Position Time Series: The Eastern North America Case Study*, DOI 10.1515/jogs-2015-0013.
- Khan, S. A., Wahr, J., Leuliette, E., Van Dam, T., Larson, K. M. & Francis, O. 2008. *Geodetic measurements of postglacial adjustments in Greenland. Journal of Geophysical Research*, 113, B02402.
- Larson, K. M., Freymueller, J. T. & Philipsen, S. 1997. *Global plate velocities from the Global Positioning System. Journal of Geophysical Research*, 102, 9961-9981.
- Linette, P., 2004, Instantaneous Global Plate Mtion Model From 12 Years of Continuous GPS Observations. Journal of Geophysical Research, vol. 109, B08405.
- Noll, C., et al., 2008, *Development of Data Infrastructure to Support Scientific Analysis for the International GNSS Service, Journal of Geodesy*, vol 83, No. 3, PP. 309–325.
- Rudenko, S., Schon, N., Uhlemann, M., and Gendt, G., 2013, *Reprocessed height time series for GPS stations*. Journal of Solid Earth, Solid Earth, 4, 23–41, 2013.
- Wahr, J., Van Dam, T., Larson, K. & Francis, O. 2001, *Geodetic Measurements in Greenland and their Implications. Journal of Geophysical Research,* 106, 16,657-16,581.

- Zumberge, J. F., Heflin, M. B., Jefferson, D. C., Watkins, M. M. & Webb, F. H. 1997. *Precise point positioning for the efficient and robust analysis of GPS data from large networks.* Journal of Geophysical Research, 102, 5005-5017

Figure 1. Iraqi CORSs Map.

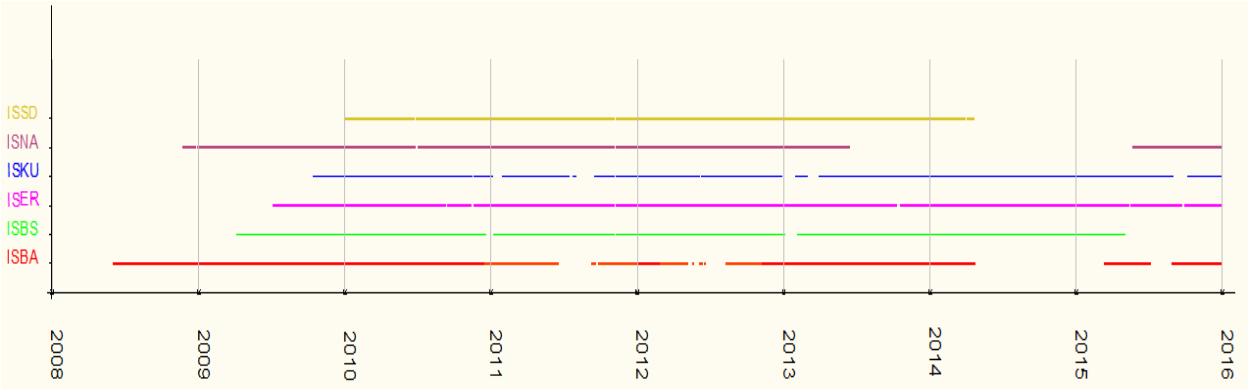

Figure 2. Iraqi CORS Data Availability.

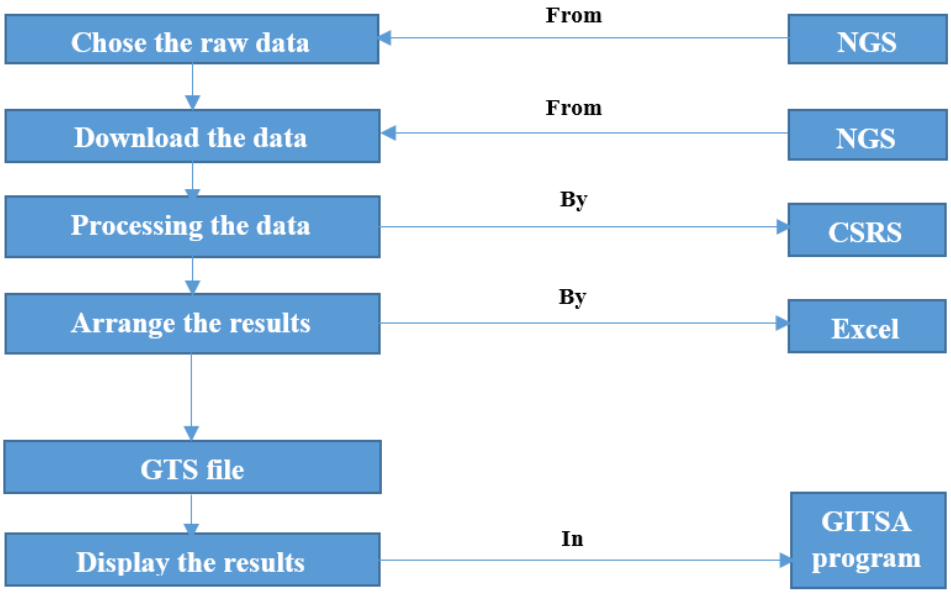

Figure 3. Structure of Research Methodology.

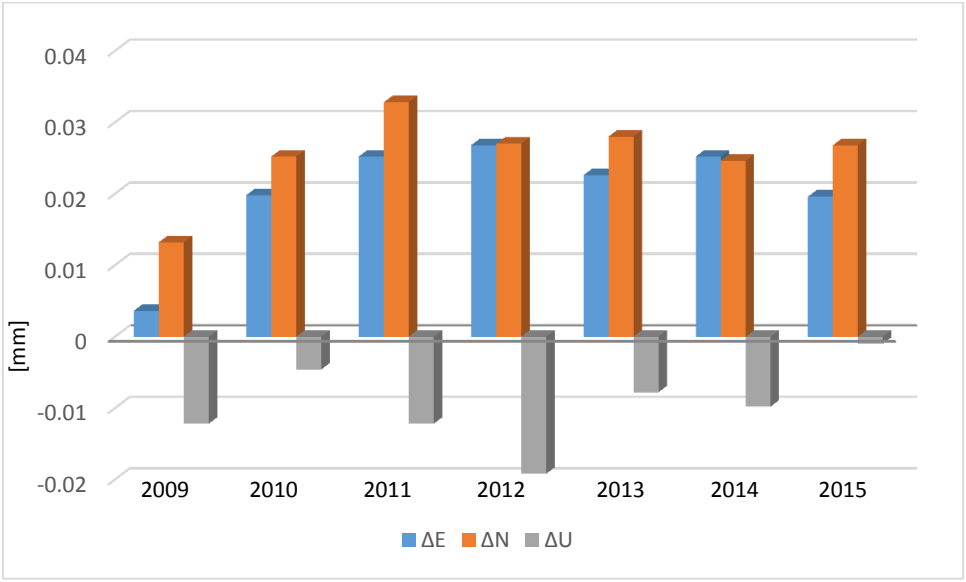

Figure 4. The Annual Changes In The Coordinates In Millimeters Unites.

.

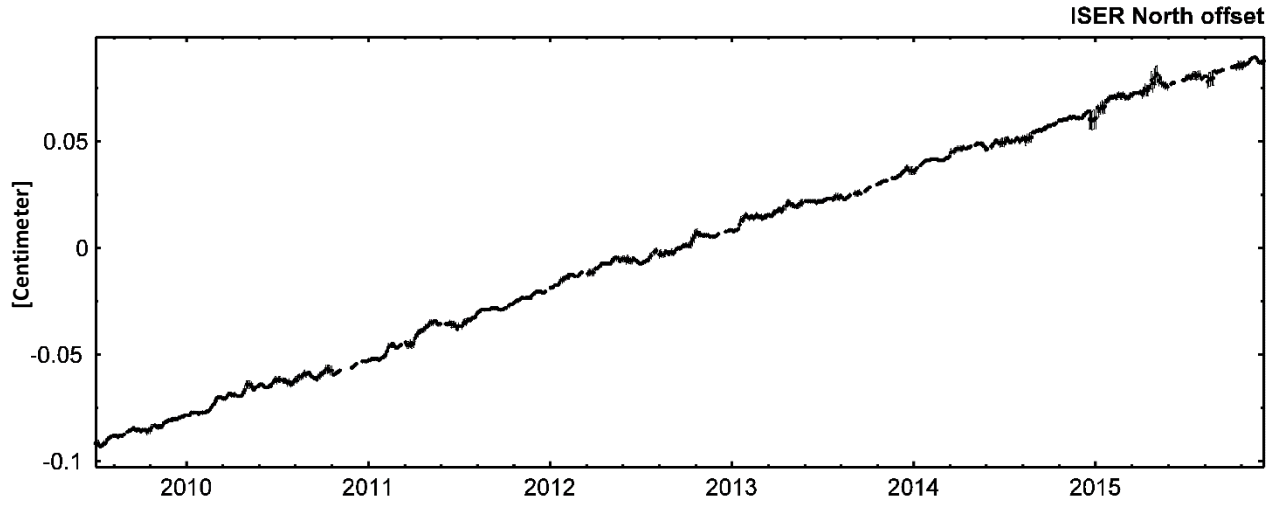

Figure 5. The coordinate time series for the North offset of ISER station.

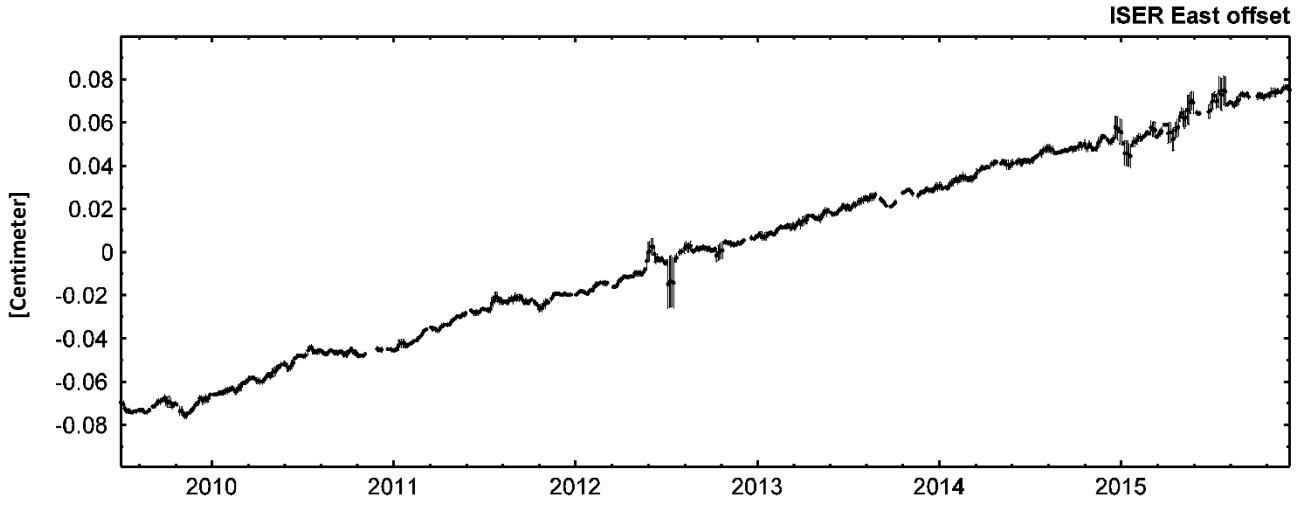

Figure 6. The coordinate time series for the East offset of ISER station.

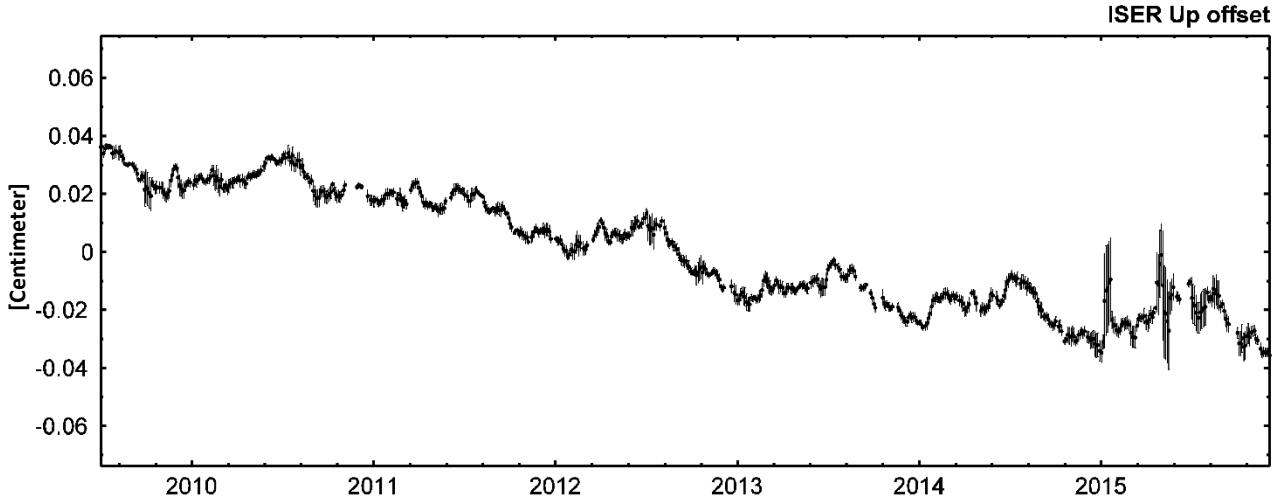

Figure 7. The coordinate time series for the Up offset of ISER station.

Table 1. The Annual Changes In The Coordinates In Millimeters Unites.

	Mid of 2009	2010	2011	2012	2013	2014	2015
ΔE	03.6	19.8	25.2	26.8	22.6	25.2	19.6
ΔN	13.2	25.2	32.8	27.0	28.0	24.6	26.8
ΔU	-12.2	-04.6	-12.2	-19.2	-07.8	-09.8	-01.0

Table 2. The Horizontal Direction Per Year And The Total Mean Horizontal Direction.

Year	Horizontal Direction
Mid 2009	N 15° 15' 18" E
2010	N 38° 09' 26" E
2011	N 37° 32' 05" E
2012	N 44° 47' 13" E
2013	N 38° 54' 31" E
2014	N 45° 41' 25" E
2015	N 36° 10' 47" E
Mean	N 38° 17' 24" E

Table 3. The Velocity Estimates In mm/year For Every Year Over The Whole Period.

	East Dir.	North Dir.	Up/Down Dir.
2009	+7.2	+26.4	-24.4
2010	+19.8	+25.2	-4.6
2011	+25.2	+32.8	-12.2
2012	+26.7	+26.9	-19.1
2013	+22.6	+28.0	-7.8
2014	+25.2	+24.6	-9.8
2015	+19.6	+26.8	-1.0
Mean	+20.9	+27.2	-11.3

ENGINEERING

College of Engineering University of Baghdad No.1 Vol. 24 January 2018

List of Contents

E-ISSN 2520-3339

P-ISSN 1726-4073

Journal of Engineering

A Scientific Refereed Journal
Published by
College of Engineering
University of Baghdad

January
2018

Number 1
Volume 24

E-ISSN 2520-3339

P-ISSN 1726-4073

مجلة الهندسة

مجلة علمية محكمة تصدرها
كلية الهندسة ـ جامعة بغداد

كانون الثاني
2018

العدد 1
المجلد 24

رقم الايداع في دار الكتب والوثائق ببغداد
2231 لسنة 2017

قـائـمـة الـمـحـتـويـات

القسم العربي: